THE
SHOCK AND VIBRATION
BULLETIN

Part 4
Structural Dynamics and
Modal Test and Analysis

DTIC
SELECTED
NOV 1 9 1987
S D
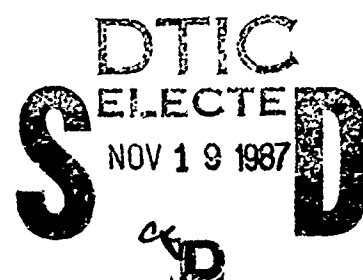
JANUARY 1987

A Publication of
THE SHOCK AND VIBRATION
INFORMATION CENTER
Naval Research Laboratory, Washington, D.C.

Office of
The Under Secretary of Defense
for Research and Engineering

87 10 28 028

THE
SHOCK AND VIBRATION
BULLETIN

JANUARY 1987

DTIC
COPY
INSPECTED
6

The 57th Symposium on Shock and Vibration was held in New Orleans, Louisiana, October 14-16, 1986. The Defense Nuclear Agency, Washington, DC and the U.S. Army Engineer Waterways Experiment Station, Vicksburg, Mississippi were the hosts.

Accesion For

NTIS CRA&I	☑	
DTIC TAB	☐	
Unannounced	☐	
Justification		

By ....
Distribution /

Availability Codes

Dist	Avail and / or Special

A-1

CONTENTS

PAPERS APPEARING IN PART 4

Structural Dynamics

Modal Test and Analysis

*This paper was presented in the Pyrotechnic Shock Workshop at the 57th Shock and Vibration Symposium

SESSION CHAIRMEN AND COCHAIRMEN

Date	Session Title	Chairmen	CoChairmen
Tuesday 14 October, A.M.	Opening Session	Dr. Don A. Linger, Defense Nuclear Agency, Washington, DC	Dr. Sam Kiger, U.S. Army Engineer Waterways Experiment Station, Vicksburg, MS
Tuesday 14 October, P.M.	Instrumentation	Mr. Richard P. Joyce, IIT Research Institute, Chicago, IL	Mr. W. Scott Walton U.S. Army Combat Systems Test Activity, Aberdeen Proving Ground, MD
Tuesday 14 October, P.M.	Shock Analysis	Mr. James D. Cooper, Defense Nuclear Agency, Washington, DC	Mr. William J. Flathau, JAYCOR, Vicksburg, MS
Wednesday 15 October, A.M.	Plenary A .	Rudolph H. Volin, P.E., Shock and Vibration Information Center, Naval Research Laboratory, Washington, DC	
Wednesday 15 October, A.M.	Nondevelopment Items Workshop, Session I, Methods	Mr. James W. Daniel, U.S. Army Missile Command, Redstone Arsenal, AL	Mr. Paul Hahn, Martin Marietta Orlando Aerospace, Orlando, FL
Wednesday 15 October, A.M.	Structural Dynamics I	Mr. Stanley Barrett, Martin Marietta Denver Aerospace, Denver, CO	Mr. W. Paul Dunn, The Aerospace Corporation, El Segundo, CA
Wednesday 15 October, A.M.	Isolation and Damping	Dr. Paul N. Sonnenburg, Physicon, Inc., Huntsville, AL	Matthew Kluesener, P.E., University of Dayton Research Institute, Dayton, OH
Wednesday 15 October, P.M.	Nondevelopment Items Workshop, Session II, Case Histories	Mr. Howard Camp, Jr., U.S. Army Communications-Electronics Command, Ft. Monmouth, NJ	Edgar K. Stewart, P.E., U.S. Army Armament Command, Dover NJ
Wednesday 15 October, P.M.	Structural Dynamics II	Dr. John L. Gubser, McDonnell Douglas Astronautics, St. Louis, MO	C. Allen Ross, Ph.D., P.E., Air Force Engineering Services Center, Tyndall Air Force Base, FL

vii

Wednesday 15 October, P.M.	Shock Testing	Mr. David Coltharp, U.S. Army Engineer Waterways Experiment Station, Vicksburg, MS	Mr. Steve Tanner, Naval Weapons Center, China Lake, CA
Thursday 16 October, A.M.	Plenary B	Mr. Jerome Pearson, Air Force Wright Aeronautical Laboratories, Wright-Patterson Air Force Base, OH	
Thursday 16 October, A.M.	Vibration Test Criteria	Mr. Tommy Dobson, 6585 Test Group, Holloman Air Force Base, NM	Mr. Edward Szymkowiak, Westinghouse Electric Corporation, Baltimore, MD
Thursday 16 October, A.M.	Modal Test and Analysis	Richard Stroud, Ph.D., P.E., Synergistic Technology, Cupertino, CA	Connor D. Johnson, Ph.D., P.E. CSA Engineering, Inc. Palo Alto, CA
Thursday 16 October, P.M.	Vibration Analysis and Test	Mr. Frederick Anderson, U.S. Army Missile Command, Redstone Arsenal, AL	Mr. David Bond, Northrop Advanced Systems Division, Pico Rivera, CA
Thursday 16 October, P.M.	Short Discussion Topics	Mr. William Wassmann, Naval Surface Weapons Center, Silver Spring, MD	

STRUCTURAL DYNAMICS

QUALIFICATION BY ANALYSIS OF IUS PLUME DEFLECTORS

R. F. Hain
Boeing Aerospace Company
Seattle, Washington

This paper describes the method for qualification by analysis of
Inertial Upper Stage (IUS) plume deflectors. The qualification
by analysis is based on a finite element model that is verified by
comparison with qualification test data from another configuration
of the plume deflector.

INTRODUCTION

Plume deflectors were added to the IUS to protect
the structure from the Reaction Control System
(RCS) rocket engine plume. Since the deflectors
were added late in the program, it was necessary to
qualify the design on an accelerated schedule. The
deflectors were qualified for the vibroacoustic
environment by a combination of test and analysis.
This paper describes the vibroacoustic test and the
finite element analysis used to qualify the
configurations in lieu of test.

There are five plume deflectors per IUS vehicle (one
under each pair of rocket engine nozzles located at
0, 90, 180 and 270 degrees around the vehicle, with
the final deflector covering the batteries located on
the Interstage) and two different configurations of
plume deflectors, one for the T-34D/IUS configura-
tion and one for the STS/IUS configuration. The
STS/IUS configuration was qualified by test while
the T-34D/IUS configuration was qualified by
analysis. A finite element (NASTRAN) model was
built for the T-34D configuration and the acoustic
noise environment applied using the frequency
response capability of NASTRAN. The T-34D model

results were compared to the test results of the STS
model qualification test responses to verify the
validity of the model. The comparison demonstra-
ted that the qualification by analysis could be
accomplished in a satisfactory manner.
It was vital that the comparison of model
predictions to test data show that the model was
acting in the proper manner to consider it a valid
model that could be used to qualify the T-34D
configuration plume deflectors and the loads
produced by them on the support stringers. Two
criteria were used to determine how well the
model would make these predictions: (1) it must
predict the fundamental resonant frequency of the
deflector within ±15%; and, (2) it must predict
acceleration response levels that would result in
conservative displacements at all locations when
compared to measured response levels. When
these two conditions are met, then the stiffness is
correct, deflections are conservative and the forces
at the support points are conservative.

MODEL DESCRIPTION

The model of the deflector at the IUS 90 degree
location is presented in Figure 1 with the coordi-

nate system identified. (Models were made for the deflector at 270 degrees as well as for the one covering the batteries.) Grid points are also identified. Views from the x-, y- and z-axes are presented in Figures 2 through 4. The plume deflector is attached to the stringers of the Equipment Support Section (ESS) of the IUS at the ends of the support structure shown schematically in Figure 5. The model was made up of NASTRAN plate elements (CQUAD4, CQUAD8, and CTRIA3) with bars to represent the supports. Instrumentation locations are also shown in Figure 5. The plume deflectors are made of Rene 51 steel with Young's Modulus equal to (29×10^6 psi = 1.31×10^5 MPA). Structural damping was used in the model. The damping forces are dependent on the frequency because NASTRAN calculates damping forces as a ratio of the stiffness matrix. This frequency dependence of the damping forces results in conservative loads and displacements. A structural damping value of 0.02 (Q = 50) was used for the analysis.

TEST AND ANALYSIS RESULTS

The plume deflectors were installed on an IUS vehicle used for structural test (designated Pathfinder Test Vehicle C (PTV-C)). They were then subjected to the 145 dB acoustic excitation shown in Figure 6. This was followed by an acoustic excitation of 151 dB for qualification. The 145 dB acoustic excitation was then repeated without the deflectors attached to the test vehicle. Comparisons of test data from the two 145 dB tests were made to determine the effects of the plume deflectors. The comparison showed some slight increases in vibration levels below 400 Hz and reductions above 400 Hz. These variations are ascribed to deflector resonant frequencies and mass damping effects of the deflectors respectively.

Model predictions were made at the same locations that were instrumented during the acoustic noise test. Mode shapes and frequencies were checked first and the model adjusted to agree with test data. A 145 db acoustic pressure loading was then applied to the model using the frequency response capabilities of NASTRAN. The loading was applied from 20 Hz to 2000 Hz. The PSD values were reduced by 30% below 150 Hz to account for the effect of simultaneous loading of both sides of the shield.

The model predicted the first mode resonant frequencies at the measurement points within the required 15% of test results except at one point on the edge of the deflector. The exception is on a portion of the deflector that is bent at a large angle to the rest of the deflector. The flexibility at this point is influenced by the inelastic behavior of the bend line. The NASTRAN frequency response solution assumes that the interaction of the plate elements used in the model is completely elastic. The inelastic response at this point results in a stiffer structure. However, the predicted displacements were conservative at all points.

A comparison of the first resonant response frequencies measured during test with the NASTRAN predictions is presented in Table 1. A comparison of 3σ peak displacements is presented in Table 2. The frequency predictions are within the 15% tolerance of the test values at all locations except for accelerometer location 204R (see Figure 5). This exception is due to the inelastic behavior already described. The displacement predictions from NASTRAN were all greater than the test results at all locations.

CONCLUSIONS

The model verification showed that the support forces and plume deflector structural deflections could be conservatively predicted using a NASTRAN finite element model. The resonant modes affected by inelastic stiffness, such as along a folded plate bend line, can not be predicted by a NASTRAN finite element model because NASTRAN treats the model as completely elastic. Testing is recommended if information is needed on this condition.

REFERENCES

MSC/NASTRAN Handbook for Dynamic Analysis,
M. A. Gockel, editor; The MacNeal-Schwendler
Corporation, 1983.

MSC/NASTRAN User's Manual; The MacNeal-
Schwendler Corporation, 1984.

TABLE 1

COMPARISON OF FIRST RESONANT RESPONSE FREQUENCIES

NASTRAN GRID POINT	PTV-C ACC LOCATION	FIRST RESONANT RESPONSE FREQ.		
		NASTRAN	PTV-C	% DIFFERENCE
31	201R	104	120	14.3%
4	202R	115	120	4.4%
4	219R	115	120	4.4%
2	203R	105	110	4.8%
1	204R	96	70	27.1%

1 NOTE: Frequency is accurate to within only ±5Hz since PSD analysis was conducted with a 10 Hz bandwidth at 10 Hz increments.

TABLE 2

COMPARISON OF 3 SIGMA PEAK DISPLACEMENTS

NASTRAN GRID POINT	PTV-C ACC LOCATION	3 SIGMA PEAK DISPLACEMENT - CM (INCHES)	
		NASTRAN	PTV-C ACOUSTIC TEST
31	201R	0.145 (0.057)	0.018 (0.046)
4	202R	0.216 (0.085)	0.016 (0.041)
4	219R	0.216 (0.085)	0.018 (0.046)
2	203R	0.438 (0.19)	0.017 (0.043)
1	204R	0.838 (0.33)	0.03 (0.076)

3
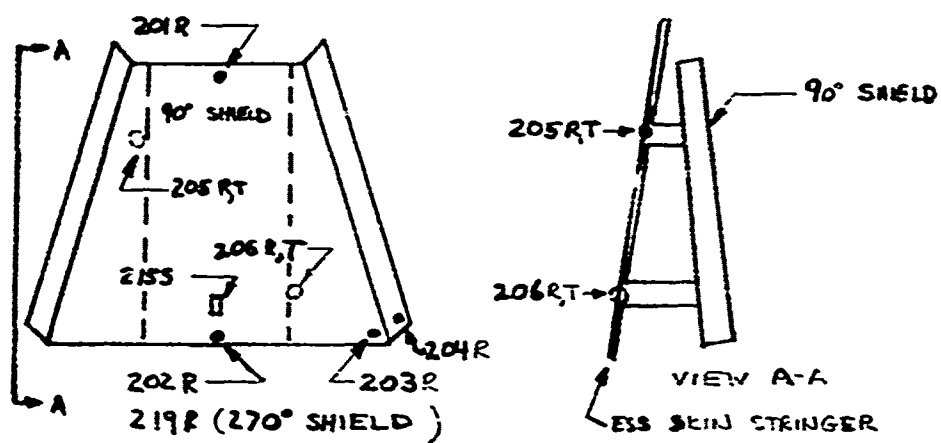
Figure 1. IUS-2 RCS Plume Shield at 90° Instrumentation

4

Figure 2 GRID POINT LOCATIONS
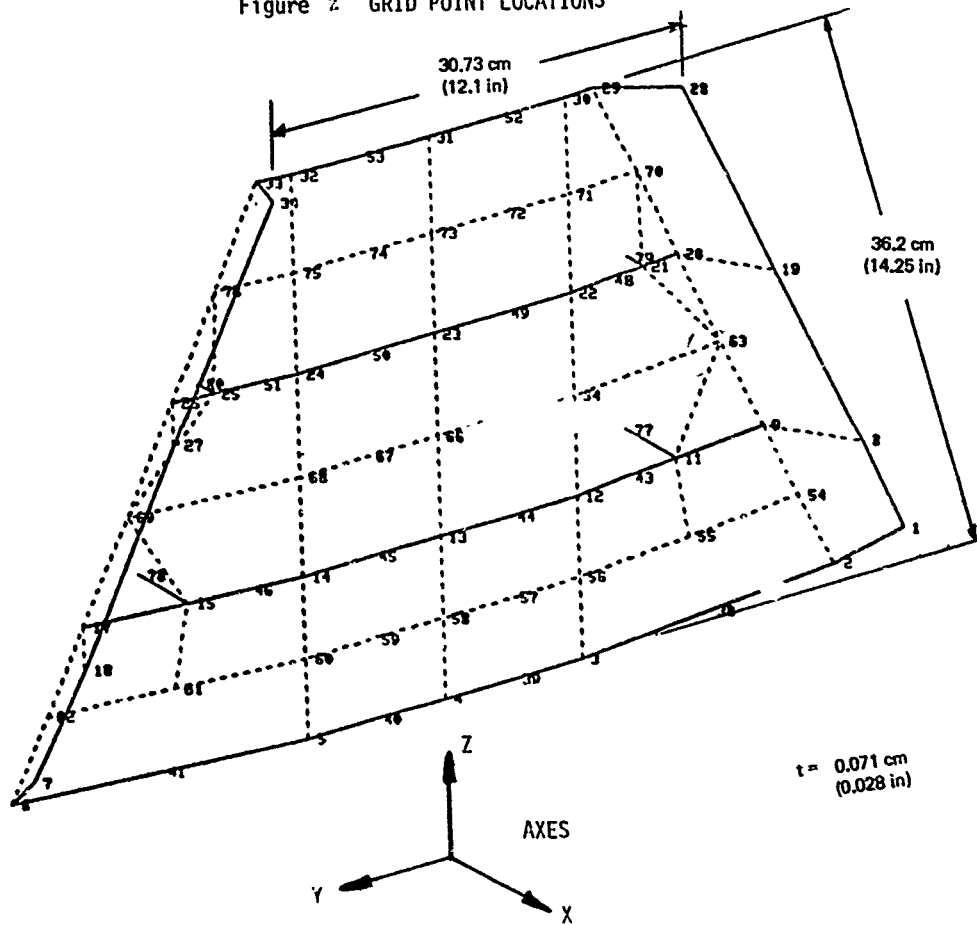
Figure 3   GRID POINT LOCATIONS
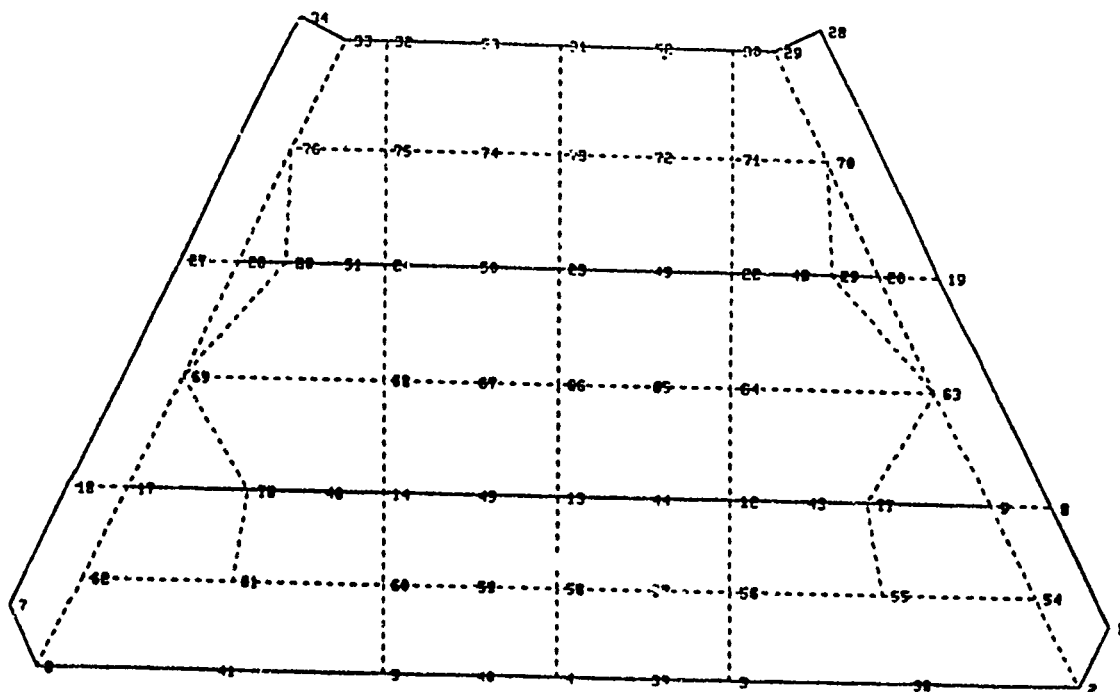
Figure 4   MODEL CONFIGURATION

6
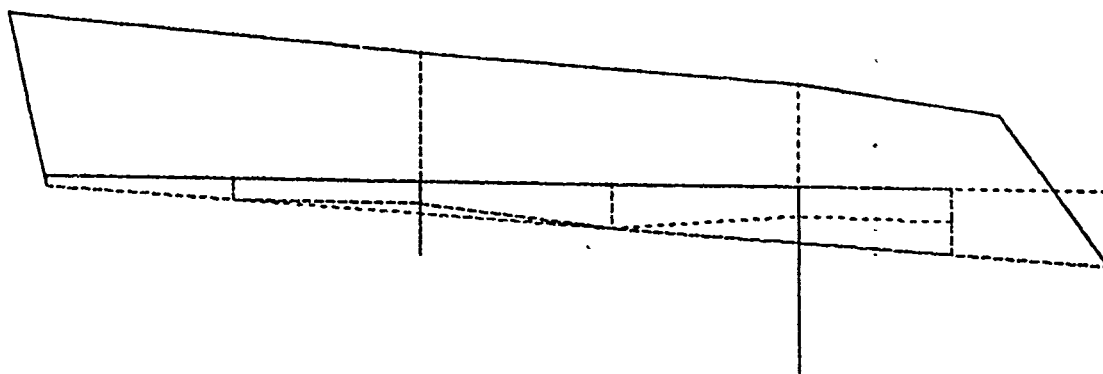
Figure 5   MODEL CONFIGURATION

7° Bend

Figure 6

ACOUSTIC PRESSURE POWER SPECTRAL DENSITY
OVERALL = .49430BE-01 PSI RMS   31.5 TO 2500 HZ
STS ACOUSTIC ACCEPTANCE TEST REQUIREMENT

PRESSURE PSD - PSI SQUARED/HERTZ

FREQUENCY - HERTZ
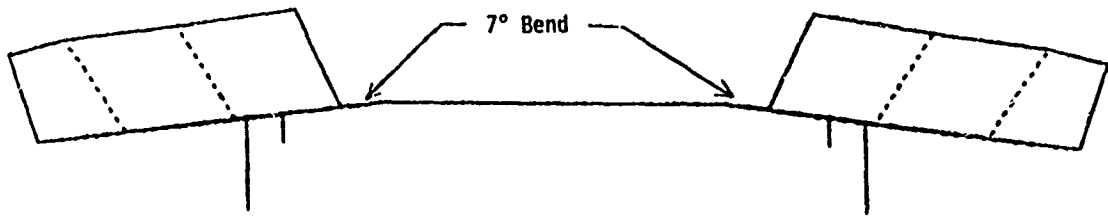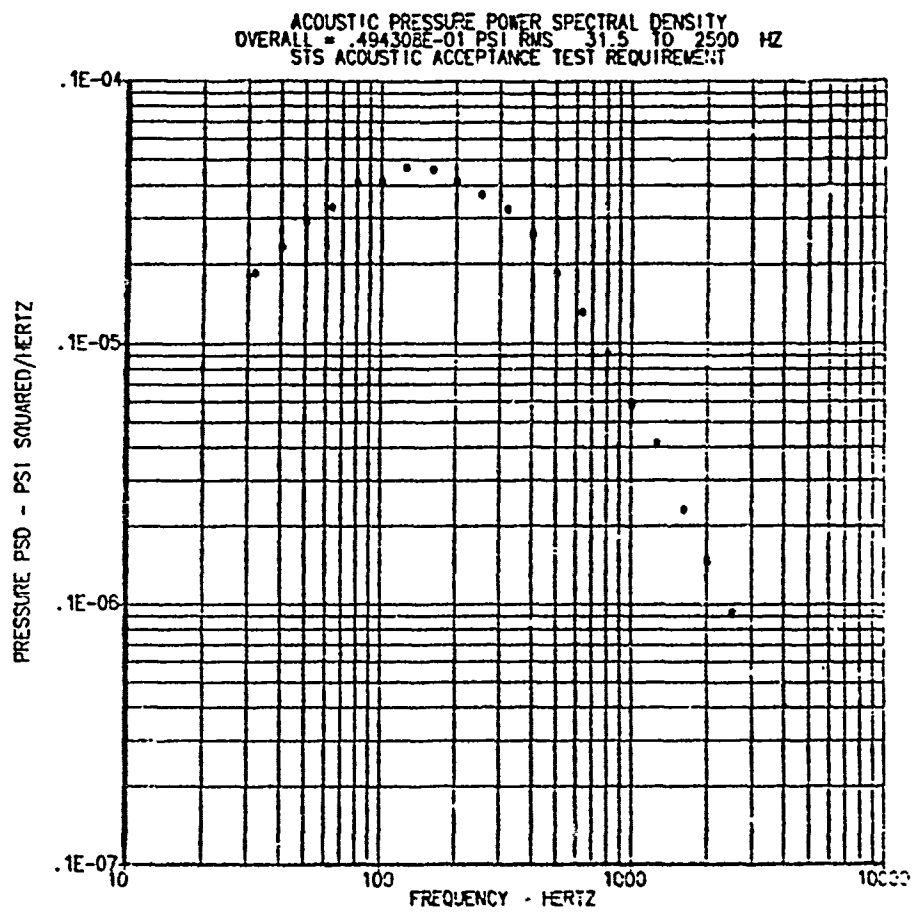
ANALYSIS OF REINFORCED CONCRETE STRUCTURES UNDER THE EFFECTS
OF LOCALIZED DETONATIONS

T. Krauthammer
Department of Civil and Mineral Engineering,
University of Minnesota
Minneapolis, Minnesota

A modified analytical method is proposed for studying the behavior of reinforced concrete structural elements under the effects of localized detonations. In this approach the combined effects of flexure, shear, and axial forces are considered for the development of accurate resistance functions which represent the structural response. These functions are then introduced into single-degree-of-freedom computations by which the dynamic response is assessed. The computational procedure employs explicit relationships between structural mechanisms for evaluating structural element behavior at any stage of existence. Based on this approach it was possible to study the contributions of longitudinal and transverse reinforcement, material properties, support and loading conditions, and to correlate these parameters with observed behavior.

INTRODUCTION

One of the most interesting and difficult area in structural engineering is the design and assessment of structures for resisting detonation effects. This field of research has been developing quite rapidly since the end of WWII, and significant gains were made in understanding the relationships between the various physical parameters of the problem and the observed structural response. Also, it is important to distinguish between effects that could be associated with conventional detonations and those which may result from nuclear explosions, as discussed in a previous publication [1]. The present paper is aimed to present a direct approach for the analyses of reinforced concrete structural elements under the effects of localized loads, such as those that could be associated with typical conventional explosives. The general approach for simplified analyses of such structures was presented and discussed previously [1, and 2], and therefore, no extensive discussions on these issues will be presented here. Nevertheless, several important items must be studied in order for preparing the required ingredients for the numerical approach, such as the development of reliable structural resistance functions, incorporating accurate load - time histories, and providing rational definitions for structural performance.

There are significant difficulties in the derivation of accurate and well understood loading functions which can represent the effects associated with conventional detonations. This is a result of the fact that the environment created by a detonation is so severe that it is very difficult to measure the effects in the zone close to the source Nevertheless, important information is available from which researchers can obtain good estimates of such effects, as discussed in [1]. Also, the work of other investigators on detonation effects provided important contributions in this field [3-7], and engineers can derive reliable load-time histories for detonations in air, soil, and liquids. Once the general pressure-time relationship is obtained (it is important to note that such relationships may include the effects of fragment impact, etc. that would be translated into equivalent pressure), the analyst must transform it to the structure under consideration, and include the spatial nature of the environment. This final step in the derivation of the loading function is also not simple, and one needs to resort to simplified assumptions, for example as proposed in [1]. Similarly, the analyst must derive reliable and accurate structural models which would be included in the analysis. Following the approach proposed in [1, and 2], where it was shown that it was possible to simulate complicated structural

systems by single-degree-of-freedom (SDOF) models, it was decided to extend that method for the analysis of reinforced concrete frame structures. The main issue at this point was the derivation of structural resistance functions that would be accurate, but simple for incorporation into SDOF analyses.

Analysis of reinforced concrete structural elements would primarily depend on not only the models that describe the material behavior, but also on assumptions with regards to structural behavior and the numerical procedure which is used to perform the analysis. The derivation of structural behavior models for reinforced concrete slabs was discussed extensively in [1, and 2], and therefore, the main emphasis of this paper will be on the development of similar relationships for beams and columns. Various material models for plain concrete, confined concrete, and steel reinforcement have been proposed in the literature [10-14] that can be employed for this purpose, and evaluation of experimental results reported in the literature indicated that several of these material models provided very good results. In addition, new formulations are proposed to account for the direct influence of transverse reinforcement on the ultimate strength of the structural member, combined with the effect of axial compressive force on the load-deformation behavior of the structural element and are incorporated into the present approach. The numerical model is subsequently applied to a number of cases that have been studied experimentally [15-17] in order for obtaining valuable comparisons between analytical and experimental data.

The present study is an extension of a previous effort in which a similar approach was adopted for structural behavior in the static domain [11]; however, several significant improved procedures, and behavioral models were incorporated in the present approach which resulted in a considerably more fundamental treatment of reinforced concrete analysis. The ultimate goal of the present study is to develop a straightforward procedure for the analysis of reinforced concrete structural systems under severe dynamic localized loads, and the present paper is aimed to address the development of structural resistance relationships (i.e., load-deformation) that would be employed for performing dynamic analyses.

FLEXURAL RESISTANCE RELATIONSHIPS

The procedure proposed for deriving flexural resistance relationships of reinforced concrete beam-type structural elements is similar to those previously presented in [10-12], and is based on the following assumptions:

1. Strains have a linear distribution over the beam cross section (plane sections before bending remain plane after bending).

2. Tensile strength of concrete below the neutral axis is ignored, and

3. The stress-strain relationships for steel and concrete are known.

The analytical procedure that follows is quite straightforward. For an arbitrary linear distribution of strain, a location of the neutral axis is assumed and the compression zone of the cross section is divided into a number of layers parallel to the neutral axis, as shown in Figure 1. Using the first assumption with specific stress-strain relationships for steel, unconfined (e.g. cover), and confined (e.g. core) concrete, the stresses and forces can be determined for all layers of concrete and longitudinal reinforcement. It is required that the computed forces in the cross-section satisfy equilibrium, as defined by Equation (1).

N.A.

☒ Confined Concrete
☒ Unconfined Concrete

1-Compressive reinforcement
2-Tensile reinforcement
3-Hoop
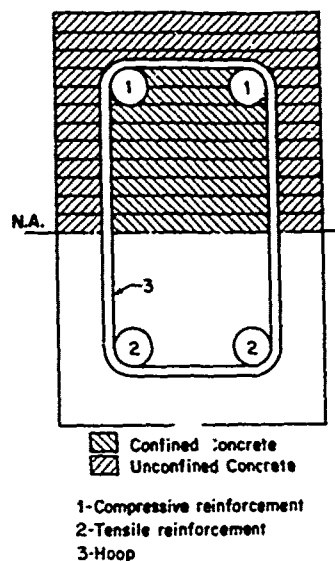
FIGURE 1   BEAM CROSS-SECTION

$$\sum T_i + P_{axial} = \sum (C_c + C_s)_i \qquad (1)$$

in which $\sum T_i$ is the sum of all tensile forces in the cross-section, P_{axial} is the externally applied thrust (this term exists in cases that a known compressive force acts on the cross-section), $\sum (C_c)_i$ is the sum of all compressive forces in the concrete, and $\sum (C_s)_i$ is the sum of all compressive forces in the steel.

If equilibrium is not satisfied, an iterative procedure will begin for a new location of the neutral axis until equilibrium is obtained, and then moment and curvature are computed. The entire procedure is repeated for other strain distributions until the ultimate capacity is reached. As mentioned earlier, such a numerical procedure requires an accurate description of the material models. The stress strain relationship for confined concrete in the compression zone that was used in this study was previously employed in [11] for representing the behavior of confined concrete in beams, or beam-columns while the stress-strain relationship for the unconfined concrete (the concrete cover) is similar to the idealized stress strain curve for concrete under uniaxial compression as proposed in [13]. The stresses in the layers of concrete cover will be computed using the unconfined stress-strain relationship while the stresses for the confined concrete layers are computed with the confined stress-strain model. The material behavior of the longitudinal tensile and compressive reinforcement is identical to that discussed by Park and Paulay [10], and later used in [11].

The computation of a complete moment curvature diagram requires a clear definition of material failure. In the present study the structural response was allowed to develop beyond the yielding of reinforcement since the behavior of the structures under consideration included the contribution of post-yield effects. As a result it was required to employ complete stress-strain relationships for the materials describing the behavior up to the material failure. For lightly to moderately underreinforced beams (i.e., beams for which the tensile reinforcement ratio is less than half the balanced ratio), failure would be reached when the tensile reinforcement reaches its fracture strain, or when concrete reaches its ultimate compressive strain, whichever occur first. A distinction between overreinforced and underreinforced beams would further require a definition of the balanced amount of reinforcement within the flexural model. In the present study ρ_b was defined as the amount of longitudinal tensile reinforcement necessary for obtaining equilibrium such that the strain of the tensile steel has just reached yield while the concrete strain at the extreme compression fiber is at 0.004.

The ultimate compressive strain of concrete, ϵ_{cu}, was defined here as the strain beyond which the unconfined concrete crushes (for unconfined concrete of moderate strength, f'_c between 3000 to 5000 psi) ϵ_{cu} was taken as 0.004, as discussed in [11]. For the concrete confined by rectangular hoops, ϵ_{cu} can be defined according to previous studies by Corley [17], and by Mattock [18] that provided lower bounds for their experimental data base. Accordingly, it was decided

to adopt and to modify the approach proposed in [18] for reflecting the current assumptions, as follows.

$$\epsilon_{cu}^c = 0.004 + 0.02 \left(\frac{b}{L_z}\right) + 0.27 \left(\frac{\rho}{\rho'}\right) \rho_c$$

(2)

in which L_z is the distance from the critical section to the point of contraflexure, b is the cross-section width, and ρ_c is the ratio of the volume of confining reinforcement (transverse and compressive) to the volume of confined concrete. The value 0.004 replaced the original assumption of 0.003, and the constant $0.27(\rho/\rho')$ replaced a previous value of 0.2, where ρ and ρ' are the tensile and the compressive reinforcement ratios, respectively. Also, it was assumed that if the strain at the mid-height of the confined concrete zone of the cross section exceeded the ultimate strain of confined concrete, before the tensile reinforcement reached its rupture strain, a compression failure in concrete would take place, and the computation was terminated. Otherwise, if the tensile reinforcement reached its ultimate strain, a tension controlled failure was assumed.

Flexural analysis of heavily reinforced ($1. \geq \rho/\rho_b > 0.5$) and overreinforced ($\rho/\rho_b > 1.$) beams of Ref. [16] that were examined using the present analytical model indicated that the neutral axis continued to move deeper into the section and eventually exceeded the effective depth of the section This situation always occurred during softening after the peak moment was reached, and since no experimental information for the softening part was available (i.e., the reported experimental data were only up to the peak resisting moment), the peak moment was chosen as the ultimate flexural resistance on the moment-curvature diagram for these beams.

EFFECT OF SHEAR ON FLEXURAL RESISTANCE

Despite the tremendous amount of research that has been devoted to the influence of shear on the performance of reinforced concrete beams, there remain considerable uncertainties about the nature of the corresponding failure mechanism and the estimation of the failure load. Generally, it is well understood that the so called "shear failure" in reinforced concrete beams is a result of flexure, shear, and axial force acting simultaneously. A failure of this kind is usually brittle and it occurs before the structure reaches its ultimate flexural capacity. In order to understand the problem associated with the influence of shear on the flexural behavior of reinforced concrete beams, the effect of shear must be first examined for beams without web reinforcement and then extended to beams with shear

11

reinforcement.

Beams without Web Reinforcement

Experimental results [19,20] indicated that when all other parameters were kept constant, the ratio of the ultimate moment with shear influence to the ultimate moment without the shear influence (M_u/M_{f1}) for simply supported beams clearly is a function of ρ and a/d, and this ratio was defined in [11] as the shear reduction factor (SRF). Those results indicated that the flexural capacity of reinforced concrete beams with certain combinations of ρ and a/d in the ranges of $0.65 \leq \rho \leq 2.8\%$ and $1 < a/d < 7$ did not fully develop. Also, it was observed in [11] that regardless of the amount of tensile reinforcement, the minimum value of that ratio, $(M_u/M_{f1})_m$, occurred in the range of $2 < a/d < 3$, and there was no shear reduction for beams with a/d larger than seven or smaller than one, as shown in Figure 2. Moreover, the minimum moment capacity line was assumed to comprise of three linear segments parallel to the ρ axis, as shown below.
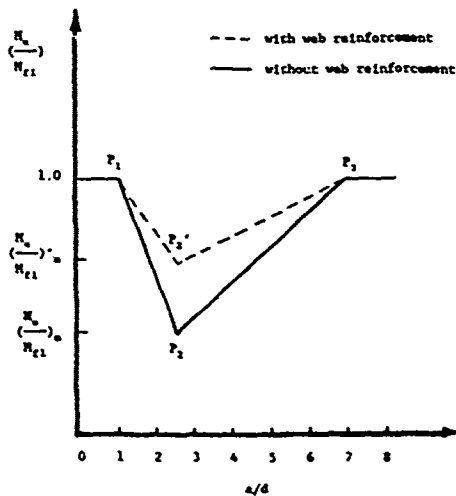
FIGURE 2   MOMENT — SHEAR INTERACTION

$0 < \rho < 0.65\%$:

$$\left(\frac{M_u}{M_{f1}}\right)_m = 1.0 \qquad (3.a)$$

$0.65\% < \rho < 1.88\%$:

$$\left(\frac{M_u}{M_{f1}}\right)_m = 1.0 - 36.6\,(\rho - 0.0065) \qquad (3.b)$$

$1.88\% < \rho < 2.80\%$:

$$\left(\frac{M_u}{M_{f1}}\right)_m = 0.6 \qquad (3.c)$$

In addition, by assuming a straight line relationship between the moment capacity ratio and the a/d of the beam on both sides of the minimum moment capacity line (Figure 2), the following expressions which define the moment capacity ratio for a specific a/d was proposed [11]:

For deep beams (1. < a/d < 2.5)

$$\left(\frac{M_u}{M_{f1}}\right) = 1.0 + \left[\left(\frac{M_u}{M_{f1}}\right)_m - 1.0\right] \frac{(a/d) - P_1}{(a/d)^* - P_1}$$

$$(4.a)$$

For slender beams (2.5 < a/d < 7.)

$$\left(\frac{M_u}{M_{f1}}\right) = 1.0 + \left[\left(\frac{M_u}{M_{f1}}\right)_m - 1.0\right] \frac{(a/d) - P_3}{(a/d)^* - P_3}$$

$$(4.b)$$

where $(a/d)^*$ is the span to depth ratio corresponding to the minimum moment capacity line, point P_2 in Figure 2. P_1 is the shear span to the effective depth ratio below which there is no reduction in the moment capacity, and similarly P_3 is the a/d beyond which there is no loss of flexural capacity (in [11] it was assumed to be constant at a/d=7). Here however, from additional numerical evaluation of experimental results in [11], P_3 may be approximated by the following expressions:

$\rho \geq 1.88\%$:

$$P_3 = 7 \qquad (5.a)$$

$0.65\% \leq \rho \leq 1.88\%$:

$$P_3 = 7 + 365.9(\rho - 0.0188) \qquad (5.b)$$

For overreinforced sections, shear would not have the same influence on reducing the moment capacity as for underreinforced cases. In an overreinforced beam, the concrete compressive zone is considerably larger at ultimate, causing a more effective aggregate interlocking mechanism, and as result the inclined flexure shear cracks do not propagate as extensively as they would in an underreinforced beam. This phenomenon was accounted for in this study by introducing the overreinforcing factor (ORF) defined as follows:

$$\rho \leq \rho_b \quad : \quad ORF = 1. \qquad (6.a)$$

and

$$\rho > \rho_b \quad : \quad ORF = \rho/\rho_b \qquad (6.b)$$

where ρ and ρ_b were defined earlier. The ORF is subsequently applied to the minimum moment capacity ratio, as obtained from Eqs. (3), in the following manner.

$$\left(\frac{M_u}{M_{f1}}\right)_m = \left(\frac{M_u}{M_{f1}}\right)_m * ORF \leq 1 \qquad (7)$$

Beams with Web Reinforcement:

The interaction between web reinforcement and the flexural capacity of a beam has been the subject of various analytical models, as discussed in [10]. Perhaps the most accepted analytical method for predicting the shear capacity of a reinforced concrete beam is the truss mechanism analogy. The truss analogy is based on the assumption that stirrups act like tension members, and the concrete compressive struts act like diagonal compression members in the web of the analogous truss with an angle α between the concrete compressive strut and the positive longitudinal axis of the beam, as defined in [10]. Based on this information it was decided here to employ a reasonable amount of experimental data for developing relationships that would represent the effects of beam properties, including shear reinforcement, on the angle α. Three such relationships were obtained, as follows.

I. Deep beams (1 ≤ a/d ≤ 2.5): The model that is proposed for deep beams is based on experimental results from a study by Clark [21], in which the beams were loaded by a single concentrated load at their midspan or by two single concentrated loads at their quarter span points. A parameter ρ^* is defined as follows:

$$\rho^* = \frac{\rho^* f_y^*}{\sqrt{f'_c}} \qquad (8)$$

where f'_c is the compressive strength of concrete and ρ^*, f_y^* were previously defined herein. When the product o the variables ρ^* and a/d were plotted against the angle of the compression strut for 27 beams, the following linear relationship was derived.

$$\alpha = 2.72 \, \rho^* \, (a/d) + 4.08 \qquad (9)$$

The scatter between data for the 27 points on the plot is not large, resulting in a statistical correlation coefficient of 0.91.

II. Slender Beams (2.5 < a/d ≤7): The experimental data for the 27 rectangular slender beams used for the derivation of the following formulation were gathered from previous studies [14,16,22, and 23]. These beams were also loaded by either a single concentrated load at their midspan or two concentrated loads at quarter span points. When the variable $\rho^* \sqrt{a/d}$ for these beams was plotted against the angle of the diagonal compression strut at ultimate, the following linear relationship was obtained.

$$\alpha = 3.06(\rho^* \sqrt{a/d}) + 7.22 \qquad (10)$$

Again, the scatter between the 27 points about the best fitted line was small, reflecting in a correlation coefficient of approximately 0.99.

III. T beams: Here the data was obtained from Refs. [22, and 24] in which tests on 29 T beams loaded by a single force at midspand were rep~ted. For these cases the following relationship was derived.

$$\alpha = 1.63 \, (\rho^* \sqrt{a/d}) + 9.55 \qquad (11)$$

In this case the correlation coefficient was 0.98.

Eqs. (9-11) represent the influence of material properties and the amount of shear reinforcement on the angle of the diagonal compression strut at failure. This relationship is illustrated in Figure 2 by shifting the minimum point P_2 upward to a new point P'_2, and according to the following expression:

$$\left(\frac{M_u}{M_{f1}}\right)'_m = \left(\frac{M_u}{M_{f1}}\right)_m + [1.0 - \left(\frac{M_u}{M_{f1}}\right)_m] * \tan \alpha \qquad (12)$$

where, $(M_u/M_{f1})'_m$ is the new value of the minimum moment capacity due to the influence of transverse reinforcement and it replaces the old value of $(M_u/M_{f1})_m$ in Eqs. (4). It is important to note that the relationship proposed in [11] was based on the definition of the shear crack inclination, while here it is based on the truss analogy. Also, in [11] the parameter cot α was employed to represent the shear reinforcement contribution. Once Eqs. (4) are modified for the effect of web reinforcement, it is possible to represent the influence of shear on the flexural capacity by the SRF. It is also proposed here to divide all computed curvatures, from zero to the ultimate, by the SRF, and thus, to compute the modified moment-curvature (M - ϕ) diagram that includes shear effects on strength and deformation.

If an external compressive force is applied to the structural member (such as from pre-, or post-tensioning), it is known

13

[10] that as long as the magnitude of the axial compressive load is below the balance point, the moment capacity of the cross section will be enhanced, and this domain of behavior was of interest in the present investigation. Furthermore, the effect of axial force on reinforced concrete beams is an increase in the strength obtained directly from the equilibrium requirement, Eq. (1), and no special provisions need to be included for that in the present approach.

Special Considerations

1. Formation and development of plastic hinges: Experimental observation from Refs. [14-16] indicate that the failure of a beam subjected to concentrated loads seems to occur over a finite length in the vicinity of the maximum moment. Thus, the formation and development of a hinge requires special attention, and the following assumptions have been used in this study for representing the influence of hinge formation on the behavior of the beam.

a. If the peak moment, M_p, is less than the yield moment, M_y, the beam will be assumed to behave elastically.

b. When the center moment exceeds the yield moment, a hinge begins to develop. The length of the hinge, L_p, is defined as the distance between the location of the yield moment, M_y, and the point of the peak moment, M_p. The curvature over the length of the plastic hinge will be assumed constant and equal to the magnitude of the curvature ϕ_p corresponding to M_p.

c. As the load increases, the length of the plastic hinge increases and may reach the full length of the plastic hinge denoted by L_p based on the model proposed in [17].

d. For beams with an axial compressive force, damage is more extensive near the point of the maximum moment at advanced stages of loading. In the present model, this was accounted for by increasing the maximum length of the plastic hinge, and it is proposed that the maximum length of the plastic hinge be modified according to the following expression.

$$L_{pp} = \frac{L_p}{\lambda} \qquad (13)$$

where λ is defined as

$$\lambda = 1 - \frac{P_{axial}}{P_b} \qquad (14)$$

P_b is the thrust at balanced condition, and L_{pp} is the maximum possible length of the plastic hinge when an axial force is also present.

A central parameter for dynamic SDOF analyses is the resistance function which defines the relationship between load and deflection. Therefore, the method described here for the derivation of a moment-curvature relationship had to be carried further in order to derive the required resistance function. All the beam-columns that were analyzed in this phase of the study were simply supported and loaded with a single concentrated load at their midspan, but the numerical approach that was developed can be applied for the analysis of beams having any combination of support conditions, and loaded with concentrated forces at any point along their span. A brief outline of the procedure for computing the load-deflection relationship from a moment-curvature relationship is presented next.

1. Consider any point on the M - ϕ diagram, M_i, ϕ_i.

2. Assume that the moment M_i occurs at the point of the maximum moment (i.e., in the case of a single load at midspan this point is at the center of the beam).

3. Compute the lateral concentrated load Q_i corresponding to the moment M_i;

4. Obtain the moment diagram corresponding to the load Q_i.

5. Obtain the curvature diagram for the entire span by using the moment diagram in conjunction with the M - ϕ diagram.

6. Compute the corresponding deflection by numerical integration of the curvature diagram over the span of the beam. This will give the deflection Δ_i.

7. Repeat the above steps for all points on the M - ϕ diagram for obtaining a complete load-deflection (Q - Δ) relationship.

DYNAMIC ANALYSIS

For dynamic SDOF analyses it is required that an equivalent mass, a resistance function, and damping effects be defined as accurately as possible. In the preceding sections a detailed discussion was presented on the derivation of a rational resistance function, however, some modifications need to be introduced for including dynamic rate effects on the material properties. The simplest approach is to include a dynamic enhancement factor, on the order of about 30%, which would provide a reasonable estimate of such effects, as discussed other publications on the this and relate subjects [1-3]. Obviously, the analyst can choose a more accurate approach provided that his knowledge of all other parameters is of equal quality. Regarding the dynamic analysis that follows, the approach outlined in [1,2] was adopted here, and that was due to the fact that the previous results from the

14

analyses of reinforced concrete slabs were judged to be very good. The dynamic SDOF method is well known, the specific information on the present approach is available for further reference [1,2], and therefore, no additional details on it are presented here. In general, the various parameters are provided to the SDOF code, and the equation of motion is solved for deriving the system's response to the given loading conditions. The corresponding results are then presented in graphical and numerical forms from which the analyst can assess the system under consideration. The following discussion contains detailed examples on the approach, and the corresponding results.

EXAMPLES AND DISCUSSION

In order to demonstrate the application of the present analytical approach and the accuracy of the numerical results the procedure was employed initially for the analysis of 29 beams and beam-columns in the static domain, and the results were compared with test data for the same structural elements. After the method was refined and verified to be accurate it was employed for obtaining their corresponding dynamic load-deflection relationships, and those were introduced into the SDOF code for studying their dynamic responses.

Static Response

Numerical results at the ultimate condition for the nine beams of Ref. [14] indicated that the present procedure is quite effective in that the mean ultimate computed load for the nine beams at failure was within 3% from the mean experimental failure load, with a standard deviation of 0.04. Moreover, the ratio of the average computed midspan deflection to the measured deflection, just before collapse, was 1.02 with a standard deviation of only 0.1, indicating that the present approach for the computation of the deflection at the ultimate curvature provides good results. But, the degree of variability for the computed deflections was larger than that for the ultimate loads.

From the results for eleven beams with axial forces [15] it was observed that on the average, the ratios of the computed to the measured values for moments and deflections at failure were 1.04 and 1.11 respectively. Comparing the analytical results of members in this group with beams of Ref. [14], it was noticed that the variability for the mean ratio of the computed ultimate deflection to the measured ultimate deflection was higher when axial forces were present. Nevertheless, the procedure was still effective in that it could provide satisfactory results for obtaining the entire moment-deflection behavior up to failure.

The nine beams of Ref. [16] had relatively small amounts of shear reinforcement and a high ratio of high strength tensile reinforcement. In fact, as indicated in Ref. [16], a number of the beams were overreinforced, and this was the reason for very little ductility exhibited by these beams. It was noticed that the proposed behavioral model for the effect of shear in reducing the ultimate flexural capacity and the proposed model for the behavior of overreinforced beams at failure is quite effective. The mean ratio of the computed ultimate load to the measured failure load for this group was 0.97 with a standard deviation of 0.08, and the average computed deflection for the nine beams at failure was only 1% less than the average of the experimental deflection values, with a standard deviation of 0.09. Furthermore, the analytical load-deflection curves for these nine cases were again very close to the experimental behavior for all stage of loading.

For the 29 cases studied here, The mean ratio of the ultimate computed load to the ultimate measured load was 1.02 with a deviation of about 8%. The mean ratio of ultimate computed deflection to the ultimate measured deflection (just before collapse of the member) was 1.05 with a deviation of 20%. The complete load deflection relationships for beam J8 is shown in Figure 3, and the experimental points which are marked on these figures were obtained from data in [14] Again, it is noticed that the present approach seems to simulate the experimental behavior quite accurately.
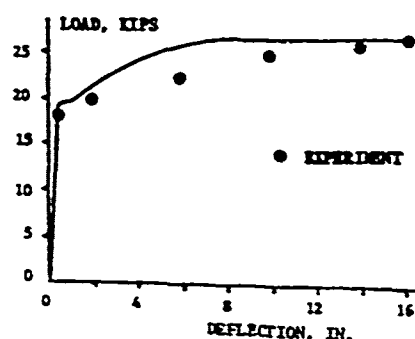
FIGURE 3   LOAD – DEFLECTION BEAM J8

In order to further demonstrate the effectiveness of the procedure with an example, the static test on beam J8 was simulated by using the dynamic SDOF approach. The ultimate experimental load for this beam was recorded as 27.0 kips, and the numerical goal was to obtain the central deflection

from the dynamic analysis for a load of 26.0 kips that would be compared to the corresponding experimental data. The resistance function employed in the dynamic analysis was the analytical load-deflection curve obtained earlier (see Fig. 3). The forcing function increased linearly from zero to a maximum of 26.0 kips in 0.45 seconds, and it was sustained on the beam at that value. This choice for the loading function did not require updating the resistance function for rate effects, and the numerical solution for the midspan deflection is shown in Figure 4. It can be seen that after sufficient time has lapsed, the displacement at the center of the beam converged to a value of approximately 6.8 inches under the sustained load of 26.0 kips, which is virtually identical to the experimental value reported in [14].

For illustration purposes the dynamic analysis of beam J8 [14] is presented here. The loading function was a triangular pulse with an instantaneous peak of 70 kips which varied linearly to zero at 12 ms. and it was based on the data presented in [1] for the detonation effects of 9.ᶜ kg TNT charges at various distances from a given structure. Those pressure-time histories were applied to the loaded areas of the present structures, thus translating the pressure pulse into an equivalent force pulse. The displacement, velocity, and acceleration time histories are shown in Figures 5 through 7, respectively. The assumptions made for the structural response under load reversals were similar to those derived in [1,2] for the direct shear model, and the general character of the results obtained in this study seem to be quite rational, as compared to observed dynamic responses.

FIGURE 4   STATIC TEST SIMULATION

Dynamic Response

The present approach was employed for the analysis of the same beams under the effects of dynamic loads which were assumed to be localized, and to have a triangular time history. It should be clear from the outset that no experimental data were available on the response of these structures to concentrated dynamic loads, and therefore, it is not known whether the results obtained from this approach are accurate. Nevertheless, based on previous results in which a similar approach was employed for the analyses of reinforced concrete slabs under uniformly distributed, or localized dynamic loads [1,2] it is anticipated that the results obtained in this study would be of similar quality. Also, it was shown in the preceding section that the method is quite accurate for simulating static, and slow dynamic structural responses. However, it is clear that the present methods needs to be further verified, and such an effort is presently underway at the University of Minnesota.

FIGURE 5   DYNAMIC DISPLACEMENT – TIME HISTORY
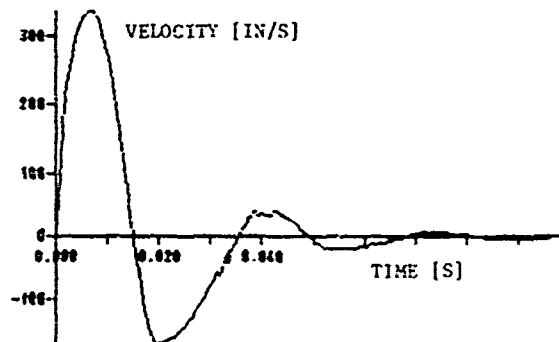
FIGURE 6   DYNAMIC VELOCITY – TIME HISTORY

16
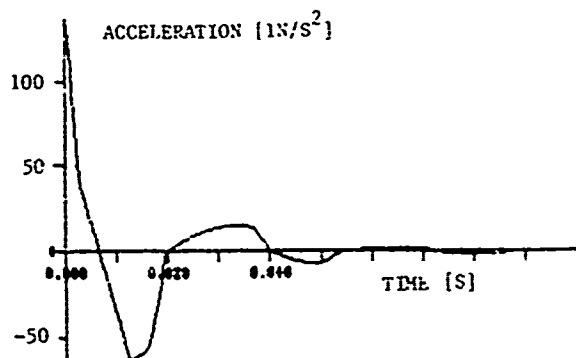
FIGURE 7 DYNAMIC ACCELERATION - TIME HISTORY

CONCLUSIONS

An analytical method is presented for the assessment of reinforced concrete beams under localized dynamic conditions that could be associated with conventional detonations. The results obtained for the structural responses in the static and slow-rate dynamic domains were quite accurate, as compared to experimental data. The response under simulated detonation effects seems to be within the anticipated range of structural behavior, but additional verification is required. The present approach complements the methods proposed previously for the assessment of box-type structures under nuclear, or conventional detonation effects.

ACKNOWLEDGEMENT

The author wishes to express his thanks to the U.S. Air Force Engineering and Services Center for funding the present study. Computations were performed on the IBM 4341 of the Department of Civil and Mineral Engineering at the University of Minnesota. Finally, the author extends his thank to S. Shahriar, and H. M. Shanaa for their assistance.

REFERENCES

1. T. Krauthammer, "A Numerical Gauge for Structural Assessment", 56th Shock and Vibration Bulletin, 1986.

2. T. Krauthammer, N. Bazeos, and T. J. Holmquist, "Modified SDOF Analysis of RC Box-Type Structures", ASCE Journal of Structural Engineering, Vol. 112, No. 4, pp 726-744, April 1986.

3. R. E. Crawford, et al., "Protection From Nonnuclear Weapons", Air Force Weapons Laboratory, Technical Report No. AFWL-TR-70-127, Feb. 1971.

4. C. H. Johansen, and P. A. Persson, Detonics of High Explosives, Academic Press, 1970.

5. Wilfred E. Baker, Explosions in Air, Wilfred Baker Engineering, San Antonio, 2nd Printing, 1983.

6. W. E. Baker, P. A. Cox, P. S. Westin, J. J. Kulesz, and R. A. Strehlow, Explosion Hazards and Evaluation, Elsevier, 1983.

7. Josef Henrych, The Dynamics of Explosions and Its Use, Elsevier, 1979.

8. W. Ammann, "Stahlbeton- und Spannbetontragwerke unter stossartiger Belastung", Bericht Nr. 142, Institute für Konstruktion ETH Zürich, Juni 1983.

9. H. M. Shanaa, and T. Krauthammer, "A Numerical Procedure for Analyzing Reinforced Concrete Beams", Structural Engineering Report ST-86-04, Department of Civil and Mineral Engineering, University of Minnesota, August 1986.

10. R. Park, and T. Paulay, Reinforced Concrete Structures, Wiley, 1975.

11. T. Krauthammer, and W. J. Hall, "Modified Analysis of Reinforced Concrete Beams", Proc. ASCE Journal of the Structural Division, Vol. 108, No. ST2, February 1982, pp. 457-475.

12. T. Brondum-Nielsen, "Ultimate Flexural Capacity of Fully Prestressed, Partially Prestressed, and Non-Prestressed Arbitrary Concrete Sections Under Symmetric Bending", ACI Journal, No. 1, Proceedings V. 83, January-February 1986, pp. 29-35.

13. D. Hognestad, "A Study of Combined Bending and Axial Load in Reinforced Concrete Members", University of Illinois Engineering Experimental Station, Bulletin No. 399, Nov. 1951.

14. N. H. Burns, and C. P. Siess, "Load Deformation Characteristic of Beam-Columns Connections in Reinforced Concrete", SRS No. 234, University of Illinois, Urbana-Champaign, Jan. 1962.

15. R. Yamashiro, and C. P. Siess, " Moment Rotation Characteristics of Reinforced Concrete Members Subject to Bending Shear and Axial load", SRS Report 260, University of Illinois, Dept. of Civil Engineering, Urbana-Champaign, Dec., 1962.

16. B. Bresler, and A. C. Scordelis, "Shear Strength of Reinforced Concrete Beams", Series 100, Issue 13, Structure and Material Research, Dept. of Civil Engineering, University of California, Berkeley, June 1961.

17. W. G. Corley, "Rotational Capacity of Reinforced Concrete Beams", Proc. ASCE Journal, Structural Division, Vol. 92, ST5, October 1966, pp. 121-146.

18. A. H. Mattock, Discussion of "Rotational Capacity of Reinforced Concrete Beams" by W.G. Corley, Proc. ASCE Journal, Structural Division, Vol. 93, ST2, April 1967, pp. 519-522.

19. G. N. J. Kani, "Basic Facts Concerning Shear Failure", ACI Journal, Vol. 63, June 1966, pp. 675-692.

20. F. Leonhardt, and R. Walther, "The Stuttgart Shear Tests, 1961", Translation No. 111, Cement and Concrete Association London, England, 1964.

21. A. P. Clark, "Diagonal Tension in Reinforced Concrete Beams", ACI Journal, Vol. 48, No.2, Oct. 1951., pp. 145-156.,

22. A. Placas, and P. E. Regan, " Shear Failure of Reinforced Concrete Beams", ACI Journal, Vol. 68, Oct.,1971. pp. 763-773.

23. A. H. Mattock, and Z. Wang, "Shear Strength of Reinforced Concrete Members Subject to High Axia_ Compressive Stress", ACI Journal, Vol. 81, May-June 1984, pp. 287-298.

24. A. H. Mattock, M. J. Haddadin, and S. T. Hong, "Stirrup Effectiveness in Reinforced Concrete Beams with Axial Force", Proc. ASCE J·urnal, Structural Division, Vol. 97, ST9, September 1971, pp. 2277-2297.

REINFORCED CONCRETE ARCHES UNDER BLAST AND SHOCK ENVIRONMENTS

by
Theodor Krauthammer
Department of Civil and Mineral Engineering
University of Minnesota
Minneapolis, MN 55455

Experimental results that were obtained from laboratory and field test of shallows buried reinforced concrete arches over a period of about thirty years were combined for the development of behavior models which accurately describe the response of these structures. Based on such development a simple analytical approach was adopted and employed for the analysis of several cases for which adequate experimental data were available, and the analytical results were found to be reasonably accurate. The present approach is a preliminary step in the development of a comprehensive numerical procedure for the assessment of such structures.

INTRODUCTION

One of the most efficient types of structures used for protection from detonation effects is the reinforced concrete arch in which the loads are transferred through the curve geometry into the foundations. Under certain conditions the state of stress in the arch would be compressive, while it is possible that other loading conditions would induce flexural nodes of response. The loading environments under which these structures are expected to perform result from the detonation of explosive devices, either nuclear or conventional. In both cases the generated pressure-time histories are characterized by a short rise time to a high peak followed by an exponential decay to zero pressure (typically, a negative pressure phase exists after that point which eventually also diminishes, but in this paper only the positive pressure phase will be considered). The duration of these pulses is generally measured in tenths of seconds for nuclear detonations, while conventional weapons produce much shorter pulses. Naturally, structural designers need to analyze either existing systems or proposed designs in order to assess their expected performance under specified conditions. This requirement leads to the initiation of theoretical and experimental studies for the development of an understanding of structural behavior, and its relationship with structural properties and loading conditions. The developments that occurred over the last 30 years with respect to deriving reliable methods for the analysis

of shallow-buried reinforced concrete arches under explosive loading conditions are presented next, followed by the introduction of a simplified numerical model for their assessment.

BACKGROUND

The field of blast- and shock-induced structural behavior can be separated into two principal system categories: the first, under the influence of nuclear detonations while the second relates to the effects of conventional explosives. In this paper the emphasis will be on structural behavior under loads which may arise from nuclear detonations where the entire structural system is loaded, while under conventional explosive effects the structural response is rather localized to the vicinity of the detonation. A description of such localized effects was presented by Kiger and Albritton [1], and it can be compared to the performance of hardened structures under nuclear detonations, as further discussed in this section.

Early studies on the effects of nuclear blast on underground structures provided a recommended design procedure for such facilities [2,3]. A static design for the peak values of the expected loads was the first step in the procedure, and based on the preliminary design one could proportion the structural members. The following step was to estimate the natural period of each member, and to compare those values to the rise time of the applied load. If the ratio

19

of the rise time to the natural period was greater than about 3, the structural design was assumed to be adequate. However, if the ratio was smaller than about 3, a dynamic design method was required. A simple dynamic analysis could be performed by applying a triangular pulse, that simulated the load, to a single-degree-of-freedom (SDOF) system which represented the structure. From the dynamic analysis the resistance of the members was evaluated, and compared to the resistance of the structural members obtained from the preliminary design. The procedure was iterative, proceeding until the analytical values and the values from the preliminary approach were reasonably close. Similar approaches were recommended also in later publications [4]. As for the material properties under dynamic loading conditions, an increase of about 25% was recommended for both the yield strength of steel and compressive strength of concrete.

Arch-type structures have been studies by a number of investigators under the possible effects of nuclear detonations. Flathau et al. [5], and Grubaugh et al. [6] studied arch and dome structures by full scale experiments under nuclear detonation effects. In those tests, buried, underground reinforced concrete arch structures were subjected to airblast-induced ground shock resulting from a nuclear detonation. Kennedy [7-9] studied the same type of structures under simulated environments, but primarily on small scaled systems. Balsara [10] studied four aluminum semicircular fixed-end buried in dense, dry sand at a depth of burial of one-half an arch diameter and tested dynamically. The maximum surface, airblast overpressure was 300 psi (2.06 MPa) (positive duration about 600 msec) which caused damage. This study showed that it was possible to successfully scale the response, and of buried model arches in the so-called inelastic range of response. The buckles formed at the springline highlighting the fact that this was the zone of higher moments. The distribution of the interface stress was not measured but apparently was the same for the models tested. Another simulation study was reported by McGrath [11] while Palacios and Kennedy [12] reported results from a test under simulated conditions similar to the real conditions as reported in Refs. [5,6]. In that test, a 500-ton surface burst provided the loading environment, and two types concrete arches were tested.

Meyer and Flathau [13] studied the response of small scale unreinforced concrete arches under simulated nuclear blast effects in the laboratory, and Tener [14] correlated experimental studies with empirical observations to form a generalized description of buried arch behavior under dynamic loading conditions. Flathau [15] proposed a modified approach for the design of buried arches and

cylinders which seems to assure a desired performance. Nevertheless, the behavior of these systems is not simple, and several attempts were made to derive analytical techniques for accurately describing their performance [16]. Lipner et al. [17] compiled information on previous twenty experimental studies in which arch-type structures were tested, and they presented that summary in tabular form for descriptions of specimens, loading conditions, type of soil backfill, observed behavior, and comments on the study.

It was concluded from sensitivity calculations that the most sensitive property was the compressive strength of concrete, which was also observed in previous studies [13]. From studying test results it was indicated that the response of a buried arch to a traveling airblast load can be characterized adequately with four modes: rigid body motion, uniform compression, symmetric bending, and asymmetric bending. The consensus in the literature was that collapse was due to response in the hoop and symmetric bending modes. This is not unreasonable when considering the stiffening effect of the surrounding soil coupled with the angle of the air-induced ground with the ground surface, especially as the surface overpressure increases. Wong and Richardson [18] studied the response of these systems under dynamic soil-structure interaction conditions, and proposed various transfer functions for explaining the observed behavior. The data in Ref. [17] combined with information from other sources, as discussed previously herein, can be used to form, at least, a qualitative description of arch-type structures under explosive loads. Some of these sources [3,4] have been used in the past for the assessment and the design of structural systems, including arches, to resist detonation effects. In those publications one can find simple procedures that the designers and experimentalists can employ for evaluating the anticipated response of test structures.

One of the main problems with many of the earlier studies, as were briefly described here, was the lack of adequate experimental data for arch performance under controlled conditions from which one could derive rational behavioral models for studying the effects of several design parameters on the response of shallow-buried reinforced concrete arches under simulated nuclear blast and shock environments. These conclusions led to the requirement for a controlled study, as described in Refs. [19-22].

EXPERIMENTAL OBSERVATIONS

Information from previous studies can be compiled to provide adequate qualitative descriptions of the expected system behavior, and from such models one could develop simplified behavioral models to be incorporated into reliable numerical procedures.

Consider the sequential structural response, as illustrated in Figure 1. As the oblique ground shock loads the structure one may observe an asymmetric bending mode, including side-sway (b), combinations of the compressive mode and the first symmetric flexural modes (c), and finally the damaged structure at (d). The dynamic loads that produce structural response are therefore expected to cause specific damage, as illustrated in Figure 2. One would expect longitudinal cracks in the floor slab with a possibility of shear failure at the arch-floor connection (that possibility would increase for certain thick floor slabs where the flexural response is limited), flexural hinges in the arch at about mid-height represented by well defined longitudinal cracks along the arch, and also a hinge with some longitudinal cracks at the arch crown.

FIGURE 2   STRUCTURAL DAMAGE [11]

Laboratory Arch Tests

One of the earlier studies on the behavior and response of small scale unreinforced concrete arches provided important information on the relationship between surface overpressure and crown deflection in the static and the dynamic domains of behavior [13].

FIGURE 1   STRUCTURAL RESPONSES

These results have been observed experimentally in several studies, for example as reported in [5].

A series of static and dynamic tests were conducted to determine the response of unreinforced concrete, fixed-end arches of different stiffnesses buried in dense, dry sand. It was hypothesized in previous work that a buried arch would respond in some type of bending-compression mode where the combination of moment and thrust at a critical arch section will result in a compression-bending type failure, i.e. failure would occur in the compression region of the failure envelope formed by a moment-thrust interaction diagram. If this was true, then steel would not be needed as bending would not play a dominant role in resisting load. Pertinent properties for the three arches were as follows: Outside radius = 6 inches (152 mm); Arch thicknesses = 1/2, 1, and 2 inches (12.7,25.4, and 51 mm); Stiffness, EI/R^3 = 66, 600, and 6400 psi (0.45,4.13, and 44.1 MPa); Concrete compression strength, f_c' ≈ 1200 to 1500 psi (8.3 to 10.3 MPa); and the Depth of soil cover = 2 inches (51 mm). Purposely a very low concrete compressive strength was used to create "weak" structures. However, only the 1/2-inch arch loaded statically collapsed at ground surface overpressure of 150 psi (1.03 MPa). In general, the modes of response for the structures tested statically and dynamically were the same, as illustrated by the sequence of structural response in Figure 3.

The confinement provided by the surrounding soil was sufficient to force the

21
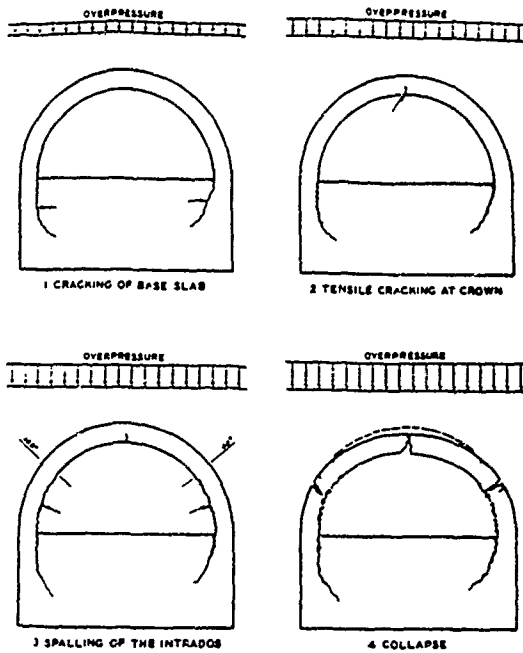
FIGURE 3   DAMAGE SEQUENCE [13]

FIGURE 4   STATIC RESISTANCE [13]
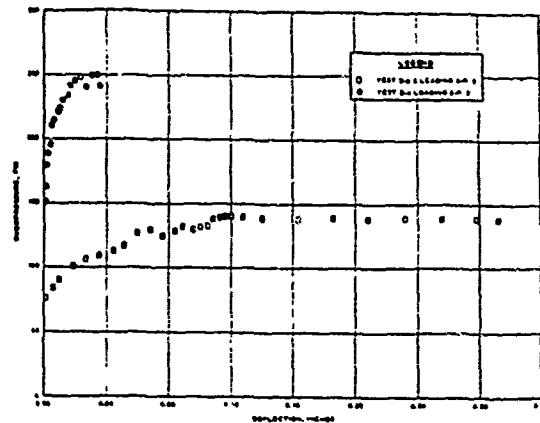
FIGURE 5   DYNAMIC RESISTANCE [13]

buried arch to accept load efficiently, i.e. the arch-soil system seeks a compressive loading in the most efficient way that an arch can accept load. This is one of the few test series where a collapse of a buried arch has been observed, and where static load-deflection relationships were recorded. It became clear that a better understanding was needed on how load is transferred to a buried structure, including the effects of soil arching. In addition, the need for describing a realistic resistance-function (i.e. load-deflection relationship) was implied.

The measured crown deflections plotted against overpressure are shown in Figure 4 for the static cases, and in Figure 5 for the structures loaded dynamically. From the static tests it was observed that the deflection of the 1/2-inch arch was greatest for the same overpressures, and the deflection of the 2-inch arch was the least at any level of pressure. The deflections of the two different 1-inch-thick arches tested agreed well, the preliminary static test arch, which showed somewhat less deflection, was made of somewhat stronger concrete than the 1-inch-thick arch of the principal static test. Taking these curves as indications of the downward deflections of the outside of the arches, it is expected that active soil arching (reduction of the vertical load on the structure due to the structural deformation) would be most likely to occur during the loading of the 1/2-inch arch and least

likely to occur during loading of the 2-inch-thick arch.

The crown deflections for the initial dynamic loadings of the 1/2- and 1-inch thick arches are shown in Figure 5. Because the frequency of the record for the 2 inch arch approached that of the mechanical measuring system, the probe probably did not remain in contact with the arch crown, and the investigators had to ignore the corresponding data. For the 1/2- and 1-inch-thick arches the rise times for the deflection records were all well below the natural frequency of the recording system, and it can be seen that the 1/2-inch arch in test D-0.5, loading S-R/3, continued to deflect considerably after the peak value of overpressure was attained, indicating that the arch underwent con-

22

siderable inelastic response. The deflection of the 1 inch (25.4 mm) thick arch showed no increase in deflection after the peak overpressure was attained, indicating that the pressure was not sufficient to cause inelastic response of the structure. However, based on the authors' assessment of the data this figure does indicate that an over-pressure slightly greater than 250 psi (1.72 MPa) could drive the arch into inelastic response if the duration of the load was long enough.

Those findings, as illustrated in Figures 4 and 5 contain significant insight on the behavior of such systems. In the static domain (see Figure 4) the load deflection relationships seem to be smooth and quite nonlinear, and in the dynamic domain (see Figure 5) such nonlinearities are even more visible. Another important behavioral aspect that is noticed from these results is the fact that arches with higher radius to wall thickness ratios (R/t) will in general exhibit a lower load resistance and a higher degree of ductility.

Field Arch Tests

The arches tested under field conditions were divided into three groups based on structural type and detailing, and were named KBM, KED, and DAT-3, respectively, and their general design specifications are presented with the following discussion.

In KBM, the HE simulation produced an overpressure of about 1972 psi. One 28-foot-long arch with cold joints, 2.15 percent circumferential reinforcement ratio, 0.6 percent longitudinal reinforcement ratio, outer arch diameter of about 7.9 ft. (2.4 m), and wall thickness of 6.3 in. (160 mm) was tested. Results showed circumferential steel was beyond yield, joint failure occurred in the region connecting the arch walls to the floor. Hinges formed at the crown and at each floor joint. Floor failure was indicated by results from strain gages but not visible. The interface pressure data indicate that the stress wave arrived nearly simultaneously on opposite sides of the arch and the magnitude were about the same.

In KED, the HE simulation produced an overpressure of about 1740 psi (12 MPa). The cross section of the arch in this series was the same as for the KBM event, but the circumferential reinforcement ratio was 1.9 percent, and the longitudinal reinforcement ratio was 0.3 percent. Three arches were tested, one 28 feet (8.53 m) long, another 11.2 feet (3.41 m) long, and the third 5.6 feet (1.7 m) long. The longer arches experienced some longitudinal bending which tended to induce failure in the joint between the arch wall and floor. Arch 1, that had been loaded twice previously in KBM, was retested again in KED (third loading) and

failed catastrophically. It should be mentioned, however, that the KBM arch was significantly damaged after the first two tests.

In DAT-3, three arch-type structures were planned to be subjected to a predicted HEST air overpressure loading of 1740 psi (12 MPa) simulating a 1.56-kt yield, while the actual peak pressure was about 1842 psi (12.7 MPa). All the arches were similar in cross section and had the following properties: Inside radius - 3.41 feet (1.04 m); Arch thickness - 6.25 inches (159 mm); Arch floor thickness - 9.3 inches (236 mm); Soil cover over crown - 2 feet (0.61 m); f_c' - 5000 psi (34.5 MPa); f_y (reinforcing steel) - 60 ksi (413.7 MPa); Reinforcement ratio - 2.15 percent; and End bulkheads - 6.3 inches (160 mm) thick. Structure A5 was composed of four 5.6 ft. (1.42 m) long segments having the above mentioned properties, while structures A6, and A7 were composed of only one such segment. The joints in A5 were keyed, or butt joints.

The arches in the KBM series had the highest overall normal stresses recorded from the three tests, followed by the KED series and, finally, with the lowest normal stress measurements recorded on the DAT-3 test. Some of the peaks on the DAT-3 test were as high as those in KED, but DAT-3 experienced relief of the load and did not accumulate a matching amount of impulse.

Vertical velocities were not as comparable, since the KBM tests had only an 8.5 m long arch and no short arch segments. However, the KBM arch remained fairly intact as far as vertical velocity comparisons throughout the structure. In rating velocity output, DAT-3 had the highest vertical velocities at all measurement locations, and very little relative displacement took place between the lower wall and floor. This was offset by the failure in the wall midsection which allowed relative displacement in the walls. The KBM arch also held its shape, and despite noticeable damage, it maintained the best post-yield integrity in the test series, especially in light of the high loads on the structure. Maximum relative displacement between the arch walls and floor occurred in the KED test, although the most severe failure was obtained in the collapsed inner segments of DAT-3 Arch A5.

The KBM arch held together because it had low relative displacements under the greatest interface loads. This is due to the size of the reinforcing bars used in the KBM arch which translated into a slightly higher circumferential reinforcement ratio. Relative displacements between the arch walls and floor were greatest in the KED test due to the small reinforcing bar sizes and the inadequate confinement of the concrete in the joint. However, this forced the failure

23

region to move up the arch wall where bending and shear stresses combined to fail the arch. This type of failure could be less desirable than the failures at the joint region connecting the wall and the floor, since they could lead to arch collapse similar to the failures in DAT-3.

Strain data from the three tests generally reflected the degree of stiffness in the sections. The KBM arch had the largest reinforcement ratio and the best stiffness configuration among these cases, so that in areas of stress concentrations, like the lower wall, higher magnitude moments were carried by the stiffer cross-section (and eventually by the reinforcement) as the corner remained fairly rigid in spite of noticeable shear failure of the concrete in the joint. The smaller reinforcement ratio in KED allowed more flexibility and ductility in the section after the concrete cracked, and therefore, the moments were lower in the joint area but higher at the crown and the floor center. The stiffness level was recovered in the DAT-3 test by arranging the steel in the joint region to enhance the contribution of the reinforcement (due to geometrical constraints the reinforcement at the joint was less than originally recommended by the author), and the failure, subjected to stress concentrations at steel cut-off points, was relocated to the weakest section which was in the arch.

ANALYTICAL CONSIDERATIONS

The response of shallow-buried rein-forced concrete arches cannot be accurately described and formulated without explicit consideration of all governing behavioral mechanisms. Among those one must include the issues of loading conditions, soil-structure interaction, structural element response, and the effects of structural parameters on that response. In order to include all these issues in the analysis one must resort to employing advanced computational procedures (such as the finite element, or the finite difference techniques) by which it would be possible to represent the individual effects, and the complicated interactions between the various parameters. This, however, is not always simple since it requires large computational resources, and a fundamental treatment of several related issues. At present such an effort is underway at the University of Minnesota, but the results will not be available in the near future. Therefore, one would have to consider the implementation of simple procedures that were shown to be very effective if used properly. One of such methods is the simulation by a single-degree-of-freedom (SDOF) system, as performed for shallow-buried box-type structures [23,24], and following an outline discussed in [16].

In order to employ a SDOF approach one must define several parametric relationships which would represent the system's mass, resistance, damping, and forcing function. The present write-up is aimed to address these issues for the development of a consistent and rational approach in this direction. First, regarding the problems of damping and loads it is proposed to adopt the conclusions presented in [23,24], as follows. Damping will be represented by a critical damping ratio in the range between 20% to 40% which includes both structural and soil-structure interaction contributions. The reasons for such crudeness are the relatively high uncertainty regarding these parameters, and the fact that the proposed approach is empirically rational. The forcing function would be represented by an approximate air-blast pressure for prediction purposes, or by blast gauge readings for post-test analysis. The remaining two parameters are more complicated. Both the effective mass, and the structural resistance must represent closely the nonlinear dynamic response. The mass would include part of the structural mass (the responding arch), and part of the soil overburden. Based on observations from field and laboratory test, as previously discussed here, it is clear that the portion of the structure between the hinges at mid-height and the crown are expected to response.

As a result one can define an effective mass which would represent that portion of the arch, as shown in Figure 6.

$$M_{eff} = \frac{\theta}{180} M_{ARCH} \qquad (1)$$
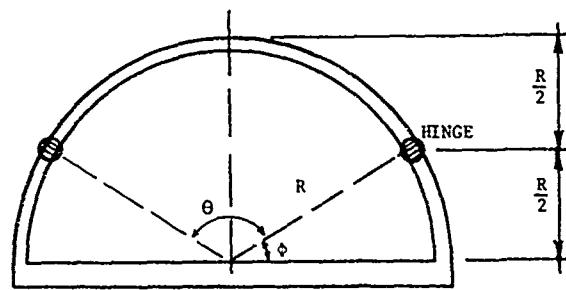
FIGURE 6 MODEL FOR EFFECTIVE MASS

from which the mass factor is clearly $\theta/180$, but from Figure 6:

$$\theta = 180 - 2\phi \qquad (2)$$

and

24

$$\sin\phi = \frac{R}{2R} = \frac{1}{2} \qquad (3)$$

$$\phi = \sin^{-1}\frac{1}{2} = 30° \qquad (4)$$

and the mass factor

$$C_M = \frac{180-60}{180} = \frac{120}{180} = \frac{2}{3} \qquad (5)$$

Also, it is proposed here to employ the soil mass above the responding portion of the arch. Both these conclusions seem to be similar to the findings and recommendations in [25].

The development of a resistance function is performed similarly as discussed in [23,24]. The peak resistance for the arch in the uniform compression and in the flexural modes of response were estimated in several publications [2,3,4, and 25].

DISCUSSION

Employing the approach proposed in [23,24] one could develop a resistance function for the arch (i.e., a relationship between the distributed load w and the corwn deflection Δ), as follows. Assume a second order polynomial relationship between the zero condition, point 0 in Figure 7, to the peak resistance, w_{max}, at point A. For that relationship one must employ rational boundary conditions, for example:

1. $w = 0$, $\Delta = 0$

2. $w = w_{max}$, $\Delta/t = 0.25$

3. $w = w_{max}$, $\partial w/\partial \Delta = 0$ $\qquad (6)$

therefore, the general relationship of the form shown in Eq. (7)

$$w = A\Delta^2 + B\Delta + C \qquad (7)$$

Introducing the conditions in (6) will result in the following relationship.

$$w = -16\frac{w_{max}}{t^2}\Delta^2 + 8\frac{w_{max}}{t}\Delta \qquad (8)$$

Also, it should be noticed that the initial stiffness for the system (i.e., the slope at $\Delta = 0$) is

$$K_o = (\frac{\partial w}{\partial \Delta})_{\Delta=0} = B = 8\frac{w_{max}}{t} \qquad (9)$$
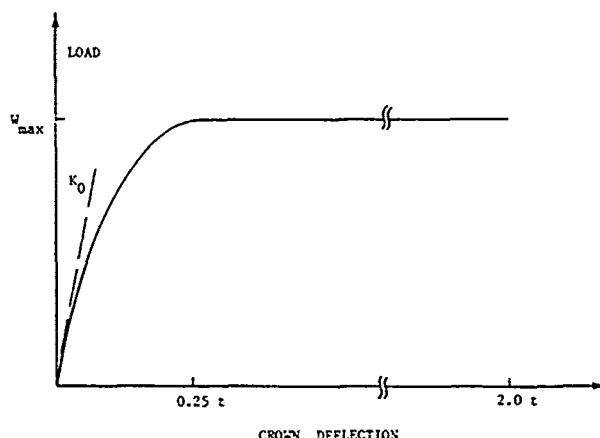
FIGURE 7 RESISTANCE MODEL

Also, it is noticed from the experimental data (Figures 4, and 5) that the resistance could remain essentially constant at w_{max} until about $\Delta = 0.5t$. No accurate experimental data was available beyond that point, but based on results from more recent studies [19-22] it was decided to try a constant resistance until $\Delta = 2t$. Combining these details results in the empirical resistance function, as shown in Figure 7.

The analysis of the system is performed by assuming that the arch would respond with respect to a stationary floor, and thus, the computed motions would correspond to the arch crown of a theoretical system which does not include the response of either the floor, or rigid body motion. The present approach was employed for the preliminary analysis of the arches described in [19-22], and the computed crown displacements are compared to test data in Table 1. In the present analysis the resistance functions do not contain length effects, and therefore, only one arch of each series was studied numerically.

DISCUSSION AND CONCLUSIONS

The behavior of buried reinforced concrete arches is of continuing interest, and several studies were conducted for providing information on the subject. The approach adopted in the present study is a preliminary one that is aimed toward the development of simplified methods of analysis. This approach is based on observed structural behavior under static and dynamic loading conditions, and empirical relationships between applied load and crown deflection. The early results obtained by this approach seem to be reasonable, but cannot be used for more than deriving qualitative conclusions on the response. Inspection of the test structures revealed that the peak displacements of the floor slabs were

TABLE 1 - KACHINA Arches Experimental and Analytical
Peak Displacements

Arch	Measured Deflection* [mm]	Computed Deflection** [mm]
KBM A2	120	55
KED A2	330	181
DAT-3 A5	235	110

* Relative Crown-floor deflection

** Crown deflection

approximately equal to the peak crown displacements, and thus, the present approach seems to be surprisingly accurate. The continuing studies at the University of Minnesota will address these issues, and are expected to provide useful structural assessment tools.

It is clear from these results that one must consider the floor response, the effects of dynamic shear, and the contributions of reinforcement detailing on the response. Several relationships on these issues were derived, and are being evaluated. Preliminary results show that the effects of confinement and shear can be incorporated very effectively into the present analysis. Also, that by employing a multi-degree-of-freedom (MDOF) approach, it is possible to compute relative motions between the arch crown and the floor slab. Nevertheless, such efforts are not yet complete, and therefore, these results will be presented at a later time. Another issue that needs to be addressed in the future is the effect of the arch length on the structural response, and how such an effect can be represented in the MDOF analysis.

ACKNOWLEDGEMENT

The author wishes to thank the Defense Nuclear Agency (DNA), and the Air Force Weapons Laboratory (AFWL/NTESA) for their continuing support and cooperation on this effort.

APPENDIX I - REFERENCES

1 . Kiger. S.A.. and Albritton. G.E.. "Response of a Buried Hardened Arch Structure to the Effects of Localized Explosions," U.S. Army Engineer Waterways Experiment Station, Technical Report SL-79-13, December 1979, (limited distribution).

2. Newmark, N.M., Hansen, R.J., Holley, M.J. and Biggs, J.M., "Protective Construction Review Guide," Vol. I, Department of Defense, June 1961.

3. Newmark, N.M., and Haltiwanger, J.D., "Air Force Design Manual, Principles and Practices for Design of Hardened Structures," Air Force Special Weapons Center, AFSWC-TDR-62-138, December 1962.

4. Crawford, E.R., Higgins C.J. and Bultman, E.H., "The Air Force Manual for Design and Analysis of Hardened Structures," AFWL-TR-74-102, October 1974.

5. Flathau, W.J., Breckenridge, R.A., and Wiehle, C.K., "Blast Loading and Response of Underground Concrete Arch Protective Structures", ITR-1420, Operation Plumbob--Project 3.1, U.S. Army Engineer Waterways Experiment Station, November 29, 1957.

6. Grubaugh, R.E., Morrison, T.G., Koike, R.S., Neidhardt, G.L., and Tuggle, W., "Full Scale Field Tests of Dome and Arch Structures," ITR-1425, Operation Plumbob--Project 3.6, Air Force Special Weapons Center, October 11, 1957.

7. Kennedy, T.E., "Comparison of Simulated and Field Tests of a Buried Concrete Arch Structure," U.S. Army Engineer Waterways Experiment Station, Miscellaneous Paper No. 1-963, January 1968.

8. Kennedy, T.E., "Dynamic Tests of a Model Flexible-Arch-Type Protective Shelter," U.S. Army Engineer Waterways Experiment Station, Miscellaneous Paper N-71-3, April 1971.

9. Kennedy, T.E., "The Dynamic Response of a Simulated Buried Arch to Blast Loading," U.S. Army Engineer Waterways Experiment Station, Technical Report N-71-9, July 1971.

10. Balsara, J.P., "Similitude Study of Flexible Buried Arches Subjected to Blast Loads," U.S. Army Engineer Waterways Experiment Station, Technical Report No. 1-807, January 1968.

11. McGrath, R.K., "Dynamic Response of Concrete Arch Bunkers: Event Dial Pack Project LN314A," U.S. Army Engineer Waterways Experiment Station, Technical Report N-71-8, July 1971.

12. Palacios, N., and Kennedy, T.E., "The Dynamic Response of Buried Concrete Arches, Project 3.2 Operation Snowball," U.S. Army Engineers Waterways Experiment Station, Technical Report No. 1-797, September 1967.

13. Meyer, G.D , and Flathau, W.J., "Static and Dynamic Laboratory Tests of Unreinforced Concrete Fixed-End Arches Buried in Dry Sand," U.S. Army Engineer Waterways Experiment Station, Technical Report No. 1-758, February 1967.

14. Tener, R.K., "Model Study of a Buried Arch Subjected to Dynamic Loading," U.S. Army Engineer Waterways Experiment Station, Technical Report No. 1-660, November 1964.

15. Flathau, W.J., "Design of Buried Arches and Cylinders," International Seminar on Design of Protective Structures, Mannheim, West Germany, September 1984.

16. Krauthammer, T., "Reinforced Concrete Arch- and Box-type Structures Under Severe Dynamic Loads," Proceedings Joint I. Struct. E./B.R.E. Seminar, Design of Concrete Structures -- The Use of Model Analysis, England, 29-30, November, 1984.

17. Lipner, N. et al., "Fragility Analysis of Hardened Structures," TRW Defense and Space Systems Group, April 1982. (limited distribution).

18. Wong, F.S., and Richardson, E., "Transfer Function Analysis for Statistical Survivability/Vulnerability Assessment of Protective Structures," Air Force Weapons Laboratory, AFWL-TR-82-32, October 1982. (limited distribution).

19. Betz, J.F., et al., "Kachina Test Series: Eagle Dancer," Air Force Weapons Laboratory, Final Report, AFWL-TR-83-35, Vol. I-III, July 1983, (limited distribution).

20. Parsons, R., and Rinehart, E., "Kachina Test Series: Butterfly Maiden," Air Force Weapons Laboratory, Final Report No. AFWL-TR-82-132, Vol. I-II, June 1983, (limited distribution).

21. Smith, J.L., "Kachina Test Series: Dynamic Arch Test-3 Pretest Report," Air Force Weapons Laboratory, Final Report No. AFWL-TR-83-56, September 1983, (limited distribution).

22. Smith, J. L., Betz, J. F., and Baird, G. T., "Kachina Test Series: Dynamic Arch Test Three (DAT-3) Analysis Report," Air Force Weapons Laboratory, Final Report AFWL-TR-85-63, March 1986.

23. T. Krauthammer, "A Numerical Gauge for Structural Asssessment", 56th Shock and Vibration Bulletin, 1986.

24. T. Krauthammer, N. Bazeos, and T. J. Holmquist, "Modified SDOF Analysis of RC Box-Type Structures", ASCE Jour. of Structural Engineering, Vol. 112, No. 4, April 1986, pp. 726-744.

25. ASCE, Design of Structures to Resist Nuclear Weapon Effects, Manual No. 42, American Society of Civil Engineering, 1985.

DYNAMIC STRESS AT CRITICAL LOCATIONS OF A STRUCTURE
AS A CRITERION FOR MATHEMATICAL MODEL MODIFICATION

by

Ching-U Ip and Charles A. Vickery, Jr
Ballistic Missiles Division
TRW Inc.
Norton Air Force Base, California
and
David I.G. Jones
Materials Laboratory (AFWAL/MLLN)
Wright-Patterson Air Force Base, Ohio

This paper describes an investigation of analysis methods for predicting dynamic stresses at specific critical locations in a structure, by finite element methods, and the development and improvement of modal models using a novel Random Walk approach to correct for differences between analytical and experimental results.

1. INTRODUCTORY REMARKS

In the design, development, and qualification of an aerospace structure, structural adequacy under actual and specified environments has to be demonstrated. Typical dynamic environments for a ballistic missile for instance, are sustained acceleration, transportation and handling, acoustic excitation, operating flight, and payload reentry. For each dynamic environment, the missile structure must be shown to have a margin of safety equal to or exceeding zero.

Should the missile pass an actual flight test unscathed, this fact by itself does not qualify the structure for the flight environments. First, while the missile structure has undergone a set of actual environments, it has not necessarily encountered the maximum expected set corresponding to the worst flight trajectory. Secondly, the environment design factor, which ideally is the ratio of the specified environment to the maximum expected actual environment, has not been taken into account.

Simulation in the laboratory of each of the dynamic environments, and subjecting the structure to the environmental test, is a realistic but impractical and costly approach. Hence, there is little practical alternative other than to qualify the missile structure by analysis. This observation reflects Morrow [1], who said "Structures are to be qualified by analysis but equipment must be qualified by testing." The latter statement mostly reflects the fact that the dynamic behavior of components such as electronic printed circuits, transistors or computers is difficult to model mathematically, and their thresholds of failure are even harder to estimate without experimental evidence.

Given the requirement that the structure must be qualified by analysis for each of the specified environments, it seems at first sight to be straightforward to perform a number of dynamic analyses equal to the number of environments, and obtain the margins of safety from a critical examination of many present practices for achieving this end. This method reveals some shortcomings which, when scrutinized in detail, leave the goal of structural qualification unaccomplished. It is the objective of this paper to discourse on the pitfalls of proving structural adequacy, and to suggest remedies for some of the deficiencies.

Ideally one would wish for an analysis method which, prior to a dynamic test to failure of an aerospace structure, predicts exactly the magnitudes and durations of the failure load, and the location in the structure where failure will occur. This prediction should work for all prescribed dynamic and vibratory loads, and for each set of load conditions in turn, for failures caused by overload or fatigue. Admittedly this is a forever elusive goal, but analysis and dynamic testing practice can be improved such that the goal is being approached step by step. The investigation reported here is an attempt, in that direction, to devise a finite-element dynamic model which will give accurate dynamic stresses at failure locations (one location for each load environment) in the structure, and only approximately accurate stresses elsewhere. Specifically, the scope of the effort will include: (a) Vibration environmental specifications, design and testing procedures of a typical aerospace substructure (e.g. one stage of a missile) are delineated to show the requirements for verification of design adequacy. Dynamic analyses, choice of failure theories, and an accurate dynamic model are shown to be crucial in fulfilling the

requirements. Vibration testing data are needed to modify the finite-element model initially constructed from engineering idealization in the search of an accurate dynamic model. This investigation chooses the dynamic strains at the location of predicted structural failure as the quantities for matching between analysis and experiment; (b) A method is devised to choose candidate points in the structure, the population of which includes the point of structural failure. To render vibration testing for model verification practical and cost effective, a criterion for a minimum number of strain, force and acceleration measurements is established. The results obtained for model matching are in the form of force-to-strain and acceleration-to-strain transfer functions; (c) Structural failures due to dynamic loads or fatigue when the aerospace substructure is subjected to the specified vibration (deterministic and/or random) environment are derivable from the transfer functions obtained. Theories of failure have to be assigned a priori, however; (d) Revised structural mode shapes become a corollary of the correct stress transfer functions, and the advantages of employing them in certain applications are discussed. A computer program using a novel Random Walk method corrects the analytical mode shapes based on the measured natural frequencies and transfer functions, and the modal damping parameters derived therefrom.

The approach and procedure are demonstrated with reference to a specific structure, namely the main frame of a very high frequency high cycle/low cycle fatigue test machine being developed at the Materials Laboratory, this being the structure whose dynamic model is adjusted for correct stresses. This structure was chosen as the example because it required finite-element modelling by rather sophisticated solid elements to match the natural frequencies between analysis and experiment.

1.1 CRUCIAL SUBTLETIES OF ANALYTICAL PREDICTION

Ideally the analytical prediction should precisely foretell actual events. Consider the case of a missile structure subjected to a deterministic, dynamic, environment with the structure designed for certain values of factor-of-safety and environmental design margin. Should the dynamic environment then be increased beyond the design margin the analysis would predict a negative margin of safety. One would assume, not necessarily correctly, that failure would then occur. The following actions explore the reasons and delineates the difficulties to be overcome.

Margin of Safety and Failure

Surprisingly, the margin of safety is not a measure of closeness to failure. For prediction of failure by analysis, some

theories of failure have to be postulated. Take the simplest case of the Maximum Stress Theory. The following formula gives the margin of safety for fracture, $(MS)_f$:

$$(MS)_f = \frac{S_u/N}{e\ S} - 1 \qquad (1)$$

where S_u is the ultimate strength of the material, N is the factor of safety: A typical value of 1.25 applies to launch and flight loads. S is the induced stress at the critical point (where failure would occur) of the structure for the maximum expected, or specified, dynamic environment, and e is the environmental design margin intensification factor; A typical value is 3½ dB or a factor of 1.5. The factor of safety N accounts for uncertainties in the ultimate strength of the material (one dimensional tensile stress versus multi-dimensional stresses in the structure), fabrication variations and a "multitude of other sins." It is best considered as a factor that lowers the material ultimate allowable to the working or design stress, S_{wf}.

The interpretation of Equation (1) is as follows: If the actual dynamic environment is intensified by a factor e which should be then the specified environment for analysis or testing, and if the dynamic margin of safety, $(MS)_f$, is calculated to be equal to zero, then the peak of the transient dynamic stress at the critical point of the structure should have a value equal to the working stress, $S_{wf} = S_u/N$,

a predetermined quantity. Hence, $(MS)_f$ is a definite, calculable, quantity in dynamic analysis and is a measure of "closeness to the design state for the structure," not a measure of "closeness to structural failure." This is in contrast to the missile flight test, which is an up-or-down threshold on structural integrity. Nevertheless, margin of safety is a good measure of structural adequacy.

It is also noted here that, because of the environmental design margin and the factor of safety, the dynamic analysis of the structure should operate within the elastic range of the material. Thus the employment of linear modal analysis is justifiable.

Verification of Dynamic Model

Unless the mathematical dynamic model, in essence, truly represents the physical structure, qualification by analysis will lack a sense of reality. The question then rests on what are the essential features of the representation which, in turn, depend on the objectives of the analysis. If, for example, the first few bending frequencies of a missile are needed for the prediction of the stability of the guidance system, then a mathematical model which gives beam bending frequencies that match those measured in a vibration survey test is a good dynamic model. On the other hand, if the analysis is to show

30

structural reliability under dynamic environments, then such a verification criterion is inadequate.

If linear structural analysis is sufficient for the purpose of qualifying the structure, and if the mathematical model provides the correct normal modes, then it is an adequate representation of the physical structure regardless of the nature of the external loading, whether harmonic, transient or random. This approach is not practical, however, since the number of dynamic measurements has to be equal to the number of degrees-of-freedom of the structure.

If the problem concerns structural reliability, then it should be related to the manner of structural failure and its location, which is termed the critical point or the "weakest link." Would a dynamic model which, upon analysis, furnishes the correct displacement or acceleration response at the critical point be a satisfactory representation? An affirmative answer is not directly obvious. The criterion of a successful dynamic model actually depends on the theory of failure postulated. For the simplest maximum stress theory, which states that failure will occur when the maximum value of the dynamic stress at the critical point reaches the ultimate strength of the material at that point, the dynamic model which gives the correct stress at the critical point is a successful one.
It is apparent that a mathematical model does not have to represent the physical structure in all aspects, but should contain the truly essential features, the latter depending on the objectives of the analysis.

1.2 SYNOPSIS OF PROPOSED METHODOLOGY FOR VERIFICATION OF DYNAMIC MODEL

The proposed methodology is outlined below and details of its development will be presented in subsequent sections of this paper.

Consider the simple case of Maximum Stress theory as criterion of structural failure. The procedure of the analysis is as follows:

(i) Set the criterion of a satisfactory dynamic model as one that yields the same dynamic stress at the critical point (point of failure) of the structure as can be obtained by measurement.

(ii) Consider the normal mode model of the structure to be suitable for the purpose of proving structural adequacy. Once this normal mode model meets the correct dynamic stress requirement, all dynamic analyses will employ this model instead of the discrete mass model.

(iii) Use standard engineering idealization to establish a finite- element mathematical

model as a starting configuration and perform an eigenvector analysis on this model.

(iv) Use a resonant mode method (described later) of selecting candidate points within which population the critical point is likely to be, and where measurements will be made in the experimental vibration survey test. Perform preliminary dynamic analyses on the unverified mathematical model to further reduce the number of choices of candidate points.

(v) Conduct a vibration survey test on a prototype of the structure, measuring natural frequencies, modal damping, and response/load transfer functions at the candidate points. This experiment should be performed with care and precision so that the measured values can be used as standards to which the analytical values will be adjusted.

(vi) Employ a novel Random Walk optimization, which eludes local minima, to minimize the differences of the strain transfer functions as measured and as calculated at the dominant response frequencies. The quantities to be adjusted are the calculated mode shapes at the candidate points, resulting in the dynamic stresses at those points being correct after mode shape modification.

(vii) Utilization of the same Random Walk method to adjust the mode shape values of the modes at points other than the candidate points, so that the mode shapes will remain orthogonal. The final adjusted dynamic model then becomes a set of normal modes which yields correct dynamic stresses at the candidate points (which include the critical point). Even though there is no absolute assurance that dynamic stresses elsewhere in the structure will be correct, the calculated results from this adjusted dynamic model should be better than those from the unadjusted model.

2. THEORETICAL DEVELOPMENT OF THE METHOD

2.1 Normal Mode Mathematical Model and Dynamic Responses (Displacements)

The differential equation model of the structure is taken in the form:

$$[m]\{\ddot{x}\}+ [k(1 + i\eta)]\{x\} = \{f(t)\} \qquad (2)$$

where $\{x\}$ is the matrix of generalized displacements. Suppose the structure has n

degrees of freedom. If the set of n^2 transfer functions (receptances) associated with the structural system, as measured experimentally and derived from analysis, are made to agree, then the finite element model giving the same transfer functions is a realistic one, and the dynamic analyses performed on it for any kind of loads would be accurate.

The formal solution of the differential equation model given in Equation (2) will be

by the classical method of normal modes. The transformation of the generalized coordinate $\{x\}$ to normal coordinate $\{q\}$ is through the modal matrix $[\phi]$. Usually, only a limited number, m, of the mode shapes can be accurately determined either analytically or experimentally. Hence the order of $[\phi]$ is (nxm). The modal mass, modal damping, and modal stiffness matrices are given by:

$$\{x\} = [\phi]\{q\}$$

$$\lceil M_s \rfloor = [\phi]^T[m][\phi] \qquad (3)$$

$$\lceil k_s \rfloor = [\phi]^T[k(1+i\eta)][\phi]$$

where the superscript T is the transpose, and the subscript s is equal to 1, 2, ...; m denotes the natural modes; ω_s is natural circular frequency.

If the system is subject to sinusoidal excitations, $\{f_o\}e^{i\omega t}$, the displacement responses of the whole system will be given by

$$\{x\} = [H(\omega)]\{f_o\}e^{i\omega t} \qquad (4)$$

where the transfer function matrix:

$$[H(\omega)] = [\phi]\lceil Y_s(\omega)\rfloor[\phi]^T \qquad (5)$$

and the sth diagonal element of the admittance matrix $\lceil Y_s(\omega)\rfloor$ is given by:

$$Y_s(\omega) = \frac{1}{M_s[\omega_s^2(1+i\eta_s)-\omega^2]} \qquad (6)$$

If the system is subject to a set of external transient loads, $\{P_r(t)\}$, the system response $\{x(t)\}$ can be found as follows: The unit impulse response matrix of the system is given by

$$[h(t)] = \frac{2}{\pi}\int_0^\infty R_e H(\omega)\cos\omega t\, d\omega \qquad (7)$$

where $ReH(\omega)$ is the real part of $H(\omega)$ and:

$$\{x(t)\} = \int_0^t [h(t-\tau)]\{P_r(\tau)\}d\tau \qquad (8)$$

If the system is subject to a set of random loads characterized by the power spectral density matrix, $Sp_r p_u(\omega)$, the system response in the form of power spectral density matrix is given by:

$$[Sx_i x_j(\omega)] = [H(\omega)]^*[Sp_r p_u(\omega)][H(\omega)]^T \qquad (9)$$

where subscript P_u is another external force acting at x_u and $[H(\omega)]^*$ is the complex conjugate of $[H(\omega)]$.

2.2 Strain Transfer Functions at the Critical Point

Since only the critical point x_c is of importance, the displacement /force transfer functions associated with it are better found using the following formula instead of calculating them from Equation (5).

$$H_{x_c P_r}(\omega) = \sum_{s=1}^{m} \phi_{x_c s}\,\phi_{p_r s} Y_s(\omega) \qquad (10)$$

for $P_r = P_1, P_2, \ldots, P_p$, the p applied loads located at stations of the same designation in the structure.

We wish to derive a similar expression for a strain/force transfer function, to be compared directly with strain gage measurements. Let the critical point x_c be encased in a finite element in the mathematical model. The strain transfer function, $\{H_{\epsilon_{cr}}(\omega)\}$, and the stress transfer function, $\{H_{\sigma_{cr}}(\omega)\}$, with the input at P_r and the output at X_c, are functions of the displacement transfer functions of all the nodes of the finite element. Formally, they are expressed as follows (See Appendix I):

$$\{H_{\epsilon_{cr}}'(\omega)\} = [B]\{H_{u_i}^{(K)}(\omega)\} \qquad (11)$$

$$\{H_{\sigma_{cr}}'(\omega)\} = [C][B]\{H_{u_i}^{(K)}(\omega)\} \qquad (12)$$

where $[B]$ is the displacement to strain transformation matrix and $[C]$ is the strain-to-stress transformation matrix. These transfer functions, however, are expressed in global coordinates. To convert the strain and stress vectors back to the local coordinates of the finite element, for the purpose of matching the strain gage measurements, we need to multiply them by the transformation matrix $[T]$. Hence, we have the result:

$$\{H_{\epsilon_{cr}}(\omega)\} = [T]\{H_{\epsilon_{cr}}'(\omega)\}$$

$$\{H_{\sigma_{cr}}(\omega)\} = [T]\{H_{\sigma_{cr}}'(\omega)\} \qquad (13)$$

Appendix I shows an example, using an 8-node solid element, for the derivation of the stress and strain transfer functions, giving explicit expressions for the transformation matrices.

2.3 Search for the Critical Point

For each given loading environment, if it is increased progressively and proportionately everywhere on the structure, failure will occur at one location in the structure. Thus there are several critical points, and the same number of dynamic margins of safety, for the missile airframe specifications. Even if an accurate dynamic model of the structure is available, the dynamic analysis performed on it has to evaluate the dynamic stress everywhere in the structure and find the location having the least margin of safety. So far, we do not have an accurate dynamic model, and hence the dilemma is still present.

32

Suppose we, by some guideline, pick a finite number of structural locations (nodes in the dynamic model) called the candidate points, within which population the critical point is likely to be included, then the task of analysis becomes more manageable. The number of candidate points can be as large as the engineer chooses. One method of choosing candidate points is suggested here.

Resonant Modes Method

Vibration responses of airframe structures are usually measured in the low frequency region, and are more prominent at the resonant frequencies of the structure. This is true even for random vibrations. Even though we do not know which natural frequency will be excited, since the frequency contents of the loading environment are not analyzed, we realize that the dynamic response will encompass the first several resonant modes in some manner.

Let the structure statically assume the first mode shape. This pseudo-displacement load will induce stresses at various locations in the structure. We will use the static margin of safety as the selection criterion, and choose say 20 candidate points. Let the same procedure be repeated for the 2nd, 3rd, and 4th modes, say. We then have q=40 candidate points or less if some points are repeated. Since any one natural mode might be prominent in the dynamic response, all the candidate points for each mode are included in the study. This method will be correct if one single mode dominates the response. With superposition of the significant modes, the highest stressed point for one mode might not be the highest stressed point of the superposition. Hence we choose 10 candidate points for each mode.

2.4 Number of Measurements for Model Verification

We have defined a successful mathematical model as one which, when used in a dynamic analysis, yields the same dynamic stress at the critical point as that measured experimentally in the actual structure, subject to the same dynamic environment. The corollary is that, for linear structures, the successful mathematical model has the same strain/load transfer functions, at the critical point, as those experimentally measured.

Consider the case of q candidate points in the structure, subject to p discrete loads. It is assumed that the prototype structure has been built and is available for dynamic measurements. Furthermore, it is assumed that the loads $P_r(t)$, and their correlations, are known (as spelled out in a specification for example) and the experiments performed in the laboratory are skillfully conducted so that

the results can be taken as standards which analyses are made to match.

The successful mathematical model must have the correct strain transfer functions, at the critical point x_c, for all p loads. Since x_c is known only among q candidates, the number of transfer functions $H_{\epsilon_i P_r}(\omega)$ would be (p x q). Taking the previous example where p = 10 and q = 40, the number of response measurements will be 400, much too large to be practical.

In measuring the strain transfer functions, in accordance with the above procedure, a sine-sweep excitation is applied to each of the P_r locations in turn and the strains are measured at all the x_i locations.

The following test method will greatly reduce the number of vibrator setups and the number of strain measurements: first we modify the scheme of numbering the candidate points and the loading locations. Table I illustrates the system.

TABLE I   CANDIDATE POINTS

Node x	Candidate Points ℓ	Load P
x_1	0	0
x_2	.	P_1
.	0	0
.	ℓ_1	P_2
.	ℓ_2	0
.	.	.
.	.	.
x_i	$\ell_i \rightarrow x_i$	.
.	0	0
x_j	0	$P_r \rightarrow P_j$
.	.	0
.	.	.
.	ℓ_q	0
.	0	P_p
x_n	0	0

Let the candidate be at $\ell_1, \ell_2, \ldots \ell_q$ (for location). Instead of numbering them sequentially thus, we just specify the locations at the nodes of the finite element model where they occur. Similarly, the loading location is specified also at the nodes. The underlying reason is to make use of the Maxwell Reciprocity Theorem:

$$H_{x_i P_j}(\omega) = H_{x_j P_i}(\omega) = H_{ij}(\omega) \qquad (14)$$

33

[H] is a symmetric matrix. Now we wish to find $H_{x_i P_k}(\omega)$, the transfer function at x_i due to a force at x_k, without having to measure it directly.

$$H_{x_i P_k} = H_{ik} = \frac{\epsilon_i}{P_k} = \frac{\epsilon_i}{P_j} \cdot \frac{P_j}{\epsilon_j} \cdot \frac{\epsilon_j}{P_k} \qquad (15)$$

$$H_{ik} = H_{ij} H_{jj}^{-1} H_{jk}$$

However:

$$H_{jk} = H_{kj} \qquad (16)$$

$$\therefore H_{x_i P_k} = H_{x_i P_j} H_{x_j P_j}^{-1} H_{x_k P_j} \qquad (17)$$

That is to say, if one vibrator is placed at x_j for the test, and strain measurements are taken for all the candidate points and also all the loading locations, including x_j, then all the required $H(\omega)$'s can be derived from these measurements. This is a total of (p+q) measurements and only one excitation input. For the previous example, the resulting 50 measurements is an improvement over the initial 400.

As a practical matter, in a case where it is difficult to measure H_{jj} with the strain gage placed at the vibrator input, the testing procedure can be as follows:

(1): Employ a vibrator at another location x_j and obtain all the $H_{ij}(\omega)$'s except for i=j, for a total of (p + q -1) measurements.

(2): Repeat the testing with the vibrator at another location X_k and measure the transfer functions at X_j and another point X_i.

$$H_{x_j P_j} = \frac{\epsilon_j}{P_j} = \frac{\epsilon_j}{P_k} \cdot \frac{P_k}{\epsilon_i} \cdot \frac{\epsilon_i}{P_j}$$

$$\therefore H_{x_j P_j} = H_{x_j P_k} H_{x_i P_k}^{-1} H_{x_i P_j} \qquad (18)$$

Noting that $H_{x_i P_j}$ was previously measured, we now have two additional measurements, making a total of (p+q+1) measurements for the experiment.

2.5 Adjustment of the Dynamic Model

As shown above, correcting the dynamic model might not be necessary if the critical point whose stress/load transfer functions are experimentally determined, and its location are selected from dynamic analyses. However, there are situations when correcting the dynamic model to match experimental data might be very desirable. For example when (1), the critical point in the structure is

inaccessible for strain measurement, and as an alternative two or more strain measurements are taken in its neighborhood, the interpolation of $H_{\epsilon p}(\omega)$ will be difficult. If we adjust the mode shape values of the points measured such that the transfer functions at those points agree with the measurements, interpolation of mode shapes will be more feasible; (2), When a portion of the structure needs to be examined later for internal loads, stresses, etc., performing another experiment to determine new $H_{\epsilon p}(\omega)$ values is usually out of the question. With a dynamic model $[\mu]$, $[\phi]$, which is only slightly different from the original model, but gives correct $H_{\epsilon p}(\omega)$ values at all candidate points including the critical point of the structure, the analysis of the selected substructure should be an improved one. The same would be the case when a portion of the structure is altered, or additional portions are required, and component mode methods are used for analysis.

In making the choice of the theoretical dynamic model on which adjustments are made, we require the theoretically calculated natural frequencies to be close to the measured ones (say, within 5%). Otherwise, another process of engineering idealization of the structure is required to produce a satisfactory starting model.

When that is accomplished, we use the measured values of resonant frequencies, ω_c, and modal damping coefficients, η_c, for the adjusted model. The theoretical values of H_s and $\{\phi\}$ at the candidate points will be adjusted to give the measured $H_{\epsilon_i P_r}(\omega)$,

knowing the mode shapes at X_i and X_r, and the location of the candidate point and input load, respectively. Hence, the quantities for adjustment are:

$$M_s; \ \phi_{x_i s}; \ \text{and} \ \phi_{P_r S}. \quad (S = 1, 2. \text{---}, \text{m modes})$$

The number of these quantities to be adjusted is quite small. Furthermore, each candidate point will have it's own quantities for adjustment, independent of the others.

An even better method for adjusting the modal values is based on our suggested approach of having only one vibrator input at X_j, and obtaining $H_{x_j P_j}$. All the transfer functions due to other loading locations are derived from it. Therefore, M_s; and the row matrix $[\phi_{j1} \phi_{j2} \phi_{jm}]$ are the only quantities to be adjusted. Since, in the experiment, we have one loading input at X_j and measure $H_{\epsilon_i P_j}(\omega)$ at (p + q) points of X_i, be they candidate points or loading points.

$$H_{\epsilon_i P_j}(\omega) = \sum_{s=1}^{m} \phi_{is} \ \phi_{js} \ \gamma_s(\omega) \qquad (19)$$

After adjusting the modal values at X_j and considering these values invariant, then each

mode shape $[\emptyset_{is}]$ will be adjusted alone. Otherwise there will be conflicting values of $[\emptyset_{js}]$ for matching the different measured $H_{\epsilon iPj}$ (ω).

The analytical form of the transfer function may be written as

$$\left| H_{ij}(\omega) \right|^2 = \sum_{s=1}^{m} \frac{\mu_s}{(\omega_s^2 - \omega^2)^2 + \eta_s^2 \omega_s^4} \quad (20)$$

where $\mu_s = \psi_{is}\psi_{js}$ s^{th} mode contribution

$\qquad M_s$ s^{th} mode mass

$\qquad \eta_s$ s^{th} mode damping
$\qquad \omega_s$ s^{th} natural frequency
$\qquad i,j$ locations on the structure

Here the ψ's are defined as "strain mode shapes". The relation between ψ and $\emptyset$ is defined in equations (10), (13) and (20).

None of the above parameters are known except for the excitation frequency and the value of $H_{ij}(\omega)$ measured at discrete locations. Note that $H_{ij}(\omega_c)$ at ω_c may not be in the processed data and, in fact, even ω_c must be extracted from the experimental data. Consider the values of $\left| H_{ij}(\omega) \right|^2$ at ω_{sa},

ω_{sb}, and ω_{sc}, within the half-power region of a resonant frequency ω_s (such an assertion can be subsequently checked). Then from Equation (20), taken at the sth mode and writing a simpler expression for $\left| H_{ij}(\omega) \right|^2$, we have

$$K_{a,b,c} = \left| H_{ija,b,c} \right|^2 = \sum_{s=1}^{m} \frac{\mu_s}{(\omega_s^2 - \omega_{a,b,c}^2)^2 + \eta_s^2 \omega_s^4} \quad (21)$$

Note from Equation (20) that the value of $H_{ij}(\omega)$ is dependent on parameters at all resonant frequencies, ω_s. Hence, Equation (21) has too many unknowns to be solvable.

To find initial, approximate values of μ_s, ω_s, and η_s as starting points in a random walk optimization method, the following procedure is chosen:

In the close neighborhood of ω_c, only one term (at ω_c) of the series in Equation (20) is significant [2]. Hence, as a first approximation equation (21) can be expressed as:

$$K_{sa} = \frac{A_s}{(\alpha_s - \alpha_a)^2 + \gamma_s \alpha_s^2}$$

$$K_{sb} = \frac{A_s}{(\alpha_s - \alpha_b)^2 + \gamma_s \alpha_s^2} \quad (22)$$

$$K_{sc} = \frac{A_s}{(\alpha_s - \alpha_c)^2 + \gamma_s \alpha_s^2}$$

where,

$$K_{sa} = \left| H_{sa} \right|^2, \text{ etc } \dots \quad (23)$$
$$A_s = \mu_s^2, \alpha_s = \omega_s^2, \gamma_s = \eta_s^2$$

and is now a set of three linear equations with three unknowns, $A, \alpha,$ and γ . Explicit solution of the equations yields.

$$A_s = \frac{1}{\Delta} \begin{vmatrix} \alpha_a^2 - \alpha_b^2 & 2(\alpha_a - \alpha_b) \\ \alpha_b^2 - \alpha_c^2 & 2(\alpha_b - \alpha_c) \end{vmatrix}$$

$$\alpha_s = \frac{1}{\Delta} \begin{vmatrix} -1 & -1 & 2 & 2 \\ K_{sa} - K_{sb} & \alpha_a^2 - \alpha_b^2 \\ -1 & -1 & 2 & 2 \\ K_{sb} - K_{sc} & \alpha_b^2 - \alpha_c^2 \end{vmatrix} \quad (24)$$

$$\gamma_s = (K_{sa}A_s + 2\alpha_s\alpha_a - \alpha_a^2 - 1) / \alpha_s^2$$

$$\Delta = \begin{vmatrix} -1 & -1 \\ K_{sa} - K_{sb} & 2(\alpha_a - \alpha_b) \\ -1 & -1 \\ K_{sb} - K_{sc} & 2(\alpha_b - \alpha_c) \end{vmatrix}$$

Hence, as seen from equations (22) and (23), the approximate values of ω_s, η_s and μ_s are found

from the experimental data only. Denote these values by $\omega_{so}, \eta_{so},$ and $\mu_{so},$ and the squared

values by $\alpha_{so}, \gamma_{so},$ and A_{so}. It is noted here

that $\omega_s, \eta_s,$ and μ_s involving the mode shape

values at X_i and X_j, are the quantities that need to be extracted from experimental data and incorporated into the dynamic model. So far, approximate and initial values of these quantities for all m significant modes have been found.

It is postulated that the total dynamic stress response is the sum total of the responses of the m modes, and in curve fitting of the $H_{ij}(\omega)$ function, the theoretical curve

derived from the finite-element model should match the experimental curve at each of the measured points in the halfpower range with minimum error. The initial theoretical values will be progressively revised by a Monte Carlo method to minimize the error. The function to be minimized is:

$$\sum_{s=1}^{m} \sum_{i=a,b,c,d\dots} \left(K_{si} - \frac{A_s}{(\alpha_i - \alpha_{si})^2 + \gamma_s \alpha_s^2} \right) = \text{Minimum} \quad (25)$$

Equation (25) can be efficiently minimized using the novel random walk method described in section (2.6). The steps for adjusting the dynamic model are as follows:

Step 1: Compare the natural frequencies calculated using the unadjusted dynamic mode to those measured, for the purpose of assuring that the finite element model is sufficiently accurate to be adjustable.

Step 2: Use Cramer's rule to approximately determine α_s and γ_s from experimental transfer functions. Consider the values of A_s to be accurate enough and not needing to be adjusted.

Step 3: Employ a novel random walk method to minimize the difference between the analytical and measured transfer functions by adjusting η_s, M_s, and the ϕ's.

2.6 Random Walk Method for Finding Extrema

A customary method for finding maxima is the gradient method which requires determining the direction of maximum change of the function by evaluating derivatives with respect to its independent variables. One proceeds along one direction, or gradient, until the function ceases to increase. At this point the gradient has changed and must be recalculated. By repeating the process until the gradient becomes zero, a local maximum is found. To find a minimum, one needs only to find the negative of the maximum.

Because of the amount of computation in derivative determination, a more efficient method is to proceed along a random direction without determining the gradient. It can be shown that the expectation of the change is in the gradient direction and the partial derivatives required to determine the gradient need not be calculated [3].
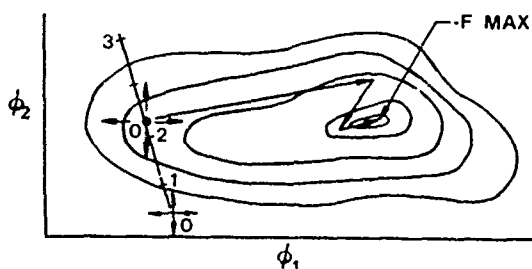
To illustrate the minimization procedure, consider the simple example shown in Figure 1, where F is a function of the two dimensional space (ϕ_1, ϕ_2). Starting with an initial guess of ϕ_1^0, ϕ_2^0 which corresponds to the point 0 in the space, -F is evaluated. A random direction is selected to proceed along, away from 0. A point 1 along the chosen direction is selected, nearby 0, and the corresponding value of -F evaluated. If the value of -F has decreased at 1, select point 2 at twice the step size of 1 from 0. If point 2 is still lower, select a point 3 at again twice the step size. Suppose point 3 yields a higher value -F than 2. Then return to point 2 and select a new point at one tenth the current step size. By continuing in this fashion until the step size effectively vanishes, a point 0' is found at the minimum along line 0-3. From 0', another direction is chosen at random and the process repeated until -F ceases to decrease. Figure 2 shows a flow chart of the process.

It may be seen that this method has some of the characteristics of the method of steepest descent, but it is more efficient in that the gradients in n-dimensional space need not be evaluated for each step. In either case, a new problem arises when a large number of extrema with insufficient magnitude to satisfy the success criteria are present in the space. Both methods will stop at a local extreme near the initial starting estimate and proceed no further. One approach is to vary the initial starting point throughout the n dimensions until one that yields an extreme of sufficient magnitude is found. This can quickly become unmanagable as n increases. One might imagine a 10-dimensional analogy to finding the bottom of a well in a plain of rolling hills. An approach is proposed here which seeks to tunnel from the bottom of one trough to the side of a deeper one. When a local minimum is reached, the procedure begins to evaluate the function in each independent direction, holding the rest constant until the function decreases. At this point the Random Walk is repeated, yielding a lower extreme than before. The large number of local extremes, which causes the problem, is an aid to the tunneling procedure by making it easy to swiftly find deeper and deeper holes in the space.

The tunneling procedure has been applied to the mode shape modification described above and found to perform exceedingly well. Transfer Functions have been optimized to match experimental data wherein the differences are indistinguishable within the plotting resolution, when steepest descent procedures have failed to make a distinguishable improvement using the same amount of computer resource.

Figure 1. Random Walk Method
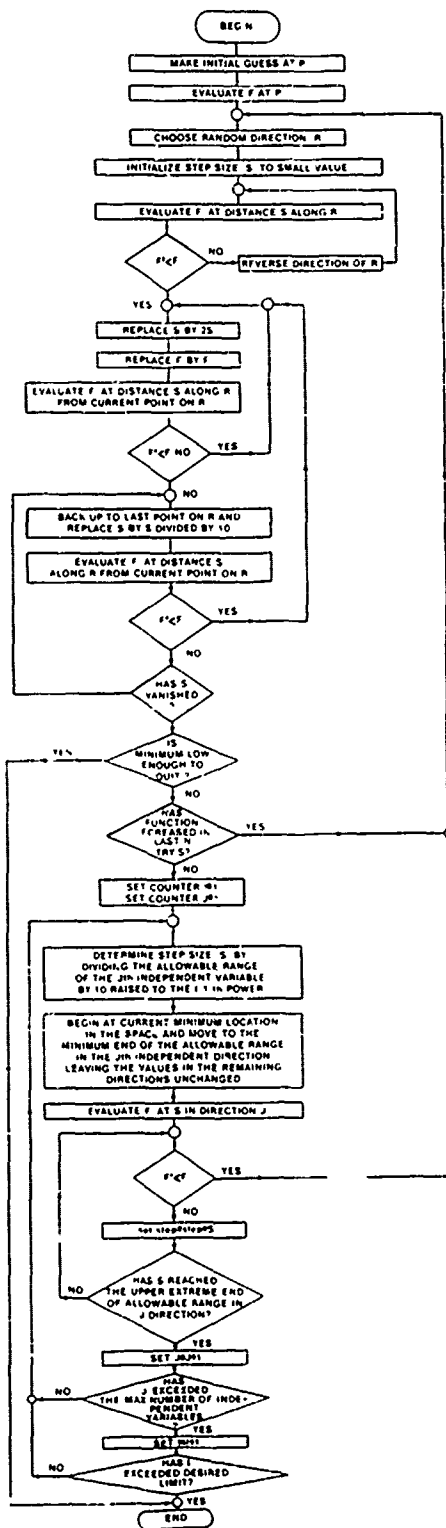
Figure 2. Flow Chart of Random Walk Optimization Procedure with Tunneling to find decreasing local minima

2.7 Orthogonality of the Adjusted Mode Shapes

Once the modal frequencies ω_s and modal damping factors have been modified to fit the significant measured data, at the candidate points in the frequency regions resonance, these values are considered satisfactory without further adjustment. The mode shape values at the candidate points then yield correct stresses at those points, and these can also be left unaltered. The mode shape values at other points of the structure, if left as calculated by the initial finite-element model, will violate the orthogonality properties of normal modes when combined with the adjusted mode shape values at the candidate points. Figure 3 shows a pictorial example of the process of adjusting mode shapes for orthogonality, while preserving the correct responses at the candidate points.
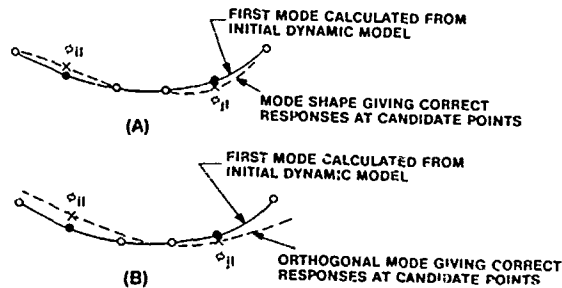
Figure 3. Mode shape adjustment process

Let the modal values of all the modes be divided into two groups: those which have been adjusted, and those which remain the same as first calculated from the approximate finite-element model. Consider the shape of the sth mode, which can be rearranged and partitioned with submatrices $\{\phi_A\}$ and $\{\phi_y\}$, the former having adjusted values, and the latter not:

$$\{\phi_s\} = \left\{\begin{array}{c} \phi_y \\ \hline \phi_A \end{array}\right\} \tag{26}$$

The Property of Orthogonality requires

$$\{\phi_s\}^T [M] \{\phi_s\} = [I] \tag{27}$$

If the modes are normalized to mass the property of orthogonality requires:

$$\left[\phi_y^T \;\vdots\; \phi_A^T\right] \left[\begin{array}{c|c} M_y & M_{yA} \\ \hline M_{Ay} & M_a \end{array}\right] \left\{\begin{array}{c} \phi_y \\ \hline \phi_A \end{array}\right\} = [I] \tag{28}$$

from which we obtain the matrix equation:

$$(\phi_y^T M_y + \phi_A^T M_{yA})\phi_y + M_{yA}\phi_A \phi_y^T = [I] - \phi_A^T M_A \phi_A \tag{29}$$

37

It should be noted that $\{\phi_y\}$ is the only vector whose elements need to be adjusted to make both sides of Equation (29) identical, or nearly so. This again can be accomplished using the Sylvester-Brooks Monte Carlo method.

Most structures act as low frequency filters, i.e. the dynamic response of the structure to a complicated frequency forcing function is significant only in the neighborhood around the modal frequencies of the structure, which are few in number. Suppose for example that there are three dominant modes. Hence we can adjust mode 1 first for orthogonality - Equation (29) - and then adjust mode 2 to be orthogonal to mode 1. Next adjust mode 3 to be orthogonal to mode 1. A further refinement is to make mode 2 orthogonal to mode 3. It is thus seen that this is a feasible method to adjusting the mode shapes for orthogonality.

3. ILLUSTRATION OF THE METHOD (EXAMPLE)

3.1 Selection of Test System

In order to demonstrate the application of the general analytical approach described in section 2, a suitable structural system was selected on the basis of timely availability. The system consisted of a non-uniform cylindrical steel ring of 203 mm (8 inches) outer diameter, 127 mm (5 inches) inner diameter and 102 mm (4 inches) width. The system was being tested in the process of development of a high-frequency test machine [4], and considerable transfer function and modal data was available. The system was ideal for the purpose of verification of the approach, being complex enough to test available finite element and modal analysis capabilities, yet not needlessly large with respect to number of modes. The test specimen is illustrated in Figure 4, showing the measurement points for accelerometers and strain gages. The specimen has several slots cut as indicated, leading to some asymmetry of the dynamic behavior. The ring was supported on soft elastomeric pads (Isomode^R) in a heavy fixture.
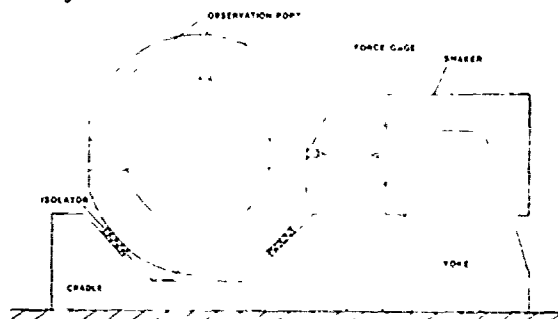
Figure 4.   Test specimen with loading and pickup points

3.2 Description of Test Methodology

The test system used to excite the specimen and gather transfer function characteristics is illustrated in Figure 5. The exciting force produced by the small electrodynamic shaker was measured by a force gage, and the response was measured by a miniature accelerometer placed in turn at all the selected test points, as well as by several strain gages, measuring the surface strain in the circumferential direction. A digital stepsine system was developed to measure and store the acceleration, strain and force signals for stepped sine-wave excitation [5,6]. In this system, the step interval and the dwell time at each frequency increment, the time for response stabilization at each step, and many other test parameters could be selected at will. A schematic of the STEPSINE system is illustrated in Figure 5.
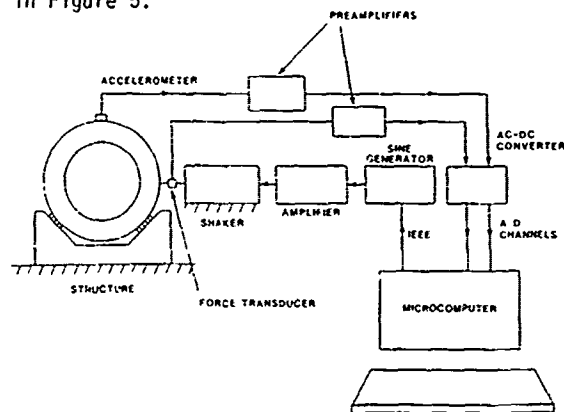
Figure 5.   Schematic of STEPSINE test system

3.3 Measured Transfer Functions and Mode Shapes - Displacement and Strain

A typical measured displacement/force transfer function is illustrated in Figure 6. Other measurements were made by moving the accelerometer around the ring at successive 15 degree increments in three axial planes. Major modes were observed at about 2820 Hz (2 nodal diameter symmetric mode), 4140 Hz (2 nodal diameter unsymmetric mode), 7480 Hz (4 nodal diameter symmetric mode), along with minor ones at 2980 Hz (2 nodal diameter symmetric mode, doublet of that at 2820 Hz), 3500 Hz (doublet of that at 4140 Hz), 6000 Hz (1 nodal diameter unsymmetric mode) etc. The minor modes were not strongly excited because the excitation point (0,0) was near a nodal line for each mode, but enough response could be generated to define the mode shapes reasonably well. Figures 7 and 8 illustrate some of the observed modes.

Strain measurements were made at 60 degree angular increments in one plane (plane 0, the plane of excitation). The number of strain gages was limited because of their finite size and the need to keep the strain gage wiring
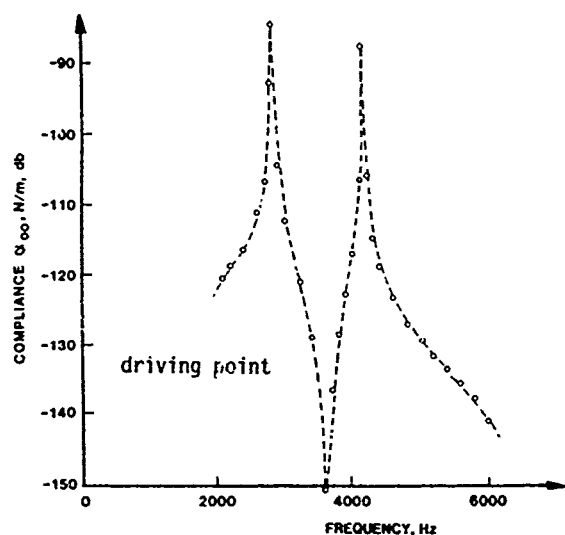
Figure 6. Typical measured compliance

under some control. The strain gage
measurements were made for each gage in turn,
using the output of a strain-gage bridge to
give a calibrated signal. Figure 9 shows a
typical strain-compliance frequency transfer
function. The high noise floor for the strain
signals was annoying, but could not be removed
at the time of the tests. However, the
response near each resonant peak was well
defined and sufficient for the purposes of this
investigation. Figure 10 shows some measured
strain modal functions for the first "major"
mode.
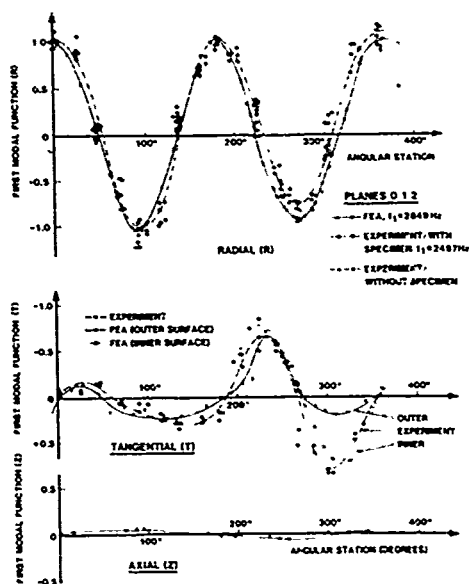
Figure 7. Measured fundamental symmetric
mode (with unmodified FEA results)
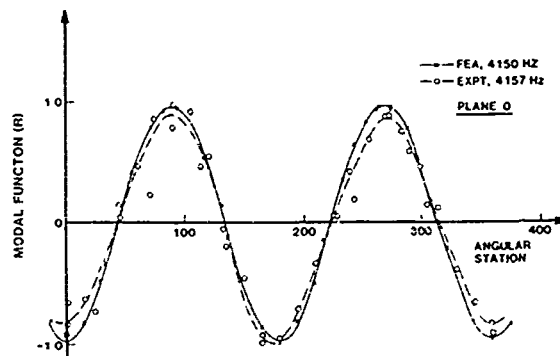
Figure 8. Measured second mode (with
unmodified FEA results)
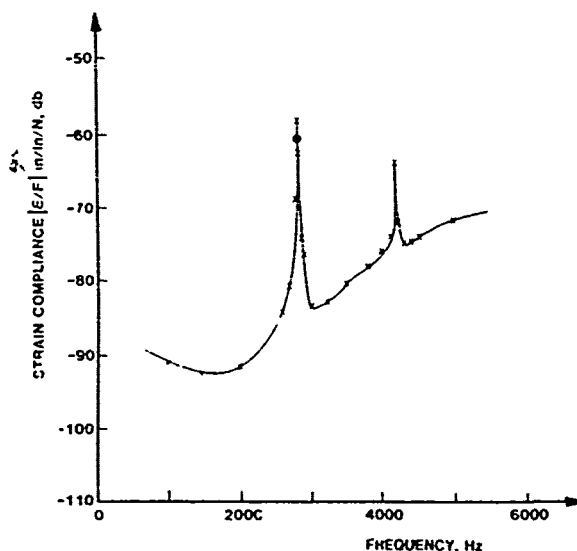
Figure 9. Typical measured strain compliance

3.4 Demonstration of the Dynamic Model Modification Procedure

The Experimental High Frequency Material
Testing Device was selected as the structure
to use for demonstration of the dynamic modal
modification procedure since it operates at
high frequency and requires complex 3
dimensional analysis techniques. The device
described previously consists of a 102 mm (4
inch) thick steel ring, approximately 203 mm
(8 inches) outside diameter and 127 mm (5
inches) inside diameter, with four 51 mm (2
inch) by 13 mm (½ inch) slots assymetrically
located. The Finite Element Model, shown in
Figure 11, consists of 20 noded hexagonal
elements, comprising 2562 degrees of freedom.
The less complicated 8 noded hexagonal
elements were first tried, and found to yield
an unsatisfactory estimate of even the first
natural frequency at 2822 hertz. Clearly,
many of the complexities of modern day
analytical technique are present in this
example.

39
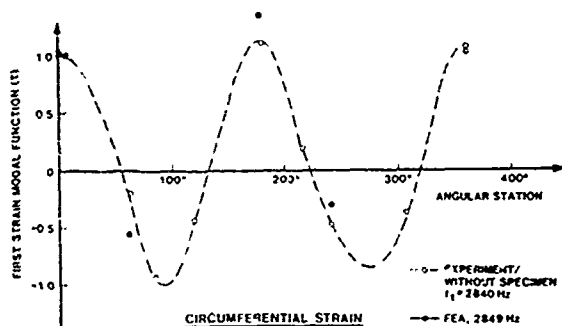
Figure 10. Measured strain modal function for first symmetric mode (with unmodified FEA results)

The dynamic model modification was performed as described in the detailed discussion of the procedure. The finite element normal modes analysis was performed using the qualified MSC/NASTRAN solution 3. A DMAP alter was written which directly saved the modal matrix in OUTPUT4 format for subsequent direct access by the modification procedure computer program. The initial finite element model, using 8 noded hexogonal elements, was found to be inadequate for realistic modification. Therefore, the idealization was repeated using 20 noded hexagonal elements, totaling 2562 degrees of freedom and yielding results satisfactory for use as a starting approximation for the modification procedure. Table 2 compares the experimental and analytical results for the first eight modes.
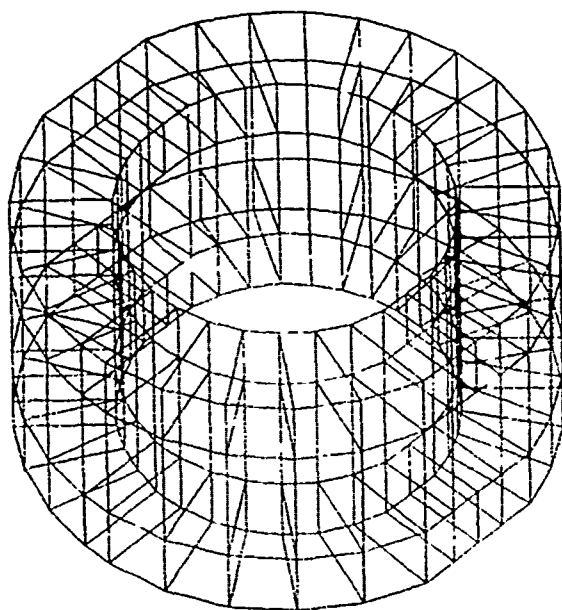
Figure 11. 2562 Degree of Freedom Finite Element model of Experimental High Frequency Fatigue Test machine

The Transfer Function (T.F.), relating the force at the shaker input location (see Figure 11) to displacement at the same location, was chosen for this example. Figure 12 shows a comparison of the experimentally measured transfer function (from Fig. 6) versus the analytically calculated transfer function. The parameters used for the analytical function were the unaltered first eight analytical natural frequencies and mode shapes, plus the initial experimental estimates of the damping. Table 3 lists the parameters for the first analysis approximation.
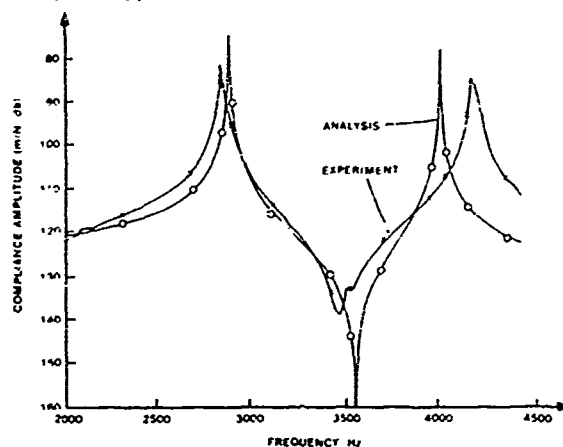
Figure 12. Comparison of unmodified analytical transfer function with experiment

TABLE 2. COMPARISON OF EXPERIMENTAL MODAL RESULTS WITH THE APPROXIMATE ANALYSIS

Mode Number	Experimental Frequency Hz	Analytical Frequency Hz	Experimental Modal Damping
1	2850	2863	0.0014
2	2973	2982	-
3	3496	3391	-
4	4163	3979	0.0010
5	5957	5942	-
6	7086	7113	-
7	7486	7493	0.0041
8	8034	7605	-

TABLE 3. UNIMPROVED ANALYTICAL TRANSFER FUNCTION PARAMETERS

Mode Number	Frequency Hz	Modal Damping	Mode Shape at T.F. location
1	2863	0.0014	4.451
2	2982	0.0014	-.1981
3	3391	0.0014	.008689
4	3979	0.0010	5.623
5	5942	0.0010	-.1119
6	7113	0.0010	-.7850
7	7493	0.0041	-4.360
8	7605	0.0041	-2.736

The first step in adjusting the analytical model was to estimate the effective modal

40

parameters from the experimental transfer function that was being matched. Since the experiment was performed at discrete frequencies 20 hertz apart, a fitting procedure was needed to interpolate for the actual natural frequency and apparent damping. The 3 point fit described in Section 2 was used to determine the parameter estimates listed in Table 4 for the 2 dominant modes (first and fourth) of the response.

Next, the estimated experimental damping and natural frequencies were substituted into the analytical model, leaving only the mode shapes to be corrected. The Random Walk Hole Seeking procedure described above was used to determine the combination of the eight parameters best matching the analysis to the experiment. Figure 13 illustrates the improvement realized. As can be seen, the agreement is very good in the area around the two major responses, which is the area of interest. However, it is also seen that the modal damping for the second major mode is too low. The next step would be to add the modal damping to the list of parameters for optimization and repeat the procedure. However, this would increase the cost significantly since changing the damping forces a recalculation of the complex admittance at each of thousands of tries in the Random Walk procedure. By estimating the needed change in damping from the plot, one can effectively improve the bandwidth characteristic for each mode without resort to a computer algorithm, and then perform the optimization of the mode shapes as before with the new damping estimates fixed. Figure 14 shows the final result obtained in this fashion. As can be seen, it is suitable for use in the most precise analysis. Table 5 shows the final analysis parameters used to generate Figure 14 and the percentage changes in the original analysis parameters required to effect the change. The final model agrees quite well the experiment without major changes from the original approximation.
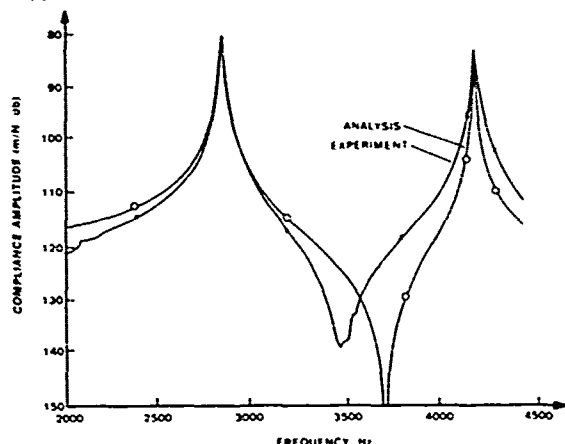
Figure 13. Comparison of analytical and experimental transfer functions after modification of analytical mode shape
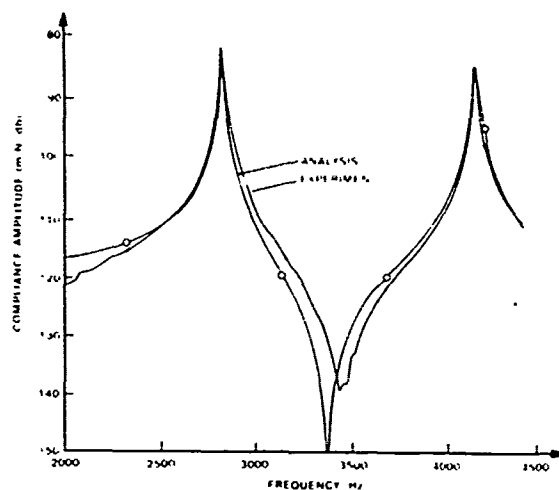
Figure 14. Comparison of modified analytical and experimental transfer funcitons

4.0 CONCLUSIONS

The main conclusions of the investigation are:

(a) A dynamic model for predicting failure of a structure has been outlined, which needs only to represent the true state of stresses at the structural location where failure occurs. It can represent the rest of the structure in an approximate manner. See Figure 15 for a flow chart of the approach.

(b) A procedure is devised to find candidate locations which include the critical location. Subsequent dynamic analysis determines the location of failure.

(c) Displacements, accelerations or dynamic stresses at critical locations of the structure can be used as criteria for the modification of the dynamic model from measured test data. The number of load application points, and of candidate structural points, determines the minimum number of load/strain measurements required to define the model.

(d) It was found, by a Random Walk approach, that the revised structural mode shapes would be perturbations of the originally calculated mode shapes, and yet preserve orthogonality relative to one another. More importantly, they produce the correct stresses at the critical point of the structure under any given deterministic or random dynamic loads. The essence of the Random Walk approach is illustrated for a two dimensional case in Figure 16. A Flow Chart is given in Fig. 2.

(e) The procedure has been proven and tested by analytical and experimental evaluations performed on the structure of a prototype high frequency test machine.

41

TABLE 4. 3 POINT FIT OF DISCRETE EXPERIMENTAL DATA FOR ESTIMATION OF MODAL PARAMETERS

Mode Number	i	4
Points Fit	2800 Hz; -90.188 Decibels	4120 Hz; -94.230 Decibels
	2820 Hz; -81.429 Decibels	4140 Hz; -84.6937 Decibels
	2840 Hz; -87.971 Decibels	4160 Hz; -86.916 Decibels
Estimated Natural Frequency	2823.06 Hz	4146.48 hz
Estimated Modal Damping	0.00593	0.00216

TABLE 5. FINAL ADJUSTED ANALYSIS MODEL

Mode Number	Frequency Hertz	Modal Damping	Mode Shape @ T.F. Location	Percent Change
1	2823	.00673	4.958	11.4
2	2973	.0014	-.1934	2.37
3	3460	.0014	.009556	9.96
4	4148	.0061	6.242	11.0
5	5997	.0010	-.1045	6.23
6	7112	.0010	-.8454	-7.65
7	7488	.0041	-.4163	4.52
8	7604	.0041	-.2657	1.44
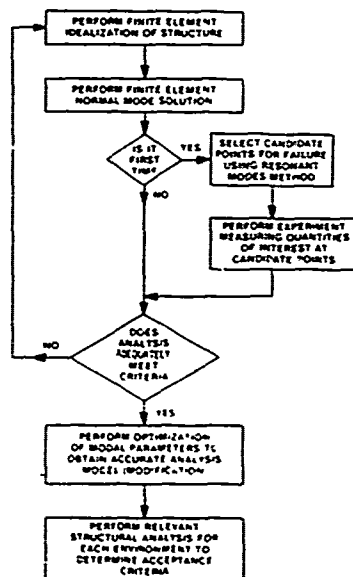
Figure 15. Flowchart of failure prediction approach.

REFERENCES

1. C. Morrow, Shock and Vibration Engineering, Vol 1, Wiley, 1963.

2. J.D. Robson, An Introduction to Random Vibration, Elsevier Publishing Co, New York, page 30, 1984.

3. Ching-U Ip, E.P. Howard and R.J. Sylvester, "Method for Improving a Dynamic Model Using Experimental Transient Response Data", Shock and Vibration Bulletin 36(5), pp 1-15, 1967.

4. D.I.G. Jones, "Initial Design and testing of a unique high frequency fatigue test system", Shock and Vibration Bulletin 55(2), 1985, pp. 17-26.

5. D.K. Rao, and D.I.G. Jones, "Measurement of dynamic characteristics of a structure using programmed sine-step test", Proc. 3rd International Modal Analysis Conference, Orlando, FL, Vol 1, Jan 1985, pp. 338-345.

6. D.K. Rao, and D.I.G. Jones, "Investigation of modes, frequencies and forced response of a high frequency fatigue test system", Shock and Vibration Bulletin 55(2), 1985, pp. 27-28.

APPENDIX I

STRAIN AND STRESS TRANSFER FUNCTIONS

1. Transfer Function

These functions measure the dynamic strain and stress responses, as functions of frequency at one location of a structure, as caused by a harmonic input of force or acceleration at another location of the structure. Let the stress or strain response as functions of time, t, be denoted by $O(t)$, the output; and the force or acceleration by $I(t)$, the input. Then the transfer function, $H(\omega)$ is defined mathematically as

$$H(\omega) = \frac{\mathcal{L}[O(t)]}{\mathcal{L}[I(t)]} \qquad (1.1)$$

where $\mathcal{L}$ is the Laplace transform with all the initial conditions of the system equal to zero.

2. Stress, Strain and Displacement Relationship of an 8-node, 3 Dimensional Finite Element.

Consider a 3-D finite element inside a thick ring as shown in Figure 17. We wish to obtain the expressions for the stress and strain at any point inside the element as functions of displacements at the 8-nodes of the element.

Let X_1, X_2, X_3 and r_1, r_2, r_3 denote the global and natural coordinate systems, respectively, as illustrated in Figure 18. The interpolation (or shape) functions of the nodes are given by

$$N^{(1)} = (1/8)(1+r_1)(1+r_2)(1+r_3)$$

$$N^{(2)} = (1/8)(1+r_1)(1-r_2)(1+r_3)$$

$$N^{(3)} = (1/8)(1+r_1)(1-r_2)(1-r_3)$$

$$N^{(4)} = (1/8)(1+r_1)(1+r_2)(1-r_3) \quad (1.2)$$

$$N^{(5)} = (1/8)(1-r_1)(1+r_2)(1+r_3)$$

$$N^{(6)} = (1/8)(1-r_1)(1-r_2)(1+r_3)$$

$$N^{(7)} = (1/8)(1-r_1)(1-r_2)(1-r_3)$$

$$N^{(8)} = (1/8)(1-r_1)(1+r_2)(1-r_3)$$

The structural point in question will then have the global coordinates (X_1, X_2, X_3). As an example, the X_1 component is given by the following expression:

$$X_1 = N^{(1)}X_1^{(1)} + N^{(2)}X_1^{(2)} + \ldots + N^{(8)}X_1^{(8)}. \quad (1.3)$$

where, $X^{(1)}$ is the X_1 component of node (1), etc.

Using the concise tensor notation, the coordinate components of the structural point are written as:

$$X_i = N^{(k)}X_i^{(k)} \quad (1.4)$$

and the displacement components as:

$$u_i = N^{(k)}u_i^{(k)} \quad (1.5)$$

with $i = 1, 2, 3$; $k = 1, 2, \ldots, 8$.

Now an element of the strain vector,

$$\{\epsilon\}^T = \begin{bmatrix} \epsilon_{11} & \epsilon_{22} & \epsilon_{33} & 2\epsilon_{12} & 2\epsilon_{23} & 2\epsilon_{31} \end{bmatrix} \quad (1.6)$$

is given by

$$\epsilon_{ij} = \tfrac{1}{2}\left[\frac{\partial u_i}{\partial X_j} + \frac{\partial u_j}{\partial X_i}\right] \quad (1.7)$$

Derivatives using global coordinates as independent variables in terms of natural coordinates take the following form:

$$\begin{Bmatrix} \dfrac{\partial}{\partial r_1} \\ \dfrac{\partial}{\partial r_2} \\ \dfrac{\partial}{\partial r_3} \end{Bmatrix} = \begin{bmatrix} \dfrac{\partial X_1}{\partial r_1} & \dfrac{\partial X_2}{\partial r_1} & \dfrac{\partial X_3}{\partial r_1} \\ \dfrac{\partial X_1}{\partial r_2} & \dfrac{\partial X_2}{\partial r_2} & \dfrac{\partial X_3}{\partial r_2} \\ \dfrac{\partial X_1}{\partial r_3} & \dfrac{\partial X_2}{\partial r_3} & \dfrac{\partial X_3}{\partial r_3} \end{bmatrix} \begin{Bmatrix} \dfrac{\partial}{\partial X_1} \\ \dfrac{\partial}{\partial X_2} \\ \dfrac{\partial}{\partial X_3} \end{Bmatrix} \quad (1.8)$$

where the square matrix is called the Jacobian operator matrix, $[J]$. Hence we obtain

$$\begin{Bmatrix} \dfrac{\partial}{\partial X_1} \\ \dfrac{\partial}{\partial X_2} \\ \dfrac{\partial}{\partial X_3} \end{Bmatrix} = [J]^{-1} \begin{Bmatrix} \dfrac{\partial}{\partial r_1} \\ \dfrac{\partial}{\partial r_2} \\ \dfrac{\partial}{\partial r_3} \end{Bmatrix} \quad (1.9)$$

From equations (1.6), (1.7), and (1.9) a mathematical operation yields

$$\{\epsilon\} = [B]\{u\} \quad (1.10)$$

where

$$\{u\}^T = \begin{bmatrix} u_1^{(1)} & u_2^{(1)} & u_3^{(1)} & u_1^{(2)} & u_2^{(2)} & u_3^{(2)} & \ldots & u_1^{(8)} & u_2^{(8)} & u_3^{(8)} \end{bmatrix} \quad (1.11)$$

and the strain displacement transformation matrix;

$$[B] = \begin{bmatrix} J_{1j}^{-1}\dfrac{\partial N^{(k)}}{\partial r_j} & 0 & 0 \\ 0 & J_{2j}^{-1}\dfrac{\partial N^{(k)}}{\partial r_j} & 0 \\ 0 & 0 & J_{3j}^{-1}\dfrac{\partial N^{(k)}}{\partial r_j} & \ldots \\ \ldots & J_{2j}^{-1}\dfrac{\partial N^{(k)}}{\partial r_j} & J_{1j}^{-1}\dfrac{\partial N^{(k)}}{\partial r_j} & 0 \\ 0 & J_{3j}^{-1}\dfrac{\partial N^{(k)}}{\partial r_j} & J_{2j}^{-1}\dfrac{\partial N^{(k)}}{\partial r_j} \\ J_{3j}^{-1}\dfrac{\partial N^{(k)}}{\partial r_j} & 0 & J_{1j}^{-1}\dfrac{\partial N^{(k)}}{\partial r_j} \end{bmatrix} \quad (1.12)$$

where the full $[B]$ matrix has 6 rows and 24 columns, and its elements are written in tensor notation, thus

$$J_{1j}^{-1}\frac{\partial N^{(k)}}{\partial r_j} = J_{11}^{-1}\frac{\partial N^{(k)}}{\partial r_1} + J_{12}^{-1}\frac{\partial N^{(k)}}{\partial r_2} + J_{13}^{-1}\frac{\partial N^{(k)}}{\partial r_3} \quad (1.13)$$

The stress vector (in global, rectangular coordinates) is

$$\{\sigma\}^T = \begin{bmatrix} \sigma_{11} & \sigma_{22} & \sigma_{33} & \sigma_{12} & \sigma_{23} & \sigma_{31} \end{bmatrix} \quad (1.14)$$

This can be derived from the strain vector by the stress-strain transformation matrix, $[C]$, obtained from the theory of elasticity. For an isotropic material, we have:

$$[C] = \frac{E(1-\nu)}{(1+\nu)(1-2\nu)} \begin{bmatrix} 1 & \frac{\nu}{1-\nu} & \frac{\nu}{1-\nu} & & & \\ \frac{\nu}{1-\nu} & 1 & \frac{\nu}{1-\nu} & & O & \\ \frac{\nu}{1-\nu} & \frac{\nu}{1-\nu} & 1 & & & \\ & & & \frac{1-2\nu}{2(1-\nu)} & & 0 \\ & O & & & \frac{1-2\nu}{2(1-\nu)} & \\ & & & 0 & & \frac{1-2\nu}{2(1-\nu)} \end{bmatrix} \quad (1.15)$$

43

where E = Young's modulus and v = Poissons ratio.

The stress vector is then given by:

$$\{\sigma\} = [C]\{\epsilon\} = [C][B]\{u\} \qquad (1.16)$$

which relates the stress state of a point (e.g. the center or a Gauss quadrature point) in the finite element to the displacements at all the nodes of the element.

3. Stress and Strain Transfer Functions

Consider a piece of structure such as the thick ring in Figure 17, excited by an external force f(t) at a point of application. The dynamic stress and strain at a chosen location (enclosed by the 3-D finite element) are being investigated. The dynamic stress can be harmonic, transient or random. For all of these cases if the stress transfer function, $H(\omega)$ (the stress response as caused by the harmonic force, $f(t) = e^{i\omega t}$) is found, then the dynamic responses to the different types of input loads can be obtained.

Rewriting Equation (1.16) we obtain:

$$\{\sigma(t)\} = [G] \quad \{u(t)\} \qquad (1.17)$$
$$\text{(6x1)} \quad \text{(6x24)} \quad \text{(24x1)}$$

where

$$[G] = [C] \quad [B] \qquad (1.18)$$
$$\text{(6x24)} \quad \text{(6x6)} \quad \text{(6x24)}$$

is the stress displacement transformation matrix. Explicitly, it can be written as:

$$
\begin{Bmatrix} \sigma_{11}(t) \\ \sigma_{22}(t) \\ \sigma_{33}(t) \\ \sigma_{12}(t) \\ \sigma_{23}(t) \\ \sigma_{31}(t) \end{Bmatrix} =
\begin{bmatrix} g_{11} & g_{12} & \cdots & g_{1,24} \\ g_{21} & g_{22} & \cdots & g_{2,24} \\ \cdot & \cdot & & \cdot \\ \cdot & \cdot & & \cdot \\ \cdot & \cdot & & \cdot \\ g_{61} & g_{62} & \cdots & g_{6,24} \end{bmatrix}
\begin{Bmatrix} u_1^{(1)}(t) \\ u_2^{(1)}(t) \\ u_3^{(1)}(t) \\ \cdot \\ u_1^{(8)}(t) \\ u_2^{(8)}(t) \\ u_3^{(8)}(t) \end{Bmatrix}
\qquad (1.19)
$$
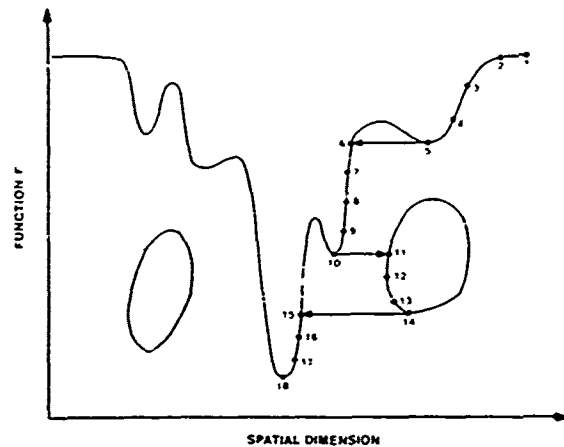
Figure 16. Two dimensional random walk procedure.

It is seen that the stress time functions are linear combinations of the displacement-time functions. Let a Laplace transform be performed on each of these quantities and the result be divided by the Laplace transform, $\mathcal{L}[f(t)]$ of the force input. It is noted that

$$H_{ui}^{(k)}(\omega) = \frac{\mathcal{L}[u_i^{(k)}(t)]}{\mathcal{L}[f(t)]} \qquad (1.20)$$

is the displacement transfer function of the degree of freedom, $u_i(t)$, and

$$H_{\sigma_{ij}}(\omega) = \frac{\mathcal{L}[\sigma_{ij}(t)]}{\mathcal{L}[f(t)]} \qquad (1.21)$$

is the stress transfer function of $\sigma_{ij}(t)$.

$$
\therefore \begin{Bmatrix} H_{11}(\omega) \\ H_{22}(\omega) \\ H_{33}(\omega) \\ H_{12}(\omega) \\ H_{23}(\omega) \\ H_{31}(\omega) \end{Bmatrix} = [G] \begin{Bmatrix} H_{u_1}^{(1)}(\omega) \\ H_{u_2}^{(1)}(\omega) \\ \vdots \\ H_{u_3}^{(8)}(\omega) \end{Bmatrix} \qquad (1.22)
$$

$$\therefore \{H_{\sigma_{ij}}(\omega)\} = [G]\{H_{u_i}^{(k)}(\omega)\} \qquad (1.23)$$
$$\text{(6 x 1)} \qquad \text{(6x24)} \quad \text{(24 x 1)}$$

is the stress transfer function matrix sought.

A similar development yields the strain transfer function matrix.

$$\{H_{\epsilon_{ij}}(\omega)\} = [B]\{H_{u_i}^{(k)}(\omega)\} \qquad (1.24)$$
$$\text{(6 x 1)} \qquad \text{(6x24)} \quad \text{(24 x 1)}$$

The analytical strain transfer function is very useful because it can be compared with processed strain measurement data directly. Given: X_1, X_2, X_3 = global coordinate; r_1,

r_2, r_3 = natural coordinates; η, ξ, ζ = local coordinates (same directions as r,s,t); $\vec{V}_r$ = unit vector in the r direction; $\vec{V}_s$ = unit vector in the s direction; $\vec{V}_t$ = unit vector in the t direction.

Define the strain tensor in the global coordinate system, X_1, X_2, X_3:

$$\{\epsilon\}^T = \begin{bmatrix} \epsilon_{11} & \epsilon_{22} & \epsilon_{33} & 2\epsilon_{12} & 2\epsilon_{23} & 2\epsilon_{13} \end{bmatrix}$$

Define the strain tensor in the local coordinates η, ξ, ζ:

$$\{\bar{\epsilon}\}^T = \begin{bmatrix} \epsilon_{\eta\eta} & \epsilon_{\xi\xi} & \epsilon_{\zeta\zeta} & 2\epsilon_{\eta\xi} & 2\epsilon_{\xi\zeta} & 2\epsilon_{\eta\zeta} \end{bmatrix}$$

Then:

$$\{\bar{\epsilon}\} = [T]\{\epsilon\}$$

$$[T] = \begin{bmatrix} \dots \end{bmatrix}$$

and V_{ri}, V_{si}, and V_t are components of the direction cosines (vectors $\vec{V}_r$, $\vec{V}_s$, $\vec{V}_t$) orientation of the natural and local coordinates with respect to the global coordinates X_1, X_2, X_3. Also:

$$\vec{V}_r = \vec{V}_s \times \vec{V}_t$$

The transformation matrix [T] is derived using tensor analysis. The transformation of tensor is performed as shown in Figure 20. The vectors $\vec{e}_1$, $\vec{e}_2$, $\vec{e}_3$ are the basis vectors of the coordinate system X_1, X_2, X_3 and define the orientation of this coordinate system. Also, $\vec{e}_3 = \vec{e}_1 \times \vec{e}_2$. The basis vectors $\vec{e}_1'$, $\vec{e}_2'$, $\vec{e}_3'$ define the coordinate system X_1', X_2', X_3'. Let the cosines of the angles between the primed and unprimed base vectors be denoted by P_{ij}, ie

$$P_{ij} = \cos(\vec{e}_i', \vec{e}_j')$$

The primed coordinates can then be defined in index notation by

$$X_i' = P_{ij}X_j$$

Therefore the first order tensors ξ_i' and ξ_k are related by

$$\xi_i' = P_{ik}\xi_k$$

The second order tensors t_{ij}' and t_{kl} are related by the relation

$$t_{ij}' = P_{ik}P_{jl}t_{kl}$$

The strain vector is actually a second order tensor. 2nd order tensors have nine components while first order tensors have three. Only six of the strain components are independent through. In the transformation matrix [T] the direction cosines P_{ij} are represented by V_{ri}, V_{si}, and V_{ti}.

As an example, consider the cylinder whose axis lies along the X_1 coordinate direction as shown in Figure 21. Consider a strain gage oriented at an angle θ from the X_2 axis with t normal to the surface of the gage and r perpendicular to the gage length and parallel to X_1. For this example:

V_{r1} = 1 and V_{r2} and V_{r3} = 0

V_{s1} = 0 V_{s2} = $\sin(\theta)$, V_{s3} = $-\cos(\theta)$

V_{t1} = 0, V_{t2} = $\cos(\theta)$. V_{t3} = $\sin(\theta)$

The strain can be calculated at any point or direction in the cylinder as long as the proper direction cosines transformation is used.

ACKNOWLEDGEMENTS
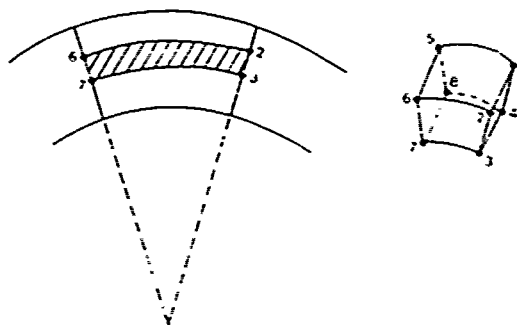
Figure 17. 3-D finite element in thick ring.
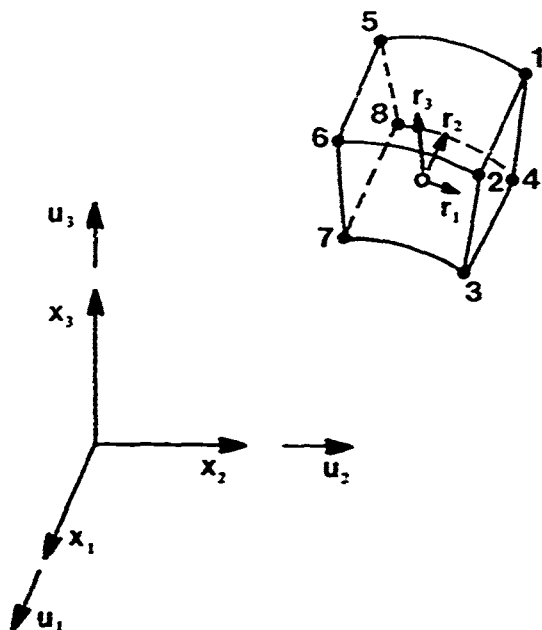
Figure 18. Global and natural coordinate systems.
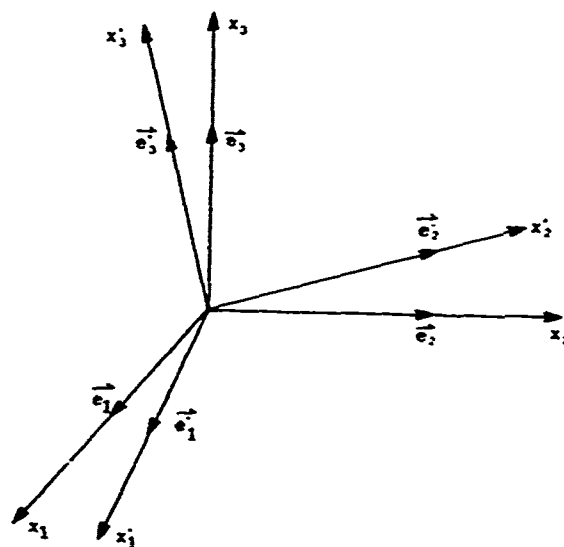
Figure 20. Transformation of tensors.
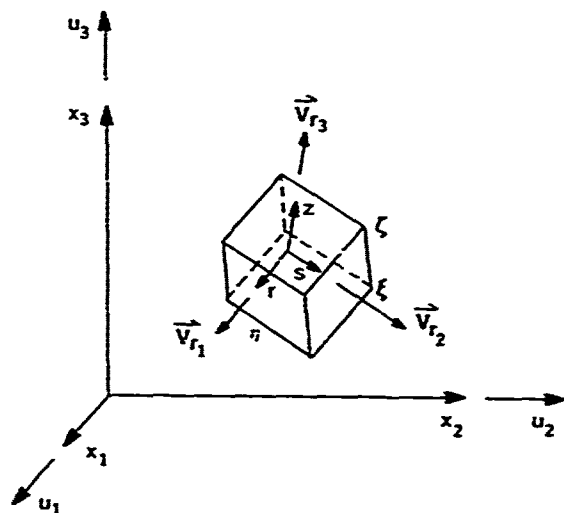
Figure 19. Coordinate transformation of the strain tensor.
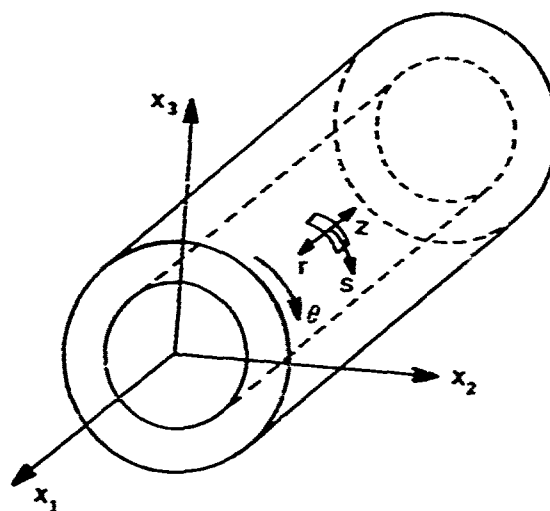
Figure 21. Cylinder with strain gage.

OPTIMIZED STRUCTURE DESIGN

USING REANALYSIS TECHNIQUES

P. H. CHU, T. E. Pollak, J. C. Reuben
RCA   Astro Electronics
Princeton, New Jersey

This paper presents a new approach for optimization of large structures with frequency constraint. The REANALYSIS technique is used to iteratively evaluate feasible directions for achieving optimum solutions. Software was developed to implement this technique with the general purpose finite element NASTRAN analyser. An example of a space truss is given to illustrate the time savings and accuracy of this approach.

NOMENCLATURE

l — number of measured natural frequencies

n — number of degrees of freedom

m — number of modes used in the REANALYSIS formulation

$[M]$ — original system mass matrix

$[K]$ — original system stiffness matrix

$[\Delta M]$ — modified Mass matrix ($n \times n$)

$[\Delta K]$ — modified Stiffness matrix ($n \times n$)

$[Mnew]$ — new mass matrix

$[Knew]$ — new stiffness matrix

$\{u\}$ — system displacement vector

$\{u'\}$ — partition of u directly connected to the modifications

$[\phi u]$ — original system modal matrix ($n \times l$)

$\{q'\}$ — generalized displacement associated with the modifications

$[Mgen]$ — generalized mass matrix

$[Kgen]$ — generalized stiffness matrix

INTRODUCTION

Minimum weight design of a large structure with natural frequency constraints is not a recent problem. Although much work has been done in this field, many problems still remain. One of the significant drawbacks in using optimization techniques for minimum weight design of these structures is the computational time required to solve the mathematical models, especially when direct iteration methods are used (Reference 1).

In recent years sensitivity analysis has been implemented into the frequency optimization problem. In this paper, another efficient approach is proposed by integrating the REANALYSIS technique (Reference 2) with the analysis code.

REANALYSIS is an efficient method to predict the new dynamic characteristics of the structure, after modification, using modal information from the original structure (References 3 5) The size of the eigenvalue problem in REANALYSIS formulation is m by m. For dynamic problems, m is much smaller than the degrees of freedom of the finite element model. Hence in each iteration to reach the optimum solution, only a reduced size eigenvalue problem needs to be solved.

Finite element programs, in general, are designed to assess the adequacy of a specified design. Varying any parameters of the design requires another analysis. The procedure presented substantially reduces

computation requirements when solving the structural problem. The method presented applies the REANALYSIS technique to iteratively reevaluate an analytical model. The REANALYSIS procedure is general enough for an analyst to use on a large class of structural weight optimization problems. The NASTRAN analyzer was coupled to the CONMIN optimization code (Reference 6) for purposes of illustrating a Space Truss example problem.

OPTIMIZATION PROBLEM

The space frame structural optimization problem may be stated as follows: find a minimum weight design such that the natural vibration frequencies and all structural design variables remain within specified limits. For the case where geometry and materials are defined, the design optimization problem can be formulated as:

$$\text{Minimize } F(x)$$

$$\text{Subject to :}$$

$$G_j(X) \leq 0 \quad j=1, a$$

$$Xil \leq Xi \leq Xiu \quad i=1, b$$

$F(x)$ is called the objective function (the weight of the structure). The components Xi of X are independent design parameters (physical properties for the problem considered). Xil and Xiu represent lower and upper bounds of the design envelope for the i th parameter. Gj represents constraints on frequency. Inequality constraints $Gj(x)$ are the response limits imposed on the design. For example, the frequency may be limited to the bound fb so the constraint function is written in normalized form as:

$$(fi/fb)-1 \leq 0$$

This problem is an implicit nonlinear nonconvex problem for which approximate solutions can be obtained, in principle, by iterative solution of feasible directions. In actuality, because a large number of eigenvalue problems have to be solved in the optimization process this may be infeasible. A more practical approach may be to solve approximate eigenvalue problems of reduced dimensionality while preserving the essential features of the original problem. If the approximate problem is a good representation of the original problem the accuracy of the solution will be close to the exact solution.

The number of independent design variables can be reduced by linking design variables. This method used in conjunction with REANALYSIS will tend to further reduce the size of the problem.

REANALYSIS FORMULATION FOR EVALUATING FEASIBLE DIRECTIONS

A method of free vibration REANALYSIS was developed at RCA Astro for application to NASTRAN. The formulation of the equations of motion are summarized. Consider the mode formulation of a structure given by:

$$[M] \{\ddot{u}\} + [K] \{u\} = \{0\} \quad (1)$$

The size of the original mass and stiffness matrices reflect the degrees of freedom of the model. Modify the mass and stiffness matrices as follows.

$$[Mnew] = [M] + [\Delta M] \quad (2)$$

$$[Knew] = [K] + [\Delta K] \quad (3)$$

The new eigenvalue problem for this system is :

$$[Mnew] \{\ddot{u}'\} + [Knew] \{u'\} = \{0\} \quad (4)$$

The mode shape corresponding to the frequency is simply given by:

$$\{u'\} = [\phi u] \{q'\} \quad (5)$$

Substituting (2), (3) and (5) into (4) and premultiply by $[\phi u]^T$ obtaining

$$([Mgen] + [\phi u]^T [\Delta M] [\phi u]) \{\ddot{q}'\} +$$

$$([kgen] + [\phi u]^T [\Delta K] [\phi u]) \{q'\} = \{0\}$$

Note that $([Mgen] + [\phi u]^T [\Delta M][\phi u])$ results in a matrix of m by m size.

REANALYSIS is an effective method which can be used to estimate the new characteristics of the structure, after modification, using information from the original structure. The procedure provides rapid turn-around of design changes to assist in structural optimization.

REANALYSIS uses reduced size matrices to reformulate the system equations. The number of modes requested (m) is chosen to contain the flexibilities important to the design variables. The time savings does not depend on the number of changes in [K] or [M] since changing all elements takes the same reduced time to reevaluate as the effect of a single variable change.

EXAMPLE

The space truss is a frame structure which can be connected to a spacecraft to carry a payload (Reference 7). The finite element model is shown in Figure 1. The lines represent sections of rectangular beams. The frame is fixed at the four points indicated in six degrees of freedom. The frame supports a total payload of 856 lbs which is represented by concentrated masses in the finite element model. Concentrated masses are located at grid points listed in Table 1. A lower limit is placed on the first mode natural frequency of 54.3 hz. The only other constraints imposed on the design are to prevent singularity.

	FREQ(HZ)	WT(LBS)	CPU TIME VAX 11/780 (MINUTES PER EACH MODAL ANALYSIS)
Initial Design	54.3	402.5	--
Optimized (Direct Iteration)	54.3	341.9	6.97
Optimized (Reanalysis Solution)	54.3	341.8	2.97

TABLE 2

SUMMARY

Effective linkage to a general purpose optimization routine completes the structural loop by effectively providing iterations on design variables which will fine-tune the simulated structure. Figure 2.

SPACE TRUSS

FIGURE 1

GRID POINT	CONCENTRATED WEIGHT
25 91 70 152	42.0 lbs
60 71 73	16.7 lbs
5501	638.1 lbs

TABLE 1

minimum design variables of Area >=.001 sq. in have been imposed. The design stayed in the feasible region during the entire optimization process The full solution is compared with the results of REANALYSIS in Table 2.

CONMIN / NASTRAN ALGORITHM

FIGURE 2

49
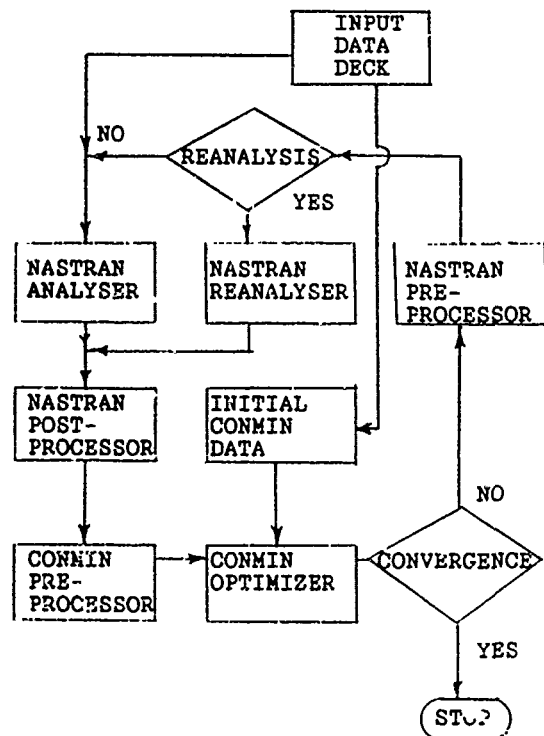
The proposed system can be used to solve a wide spectrum of structural optimization problems. The NASTRAN finite element analysis code was chosen as the structural analyzer because of its widespread industry use. An application of the technique to a truss structure using REANALYSIS is presented.

REFERENCES

1. Vanderplaats. B. N., "Structural Optimization - Past.Present and and Future", AIAA Journal. Vol. ٤٦. No. 7, pp.992-1000. July 1982.

2. Wang. B. P., Chu ,F. H. and Gross, D. W., "REANALYSIS- A User-oriented Computer Program for the Reanalysis of Structural Systems", Proceedings of the 2nd International Modal Analysis Conference. 1984.

3. Wang. B.P. and Chu F.H., "EFFECTIVE DYNAMIC REANALYSIS CF LARGE STRUCTURES". 51th Shock and Vibration Bulletin. 1981.

4. Chu, F.H. and Walker P., "APPLICATION OF REANALYSIS TECHNIQUES IN DYNAMIC SPACECRAFT STRUCTURES", to be presented at the ASME Winter Meeting. Anaheim. CA.. Dec 7-12.1986.

5. Wang. B. P., Chu ,F. H. and Trundle. C. T., "REANALYSIS Techniques Used To Improve Local Uncertainties In Modal Analysis". Proceedings of the 3rd International Modal Analysis Conference. 1983.

6. Vanderplaats. B. N., "CONMIN - A FORTRAN PROGRAM FOR CONSTRAINED FUNCTION MINIMIZATION USER'S MANUAL", NASA TM X-62.282, 1973.

7. Woo.Tze Hsin. "SPACE FRAME OPTIMIZATION SUBJECT TO FREQUENCY CONSTRAINTS". Proceedings of the 27th Structures.Structural Dynamics and Materials Conference. pp.103-115, May 19-21.1986.

Reliability of Structures with Stiffness and Strength Degradation

Fashin Craig Chang, Research Associate

and

Frederick D. Ju, Professor

The Department of Mechanical Engineering

The University of New Mexico, Albuquerque, New Mexico

ABSTRACT

The present paper establishes a theory that can be used to evaluate the reliability of a generic class of nonlinear system, especially for the structural system shows stiffness and strength degradations. The response random process is modeled as a Markov chain in a random environment (MCRE). The random characteristics of the nonlinearity of the structural system is represented by a random process, which is called structural noise. The structural noise is evaluated only when the energy dissipation sequences, which is a random environment, is given. The intensity of the structural noise is deterministic if the structural system is linear. However, for highly nonlinear structural responses, such as the concrete structures subjected to large excitation, the intensity of the structural noise changed, and its probability density function is evaluated for the independent case. The first passage probability and mean square response are also computed in the numerical examples.

1.0 INTRODUCTION

When a structure of frictional materials, such as reinforced concrete, is subjected to strong random excitations, the structure may undergo inelastic deformations during certain cycles of loading, with associated cyclic degradation in stiffness or strength, or both. The exact nature of system degradation is a function of the structural materials and the configuration, and may vary considerably from structure to structure. Basically, the deteriorated phenomenon is due to the extension of crack in the concrete, bond deterioration, bar slippage, shear deformation, and inelastic deformation of reinforcement. The most important factor is the opening and closing of the crack in the structure that alternate between compression and tension during the response cycle. Thus, the opening and closing of these cracks may eventually lead to a deteriorated stiffness and strength. As a consequence, energy is dissipated through the degradated hysteresis. It has been experimentally verified by Ju et al [1] that the rate of degradation is related to the energy dissipation through the degrading restoring hysteretic loop.

Deterministic models that were used to predict the behavior of degradation in stiffness and/or strength has been studied extensively. Among these are Taketa and Sozen [2], Saiidi and Sozen [3], Sucuoglu et al [4], and some others [5,6]. However, because of the randomness in excitation and the considerable variation of the system degradation from structure to structure, the stochastic evaluation of the stiffness and strength deterioration becomes a necessity.

Quite frequently, the excitations of the structural system are not predictable. Examples of such loading sources are earthquake, wind, aerodynamic loads, etc. Under these types of excitations, the structural response apparently behaves randomly. The random characteristics of the loading sources together with the random system degradation lead to the desire of a coherent damage model that can be used to assess the reliability of such system.

There are several works [7,8,9] studied the random vibration of the degrading system. However, they either considered only the random

characteristics of degrading system as a random variable or didn't consider the randomness of the system degradation. In practice, the randomness of the excitation, together with the randomness of the system degradation, will lead to the randomness of the deteriorated restoring force to be a random process, which we refer as structural random noise. The characteristics of the structural noise will discussed in Section 2.

It is noted that the prediction of reliability and assessment of damage depend upon the proper modeling of such structures, taking into consideration of the random characteristics of the materials as well as the excitations. Therefore, the present paper establishes such a model that can be used to predict the reliability of a generic nonlinear structural system, especially for those show stiffness and strength degradation

2. FORMULATION

The nonlinear system to be considered herein is a single-degree-of-freedom (SDF) system, as shown in Figure 1, with the governing differential equation of motion

$$m\ddot{z} + c\dot{z} + R(z) = f(t) \qquad (1)$$

where m, c are the mass and damping, respectively; $f(t)$ is the external random excitation, z, $\dot{z}$, $\ddot{z}$ are the displacement, velocity and acceleration response of the structural system, respectively. $R(z)$ is the system hysteretic restoring force. In this investigation, m, c are assumed to be deterministic and constant. Further, it is assumed that $f(t)$ is a band limited zero-mean stationary white noise with constant power spectral density ϕ_{ff}, namely,

$E[f(t)f(s)]=\phi_{ff}\delta(t-s)$. The behavior of the system hysteretic restoring force for system that shows stiffness and strength degradation has been studied extensively. A typical behavior of such hysteretic loop subjected to monotonic increasing loading is shown in Figure 2 [10]. Among those system-degradation hysteretic mosels, the Q-hysteresis can reproduce the behavior of system degradation in a simple and efficient way. Hence, it is adopted here in the present study to describe the determi-
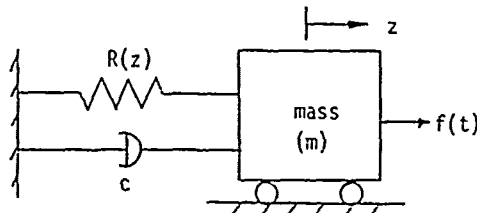
Fig. 1: The SDF System.

nistic behavior of system degradation. The rules of Q-hysteresis are summarized in Figure 3 [3], in which k_1 is the initial stiffness. The unloading stiffness k_3 is determined by

$$k_3 = k_1 \left(\frac{\dot{z}_y}{\dot{z}_{max}} \right)^{\gamma} \qquad \gamma=0.4. \qquad (2)$$

It is noted that the the parameters k_i, $i=1,\ldots 5$ in Figure 3 define the rules of loading, unloading and loading reversal. On a simpler level, all these parameters can be assumed that they do not manifest any randomness. However, on a more realistic level, all these parameters can not accurately describe the origional behavior of system degradation. Moreover, due to the material randomness, even two identical samples can not yield the same hysteretic curve as shown in Figure 2. Therefore, the error that between real behavior of system degradation and the model we developed, together with the random characteristics of the material, lead us to the realization that the hysteretic restoring force must behaves randomly. Further, in view of the fact that the restoring force is a function of the random displacement response, the randomness of the hysteretic restoring force must be time dependent. Without loss of generality, the hysteretic restoring force can be rewritten as

$$R=R(\alpha_1 ,\ldots \alpha_6) \qquad (3)$$

where $\alpha_i=k_i$, $i=1,\ldots 5$, $\alpha_6=z$. By using the Taylor's expansion, R can be expanded about the means of its underlying random parameters to obtain

$$R = R(\mu_1 ,\ldots \mu_6) + \sum_{i=1}^{6} (\alpha_i-\mu_i)\frac{\partial R}{\partial \alpha_i} +$$

$$+ \frac{1}{2} \sum_{i=1}^{6}\sum_{j=1}^{6} (\alpha_i-\mu_i)(\alpha_j-\mu_j)\frac{\partial^2 R}{\partial \alpha_i \partial \alpha_j} + \ldots =$$

$$= R(\mu_1 ,\ldots \mu_6) + N(\xi_1 ,\ldots \xi_6) \qquad (4)$$

where $\mu_i=E[\alpha_i]$, $\xi_i=\alpha_i-\mu_i$, $i=1,\ldots 6$. It is noted that the derivatives in the above equation are evaluated at μ_i, $i=1,\ldots 6$. The $N(\xi_1 ,\ldots \xi_6)$ is the generalized structural noise. The structural noise arises from the uncertainty of the materials, the errors in the model and the randomness of the response. Apparently, the structural noise is a wide band random process. A typical such structural noise is shown in Figure 4. According to Reference [11], the structural noise can be approximately assumed to be zero-mean with less 1 percent error. Moreover, from Figure 4 it can be seen that the structural noise indeed shows the property of zero-mean. Substitution of Equation (4) into (1) yields

$$m\ddot{z} + c\dot{z} + R + N(t) = f(t). \qquad (5)$$

52
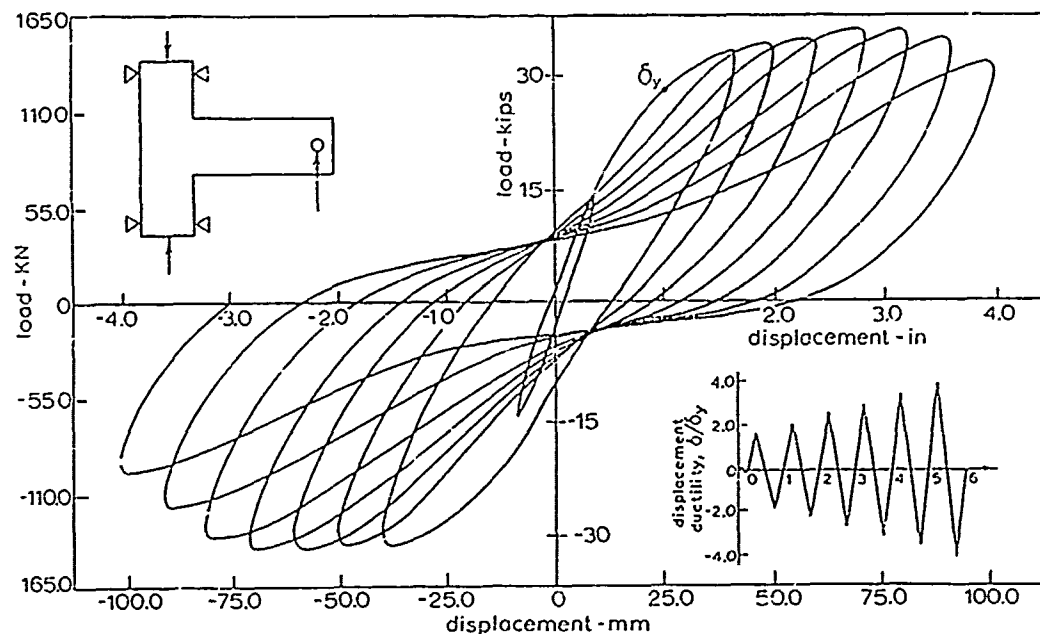
Fig. 2: The typical behavior of system degradation [10].
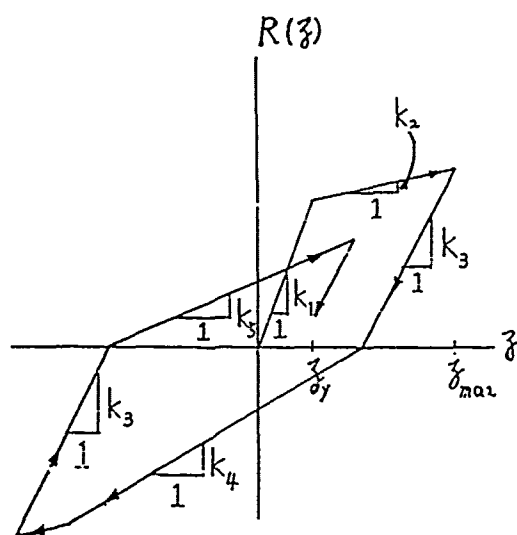
Fig. 3: The Q-hysteresis [3].

The structural noise $N(t)$ is introduced in the above equation and is represented as a function of time for simplicity. According to Reference [12], in order to specify the characteristics of a random process, the probability structure of such random process must be given. Namely, the probability density functions of the random process up to infinite order must be known. In practice, this is impossible. However, the difficulty is alleviated by adding more restriction when evaluating the structural noise. In the present investigation, the restriction is made by adding the energy dissi-

pation as an given condition. In such situation, the autocorrelation function of the structural noise can be evaluated. According to the above statements, if the wide band random noise assumption is made, the autocorrelation function can be written as

$$E[N(t)N(t+s)|E_d, \gamma(t)] = S(t)\delta(s).$$

It is noted that $S(t)$ is time dependent which reflects the nonstationary characteristics of $N(t)$.

Furthermore, if the input excitation $f(t)$ is assumed to a band limited white noise, it becomes necessary that the theory of Markov process need to be used here. In view of this, the transition probability density function is defined as

$$P \equiv P(t,\zeta,t+\Delta t,y) = P(\gamma(t+\Delta t)=y|\gamma(t)=\zeta, E_d).$$

(6)

Equation (6) implies that the random process at time $t+\Delta t$ is evaluated with the conditions that not only $\gamma(t)=\zeta$ has to be given, but also the energy dissipation sequence E_d must be

realized. The energy dissipation sequence E_d, therefore, may be viewed as the random environment. Given different environments, the transition probability that governs the random evolution varies. Similarly to (6), the first and second moments of the random increments that associated with $\gamma(t)$ can be defined as

$$\mu(t) = \lim_{\Delta t \to 0} \frac{1}{\Delta t} E[\Delta \gamma | \gamma(t)=\zeta, E_d] \qquad (7)$$

53

6640.0
(29500)

-7050.0
(31300.)

Structural Noise, N(t), # (N)

TIME (SEC)

0.   0.6   1.2   1.8   2.4   3.0
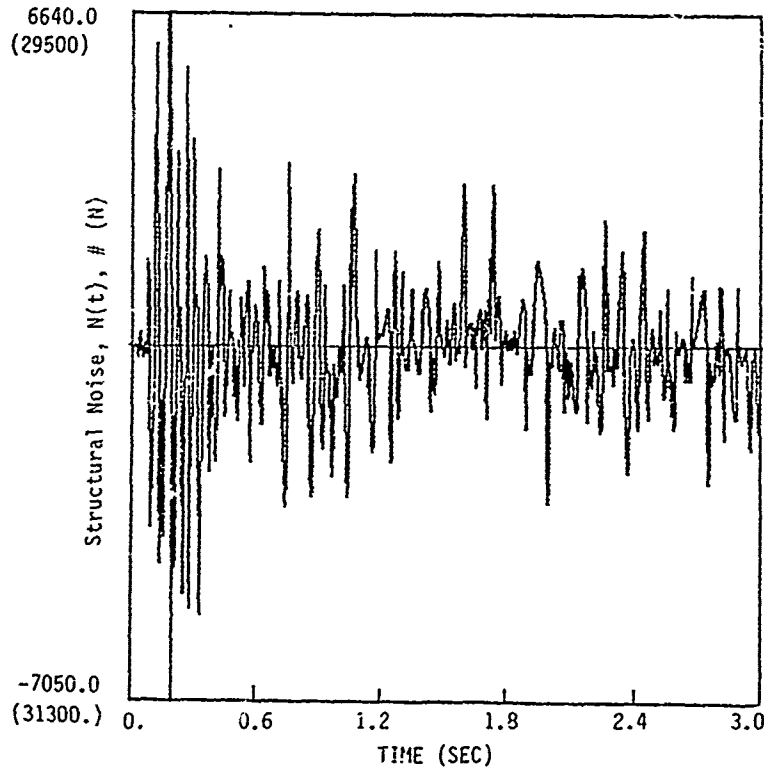
Fig. 4: A typical example of structural noise.

$$\sigma^2(t) = \lim_{\Delta t \to 0} \frac{1}{\Delta t} \ E[\Delta \gamma^2 \ | \ \gamma(t)=\zeta, \ E_l]. \qquad (8)$$

The Kolmogorov backward equation still holds if the derivations are followed by Karlin and Taylor [13]. The reason is that the given random environments didn't change the characteristics of $\mu(t)$, $\sigma(t)$, and P. Hence, from Equations (6), (7) and (8), the Kolmogorov backward equation is

$$-\frac{\partial P(t,\zeta,t',y)}{\partial t'} = \mu(t) \ \frac{\partial P(t,\zeta,t',y)}{\partial \zeta} \ +$$

$$+ \ \frac{\sigma^2(t)}{2} \ \frac{\partial^2 P(t,\zeta,t',y)}{\partial \zeta^2} \qquad (9)$$

where $t'=t+\Delta t$, with initial condition

$$P(t,\zeta,t,y)=\delta(\zeta-y). \qquad (10)$$

It is reasonable to assume that P is stationary within time τ, $t+\Delta t$ if Δt is small. Based upon this assumption, Equation (9) becomes

$$\frac{\partial P(t,\zeta,t',y)}{\partial t} = \mu(t) \ \frac{\partial P(t,\zeta,t',y)}{\partial \zeta} \ +$$

$$+ \ \frac{\sigma^2(t)}{2} \ \frac{\partial^2 P(t,\zeta,t',y)}{\partial \zeta^2} \ . \qquad (11)$$

The evaluation of $\mu(t)$ and $\sigma^2(t)$ are discussed briefly as follow. Let $\Delta \gamma = \Delta u + \Delta Z$ where $u=E[\gamma]$. When taking conditional expectation on $\Delta \gamma$, from Equation (5), it is easy to show that

$$\mu(t) = \dot{u}(t) + \frac{1}{m} \ E[\int_0^t \exp\left(-\frac{c}{m} \ (t-\tau)\right) f(\tau) d\tau] =$$

$$= 0 \qquad (12)$$

since $f(t)$ is zero-mean and $f(t)$, E_d are independent. Similarly, from Equation (5)

$$\sigma^2(t)=$$

$$=\lim_{\Delta t \to 0} \frac{1}{\Delta t} \ E[(1/c)^2 \int_t^{t'} d\tau \int_t^{t'} d\gamma \ h(\tau)h(\gamma)\psi(t'-\tau)$$

$$\psi(t'-\gamma) \ | \ \gamma(t)=\zeta, E_d)] \qquad (13)$$

in which $\psi(t)=f(t)-N(t)$, $h(t)=1-\exp(-ct/m)$, where uses have been made the facts that $\lim_{\Delta t \to 0} \frac{\Delta u^2}{\Delta t} \to 0$ and $f(t)$ is zero-mean.

Equation (13) can be reduced further by noting the fact that $E[N(t)f(t)]=0$ since $f(t)$ is white noise [11],

54

$\sigma^2(t) =$

$$= (1/c)^2 \phi_{ff} \left(1-\exp(-ct/m) \right)^2 + \lim_{\Delta t \to 0} \frac{1}{\Delta t} (1/c)^2$$

$$\int_t^{t'} d\tau \int_t^{t'} d\gamma \, h(\tau)h(\gamma) E[N(t'-\tau)N(t'-\gamma) | \gamma(t), E_d] =$$

$$= (1/c)^2 \phi_{ff} \left(1-\exp(-ct/m) \right)^2 + \lim_{\Delta t \to 0} \frac{1}{\Delta t} (1/c)^2$$

$$\int_t^{t'} d\tau \int_t^{t'} d\gamma \, h(\tau)h(\gamma)\delta(\tau-\gamma). \quad (14)$$

In the derivation of Equation (14), it is noted that the evaluation of the autocorrelation function of the structural noise uses the fact that the realizations of the energy dissipation sequences have been given. In other words, it is difficult to specify the characteristics of the structural noise without the given random environment. Apparently, $N(t)$, and E_d are not independent.

As matter of fact, the power spectral density $S(t)$ is a random variable at time t and its value depends upon E_d. Carry out the integration

of Equation (14) yields

$$\sigma^2(t) = (1/c)^2 \left(\phi_{ff} + S(t) \right) \left(1-\exp(-ct/m) \right)^2. \quad (15)$$

It is noted that $\sigma^2(t)$ is also a random variable at time t since it contains $S(t)$.

Also $\sigma^2(t)$ approaches to $(1/c)^2 \left(\phi_{ff} + S(t) \right)$ as $t \to \infty$.

Now the solution of Equation (11) can be solved easily using the Fourier transform if $\mu(t)$ and $\sigma^2(t)$ are given by Equations (12) and (15), reapectively. The solution is Gaussian distribution with parameters ζ and V; namely,

$P(t,\zeta,t',y,S(t)) =$

$$= P(\gamma(t+\Delta t)=y \mid \gamma(t)=\zeta, E_d) =$$

$$= \frac{1}{\sqrt{2\pi V}} \exp \left\{ -\frac{1}{2} \left(\frac{y-\zeta}{\sqrt{V}} \right) \right\} \quad (16)$$

where

$$V=(1/c)^2 \left(\phi_{ff} + S(t) \right) \left[t+\frac{2m}{c} \left(1-\exp(-ct/m) \right) + \right.$$
$$\left. + \frac{m}{2c} \left(1-\exp(-2ct/m) \right) \right].$$

It is noted that the transition probability given by Equation (16) contains a random variable. This means that the characteristics of the transition probability is random and its value depends upon the given condition of the energy dissipation. This satisfies the original assumption which states that given different environments, the transition

probability that governs the random evolution varies. The transition probability that contains random variables are called Markov chain in random environment (MCRE) [14,15].

The transition probability established above is based on the assumption that $\gamma(t)$ is continuous. However, in digital computation, a discretized form is necessary. Also, the nonlinear characteristics of $R(\gamma)$ and the nonstationary property of $N(t)$ make the transition probability solved above only valid within small time interval. Hence, these conditions necessitate the use of discretized form of Equation (16). If discrete form is used, Equation (16) becomes

$$\left[P(n,\zeta,n+1,y,S_n) \right] = P_n =$$

$$= \left[p(\gamma_{n+1}=y | \gamma_n=\zeta, \gamma_{n-1}, \cdots \gamma_0, E_d \right]. \quad (17)$$

It is noted that $\gamma_0, \cdots \gamma_{n-1}$ are also putted into the given condition since the future may not independent of the past for this case. For more detail about the past may not independent of the future, a completely discussion may be found in Reference [16].

The n-step transition probability is given by Equation (18).

$$P^{(n)} = \left[P(\gamma_{n+1}=y \mid \gamma_0, E_d') \right] =$$

$$= P_0 \prod_{j=1}^{n} P_j \quad (18)$$

where P_j, $j=1, \cdots n$ are the transition probability at time step j, and P_0 is the initial probability distribution of γ_0. The proof of Equation (18) can be easily derived by using induction and is demonstrated as below.

⟨i⟩ $n=0$, this is trivial.

⟨ii⟩ Assuming true for $n=k$, namely,

$$\left[P(\gamma_{n+1}=y \mid \gamma_0, E_d') \right] = P_0 \prod_{j=1}^{n} P_j.$$

⟨iii⟩ For $n=k+1$, then

$$\left[P(\gamma_{k+2}=y \mid \gamma_0, E_d') \right] =$$

$$= E[P(\gamma_{k+2} \mid \gamma_0, \cdots \gamma_{k+1}, E_d') \mid \gamma_0, E_d] =$$

$$= E[P_{k+1} \mid \gamma_0, E_d] =$$

$$= \sum_{q_{k+1}} P_{k+1} \, P(\, \gamma_{k+1} = q \mid \gamma_c, E_d \,) =$$

$$= P_0 \prod_{j=1}^{k+1} P_j.$$

The last equality is based upon the result of (ii).

There are two cases can be considered here. The first case is that each the S_n is independent. For such case, the structural response is then a random process moving in the average environment. The mean of the n-step transition probability, in this case, is obtained by taking expectation on both sides of Equation (18) yields

$$E[P^{(n)}] = E[P_0] \prod_{j=1}^{n} E[\, P_j \,] \qquad (19)$$

where $E[P_j]$ is the mean transition probability at time j. This is a special case of MCRE. In other words, $\gamma(t)$ is a nonstationary Markov chain with one step transition probability $E[P_j]$.

It is very interested to note that $E[P(n,\zeta,n+1,y,S_n)]$ is still a valid representation of a probability density function, where $P(n,\zeta,n+1,y,S_n)]$ is given by Equation (17). The reason can be seen easily by noting that

$$E[\int_y P(n,\zeta,n+1,y,S_n) \, dy \,] =$$

$$= \int_y E[\, P(n,\zeta,n+1,y,S_n)] \, dy = 1. \qquad (20)$$

By using the definition of the expectation, Equation (20) can be rewritten as

$$\int_y dy \int_{S_n} P(n,\zeta,n+1,y,S_n) \, P(S_n) \, dS_n =$$

$$= \int_{S_n} P(S_n) \, dS_n \int_y P(n,\zeta,n+1,y,S_n) \, dy = 1 \qquad (21)$$

where $P(S_n)$ is the probability density function of S_n at time step n. Equation (21) can be used as a tool for the numerical computation and will be discussed in Section 3.

The second case is that S_n, n=1,2,... are also Markovian. In such case, the one step transition probability which is given by Equation (7) can be rewritten by using the law of total probability.

$$P(j,\zeta,j+1,y,S_j) =$$

$$= \sum_{S_j} \sum_{S_0} P^*(j,\zeta,j+1,y,S_j) \, P(S_j \mid S_0) \, P(S_0) =$$

$$= \sum_{S_j} \sum_{S_{j-1}} \cdots \sum_{S_0} P^*(j,\zeta,j+1,y,S_j)$$

$$P(S_j \mid S_{j-1}) \cdots P(S_1 \mid S_0) P(S_0) \qquad (22)$$

where S_j in $P^*(j,\zeta,j+1,y,S_j)$ is a given, deterministic value. If we let

$$\left[P(S_i \mid S_{i-1}) \right] = \theta_i \, , \; i=1, \ldots j \qquad (23)$$

and

$$\left[P(S_0) \right] = \theta_0. \qquad (24)$$

Then

$$P_j = \left[P(j,\zeta,j+1,y,S_j) \right] =$$

$$= P^*(j,\zeta,j+1,y,S_j) \prod_{i=1}^{j} \theta_i. \qquad (25)$$

The n-step transition probability then can be evaluated based upon Equation (18).

3. NUMERICAL EXAMPLES

Case (I): S_n, n=1,2,... are independent.

In the case of S_n, n=1,2,... are independent, the most important term that needs to be evaluated is the probability desnisty function of S_n, n=1,2,... . However, as mention earlier, S_n, n=1,2,... depended upon the energy dissipation sequence. In other words, S_n can not be evaluated unless some energy dissipation sequences are realized. In order to establish the energy dissipation sequences, the Q-hysteresis has been used here to generate such sequences and are shown in Figure 5, where the number of samples used are 130. The mean input datas for the Q-hysteresis are given in Table 1. The randomness of these datas are assumed uniform between $\mu \pm 0.05\mu$ where μ is the mean of k_1, k_2 etc.
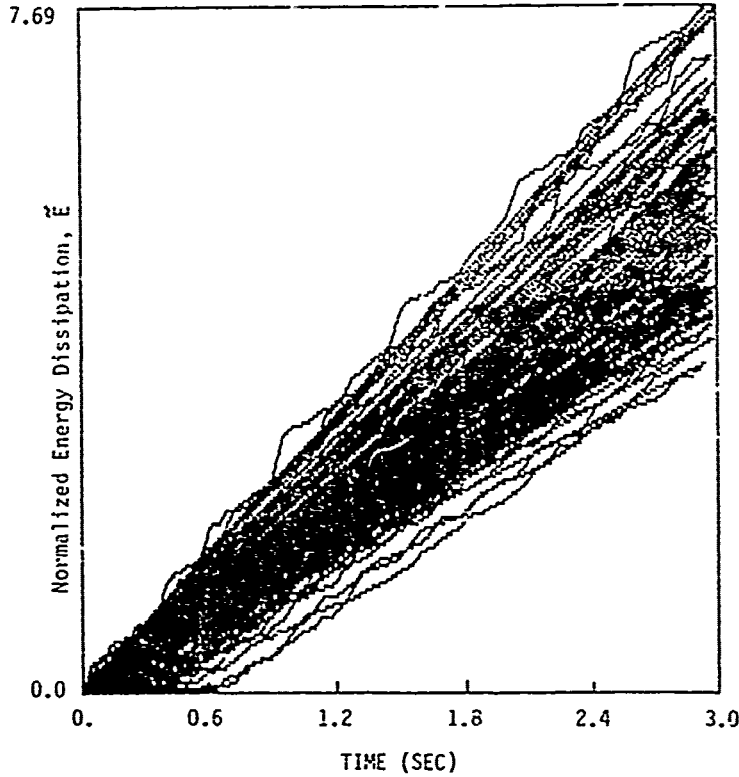
Fig. 5: The energy dissipation sequences.

Table 1: The Input datas for Q-Hys.

k_1	k_2	α
7.33E+06(N/m)	7.33E+05(N/m)	.4

In Figure 5, $\tilde{E}$ is the normalized energy dissipation.

$$\tilde{E} = E_d / E_s$$

where E_d is the energy dissipation obtained from the Q-hysteresis and E_s is the energy dissipation due to static load at failure point. If a beam to column joint is used as shown in Figure 2, $E_s = 3.9215E+06(N-m)$

(34712 k-in). The data is obtained from Ref. [17].

It is noted that in order to obtain the energy dissipation quences, the random input excitations are generated by using the following formula.

$$f(t) = \sum_{j=-N}^{N} C_j \cos(\omega_j t - \Omega_j) \tag{26}$$

where

$C_j = 5.337E+06(N)$ (1200K) for $j=-N, \ldots N$; $j \neq 0$,

$C_0 = C_j/\sqrt{2}$

$\omega_j = -\omega_{max} + (j-1)\Delta\omega$, $j=-N, \ldots N$

$\omega_{max} = 2\omega_n$; $\omega_n = 51.24$ Hz

$\Delta\omega = \omega_{max}/23$

and Ω_j, $j=-N \ldots N$ are the random variables with uniform distribution between $(0,2\pi)$. The constant power spectral density of $f(t)$ is computed easily if $f(t)$ is given by Equation (26). The result is

$$\phi_{ff} = C_j^2 /4\Delta\omega.$$

The mean and standard deviation of the rate of energy dissipation θ, as shown in Figure 6, are computed from samples and the results are

$\bar{\theta} = 1.0264$ (rad)

$\sigma_\theta = 0.09152$ (rad). (27)

After the energy dissipation sequences are determined, the probability density function of S_n, $n=1,2,\ldots$ then can be evaluated. It is
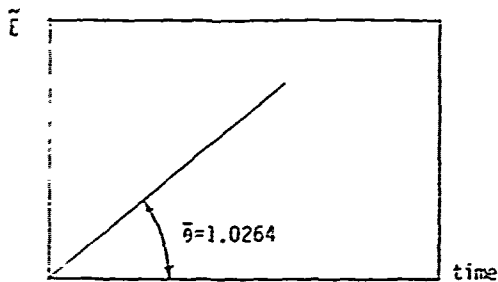
Fig. 6: The mean value of the rate of energy dissipation.

noted that S_n is the power spectral density of $N(t)$ and is related to the mean square of structural noise by

$$E[N^2(t)] \frac{\Delta t}{2\pi} = S(t) \qquad (28)$$

if $N(t)$ is a band-limited white noise. Therefore, in order to obtain $S(t)$, the $E[N^2(t)]$ is also evaluated by using Q-hysteresis and Equation (4). The result is shown in Figure 7.

In Figure 7, it is noted that a linear regression line which can be used as an ensemble

average of $E[N^2(t)]$ is evaluated. It can be seen from Figure 7 that $E[N^2(t)]$ is inversely proportional to time. This is because the structural system shows degradation in stiffness and strength. The linear regression line can be represented by Equation (29).

$$t = C_1 - C_2 S \qquad (29)$$

where $C_1 = 11.6957$, $C_2 = 0.02737$.

To see how energy dissipation is related to the $S(t)$, a configuration of $\tilde{E}$, S, and t is constructed and is shown in Figure 8. From Figure 8, it can be seen that given $\tilde{E} = E_n$, the possible values of S_n could be $S^{(1)}$, $S^{(2)}$, etc., since the random characteristics of the energy dissipation. Each possible value of $S_n^{(i)}$, $i=1,2,\ldots$ will have probability $P(S_n^{(i)})$, $i=1,2,\ldots$ and satisfies the normalization condition

$$\sum_i P(S_n^{(i)}) = 1. \qquad (30)$$
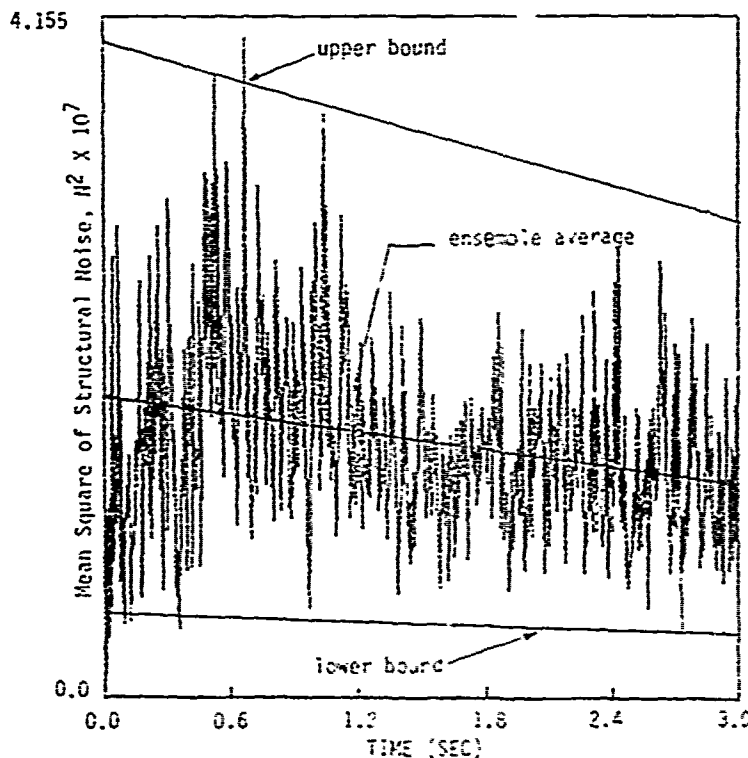
Fig. 7: The mean square of structural noise.
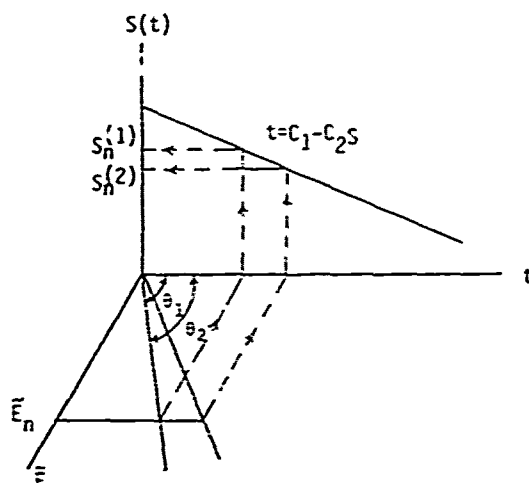
Fig. 8: The configuration of $\bar{E}$, $S(t)$.

According to Figure 8, the relationship between S_n and $\bar{E}$ can be evaluated easily. The result is

$$S_n = \frac{C_1 - \bar{E}\cot\theta}{C_2} \qquad (31)$$

where θ is Gaussian with mean and standard deviation given by Equation (27). The cumulative distribution function (CDF) of S_n can be derived easily if S_n and θ are related by Equation (31). The result is

$$P(S_n\langle\zeta) = \hat{\phi}\left(\frac{\tan^{-1}[\beta(\zeta)^{-1}]-\bar{\theta}}{\sigma_\theta}\right) - \hat{\phi}\left(\frac{-\theta}{\sigma_\theta}\right) \qquad (32)$$

where $\beta(\zeta) = (C_1 - C_2\,\zeta)/\bar{E}$, $\qquad (33)$

and $\hat{\phi}(x) = \frac{1}{\sqrt{2\pi}}\int_{-\infty}^{x}\exp(-\frac{1}{2}u^2)\,du.$ $\qquad (34)$

The probability density function (PDF) of S_n is then evaluated by using the following approximation.

$$P(S_n=\zeta)=P(\zeta-\frac{\Delta\zeta}{2} \langle S_n \langle \zeta+\frac{\Delta\zeta}{2})$$

$$= \hat{\phi}\left(\frac{\tan^{-1}[\beta(\zeta+\Delta\zeta/2)^{-1}]-\bar{\theta}}{\sigma_\theta}\right)-$$

$$- \hat{\phi}\left(\frac{\tan^{-1}[\beta(\zeta-\Delta\zeta/2)^{-1}]-\bar{\theta}}{\sigma_\theta}\right). \qquad (35)$$

The CDF of S_n for different $\bar{E}$ is plotted and is shown in Figure 9 by using Equation (32). The PDF of S_n is also plotted and is shown in

figure 10. From Figure 10, it can be seen that as energy dissipation increasing, the PDF of S becomes flat. This implies that the uncertainty of the intensity of the structural noise spreading out, as it should. On the

other hand, as $\bar{E}$ is small, the uncertainty of the intensity of the structural noise concentrates within small range. It is noted

from Figure 10 that when $\bar{E} = 0$, the PDF of S is a delta function. The reason is that when

$\bar{E}=0$, the system is linear. Hence, the structural noise in a random variable rather than a random process. In such case, the random environment does not exist. As a consequence, the intensity of the structural noise is a constant, deterministic value, as it should.

The first passage probability for such case can be computed easily since the transition probability provides enough information to evaluate it. For instance, if we assume that the absorbing barrier, or the failure state, is at $z=50.8$ mm $(2")$, then the first passage probability is computed according to Equation (19). The result is shown in Figure 11. The mean square response is also computed and the result is shown in Figure 12.

Case (ii): S_n, $n=1,2,\ldots$ are Markovian.

In this case, the difficulty is to determine the transition probability θ_i.

However, in view of Figure 7, the randomness of $S(t)$ can be assumed that the transition probability θ_i behaves like a Brownian motion

with mean $\bar{S}$, which is linearly proportional

to t, and the standard deviation $\hat{\sigma}$, which is inversely proportional to t. The reason is that from Figure 7, the upper bound and lower bound of $S(t)$ tend to converge to the mean. If this assumption is made, we can write

$$\bar{S}(t) = \alpha + \beta t \qquad (36a)$$

$$\hat{\sigma}^2(t) = \sigma^2/(t+1)^2. \qquad (36b)$$

The values of α, β, σ^2 can be obtained from nonlinear regression [18].

$$\alpha = \frac{\sum_i v_i S_i - \beta \sum_i v_i t_i}{\sum v_i} \qquad (37a)$$

59
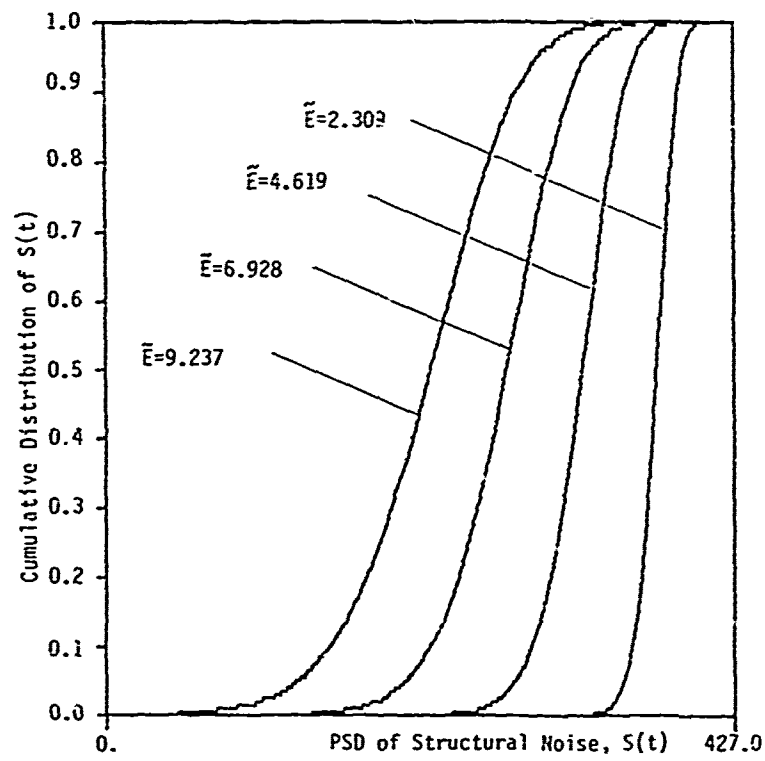
Fig. 9: The CDF of S_n.
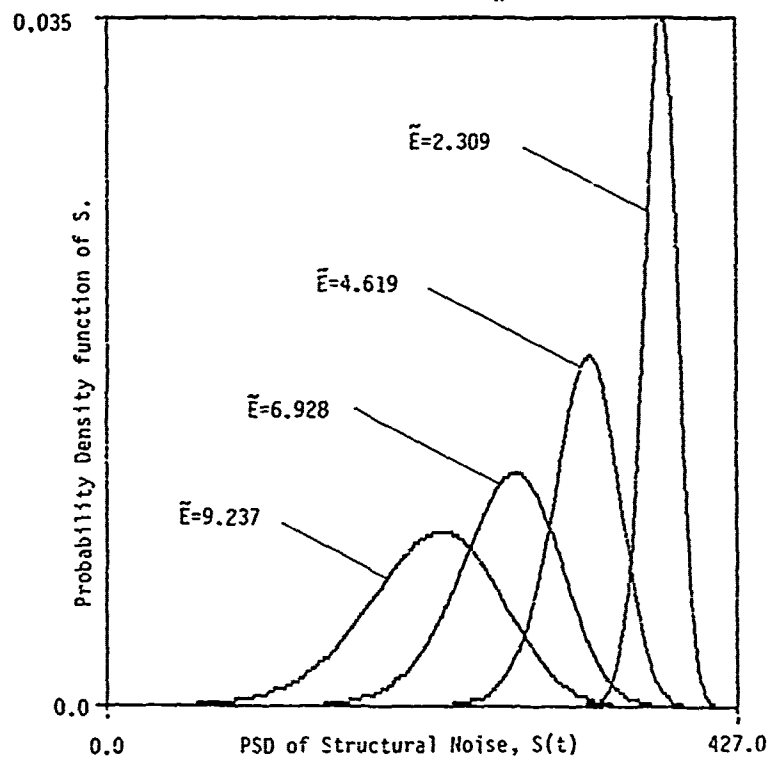
Fig. 10: The PDF of S_n.
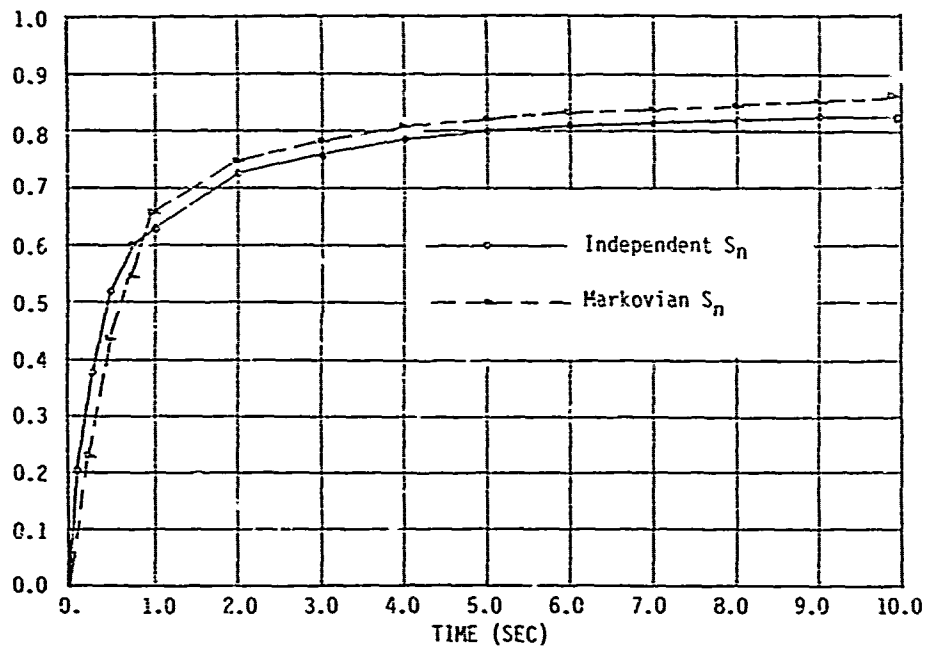
Fig. 11: The first passage probability of $\gamma(t)$.
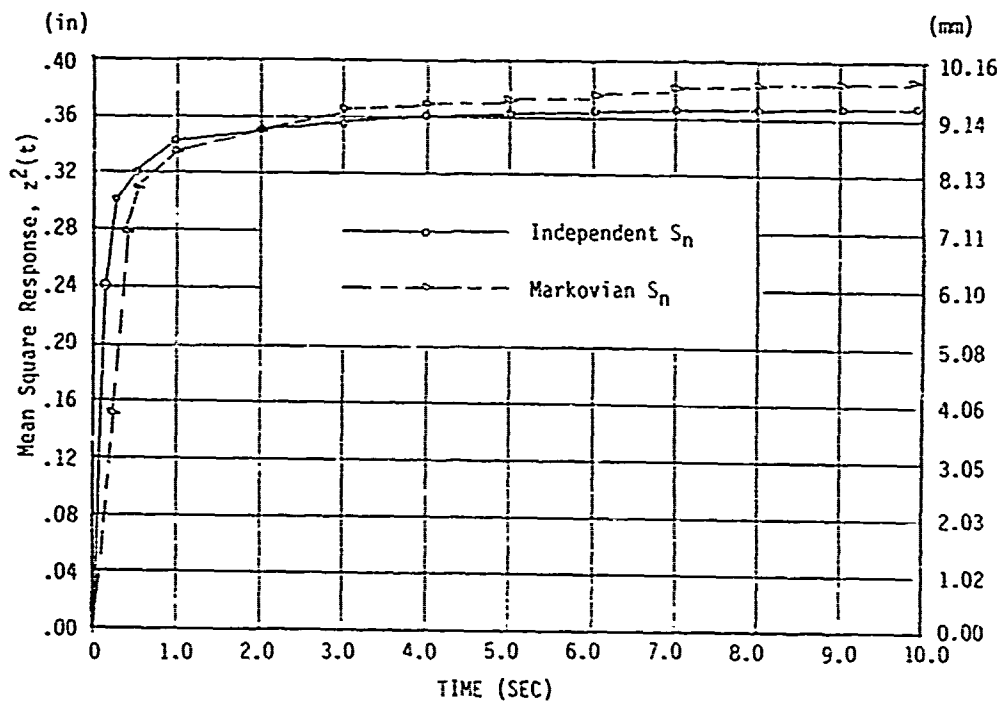
Fig. 12: The mean square response of $\gamma(t)$.

61

$$\beta = \frac{\sum_i w_i \left(\sum_i w_i S_i t_i \right) - \left(\sum_i w_i S_i \right) \left(\sum_i w_i t_i \right)}{\sum_i w_i \left(\sum_i w_i t_i^2 \right) - \left(\sum_i w_i t_i \right)^2} \quad (37b)$$

$$w_i = (t_i + 1)^2 \quad (37c)$$

$$\sigma^2 = \frac{\sum_i w_i (S_i - \alpha - \beta t_i)^2}{n-2}$$

where n is the total number of point. In this example, n=1024.

The results of α, β, σ^2 are computed by using the above equation.

$\alpha=442.118$, $\beta=-44.6587$, $\sigma^2=30948.6$

The θ chain then can be established by using Gaussian distribution; namely

$$\theta = P(S_{n+1} < \zeta_{n+1} \mid S_n = \zeta_n) =$$

$$= \frac{1}{\sqrt{2\pi}\sigma_n} \int_{-\infty}^{\zeta_{n+1}} \exp\left[-\frac{1}{2} \left(\frac{x - \zeta_n}{\sigma_n} \right)^2 \right] dx \quad (38)$$

where $S_n = \alpha + \beta(n \Delta t)$ $\quad (39a)$

$\sigma_n = \sigma / (n\Delta t + 1)$. $\quad (39b)$

The first passage probability and the mean square response of $\gamma(t)$ then can be computed similarly to the case of independent S_n if the

θ chain is given by Equation (38). The results are plotted in Figure 11 and 12, respectively. The comparison between the case of independent S_n, and the case of Markovian S_n

is made in Figure 11 and 12. It can be seen that the results are close.

4. CONCLUSIONS

According to the analysis in the above sections, the following conclusion can be made.

(1) The advantage of present investigation is that the randomness of the random response is characterized by a linear differential equation if we treat the structural noise as an external excitation. This can be seen easily by taking expectation on Equation (5). However, restriction must be made here that the structural noise can be evaluated by given the realization of the energy dissipation sequences which may be viewed as a random environment. Since the given environment is random, it will cause the response evolution moving in a fluctuated environment. However, if the characteristics of the random environment is specified, the probabilistic characteristics of the response is still enumerable.

(2) The power spectral density (PSD) of the input excitation and the structural noise dominate the random evolution, as seen from Equation (16). If the PSD of the input excitation significantly greater than that of the structural noise, the probability of failure will heavily depend upon the input excitation. This means that the uncertainty of the structural system does not play an important role in determining the probability of structural failure. On the other hand, if the PSD of the structural noise is significantly greater than that of input excitation, then the uncertainty in the structural system will dominate the probability of structural failure.

(3) From Figure 11, one can see that the case of independent S_n and the case of Markovian S_n

didn't show significant difference in either the first passage probability or the mean square response of $\gamma(t)$. Hence, it can be concluded that the case of independent S_n can

be used for the computation of structural reliability analysis if the PSD of the external excitation is significantly greater than that of the structural noise. However, if the PSD of the structural noise is greater than that of the input excitation, the Markovian case should be used since it describes the phenomenon more precisely and closely.

REFERENCES

1. Ju, F. D. et al,"Identification of Damage in Hysteretic Structures," UNM Technical Report, CE-72(84)AFOSR-993-1, Feb. 1983, Albuquerque, NM.

2. Taketa, T., Sozen, M. A., Nielson, N. N.,"Reinforced Concrete Response to Simulated Earthquake," J. of Structural Div., ASCE, Vol. 96, ST12, Dec. 1970.

3. Saiidi, M., Sozen, M. A.,"Simple and Complex Models for Nonlinear Seismic Response of Reinforced Concrete Structures," UI Report, CE, UILU-ENG-79-2013, Aug 1979, Urbana, Illinois.

4. Sucuoglu, H., Aktan, A. E., "Hysteretic Response of Reinforce Concrete Frames," ACI Publication SP-63-7, P153-172.

5. Clough, R. W., Johnston, S. B.,"Effect of Stiffness Degradation on Earthquake Ductility Requirements," Proceedings, Japan Earthquake Eng. Symposium, Tokyo, Oct. 1966, p 195-198.

6. Otani, S., Sozen, M. A., "Simulated Earthquake Test of R/C Frames," J. of Structural Division, ASCE, Vol 100, No ST3, March 1974, P 687-701.

7. Wen, Y. K., "Method for Random Vibration of Hysteretic system," J. of Eng. Mechanics Division, ASCE, EM2, April 1976, p 249-263.

8. Baber, T. T., Wen, Y. K., "Random Vibration of Hysteretic Degrading System," J. of Engin. Mechanics Division, ASCE, EM6, Dec. 1981, pp 1069-1087.

9. Baber, T. T., Noori, M. N., "Random Vibration of Degrading Pinching Systems," J. of Eng. Mechanics, ASCE, Aug. 1985, P 1010-1026.

10. Ehsani, M. R., Wight, J. K., "Behavior of External Reinforced Concrete Beam to Column Connections Subjected to Earthquake Type Loading," Report No. UMEE 82R5, U. of Michigan, Dept. of Civil Eng., 1982.

11. Chang, F. C., Ju, F. D., Paez, T., "Damage Diagnosis for MDF System with Material Nonlinearity," ASME Publication AMD-Vol. 7, ed by M. Sathyamoorthy, Nov. 1985.

12. Lin, Y. K., "Probabilistic Theory of Structural Dynamics," Robert E. Krieger Publishing Company, 1967.

13. Karlin, S., Taylor, H. M.,"A Second Course in Stochastic Processes," Academic Press, NY, 1981.

14. Takahashi, Y., "Markov Chain with Random Transition Matrices," Kodai Math. Sem. Rep. 21, 426-447 (1969)

15. Cogburn, R., "Markov Chain in Rand   /ironments, The Case of Markovian Environments," Ann. Probability 8, 508-916(1980).

16. Solomon, F.,"Random Walks in a Random Environment," Ann. of Probability 3, 1975, 1-31.

17. Scribner, C. F., Wight, J. K., "Delaying Shear Strength Decay in Reinforced Concrete Load Reversal," Dept. of CE, University of Michigan, May, 1978, P. 220.

18. Ang, A H-S., Teng W. H., "Probability Concepts in Engineering Planning and Design," vol 1, Johy Wiley & Sons, Inc., 1975.

A NEW LOOK AT THE USE OF LINEAR METHODS
TO PREDICT AIRCRAFT DYNAMIC RESPONSE
TO TAXI OVER BOMB-DAMAGED AND REPAIRED AIRFIELDS

Dr. James J. Olsen
Assistant for Research and Technology
Structures and Dynamics Division

October 1986

FLIGHT DYNAMICS LABORATORY
AIR FORCE WRIGHT AERONAUTICAL LABORATORIES
WRIGHT-PATTERSON AIR FORCE BASE, OHIO 45433

ABSTRACT

This paper explains the dynamic response of an aircraft that taxies over two arbitrary disturbances, under the assumption that the aircraft can be represented as a linear, one degree-of-freedom system . That analysis produces the concept of the BUMP MULTIPLIER which explicitly and simply determines whether a second discrete disturbance will amplify or attenuate the response from a first disturbance. The BUMP MULTIPLIER also simplifies the understanding and presentation of the results. While the assumptions are very severe, the resulting formulas can be very useful to gain physical insight, to guide more elaborate nonlinear calculations and to plan test programs.

1. INTRODUCTION

The problem of aircraft dynamic response to taxiing over rough surfaces has been a topic of research for many years. For the most part, the research has been limited to predicting and/or measuring the dynamic response of an aircraft due to the (nearly) random roughness of the terrain or by wear and tear on runways and taxiways. Within the last several years, however, concerns have arisen within the Defense agencies of the NATO countries about the safety of aircraft operations over the discrete disturbances which can arise from bomb-damage to the runways. Those concerns also extend to the dynamic response due to taxi over repaired runways and repetitive aircraft operations on the (potentially) yielding surfaces.

As a result of those concerns the United States Air force instituted program HAVE BOUNCE which performs flight (taxi) tests over simulated (relatively mild) runway damage and repairs for several USAF combat

and transport aircraft. HAVE BOUNCE also develops computer programs to predict the dynamic response to the simulated runway profiles . Other NATO nations are performing similar test and analysis programs on their aircraft.

HAVE BOUNCE considers the computer programs to be *validated* when they produce satisfactory comparisons with the experimental results from flight (taxi) tests. Then HAVE BOUNCE uses the *validated* computer programs to extrapolate from the relatively mild test conditions to more severe operational cases. Since the computer programs account for the nonlinear properties of the landing gears and tires, the extrapolation of the results beyond their *validated* range of parameters is always open to some question.

Because the taxi test programs have proven to be very expensive, difficult to control and repeat and (sometimes) dangerous, the USAF also created the Aircraft

Ground-Induced Loads Excitation (AGILE) facility which measures the dynamic response of operational aircraft to damaged and repaired runways within the controlled conditions of the laboratory. AGILE supports an operational aircraft on its tires on massive hydraulic shakers and drives the shakers vertically to represent the vertical events of the aircraft taxiing over damaged and repaired runways. Each (of the three integrated) shakers can sustain a static weight of 50,000 lb, can displace amplitudes of 10 in, can impose dynamic forces up to 50,000 lb and can be driven sinusoidally (frequencies up to 25 Hz), randomly or to follow prescribed discrete motions. In its first major test, agreement between the AGILE tests and HAVE BOUNCE taxi tests for an operational A-7D aircraft was excellent.

All three evaluation methods–computer programs, HAVE BOUNCE taxi tests on operational aircraft and AGILE tests on operational aircraft–have been dominated by one major consideration–the nonlinearities in the landing gear. As a result, nearly all of the computations have been done with numerical time-integration of the nonlinear differential equations of motion. The taxi tests and AGILE tests also have been forced to adopt a tedious approach of repetitive, trial–and–error test cases, again because concerns over strong nonlinearities prevented the consideration of the superposition of simple disturbances to synthesize more complex responses.

In this paper we contend that the nonlinearities do indeed strongly influence the computational and test results, especially the exact levels of the loads obtained. However, the qualitative response and the selection of speeds, bump heights, and bump spacings which produce large dynamic responses ought to be predictable, for the most part, by simpler linear methods. Nonlinear calculations, taxi tests and AGILE tests all ought to be preceded by a substantial amount of linearized calculations which can be done rapidly and can yield much physical insight into those conditions which produce extensive dynamic response. A clever analyst may be able to find the simplicity and intuitive understanding in seemingly complex time-histories, which in fact may be not much more than superpositions of many relatively simple events.

The purpose of this paper is to review those linear methods, to show how they yield an understanding of complex time histories and how they can be used to plan nonlinear calculations, taxi tests and AGILE tests. The paper illustrates the principles by treating the response of a linear one degree-of-freedom oscilllator as it taxies over two successive discrete disturbances, introducing the concept of the BUMP MULTIPLIER.

2. THE ACCELERATION RESPONSE OF A SINGLE DEGREE-OF-FREEDOM OSCILLATOR TO A SINGLE DISTURBANCE

Assume a single degree-of-freedom oscillator, with damping less than the critical value, receives some excitation over a period of time, but that the excitation stops at time $t = t_1$.
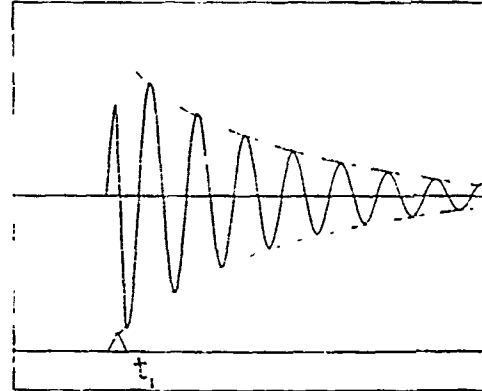
For times after t_1, when the acceleration response is decaying freely, the acceleration acceleration response can be written:

$$\ddot{z}(t)\big|_{t>t_1} = e^{-\alpha\omega(t-t_1)}\left\{A_1\sin\left[\omega(t-t_1)\right] + B_1\cos\left[\omega(t-t_1)\right]\right\}$$

(2.1)

where:

t_1 = the time the excitation ends

ω = damped frequency

$\alpha\omega$ = damping

A_1, B_1 = Constants which depend on α, ω, the excitation and the initial conditions

Note that the damping parameter α above is *not quite the same* as ς, the frequently used fraction of critical damping, which comes from the analysis of a *classical* single degree-of-freedom oscillator. The product $\alpha\omega$ controls the exponential decay of the damped system, perhaps as observed experimentally. The use of the parameter α allows us to refer the damping to the observed damped frequency ω rather than the fictitious undamped frequency ω_0. In the special case of the *classical* single degree-of-freedom oscillator $\alpha = \varsigma/\sqrt{1-\varsigma^2}$ and $\alpha\omega = \varsigma\omega_0$.

The decaying acceleration response also can be written as.

$$\ddot{z}(t)\big|_{t>t_1} = R_1 e^{-\alpha\omega(t-t_1)}\sin\left[\omega(t-t_1) + \phi_1\right]$$ (2.2)

where:

$$R_1 = \sqrt{A_1^2 + B_1^2}$$

$$\tan\phi_1 = B_1/A_1$$

66

We loosely refer to R_1 as the *potential amplitude* of the acceleration response. It is an upper bound on the amplitude of the acceleration response to a single disturbance. The phase shift ϕ_1 depends only on A_1 and B_1 and will therefore be different for various forms of the excitation.

For small damping ($\alpha \ll 1$) the behavior of the acceleration response will be dominated by the term $\sin[\omega(t - t_1) + \phi_1]$ in Equation (2.2), so we would expect its local maxima and minima (extrema) to be obtained from solutions of

$$\omega(t - t_1) + \phi_1 \approx (2n - 1)\frac{\pi}{2}; \quad n = 1, 2, 3, \dots \quad (2.3)$$

However, the term $e^{-\alpha\omega(t-t_1)}$ causes a shift in the values of time for which the local extrema of the acceleration response occur. In fact, the third derivative of the displacement (derivative of the acceleration) is:

$$\frac{d\ddot{z}(t)}{dt}\Big|_{t>t_1} = R_1 e^{-\alpha\omega(t-t_1)}\omega\sqrt{1 + \alpha^2}\cos[\omega(t - t_1) + (\phi_1 + \delta_1)]$$
$$(2.4)$$

where:
$$\tan\delta_1 = \alpha$$

Therefore, the local extrema of the decaying acceleration response will occur at the values of time for which

$$\omega(t - t_1) = (2n - 1)\frac{\pi}{2} - (\phi_1 + \delta_1); \quad n = 1, 2, 3, \dots \quad (2.5)$$

The additional phase shift δ_1 will be small for values of damping that are small with respect to the critical value, ($\alpha \ll 1$). Note, however, that the first phase shift ϕ_1 depends on the disturbance and the initial conditions and need not be small.

We can use these results to obtain an even better upper bound on the amplitude of the acceleration response. If we plug the above value of $\omega(t -)$ into Equation (2.1) for $\ddot{z}(t)\big|_{t>t_1}$, we find that the local extrema for $\ddot{z}(t)\big|_{t>t_1}$ equal:

$$\frac{R_1}{\sqrt{1 + \alpha^2}}e^{-\alpha\left[(2n-1)\frac{\pi}{2} - (\phi_1 + \delta_1)\right]}; n = 1, 2, 3, \dots$$

3. TWO SUCCESSIVE DISTURBANCES

Now suppose the single degree-of-freedom oscillator receives a subsequent excitation over another period of time and that excitation stops at time $t = t_2$.
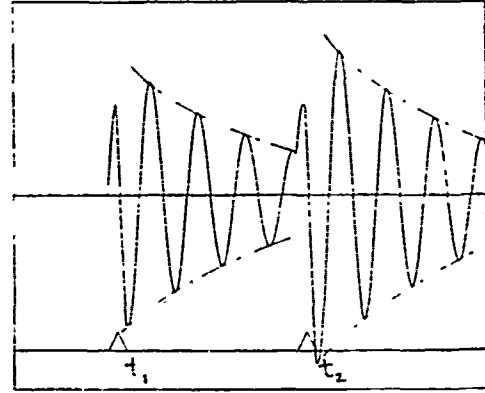
If there had been no previous acceleration response from the first disturbance the acceleration response to the second disturbance would have been:

$$\ddot{z}(t)\big|_{t>t_2} = e^{-\alpha\omega(t-t_2)}\left\{A_2\sin[\omega(t - t_2)] + B_2\cos[\omega(t - t_2)]\right\}$$

However, because of the presence of the decaying acceleration response to the first disturbance, the acceleration response to the combined disturbances must be written:

$$\ddot{z}(t)\big|_{t>t_2} = e^{-\alpha\omega(t-t_1)}\left\{A_1\sin[\omega(t - t_1)] + B_1\cos[\omega(t - t_1)]\right\} +$$
$$e^{-\alpha\omega(t-t_2)}\left\{A_2\sin[\omega(t - t_2)] + B_2\cos[\omega(t - t_2)]\right\}$$
$$(3.1)$$

For convenience in manipulating the terms in Equation (3.1) we abbreviate:

$$e_i = e^{-\alpha\omega(t-t_i)}$$
$$S_i = \sin[\omega(t - t_i)]$$
$$C_i = \cos[\omega(t - t_i)]$$

Then the acceleration response to the combined disturbances is:

$$\ddot{z}(t)\big|_{t>t_2} = e_1(A_1 S_1 + B_1 C_1) + e_2(A_2 S_2 + B_2 C_2) \quad (3.2)$$

The trick is write Equations (3.1) and (3.2) with respect to the time of the most recent disturbance, t_2. To that end we write:

$$t - t_1 = (t - t_2) + (t_2 - t_1)$$

We need the additional abbreviations:

$$e_{21} = e^{-\alpha\omega(t_2-t_1)}$$
$$S_{21} = \sin[\omega(t_2 - t_1)]$$
$$C_{21} = \cos[\omega(t_2 - t_1)]$$

To obtain:

$$e_1 = e_2 e_{21}$$
$$S_1 = S_2 C_{21} + C_2 S_{21}$$
$$C_1 = C_2 C_{21} - S_2 S_{21}$$

The acceleration response to the combined excitations becomes

$$\bar{z}(t)\big|_{t>t_2} = e_2 \left(A_2^* S_2 + B_2^* C_2\right) \tag{3.3}$$

where:

$$A_2^* = A_2 + e_{21}(A_1 C_{21} - B_1 S_{21})$$
$$B_2^* = B_2 + e_{21}(A_1 S_{21} + B_1 C_{21})$$

Following the same procedure we used for the single disturbance, the acceleration response to the combined disturbances can be rewritten as:

$$\bar{z}(t)\big|_{t>t_2} = R_2 e^{-\alpha\omega(t-t_2)} \sin\left[\omega(t - t_2) + \phi_2\right] \tag{3.4}$$

where:

$$R_2 = \sqrt{A_2^{*2} + B_2^{*2}} \tag{3.5}$$

$$= \sqrt{(A_2^2 + B_2^2) + 2e_{21}\left[C_{21}(A_1A_2 + B_1B_2) + S_{21}(A_1B_2 - B_1A_2)\right] + e_{21}^2(A_1^2 + B_1^2)}$$

$$\tan\phi_2 = \frac{B_2^*}{A_2^*} = \frac{B_2 + e_{21}(A_1 S_{21} + B_1 C_{21})}{A_2 + e_{21}(A_1 C_{21} - B_1 S_{21})}$$

Equation (3.5) for R_2, the potential amplitude of the acceleration response to the combined disturbances, is one of the major findings of this paper. Much of the subsequent work here will be concerned with finding the conditions which maximize and/or minimize (extremize) R_2.

As we did for the single disturbance, we can differentiate Equation (3.4) with respect to time to search for the times for the local extrema of the acceleration response. We obtain:

$$\frac{d\bar{z}(t)}{dt}\bigg|_{t>t_2} = R_2 e^{-\alpha\omega(t-t_2)}\omega\sqrt{1+\alpha^2} \cos\left[\omega(t-t_2) + (\phi_2 + \delta_2)\right] \tag{3.6}$$

where

$$\tan\delta_2 = \alpha$$

Even though the first phase shifts are not necessarily equal ($\phi_1 \neq \phi_2$), we see the same second phase shifts ($\delta_2 = \delta_1$) in the times for local extrema of the acceleration response to the combined disturbances. Those local extrema will occur when:

$$\omega(t - t_2) = (2n-1)\frac{\pi}{2} - (\phi_2 + \delta_2); \quad n = 1, 2, 3, \ .. \tag{3.7}$$

As we did for the single disturbance, we can use these results to obtain an even better upper bound on the amplitude of the acceleration response. If we plug the above value of $\omega(t - t_2)$ into Equation (3.4) for $\bar{z}(t)\big|_{t>t_2}$, we find that the local extrema for $\bar{z}(t)\big|_{t>t_2}$ equal:

$$\frac{R_2}{\sqrt{1+\alpha^2}} e^{-\alpha\left[(2n-1)\frac{\pi}{2} - (\phi_2 + \delta_2)\right]} \ ; n = 1, 2, 3, \ldots$$

We have seen how to find the times for local extrema of the decaying acceleration response, assuming we know $A_1, B_1, A_2, B_2, \alpha, \omega, t_1$ and t_2. However, we are searching for the best and worst possible runway profiles, so the most critical aspect is to find the values of t_2, the time of the second disturbance, which will locally extremize the potential amplitude R_2. We differentiate Equation (3.5) for R_2 with respect to t_2 and set the result to zero to obtain:

$$S_{21}\left[(A_1A_2 + B_1B_2) + \alpha(A_1B_2 - B_1A_2)\right] +$$
$$C_{21}\left[\alpha(A_1A_2 + B_1B_2) - (A_1B_2 - B_1A_2)\right] + \alpha(A_1^2 + B_1^2)e_{21} = \tag{3.8}$$

or

$$\tilde{R}_{12}\sin\left[\omega(t_2 - t_1) + \psi_{12}\right] + \frac{\alpha}{\sqrt{1+\alpha^2}} e^{-\alpha\omega(t_2-t_1)} = 0 \tag{3.9}$$

where

$$\tilde{R}_{12} = \sqrt{\frac{A_2^2 + B_2^2}{A_1^2 + B_1^2}}$$

$$\tan\psi_{12} = \frac{\alpha(A_1A_2 + B_1B_2) - (A_1B_2 - B_1A_2)}{(A_1A_2 + B_1B_2) + \alpha(A_1B_2 - B_1A_2)}$$

The exact solution for the time delays $(t_2 - t_1)$ which locally extremize R_2 would require a numerical or graphical solution of Equations (3.8) or (3.9), however for small damping we would expect

$$\omega(t_2 - t_1) \approx n\pi - \psi_{12}; \quad n = 1, 2, 3 \ldots \tag{3.10}$$

We will give the determination of the time delays $(t_2 - t_1)$ an exact treatment in the next Section.

4. THE BUMP MULTIPLIER

Recall that R_1 represented the potential amplitude of the decaying acceleration response to the first disturbance and that R_2 represented the potential amplitude of the acceleration response to the combined disturbances, where in each case we measured time from the time of the most recent disturbance. *We call the ratio R_2/R_1 the BUMP MULTIPLIER, since it defines the extent to which the second disturbance amplifies (or attenuates) the acceleration response to the first disturbance.* The BUMP MULTIPLIER is

68

$$\frac{R_2}{R_1} = \sqrt{\frac{(A_2^2 + B_2^2) + 2\epsilon_{21}\left[C_{21}(A_1A_2 + B_1B_2) + S_{21}(A_1B_2 - B_1A_2)\right] + \epsilon_{21}^2(A_1^2 + B_1^2)}{A_1^2 + B_1^2}}$$

(4.1)

To assist in the interpretation of the BUMP MULTI-PLIER we add another set of abbreviations:

$$\epsilon_i = \frac{B_i}{A_i} \; ; i = 1, 2$$

With this definition, the potential amplitudes and phase angles for the acceleration responses to the first disturbance and the combined disturbances become:

$$R_1 = |A_1|\sqrt{1 + \epsilon_1^2} \qquad (4.2)$$
$$\tan\phi_1 = \epsilon_1$$

$$R_2 = \sqrt{A_2^2(1 + \epsilon_2^2) + 2A_2(A_1\epsilon_{21})\left[C_{21}(1 + \epsilon_1\epsilon_2) + S_{21}(\epsilon_2 - \epsilon_1)\right] + (A_1\epsilon_{21})^2(1 + \epsilon_1^2)}$$

$$= |A_2|\sqrt{(1 + \epsilon_2^2) + 2(\frac{A_1}{A_2}\epsilon_{21})\left[C_{21}(1 + \epsilon_1\epsilon_2) + S_{21}(\epsilon_2 - \epsilon_1)\right] + \left(\frac{A_1}{A_2}\epsilon_{21}\right)^2(1 + \epsilon_1^2)}$$

(4.3)

$$\tan\phi_2 = \frac{\epsilon_2 + (\frac{A_1}{A_2}\epsilon_{21})(S_{21} + \epsilon_1 C_{21})}{1 + (\frac{A_1}{A_2}\epsilon_{21})(C_{21} - \epsilon_1 S_{21})}$$

The BUMP MULTIPLIER becomes:

$$\frac{R_2}{R_1} = \left|\frac{A_2}{A_1}\right|\sqrt{\frac{(1 + \epsilon_2^2) + 2(\frac{A_1}{A_2}\epsilon_{21})\left[C_{21}(1 + \epsilon_1\epsilon_2) + S_{21}(\epsilon_2 - \epsilon_1)\right] + (\frac{A_1}{A_2}\epsilon_{21})^2(1 + \epsilon_1^2)}{1 + \epsilon_1^2}}$$

(4.4)

Note in Equation (4.4) that the magnitude effects are contained mostly in the term $\left|\frac{A_2}{A_1}\right|$, whereas the spacing effects are in the radical. The spacing effects are dominated by the terms

$$S_{21} = \sin\left[\omega(t_2 - t_1)\right]$$
$$C_{21} = \cos\left[\omega(t_2 - t_1)\right]$$

and those terms are always modulated by the combination

$$\frac{A_1}{A_2}\epsilon_{21} = \frac{A_1}{A_2}e^{-\alpha\omega(t_2 - t_1)}$$

When we use these abbreviations in Equation (3.9) to find the time delays $(t_2 - t_1)$ which locally extremize the potential amplitude R_2, we obtain

$$\left|\frac{A_2}{A_1}\right|\sqrt{\frac{1 + \epsilon_2^2}{1 + \epsilon_1^2}}\sin\left[\omega(t_2 - t_1) + \psi_{12}\right] + \frac{\alpha}{\sqrt{1 + \alpha^2}}e^{-\alpha\omega(t_2 - t_1)} = 0$$

(4.5)

where

$$\tan\psi_{12} = \frac{\alpha(1 + \epsilon_1\epsilon_2) - (\epsilon_2 - \epsilon_1)}{(1 + \epsilon_1\epsilon_2) + \alpha(\epsilon_2 - \epsilon_1)}$$

A first approximation for $\alpha \ll 1$ for the time delays would be:

$$\omega(t_2 - t_1) \approx n\pi - \psi_{12} \; ; n = 1, 2, 3, \ldots \qquad (4.6)$$

To get a second approximation we search for small angles β_n such that

$$\omega(t_2 - t_1) = n\pi - (\psi_{12} + \beta_n) \qquad (4.7)$$

With this change of variables Equation (4.5) takes a new form

$$C_n \sin\beta_n = \frac{\alpha e^{\alpha\beta_n}}{\sqrt{1 + \alpha^2}} \qquad (4.8)$$

where

$$C_n = (-1)^n e^{\alpha(n\pi - \psi_{12})}\left|\frac{A_2}{A_1}\right|\sqrt{\frac{1 + \epsilon_2^2}{1 + \epsilon_1^2}} \qquad (4.9)$$

If we expand Equation (4.8) for small β_n, keeping only first order terms, we obtain

$$\beta_n \approx \frac{\alpha}{C_n\sqrt{1 + \alpha^2} - \alpha^2} \qquad (4.10)$$

This then is the (hoped for) small correction we use in Equation (4.7) to find the second approximation for the time delays $(t_2 - t_1)$.

5. USE OF THE AVERAGE SPEED

We have made no assumption of a constant taxi speed between the two disturbances; in fact we will show in this Section that the spacing effects are dominated by the average speed between them.

If l is the distance between the two disturbances, the average speed is

$$\bar{V} = \frac{l}{t_2 - t_1} \qquad (5.1)$$

6.

Then we can express the term

$$\omega(t_2 - t_1) = \frac{l\omega}{\bar{V}} = \bar{\lambda} \qquad (5.2)$$

The usual terminology for $\lambda = l\omega/V$, based on the instantaneous speed, is the reduced frequency. Therefore $\bar{\lambda} = l\omega/\bar{V}$ is the reduced frequency based on the average speed between the two disturbances.

Amplitude and Bump Multiplier

Equations (4.2) and (4.3) for the potential amplitudes and phase angles, and Equation (4.4) for the BUMP MULTIPLIER remain unchanged, except that now we note

$$e_{21} = e^{-\alpha\bar{\lambda}}$$

$$S_{21} = \sin\bar{\lambda}$$

$$C_{21} = \cos\bar{\lambda}$$

Best/Worst Runway Profiles

The process for finding the exact and approximate solutions for the time delays which extremize R_2 remains unchanged, except Equation (4.5) now becomes:

$$\left|\frac{A_2}{A_1}\right|\sqrt{\frac{1+\epsilon_2^2}{1+\epsilon_1^2}}\sin\left(\bar{\lambda}+\psi_{12}\right) + \frac{\alpha}{\sqrt{1+\alpha^2}}e^{-\alpha\bar{\lambda}} = 0 \quad (5.3)$$

The first approximation for the time delays becomes an equation for $\bar{\lambda}$:

$$\bar{\lambda} \approx n\pi - \psi_{12} \; ; n = 1, 2, 3, \ldots \qquad (5.4)$$

The process of finding exact solutions and second approximations for the time delays also remains unchanged, except that Equation (4.7) becomes

$$\bar{\lambda} = n\pi - (\psi_{12} + \beta_n) \qquad (5.5)$$

6. SPECIAL CASE: SIMILAR DISTURBANCES|

We now define similar disturbances as discrete disturbances that have the same shape but differ only in magnitude and/or sign. Examples would be the entire family of infinite ramps or a family of sine waves of the same wavelength but varying heights. *The assumption of similar disturbances is not a very limiting one. In fact, nearly all of the profiles tested in the HAVE BOUNCE program and all of the NATO/AGARD profiles can be broken down into sequences of similar ramp disturbances.* For linear systems with zero initial conditions similar disturbances will produce similar acceleration responses, and when disturbances are similar $\epsilon_1 = \epsilon_2 = \epsilon$.

Amplitude

Under the assumption of similar disturbances, Equation (4.2) and (4.3) for the potential amplitudes and phase angles become:

$$R_1 = |A_1|\sqrt{1+\epsilon^2} \qquad (6.1)$$

$$\tan\phi_1 = \epsilon$$

$$R_2 = \sqrt{1+\epsilon^2}\sqrt{A_2^2 + 2A_2(A_1 e_{21})C_{21} + (A_1 e_{21})^2}$$

$$= |A_2|\sqrt{1+\epsilon^2}\sqrt{1 + 2(\frac{A_1}{A_2}e_{21})C_{21} + (\frac{A_1}{A_2}e_{21})^2} \quad (6.2)$$

$$\tan\phi_2 = \frac{\epsilon + (\frac{A_1}{A_2}e_{21})(S_{21} + \epsilon C_{21})}{1 + (\frac{A_1}{A_2}e_{21})(C_{21} - \epsilon S_{21})}$$

Bump Multiplier

Equation (4.4) for the BUMP MULTIPLIER reduces to:

$$\frac{R_2}{R_1} = \left|\frac{A_2}{A_1}\right|\sqrt{1 + 2(\frac{A_1}{A_2}e_{21})C_{21} + (\frac{A_1}{A_2}e_{21})^2} \qquad (6.3)$$

Figures (6.1) and (6.2) illustrate the BUMP MULTIPLIER versus $\bar{\lambda}$ with the damping as a parameter for the special case of equal (or opposite) disturbances at constant speeds.

70
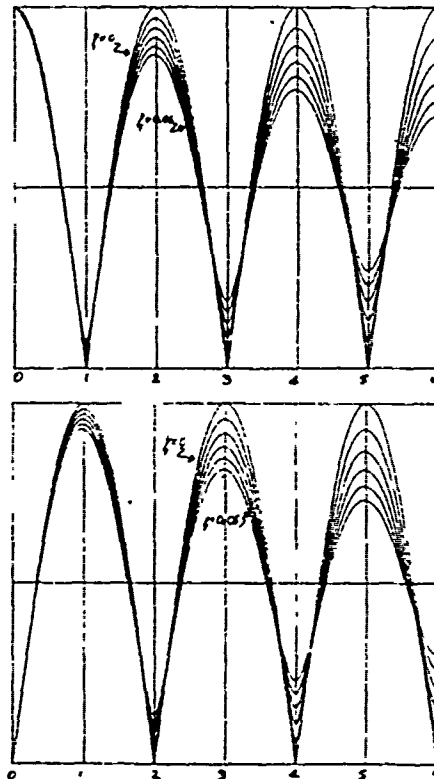
The major conclusion to be drawn is the dependence of the BUMP MULTIPLIER on the nondimensional spacing (or speed or frequency) parameter

$$\tilde{\lambda} = \omega(t_2 - t_1) = l\omega/\tilde{V}$$

The spacing of the disturbances, the average speed of the vehicle and the natural frequency all combine into the one parameter, the reduced frequency based on the average speed. Also, while the BUMP MULTIPLIER clearly diminishes with $\tilde{\lambda}$ for significant values of α, the values of $\tilde{\lambda}$ that produce the local minima and maxima are fairly weak functions of α.

Best/Worst Runway Profiles

In order to find the time delays that locally extremize R_2 Equation (5.3) reduces to:

$$\left|\frac{A_2}{A_1}\right| \sin\left(\tilde{\lambda} + \psi_{12}\right) + \frac{\alpha e^{-\alpha\tilde{\lambda}}}{\sqrt{1+\alpha^2}} = 0 \qquad (6.4)$$

where

$$\tan\psi_{12} = \alpha$$

The definition of C_n reduces to:

$$C_n = (-1)^n e^{\alpha(n\pi - \psi_{12})}\left|\frac{A_2}{A_1}\right| \qquad (6.5)$$

Tables (6.1) and (6.2) give values of the first approximation, second approximation and exact solution for $\tilde{\lambda}$ which locally maximize and minimize the BUMP MULTIPLIER for the same special case of equal (or opposite) disturbances and constant speeds.

The major conclusions to be drawn are:

(a) Again the spacing that maximizes or minimizes the acceleration response depends very weakly on the damping parameter, α,

(b) the First approximation

$$\tilde{\lambda} = n\pi - \psi_{12} \approx n\pi - \alpha$$

is an excellent approximation to the exact solution for reasonably small values of damping.

ζ	n	1st	2nd	Exact
0.0000				
	1	1.0000	1.0000	1.0000
	2	2.0000	2.0000	2.0000
	3	3.0000	3.0000	3.0000
	4	4.0000	4.0000	4.0000
	5	5.0000	5.0000	5.0000
	6	6.0000	6.0000	6.0000
0.0100				
	1	0.9968	0.9937	0.9999
	2	1.9968	1.9938	1.9938
	3	2.9968	2.9939	2.9997
	4	3.9968	3.9940	3.9940
	5	4.9968	4.9941	4.9955
	6	5.9968	5.9942	5.9942
0.0200				
	1	0.9936	0.9877	0.9996
	2	1.9936	1.9883	1.9880
	3	2.9936	2.9884	2.9989
	4	3.9936	3.9887	3.9887
	5	4.9936	4.9890	4.9983
	6	5.9936	5.9893	5.9893
0.0300				
	1	0.9905	0.9818	0.9991
	2	1.9905	1.9825	1.9825
	3	2.9905	2.9832	2.9977
	4	3.9905	3.9839	3.9839
	5	4.9905	4.9845	4.9964
	6	5.9905	5.9850	5.9850
0.0400				
	1	0.9873	0.9760	0.9985
	2	1.9873	1.9774	1.9773
	3	2.9873	2.9785	2.9960
	4	3.9873	3.9796	3.9796
	5	4.9873	4.9805	4.9941
	6	5.9873	5.9813	5.9813
0.0500				
	1	0.9841	0.9704	0.9977
	2	1.9841	1.9724	1.9724
	3	2.9841	2.9741	2.9940
	4	3.9841	3.9756	3.9756
	5	4.9841	4.9768	4.9914
	6	5.9841	5.9779	5.9779

ζ	n	1st	2nd	Exact
0.0000				
	1	1.0000	1.0000	1.0000
	2	2.0000	2.0000	2.0000
	3	3.0000	3.0000	3.0000
	4	4.0000	4.0000	4.0000
	5	5.0000	5.0000	5.0000
	6	6.0000	6.0000	6.0000
0.0100				
	1	0.9968	0.9999	0.9937
	2	1.9968	1.9998	1.9998
	3	2.9968	2.9997	2.9939
	4	3.9968	3.9996	3.9956
	5	4.9968	4.9955	4.9941
	6	5.9968	5.9955	5.9995
0.0200				
	1	0.9936	0.9996	0.9877
	2	1.9936	1.9992	1.9992
	3	2.9936	2.9989	2.9884
	4	3.9936	3.9986	3.9986
	5	4.9936	4.9983	4.9893
	6	5.9936	5.9980	5.9980
0.0300				
	1	0.9905	0.9991	0.9818
	2	1.9905	1.9984	1.9984
	3	2.9905	2.9976	2.9832
	4	3.9905	3.9970	3.9970
	5	4.9905	4.9964	4.9845
	6	5.9905	5.9959	5.9959
0.0400				
	1	0.9873	0.9985	0.9760
	2	1.9873	1.9972	1.9972
	3	2.9873	2.9960	2.9785
	4	3.9873	3.9950	3.9950
	5	4.9873	4.9941	4.9805
	6	5.9873	5.9933	5.9933
0.0500				
	1	0.9841	0.9977	0.9704
	2	1.9841	1.9957	1.9957
	3	2.9841	2.9940	2.9741
	4	3.9841	3.9926	3.9926
	5	4.9841	4.9914	4.9768
	6	5.9841	5.9903	5.9903

7. EXAMPLE: THE CLASSICAL, UNDERDAMPED SPRING-MASS-DAMPER TAXIING OVER TWO RAMPS.

We consider the example of a *classical*, single degree-of-freedom oscillator that encounters two ramp disturbances. The disturbances are separated by a distance l and occur at times t_1 and t_2, respectively. The taxi speeds V_1, V_2 are not necessarily equal at the time of the encounters, nor are the ramp angles θ_1, θ_2.
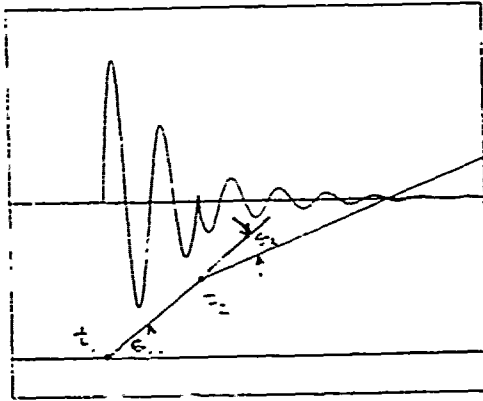
The differential equation of motion is:

$$m\ddot{z} + c\dot{z} + kz = c\dot{g} + kg \qquad (7.1)$$

where:

$$g(t) = V\theta l\, u(t)$$

$$u(t) = \text{unit step function}$$

We make the usual abbreviations:

ς = ratio of damping to critical value, $c/2m\omega_0$

ω_0 = undamped natural frequency, $\sqrt{k/m}$

By solving the ordinary differential equation of motion for the displacement in acceleration response to the ramp inputs (with zero initial conditions) and then differentiating those results twice with respect to time we find the various parameters to use in Equations (2.1) and (3.1):

$$A_i = V_i\omega_0\theta_i\,(1 - 2\varsigma^2)$$

$$B_i = 2V_i\omega_0\theta_i\,\varsigma\sqrt{1 - \varsigma^2} \qquad (7.2)$$

$$\omega = \text{damped frequency, } \omega_0\sqrt{1 - \varsigma^2}$$

$$\alpha = \varsigma/\sqrt{1 - \varsigma^2}$$

We also note the nondimensional reduced frequencies :

$$\lambda_0 = \frac{l\omega_0}{V}$$

$$\lambda = \frac{l\omega}{V} = \lambda_0\sqrt{1 - \varsigma^2} \qquad (7.3)$$

and the relationship:

$$\alpha\omega = \varsigma\omega_0 \qquad (7.4)$$

Note the distinction between the hypothetical undamped frequency ω_0 and the actual damped frequency ω. Note also the distinction between ς, the fraction of critical damping as related to the hypothetical undamped frequency ω_0, and α which we use to relate damping to the actual damped frequency ω.

For purposes of illustration we pick the fictitious undamped natural frequency to be

$$\omega_0 = 2\pi \ rad/sec$$

$$f_0 = \omega_0/2\pi = 1.0\,Hz,$$

and we pick the damping value

$$\varsigma = c/2m\omega_0 = 0.1$$

so that

$$\sqrt{1 - \varsigma^2} = 0.9950$$

$$\alpha = \varsigma/\sqrt{1 - \varsigma^2} = 0.1005$$

Note that this means the actual damped frequency is:

$$\omega = 1.99\pi \ rad/sec; \ f = 0.9950\,Hz$$

All members of the family of infinite ramps are similar. Therefore, For every ramp input (regardless of speed V, frequency ω or slope θ) the similarity parameter ϵ is:

$$\epsilon_1 = \epsilon_2 = \epsilon = \frac{B}{A} = \frac{2\varsigma\sqrt{1 - \varsigma^2}}{1 - 2\varsigma^2} = \tan\phi_1 = 0.2030 \qquad (7.5)$$

The second phase shifts for the location of the local extrema of the decaying acceleration response will be identical:

$$\delta_1 = \delta_2 = \delta = \sin^{-1}\varsigma = 0.1002\,rad = 5.739°$$

Figure (7.1) illustrates the two phase shifts ϕ_1 and δ versus the damping ratio ς.

Amplitude

The potential amplitudes of the decaying acceleration responses are obtained by applying the definitions in equations (7.2)-(7.4) to the equations for similar disturbances. Equations (6.1)-(6.5).
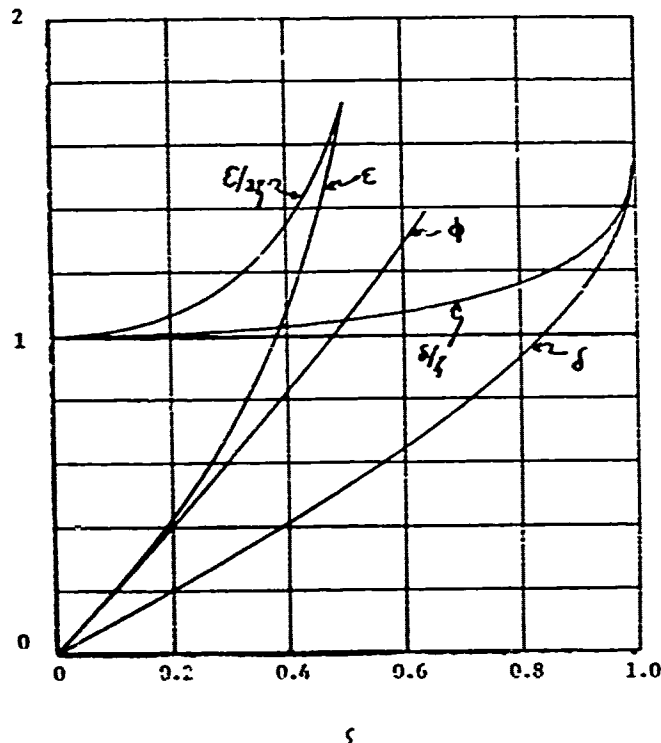
Figure 7.1 The Similarity parameter ϵ and the Phase Angles ϕ and δ

Figure (7.2) illustrates the decaying acceleration response of the *classical* spring-mass-damper for a typical single ramp input at a constant speed of $V = 10.0\ l/sec$, where the length units are in any convenient, consistent system. Figure (7.3) illustrates the sensitivity to speed by plotting the acceleration response for a range of speeds $V = 10, 11, \ldots, 20\ l/sec$. Note that the amplitude of the acceleration response to the single disturbance grows monotonically with increasing speed. Figure (7.4) illustrates a curious feature in the dependence of the acceleration response on damping for

$$\varsigma = 0.1, 0.2, \ldots, 0.5$$

at a constant speed of $V = 10.0\ l/sec$. Large values of damping actually increase the peak acceleration response at the earliest instants of time. These effects are the result of the term

$$B_t = 2V_t \omega_0 \theta_t \varsigma \sqrt{1 - \varsigma^2}$$

which reaches its maximum value at $\varsigma = \frac{\sqrt{2}}{2}$

Figure (7.5) illustrates the decaying acceleration response for traversing two equal (but opposite) ramps, separated by a distance of 20.0 l, at a constant speed of $10.0\ l/sec$. Note that the maximum amplitude of the acceleration response to the combined disturbances at a speed of $10.0\ l/sec$ is actually smaller than the acceleration response to the first disturbance alone at the same speed. Figures (7.6) and (7.7) show that this will not always be the case. By changing the constant speeds to $V = 8.02$ and $13.46\ l/sec$ for the same ramp geometry, the acceleration response to the combined disturbances can be markedly greater than the acceleration response to the first disturbance alone. Figure (7.8) further illustrates the sensitivity to speed by plotting the acceleration response for a range of speeds $V = 10, 11, \ldots, 20\ l/sec$. While the amplitude of the acceleration response to the single disturbance grew monotonically with increasing speed, the amplitude of the acceleration response to the combined disturbances displays a much more complicated structure.

Figure (7.9) shows the damping effect on the acceleration response to the combined disturbances. Note how the maximums, zeroes and minimums occur at nearly the same periodic values of λ, regardless of the value of the critical damping ratio ς.

73
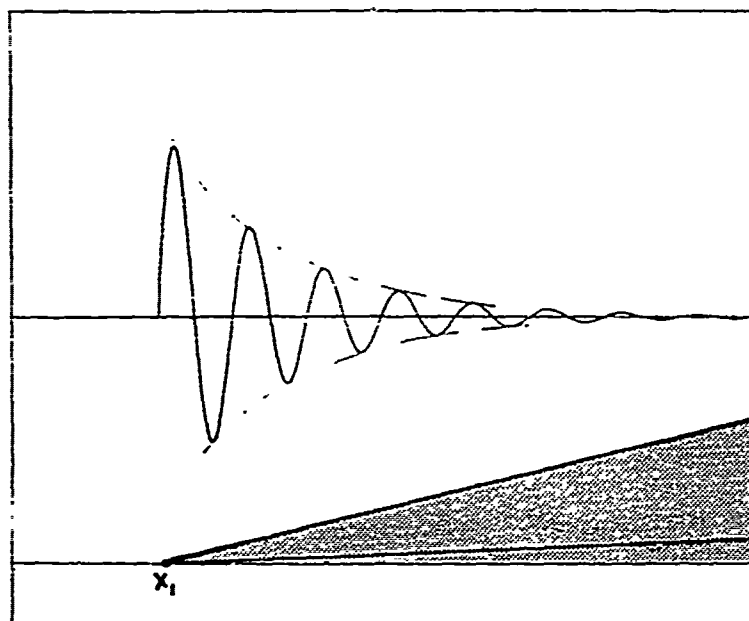
Figure 7.2 Acceleration Response to a Single Ramp at $V = 10.0 l/sec$
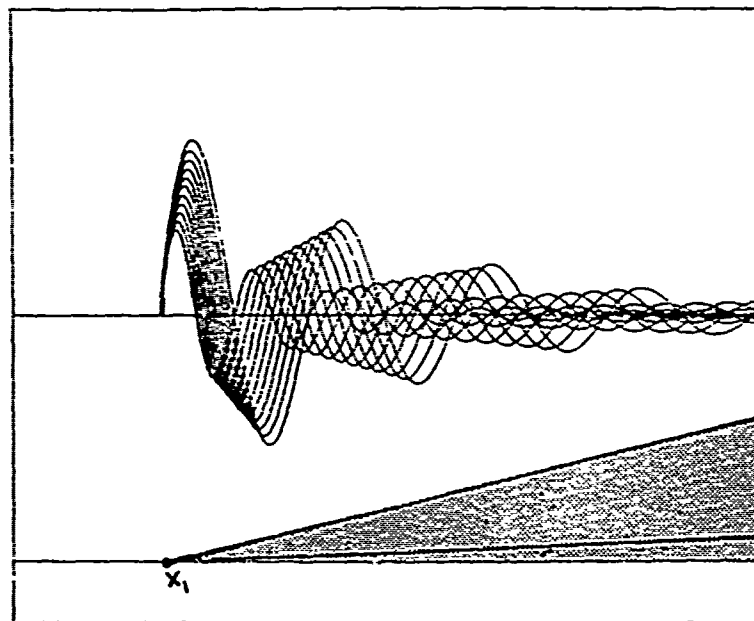
Figure 7.3 Acceleration Response to a Single Ramp at $V = 10, 11, \ldots, 20 l/sec$
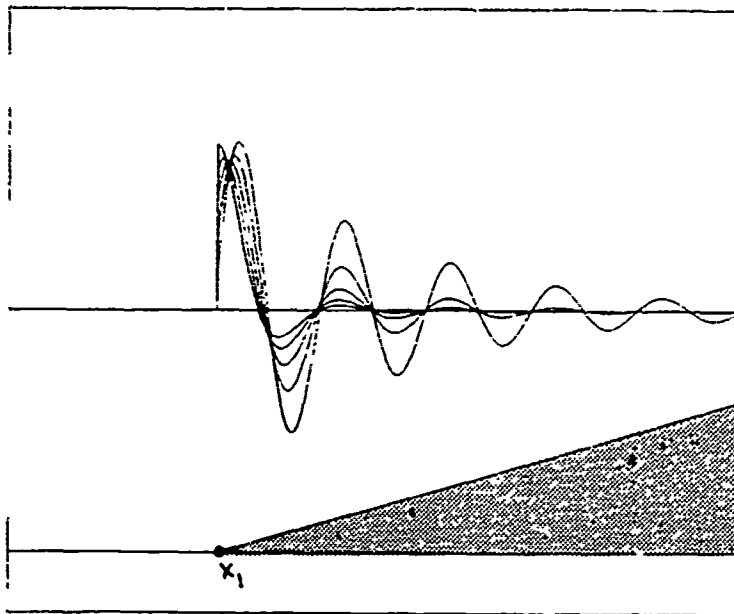
Figure 7.4 Acceleration Response to a Single Ramp for $\varsigma = 0.1, 0.2, \ldots, 0.5$
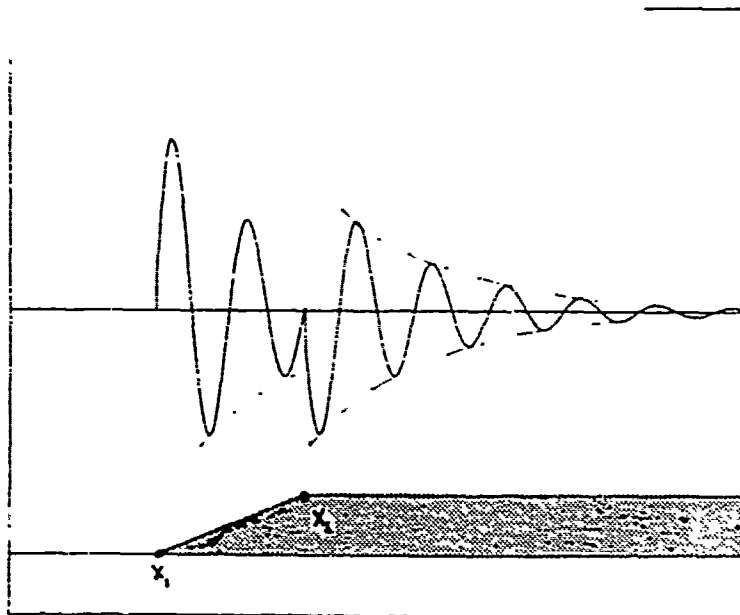
Figure 7.5 Acceleration Response to Two Equal and Opposite Ramps at $V = 10\ 0\ l/sec$
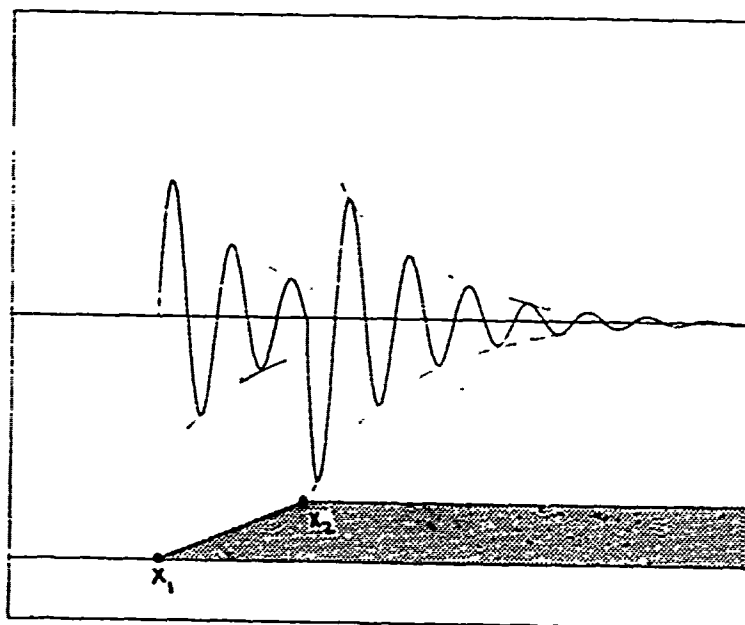
Figure 7.6 Acceleration Response to Two Equal and Opposite Ramps at $V = 8.92 l/sec$
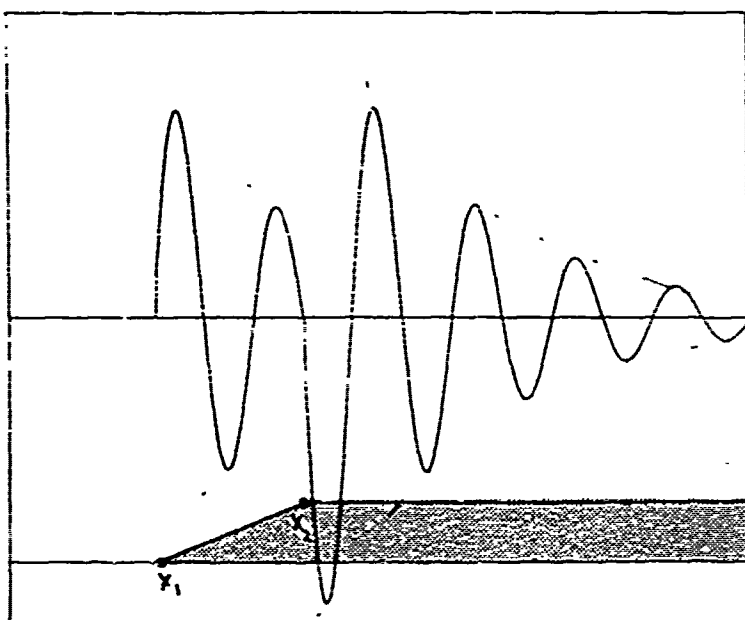
Figure 7.7 Acceleration Response to Two Equal and Opposite Ramps at $V = 13.46 l/sec$
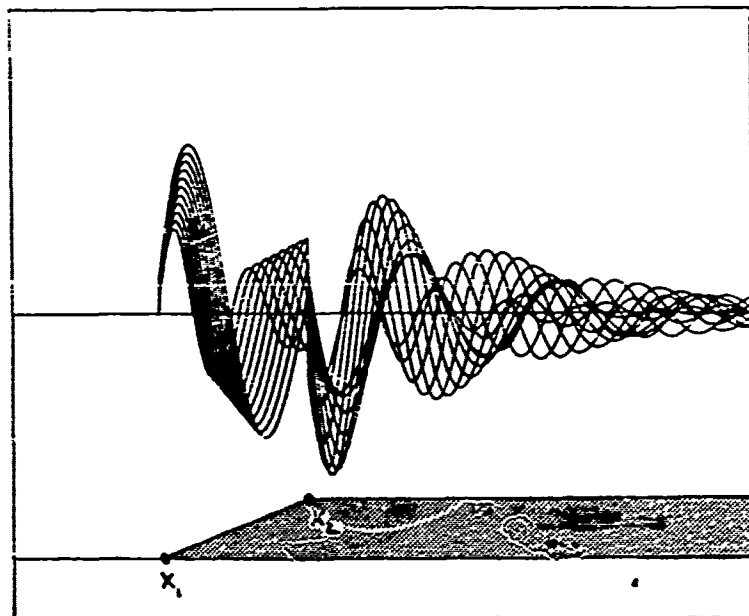
Figure 7.8 Acceleration Response to Two Equal and Opposite Ramps at $V = 10, 11, \ldots, 20 \, l/sec$
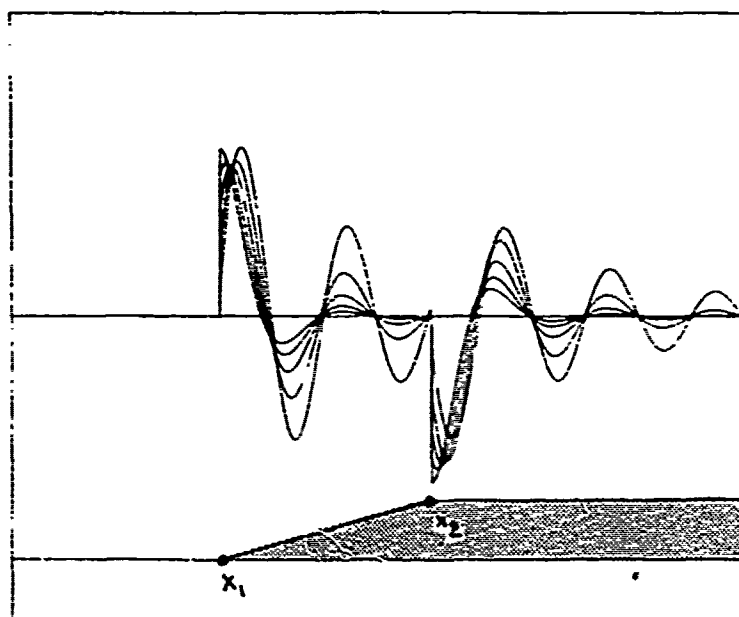
Figure 7.9 Acceleration Response to Two Equal and Opposite Ramps for $\varsigma = 0.1, 0.2, \ldots, 0.5$

77

Bump Multiplier

Reverting to the general case of non-constant speeds and ramp angles, the potential amplitude for the dynamic acceleration response to the combined disturbances is given by:

$$R_2 = \omega_0 \sqrt{(V_2\theta_2)^2 + 2\,(V_1\theta_1 e_{21})\,C_{21} + (V_1\theta_1 e_{21})^2}$$

$$= \omega_0 V_2 |\theta_2| \sqrt{1 + 2\left(\frac{V_1\theta_1 e_{21}}{V_2\theta_2}\right)C_{21} + \left(\frac{V_1\theta_1 e_{21}}{V_2\theta_2}\right)^2} \quad (7.6)$$

where:

$$e_{21} = e^{-\alpha\omega(t_2-t_1)} = e^{-\alpha\tilde\lambda} = e^{-0.1005\tilde\lambda}$$

$$C_{21} = \cos\left[\omega(t_2-t_1)\right] = \cos\tilde\lambda$$

The BUMP MULTIPLIER from Equation (6.3) is

$$\frac{R_2}{R_1} = \left|\frac{V_2\theta_2}{V_1\theta_1}\right| \sqrt{1 + 2\left(\frac{V_1\theta_1 e_{21}}{V_2\theta_2}\right)C_{21} + \left(\frac{V_1\theta_1 e_{21}}{V_2\theta_2}\right)^2} \quad (7.7)$$

The term $\left|\frac{V_2\theta_2}{V_1\theta_1}\right|$ in Equation (7.7) gives the pure magnitude effect of the two disturbances. The radical gives the spacing effect. The dominant term is $C_{21} = \cos\tilde\lambda$, which is modified by

$$\left(\frac{V_1\theta_1}{V_2\theta_2}\right)e_{21} = \left(\frac{V_1\theta_1}{V_2\theta_2}\right)e^{-\alpha\tilde\lambda} = \left(\frac{V_1\theta_1}{V_2\theta_2}\right)e^{-0.1005\tilde\lambda}$$

Equations (7.6) and (7.7) are very powerful results which relate the potential amplitude R_2 and the BUMP MULTIPLIER to the instantaneous speeds V_1, V_2, the average speed $\bar V$, the ramp angles θ_1, θ_2, the damping parameter α and the average reduced frequency $\tilde\lambda = l\omega/\bar V$.

Best/Worst Runway Profiles

Recall that the equations which determine the best/worst runway profiles or speeds were:

$$\left|\frac{A_2}{A_1}\right|\sin\left(\tilde\lambda + \psi_{12}\right) + \frac{\alpha e^{-\alpha\tilde\lambda}}{\sqrt{1+\alpha^2}} = 0 \quad (6.4)$$

where

$$\tan\psi_{12} = \alpha$$

For this example:

$$\psi_{12} = \sin^{-1}\varsigma = 0.1002\ rad = 5.739^\circ$$

For constant speeds and equal (but opposite) ramps Equation (6.4) reduces to

$$\varsigma e^{-\tilde\lambda} + \sin\left(\tilde\lambda + \psi_{12}\right) = 0 \quad (7.8)$$

a. First Approximation

The first approximation to the time delays that locally maximize and minimize the acceleration response to the combined disturbances is:

$$\lambda \approx n\pi - \psi_{12}; \quad n = 1, 2, 3\ldots \quad (5.4)$$

or

$$\lambda = 3.0414, 6.1830, 9.3246, 12.4662, \ldots$$

$$\frac{\lambda}{n\pi} = 0.9681, 0.9841, 0.9894, 0.9920, \ldots; n = 1, 2, 3\ldots$$

b. Exact Solution

In obtaining the exact solution for the time delays, the values of C_n for $n = 1, 2, 3\ldots$ are:

$$C_n = 21.04;\ -486.9;\ 11270;\ -310,700\ldots$$

The corresponding exact (rapidly diminishing) values of β_n are:

$$\beta_n = 4.779*10^{-3}, -2.064*10^{-4}, 8.920*10^{-6}, -3.855*10^{-7}\ldots$$

and the exact values of λ are:

$$\lambda = 3.0366, 6.1832, 9.3246, 12.4662, \ldots$$

$$\frac{\lambda}{n\pi} = 0.9666, 0.9841, 0.9894, 0.9920, \ldots; n = 1, 2, 3, \ldots$$

These small values of β_n illustrate why the first approximation is such an excellent approximation.

c. Second Approximation

The approximate solutions for small ς would be:

$$\beta_n \approx \frac{\alpha}{C_n\sqrt{1+\alpha^2} - \alpha^2} \quad (4.10)$$

These approximations to β_n are:

$$\beta_n = 4.774*10^{-3};\ -2.064*10^{-4}, \ldots$$

They differ from the exact values only for $n = 1$, and then very slightly. In addition, both the exact solutions and the second approximations are very small corrections to the first approximation:

$$\lambda = n\pi - \psi_{12} \approx n\pi - \alpha \quad (5.4)$$

Earlier in this section, when we found the speeds $8.02\ and\ 13.46\ l/sec$ that increased the acceleration response to two equal (but opposite) disturbances separated by a distance $20.0l$, we used the results in Table (6.2). Table (6.2) shows that, for $\alpha \approx 0.1$, the exact solutions for the values of the reduced frequency $\tilde\lambda = l\omega/\bar V$ that extremize the acceleration response to the combined disturbances are:

78

Maximize: $\tilde{\lambda}/\pi = 0.9447, 2.9558, 4.9616, \ldots$

Minimize: $\tilde{\lambda}/\pi = 1.9853, 3.9774, 5.9731, \ldots$

For a length $l = 20.0 \, l$, and noting that $f = \omega/2\pi = 0.995 \, Hz$, these results translate to the follow speeds:

Maximize: $V = 42.13, 13.46, 8.02 \, l/sec, \ldots$
Minimize: $V = 20.05, 10.01, 6.66 \, l/sec, \ldots$

Note that Table (6.1) or (6.2) requires the use of the damped reduced frequency, $\tilde{\lambda} = l\omega/\tilde{V}$ rather than the the fictitious undamped reduced frequency $\tilde{\lambda}_0 = l\omega_0/\tilde{V}$.

8. APPLICATION TO NONLINEAR CALCULATIONS AND TEST PROGRAMS

a. Three Principles

The first set of basic ideas to keep in mind when when using these results to plan nonlinear calculations, HAVE BOUNCE (taxi) tests or AGILE tests is that a useful building block is the *infinite ramp*, that two infinite (opposite) ramps can combine to produce an *AGARD Bump*, and that two (opposite) AGARD bumps can combine to produce an *AGARD Repair Mat*.
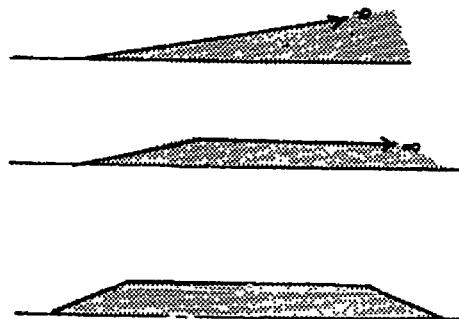
Second, recall that for two disturbances separated by a distance l, the best/worst combinations tend to occur when:

$$\tilde{\lambda} = \frac{l\omega}{\tilde{V}} = 2\pi \frac{lf}{\tilde{V}} \approx n\pi - \alpha \; ; n = 1, 2, 3 \ldots$$

or

$$\tilde{V} \approx \frac{2lf}{n - \frac{\alpha}{\pi}} \; ; n = 1, 2, 3 \ldots \qquad (8.1)$$

Third, the *potential amplitudes* of the acceleration response of a *classical* single degree-of-freedom oscillator to a single infinite ramp and to two combined ramps are:

$$R_1 = V_1 \omega_0 |\theta_1|$$

$$R_2 = \omega_0 \sqrt{(V_2\theta_2)^2 + 2(V_2\theta_2)(V_1\theta_1 e_{21})C_{21} + (V_1\theta_1 e_{21})^2}$$

$$= \omega_0 V_2 |\theta_2| \sqrt{1 + 2\left(\frac{V_1\theta_1 e_{21}}{V_2\theta_2}\right)C_{21} + \left(\frac{V_1\theta_1 e_{21}}{V_2\theta_2}\right)^2} \qquad (7.6)$$

where:

$$e_{21} = e^{-\alpha\omega(t_2 - t_1)} = e^{-\alpha\tilde{\lambda}}$$

$$C_{21} = \cos[\omega(t_2 - t_1)] = \cos\tilde{\lambda}$$

b. The Acceleration Response on the Initial Slope of

Beginning with the basic building block of the *infinite ramp* we have shown that the acceleration response is given by:

$$\ddot{z}(t)\big|_{t > t_1} = R_1 e^{-\alpha\omega(t - t_1)} \sin[\omega(t - t_1) + \phi_1] \qquad (2.2)$$
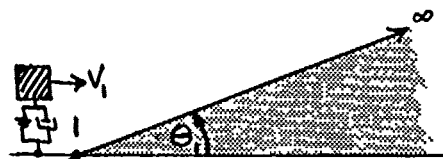
The initial acceleration response at the first corner will be given by:

$$\ddot{z}\big|_{t = t_1^+} = R_1 \sin\phi_1 \qquad (8.2)$$

We have also shown that the local extrema of the acceleration response are given by:

$$\frac{R_1}{\sqrt{1 + \alpha^2}} e^{-\alpha[(2n-1)\frac{\pi}{2} - (\phi_1 + \delta_1)]} \; ; n = 1, 2, 3, \ldots$$

and that they occur when

$$\omega(t_{peak} - t_1) = (2n - 1)\frac{\pi}{2} - (\phi_1 + \delta_1) \; ; n = 1, 2, 3, \ldots$$

This translates to distances of:

$$x_{peak} - x_1 = \frac{V_1}{\omega}\left[(2n - 1)\frac{\pi}{2} - (\phi_1 + \delta_1)\right] \; ; n = 1, 2, 3, \ldots$$

$$= \frac{(2n-1)V_1}{4f} \left[1 - \frac{2(\phi_1 + \delta_1)}{\pi(2n-1)} \right] \;; n = 1,2,3,\dots \quad (8.3)$$

These are the expressions for the peak amplitudes of the acceleration response and the locations of those peak acceleration responses on the initial slope of an *AGARD Repair Mat*. Conversely, if the length of the initial ramp is l_1, we know that the local extrema of the acceleration response will occur somewhere on the initial ramp for speeds:

$$V_1 \leq \frac{4fl_1}{(2n-1)\left[1 - \frac{2(\phi_1+\delta_1)}{\pi(2n-1)}\right]} \;; n = 1,2,3,\dots \quad (8.4)$$

Otherwise the peak acceleration responses on the initial slope will occur at the first corner or at the second cornerwhere the value is:

$$\bar{z}\Big|_{t=t_2^-} = R_1 e^{-\alpha\left(\frac{l_1\omega}{V}\right)} \sin\left(\frac{l_1\omega}{V} + \phi_1\right) \quad (8.5)$$

c. The Flat Area of a Repair Mat

We assume that angles θ_1, θ_2 are equal and opposite and that l_1, the length of the ramp, is small enough so that the speed over the initial slope is constant, $V_1 = V_2$. Then the acceleration response to the combined disturbances is:

$$\bar{z}(t)\Big|_{t>t_2} = R_2 e^{-\alpha\omega(t-t_2)} \sin\left[\omega(t-t_2) + \phi_2\right] \quad (3.4)$$

where

$$R_2 = \omega_0 V_1 |\theta_1| \sqrt{1 - 2e_{21}C_{21} + e_{21}^2}$$

$$\tan\phi_2 = \frac{\epsilon - e_{21}(S_{21} + \epsilon C_{21})}{1 - e_{21}(C_{21} - \epsilon S_{21})}$$

The acceleration response just after the second corner is:

$$\bar{z}_2\Big|_{t=t_2^+} = R_2 \sin\phi_2 \quad (8.6)$$

The local local extrema of the acceleration response on the flat part of the repair mat are given by:

$$\frac{R_2}{\sqrt{1 - \alpha^2}} e^{-\alpha\left[\frac{(2n-1)\pi}{2} - (\phi_2+\delta_2)\right]} \;; n = 1,2,3,\dots$$

and they occur when

$$\omega(t_{peak} - t_2) = \frac{(2n-1)\pi}{2} - (\phi_2 + \delta_2) \;; n = 1,2,3,\dots$$

This translates to distances of:

$$x_{peak} - x_2 = \frac{\tilde{V}}{\omega}\left[\frac{(2n-1)\pi}{2} - (\phi_2 + \delta_2)\right] \;; n = 1,2,3,\dots$$

$$= \frac{(2n-1)\tilde{V}}{4f}\left[1 - \frac{2(\phi_2+\delta_2)}{\pi(2n-1)}\right] \;; n = 1,2,3,\dots \quad (8.7)$$

where in this case $\tilde{V}$ is the average speed over the flat part of the repair mat. If the length of the flat part is l_2, we know that local extrema acceleration responses will occur somewhere on the flat part for speeds:

$$\tilde{V} \leq \frac{4fl_2}{(2n-1)\left[1 - \frac{2(\phi_2+\delta_2)}{\pi(2n-1)}\right]} \;; n = 1,2,3,\dots \quad (8.8)$$

Otherwise it will occur at the second or third corners.

d. Obtaining the Infinite Ramp Data from the Test

Because of the impossibility of experimentally developing an *Infinite Ramp*, it will be more practical to excite the oscillator with an *AGARD Bump* and then infer what the acceleration response would have been to an *Infinite Ramp*. We assume that we have excited the oscillator with an *AGARD Bump* and, therefore, we will know e_{21}, S_{21} and C_{21} and will have measured $R_2, \alpha, \omega, \phi_2$ in the equation:

$$\bar{z}(t)\Big|_{t>t_2} = R_2 e^{-\alpha\omega(t-t_2)} \sin\left[\omega(t-t_2) + \phi_2\right] \quad (3.4)$$

The potential amplitude R_1 can be obtained from:

$$R_1 = \frac{R_2}{\sqrt{1 - 2e_{21}C_{21} + e_{21}^2}} \quad (8.9)$$

Then the phase lag ϕ_1 can be obtained from:

$$Q = \frac{e_{21}S_{21}}{1 - e_{21}C_{21}} \quad (8.10)$$

$$\epsilon = \frac{\tan\phi_2 + Q}{1 - Q\tan\phi_2} \quad (8.11)$$

$$\tan\phi_1 = \epsilon$$
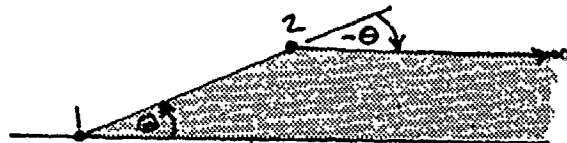
e. Guidelines for Nonlinear Calculations, AGILE Tests and Taxi Tests

We begin by calculating or measuring the acceleration response to an *AGARD Bump*
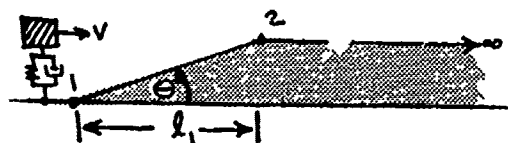
over a range of speeds V and angles θ. Since the acceleration response will undoubtedly not be purely in a single degree-of-freedom, we must process the test data to obtain separate values of R_2, α, ω and ϕ_2 for *each degree-of-freedom*. Then for each speed, angle and degree-of-freedom we calculate:

$$e_{21} = e^{-\alpha\omega(t_2-t_1)}; \quad C_{21} = \cos[\omega(t_2 - t_1)]$$

and we use Equations (8.9)-(8.11) to calculate R_1 and ϕ_1. A good test of our assumed linearity is to form $\frac{R_1}{V\theta}$. The values for each degree of freedom should be approximately independent of speed V or angle θ.

The next step should be to test the linear result that the Best/Worst *AGARD Bumps* will be those for which

$$\tilde{\lambda} = \frac{l_1\omega}{V} = n\pi - \alpha \; ; n = 1,2,3\dots$$

Since l_1 is fixed by the AGARD geometry, we can accomplish this variation by choosing the speeds to be:

$$V = \frac{l_1\omega}{n\pi - \alpha}$$

We can interpret the final slope of the *AGARD Repair Mat* between points x_3 and x_4
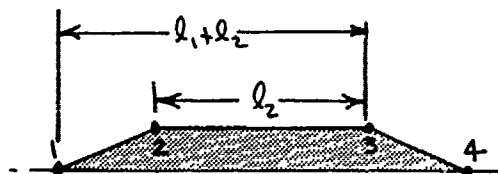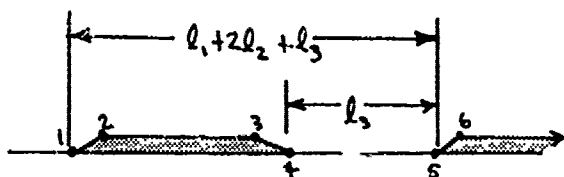
as just the negative of the initial slope; with the only distinction that it begins at a distance of $l_1 + l_2$ after the initial slope. Then we can search for the Best/Worst length of the repair mat by setting:

$$\tilde{\lambda} = \frac{(l_1 + l_2)\omega}{\tilde{V}} = n\pi - \alpha; \quad n = 1,2,3,\dots$$

where $\tilde{V}$ is the average speed over the distance between x_2 and x_3. In this case we have both the average speed $\tilde{V}$ and the length l_2 to use as variables.

Now we note that the total length of the *AGARD Repair Mat* is $2l_1 + l_2$ and assume that another repair mat is placed a distance l_3 behind the first mat.

Therefore, to look for the Best/Worst spacings we set:

$$\tilde{\lambda} = \frac{(2l_1 + l_2 + l_3)\omega}{\tilde{V}} = n\pi - \alpha; \quad n = 1,2,3\dots$$

where $\tilde{V}$ is the average speed between the two repair mats.

9. CONCLUSIONS

We have treated the dynamic response of an aircraft taxiing over runway disturbances, under the assumption that the gross aspects of the dynamic response can be found in the analysis of a linear, one degree-of-freedom system, excited by two successive disturbances. We have found:

a. There is a great deal that can be learned about the governing physics for aircraft dynamic response to taxi over damaged and repaired runways by examining the results of calculations with relatively simple, linear models.

81

b. The seemingly complicated time histories can be merely superpositions of relatively simple, time-phased events.

c. Relatively simple expressions are available for the potential amplitude (an upper bound) of the acceleration response excited by one or two disturbances. In the (not too) special case of *similar*, disturbances separated by a distance l, with nonconstant speeds and ramp angles, the expression for the potential amplitude R_2 is:

$$R_2 = \omega_0 \sqrt{(V_2 \theta_2)^2 + 2 V_2 \theta_2 (V_1 \theta_1 e_{21}) C_{21} + (V_1 \theta_1 e_{21})^2}$$

$$= \omega_0 V_2 |\theta_2| \sqrt{1 + 2\left(\frac{V_1 \theta_1 e_{21}}{V_2 \theta_2}\right) C_{21} + \left(\frac{V_1 \theta_1 e_{21}}{V_2 \theta_2}\right)^2}$$

where

$$e_{21} = e^{-a\tilde{\lambda}}$$

$$C_{21} = \cos \tilde{\lambda}$$

$$\tilde{\lambda} = l\omega/\tilde{V}$$

d. The effects of disturbance spacing and variable taxi speed are controlled by the reduced frequency, based on the average speed between disturbances:

e. One need not actually calculate the time histories to find the best/worst profiles and speeds, but can use the expressions for the potential amplitude R_2 and the BUMP MULTIPLIER $\frac{R_2}{R_1}$.

f. To maximize/minimize dynamic response a good approximation for $\tilde{\lambda}$ is

$$\tilde{\lambda} \approx \pi - \alpha$$

g. While damping obviously controls the dynamic response to the disturbances, the critical speeds and disturbance spacings are weak functions of damping.

h. These results can easily be extended from two disturbances to an arbitrary number of disturbances and multiple degree-of-freedom systems with multiple landing gear.

i. The results of calculations based on these linear methods should be compared with results from flight(taxi) tests, AGILE tests and nonlinear calculations. This is not to say that the linear results should be relied on to predict detailed loads; rather the question should be *do the simple linear models predict the critical speeds and spacings so that we can use them to guide our test programs and nonlinear solutions.*

FREQUENCY RESPONSE FUNCTIONS OF A NONLINEAR SYSTEM *

D. A. Dederman
T. L. Paez
L. L. Gregory
R. G. Coleman

Sandia National Laboratories
Albuquerque, New Mexico

The presence of nonlinear elements in a structural system can have a substantial effect on measures of structural response which characterize linear behavior. A form of nonlinearity frequently observed in complicated structures is the rattling nonlinearity that results from impact of structural elements. The objective of this investigation is to establish the effects on the frequency response function of a simple system caused by structural rattling. The study uses a Monte Carlo approach in conjunction with numerical response analysis and laboratory experiments to assess the characteristics of the system. It is shown that the presence of rattling components in a structural system tends to diminish amplification of motion at structural modal frequencies and introduce additional frequency response throughout the remainder of the excitation bandwidth.

INTRODUCTION

Many structural systems are subjected to dynamic environments during their service lives. To assess the behavior of proposed systems we model and analyze them using the methods of structural dynamics [1]. To assess the dynamic behavior of existing systems we run vibration tests. Typically, a variety of test measurements are recorded and analyzed to describe system character [2]. These measures include response time histories, modal parameters, frequency response functions, etc [3].

The linear system assumption is the simplest behavior to model. Therefore, the most frequently used measures of response behavior come from the linear theory [4]. Yet most structures exhibit some degree of nonlinear behavior. When we test a structure which is nonlinear it is often difficult to interpret the measures of response. Specifically, questions arise with regard to the system character obtained through data analysis. For example, the frequency response functions of a nonlinear system may not resemble those for a classical linear system.

This study investigates the frequency response functions of a specific nonlinear system using a Monte Carlo approach and laboratory experiments. In particular, the frequency response functions of a structure containing loose (potentially rattling) components are studied. The model used is a discrete, lumped mass two degrees of freedom system. One mass, m_1 is assumed rigid and base excited, while the second mass, m_2 slides freely between end constraints on mass one.

A random vibration approach is used to estimate the frequency response functions of the system under consideration [5]. This method is presented with numerical and experimental examples. Numerical examples are worked to investigate the effect of parametric variations in the system. Three parametric variations are studied. First, the effect of varying the distance available for mass two to slide between mass one's end constraints is investigated. Second, different base excitation levels are considered. The third variation involves using a coefficient of restitution which is less than one to compute the system's frequency response function.

ANALYSIS

The frequency response funct:ons of a structural system are a fundamental measure of system character. They can be used to establish modal frequencies, modal damping factors and mode shapes in linear systems. Further, they can be used to predict the response of linear systems to arbritrary excitations. When a system is slightly nonlinear its frequency response functions can still be used for these purposes, but the degree of accuracy in the modal characteristics and the response predictions is inversely proportional to the degree of nonlinearity. The objective of this investigation is to determine the effect of a rattling-type nonlinearity on the predicted frequency response functions of a simple structure when the linear random vibration approach is used to estimate the structure's frequency response function.

The acceleration frequency response function of a simple structure containing a rattling component is established using five major analysis steps. In the first step the equations of motion for the nonlinear system are defined. Second, the method for solving these equations of motion is established. Third, the equations for generating band-limited white noise excitation are developed. Next, formulas for estimating the autospectral density of the excitation and the cross spectral density between the excitation and response are written. The final step discusses using these spectral density computations in estimating the system's frequency response function.

This analysis approach was implemented using Fortran 77 on a personal computer. The procedure involved in implementing this solution on the computer is detailed.

The model chosen to investigate a structure containing rattling components is shown in Fig. 1. The model is a discrete, lumped mass two degrees of freedom system. Mass one, m_1, is assumed rigid and base excited. Mass two, m_2, is assumed to slide without friction between the end constraints on m_1. Mass two represents the system rattle mass.

In order to define the governing equations of motion for this model, a set of coordinate systems were selected as shown in Fig. 1. In this investigation the system response of particular interest is the acceleration response of mass one.

The major assumption for expressing the differential equations of motion for this system is that the system responds at all times in one of two modes. Specifically, masses m_1, and m_2 respond in one manner, governed by one pair of equations when they are not in contact; and masses m_1 and m_2 respond in a different manner,
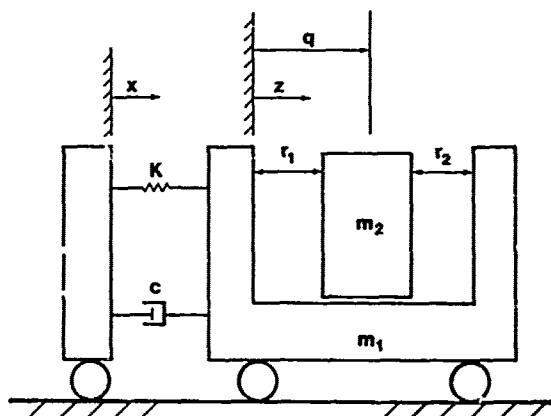
Fig. 1 - A simple structure containing a rattling component (r_1+ r_2= RGAP, which defines the rattle space).

governed by another set of equations when they contact. When the masses are not in contact, m_1 is assumed to behave as a linear, base excited single degree of freedom (SDF) system, and m_2 is assumed to move with constant velocity. When the masses contact, their initial and final velocities are related by a coefficient of restitution and the conservation of momentum.

The set of go erning equations of motion can be written for the two possible conditions which affect the response of mass one. For the case when m_1 and m_2 are not in contact, the equations of motion for m_1 and m_2 are independent and defined as follows:

$$\ddot{y} + 2\zeta\omega_n\dot{y} + \omega_n^2 y = -\ddot{x} \qquad (1)$$

$$\dot{q} = \text{constant} \qquad (2)$$

where,

$$y = z - x \qquad (3)$$

$$\omega_n = \sqrt{k/m_1} \qquad (4)$$

$$\zeta = c/(2m_1\omega_n) \qquad (5)$$

and,

$\ddot{x}$ = base acceleration

$\dot{q}$ = absolute velocity of mass m_2

z = absolute displacement of mass m_1

ω_n = natural frequency of system when no contact between m_1 and m_2

ζ = system viscous damping ratio.

and dots denote differentiation with respect to time.

84

The motions of m_1 and m_2 are dependent when a collision occurs. Assuming translational motion for m_1 and m_2 during the impact, an expression relating the velocities of the mass centers before and after impact based on the definition of coefficient of restitution is

$$(\dot{q}_f - \dot{z}_f) = e(\dot{z}_i - \dot{q}_i) \qquad (6)$$

where,

$\dot{q}_f$ = velocity of m_2 after impact

$\dot{q}_i$ = velocity of m_2 before impact

$\dot{z}_f$ = velocity of m_1 after impact

$\dot{z}_i$ = velocity of m_1 before impact

e = coefficient of restitution between m_1 and m_2.

Assuming the initial velocities and the coefficient of restitution between m_1 and m_2 are known, an additional equation is required to determine the mass velocities after impact. This additional equation is based on the requirement for conservation of momentum. It is

$$m_1\dot{z}_i + m_2\dot{q}_i = m_1\dot{z}_f + m_2\dot{q}_f \qquad (7)$$

This condition (describing an instantaneous change in motion when m_1 and m_2 collide) is the nonlinearity in our system.

A recursive response formulation was selected for estimating the time domain response of mass m_1. Since the structure behaves as a linear, base-excited, SDF system when the masses are not in contact, the relative displacement and velocity solution can be expressed as follows,

$$y(t) = \int_{t_o}^{t} h_1(t-\tau)(-\ddot{x}(\tau))d\tau +$$

$$e^{-\zeta\omega_n(t-t_o)}[A_1\cos \omega_d(t-t_o)+A_2\sin \omega_d(t-t_o)]$$
$$t \geq t_o \qquad (8)$$

$$\dot{y}(t) = \int_{t_o}^{t} h_2(t-\tau)(-\ddot{x}(\tau))d\tau +$$

$$e^{-\zeta\omega_n(t-t_o)}[B_1\cos \omega_d(t-t_o)+B_2\sin \omega_d(t-t_o)]$$
$$t \geq t_o \qquad (9)$$

where,

$$h_1(t) = \frac{e^{-\zeta\omega_n t}}{\omega_d} \sin \omega_d t, \qquad t \geq 0.0$$

$$= 0.0, \qquad t < 0.0 \qquad (10)$$

$$h_2(t) = e^{-\zeta\omega_n t}[\cos \omega_d t - \frac{\zeta}{\sqrt{1-\zeta^2}} \sin \omega_d t],$$
$$t \geq 0.0$$

$$= 0.0, \qquad t < 0.0 \qquad (11)$$

$$\omega_d = \omega_n\sqrt{1-\zeta^2} \qquad (12)$$

and A_1, A_2, B_1, B_2 are constants that depend on the displacement and velocity of the structure at time t_o.

Numerical expression of this time domain solution requires knowledge of the system base excitation, $\ddot{x}(t)$. To define a general representation of $\ddot{x}(t)$ an assumption of linear variation over small time steps is made. Specifically, it is assumed that in the time interval $(t_j, t+\Delta t)$ the excitation can be represented as

$$\ddot{x}(\tau) = \ddot{x}_j + [(\ddot{x}_{j+1} - \ddot{x}_j)/ \Delta t](\tau-t_j) \qquad (13)$$

where,

$\ddot{x}_j$ = base excitation at time t_j

$\ddot{x}_{j+1}$ = base excitation at time $t_j+\Delta t$

t_j = $j\Delta t$, $j=0,1,2,\ldots,$ is a discrete sequence of times.

For this analysis, $\ddot{x}(\tau)$ was chosen to be a band-limited, white noise base acceleration excitation with mean zero and normal distribution. Since an incremental time step approach is used to solve for the acceleration response of mass one, generation of a discretized base acceleration, $\ddot{x}_j$ is required. The method used to generate this random white noise excitation is derived from the discrete Fourier transform (DFT) definition and linear random vibration principles. By definition, the DFT expression for $\ddot{x}_j$ is

$$\ddot{x}_j = \sum_{k=0}^{N-1} X_k e^{i2\pi jk/N}, \qquad j =0,1,2,\ldots N-1 \qquad (14)$$

when X_k is expressed as

$$X_k = c_k e^{i\phi_k}, \qquad k =0,1,2,\ldots N-1$$

with

$$c_k = \sqrt{G_o\Delta f/2}, \qquad f_1 N t < k < f_2 N t$$

and
$$= 0.0, \qquad \text{elsewhere}$$

$$c_{N-k} = c_k, \qquad k = 1,2,\ldots,N/2$$

where,

f_1 = lover frequency band-limit of signal

f_2 = upper frequency band-limit of signal $\leq 1/(2\Delta t)$

G_o = constant spectral density amplitude, g^2/Hz.

Where the ϕ_K, $k = 1,2,\ldots,N/2$, are uniformly distributed random variables on $(-\pi,\pi)$, and

$$\phi_o = 0.0$$

$$\phi_{N-k} = -\phi_K , \qquad k = 1,2,\ldots,N/2$$

Then $\ddot{x}_j$, $j = 0,1,2,\ldots,N-1$, is a segment of band-limited white noise with duration $N\Delta t$, and range (f_1,f_2). The expressions for the corresponding velocity and displacement are

$$\dot{x}_j = \sum_{k=0}^{N-1} \frac{Xe^{i\phi_K} e^{i2\pi jk/N}}{[i2\pi k/(N\Delta t)]} \tag{15}$$

$$x_j = \sum_{k=0} \frac{-Xe^{i\phi_K} e^{i2\pi jk/N}}{[i2\pi k/(N\Delta t)]^2} \tag{16}$$

When the excitation is specified, as in equations (13) and (14), the integrals in equations (8) and (9) can be evaluated and the response can be expressed (assuming no collisions occur in (t_j,t_{j+1})) as

$$\begin{Bmatrix} y_{j+1} \\ \dot{y}_{j+1} \end{Bmatrix} = \begin{bmatrix} a_{11} & a_{12} \\ a_{21} & a_{22} \end{bmatrix} \begin{Bmatrix} y_j \\ \dot{y}_j \end{Bmatrix} + \begin{bmatrix} b_{11} & b_{12} \\ b_{21} & b_{22} \end{bmatrix} \begin{Bmatrix} \ddot{x}_j \\ \ddot{x}_{j+1} \end{Bmatrix} \tag{17}$$

where the elements of the $\underline{A}$ and $\underline{B}$ matrices are

$$a_{11} = e^{-\zeta\omega_n\Delta t}[\zeta\omega_n\sin\omega_d\Delta t + \omega_d\cos\omega_d\Delta t]/\omega_d \tag{18}$$

$$a_{12} = e^{-\zeta\omega_n\Delta t}[\sin\omega_d\Delta t]/\omega_d \tag{19}$$

$$a_{21} = -e^{-\zeta\omega_n\Delta t}[\omega_n^2/\omega_d]\sin\omega_d\Delta t \tag{20}$$

$$a_{22} = e^{-\zeta\omega_n\Delta t}[\cos\omega_d\Delta t - (\zeta\omega_n/\omega_d)\sin\omega_d\Delta t] \tag{21}$$

$$b_{11} = \{e^{-\zeta\omega_n\Delta t}[(1-2\zeta^2-\zeta\omega_n\Delta t)\sin\omega_d\Delta t - (2\zeta\sqrt{1-\zeta^2}+\omega_d\Delta t)\cos\omega_d\Delta t] + 2\zeta\sqrt{1-\zeta^2}\} / (\omega_n^2\omega_d\Delta t) \tag{22}$$

$$b_{12} = \{e^{-\zeta\omega_n\Delta t}[-(1-2\zeta^2)\sin\omega_d\Delta t + (2\zeta\sqrt{1-\zeta^2})\cos\omega_d\Delta t] + \omega_d\Delta t - 2\zeta\sqrt{1-\zeta^2}\} / (\omega_n^2\omega_d\Delta t) \tag{23}$$

$$b_{21} = \{e^{-\zeta\omega_n\Delta t}[(\zeta\omega_n+\omega_n^2\Delta t)\sin\omega_d\Delta t + \omega_d\cos\omega_d\Delta t] - \omega_d^2\} / (\omega_n\omega_d\Delta t) \tag{24}$$

$$b_{22} = \{-e^{-\zeta\omega_n\Delta t}[\zeta\omega_n\sin\omega_d\Delta t + \omega_d\cos\omega_d\Delta t] + \omega_d^2\} / (\omega_n\omega_d\Delta t) \tag{25}$$

This formulation of response is discussed in reference [6].

The displacement of mass two as a function of time, when no collision occurs, comes from integrating equation (2). The absolute displacement of mass two expressed at discrete time, t_j is

$$q_j = q_o + \dot{q}_j(t_j-t_o) \tag{26}$$

where,

q_o = absolute displacement of mass two at time t_o

$\dot{q}_j$ = absolute velocity of mass two at time t_j

t_o = the system initial starting time or the time the most recent impact between m_1 and m_2 occured (after the first impact).

Using the base excitation and associated velocity and displacement equations (14)-(16), we can compute the absolute response of mass one from equations (1), (3), and (17). These absolute responses are

$$\ddot{z}_{j+1} = -\zeta\omega_n\dot{y} - \omega_n^2y \tag{27}$$

$$\dot{z}_{j+1} = \dot{y}_{j+1} + \dot{x}_{j+1} \tag{28}$$

$$z_{j+1} = y_{j+1} + x_{j+1} \tag{29}$$

In addition, recursive equation (17) was made realizable by assuming initial conditions for the system uch that m_1 and m_2 were not in contact at time zero. This condition was enforced by setting the initial velocity and displacement of mass two equal to the arbitrary initial absolute velocity and displacement of

mass one, $\dot{z}_o$, and z_o, respectively.

The approach used to analyze the response when contact occurs between masses one and two involves a multiple step computation. Consider the time interval (t_j, t_{j+1}). First, given that all response measures are known at t_j, the linear response is estimated at t_{j+1} using equations (15) – (17) and (26) – (29). The inequalities

$$q_{j+1} - z_{j+1} \leq 0.0$$

$$q_{j+1} - z_{j+1} \geq RGAP \qquad \text{(see Fig. 1)}$$

are checked and if either one is satisfied then an impact between m_1 and m_2 has occurred in (t_j, t_{j+1}) and the response computed at t_{j+1} must be corrected. To do this, the time when

$$q_k - z_k = 0.0 \qquad (30)$$

$$q_k - z_k = RGAP \qquad (31)$$

(depending on which of the above corresponding inequalities is satisfied) must be estimated. The q_k and z_k are displacements at a time t_k equal to t_j plus $\Delta\tau$, where $\Delta\tau$ is in the interval $(0, \Delta t)$. The collision time is estimated by approximating $z(\tau)$, $t_j < \tau < t_{j+1}$, as a quadratic. The coefficients of the quadratic are evaluated by setting

$$z(t_j) = z_j , \qquad z(t_{j+1}) = z_{j+1}$$

and

$$\ddot{z}(t_j + (\Delta t/2)) = (\ddot{z}_j + \ddot{z}_{j+1})/2$$

The values on the right sides are known from the initial linear computation. A linear expression, equation (26), is used for computing q_k. Now the quadratic approximation for $z(\tau)$ and the linear expression for q_k are used in equations (30) or (31) to evaluate t_k, the collision time.

Next, the impact velocities of m_1 and m_2 must be estimated. Recalling the assumption for the velocity of m_2 from equation (2),

$$\dot{q}_i = \dot{q}_j \qquad (32)$$

To estimate the impact velocity of m_1 we return to recursive equation (17) and compute the response using a time step equal to the newly computed time of collision, $\Delta\tau$ (the matrices A

and B must be modified based on $\Delta\tau$. In addition, the base acceleration at t_{j+1} is modified by linear interpolation to be

$$\ddot{x}_{j+\Delta\tau} = \ddot{x}_j + \Delta\tau * [(\ddot{x}_{j+1} - \ddot{x}_j)/\Delta t] \qquad (33)$$

In order to compute the absolute velocity $\dot{z}_i$, a similar interpolation is used for calculating the base velocity at the time of collision. This estimate is

$$\dot{x}_{j+\Delta\tau} = \dot{x}_j + \Delta\tau * [(\ddot{x}_j + \ddot{x}_{j+\Delta\tau})/2.0] \qquad (34)$$

Thus, the impact velocity for mass one is

$$\dot{z}_i = \dot{y}_{j+\Delta\tau} + \dot{x}_{j+\Delta\tau} \qquad (35)$$

The final velocities after impact are computed from equations (6) and (7). Rearranging terms and solving for the final velocity of mass one yields,

$$\dot{z}_f = m_2[e(\dot{q}_i - \dot{z}_i) + m_1\dot{z}_i + m_2\dot{q}_i]/(m_1 + m_2) \qquad (36)$$

and

$$\dot{q}_f = \dot{z}_f - e(\dot{q}_i - \dot{z}_i) \qquad (37)$$

These new mass velocities are then used to recompute the response at time t_{j+1}. This requires computation of new matrix A and B coefficients for the time between the collision and the end of the interval in equation (17). The conditions at the time of collision are used to represent time t_j in equation (17). Once the response is computed at t_{j+1}, the original A and B matrix coefficients are used to compute responses following t_{j+1} until another collision occurs. The process is repeated as outlined before with each impact until all N response calculations have been made. This same logic format was used to handle cases when more than one impact per time interval occurred.

After the time domain response of mass one has been computed over the sample period, the next step towards estimating the system's (m_1) acceleration frequency response function involves spectral density estimation. Specifically, the autospectral density of the base acceleration and the cross spectral density between the base acceleration and the response acceleration of mass one are computed. These estimates are defined using the following DFT relationships,

$$\bar{G}_{XX}(f) = (2/TN_d) \sum_{k=1}^{N_d} \left| X_k(f,T) \right|^2 \qquad (38)$$

87

$$\bar{G}_{XZ}(f) = (2/TN_d) \sum_{k=1}^{N_d} [\bar{X}_k^*(f,T) \; \bar{Z}_k(f,T)] \qquad (39)$$

where,

$\bar{X}_k(f,T)$ = DFT of base acceleration

$\bar{Z}_k(f,T)$ = DFT of response acceleration of

    mass one

  T = sample period of analysis

  N_d = the number of ensemble averages.

The equation for estimating the acceleration frequency response function magnitude for mass one is

$$|FRF| = \left| \frac{\bar{G}_{XX}(f) \; \bar{G}_{XZ}^*(f)}{\bar{G}_{XX}(f) \; \bar{G}_{XX}^*(f)} \right|^{1/2} \qquad (40)$$

This analysis approach is implemented using fortran 77 on a personal computer. The results of this implementation are presented in the numerical examples section of this investigation.

EXPERIMENTS

Experiments were conducted to validate the analysis approach used to compute the frequency response function of a simple, nonlinear structure. The structure selected for verifying the analysis model is illustrated in Fig. 2. This structural system consists of two 12 x 1.688 x 0.125 inch (304.8 x 17.463 x 3.175 mm) aluminum beams, fastened in parallel with a lumped mass configuration of threaded stock, nuts, washers and a steel plate rattle mass. This lumped mass configuration is attached at the midpoints of both beams. The beams are preloaded at each end and fastened to the shaker armature such that the armature motion is transmitted through these retaining bolts to the system. The dimensions of the rattle mass are 2 x 2 x 0.25 inch (50.8 x 50.8 x 6.35 mm). Mass one is 0.249 kg and mass two is 0.117 kg.
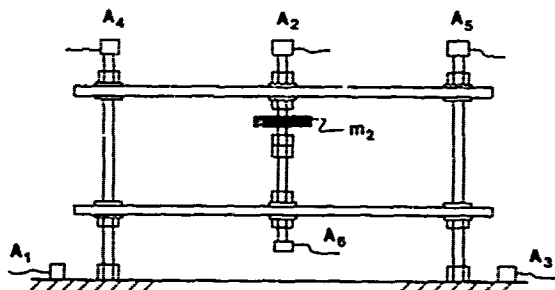
Fig. 2 - The experimental test structure.

The experimental objective was to measure the acceleration frequency response function of the lumped mass when the plate rattle mass was held rigid and when the plate mass was allowed to rattle. A linear, SDF system condition was represented when the rattle mass was fixed. The nonlinear condition was generated when the two retaining nuts around the plate mass were loosened to create a rattle gap.

The experimental approach was to excite the structural system with a band-limited white noise acceleration excitation. Using a digital random vibration control system, single point control on the armature acceleration was monitored to generate the desired base acceleration autospectral density. Six accelerometer measurements were recorded during each test (see Fig. 2). Two accelerometers were mounted on the armature and two accelerometers were mounted on the tops of the retaining bolts at the ends of the beams. The other two accelerometers were mounted on the ends of the threaded stock. This was where the lumped mass acceleration of mass one was measured for later comparison with the analysis. All accelerometers were piezoelectric type transducers. Response measurements were recorded on analog FM magnetic tape during testing.

The data were analyzed using standard digital signal analysis procedures applicable to linear random vibration testing. The test system acceleration responses were analyzed through estimation of their associated transfer function magnitudes and coherences. These measures of system character were made with respect to the spectrum of the test system control accelerometer. The data were analyzed with an effective noise bandwidth of 2.00 Hertz (equivalent rectangular bandpass filter width).

Initial testing verified the simple structure responded as a linear, SDF system when the rattle plate was held fixed. The structure's first bending mode was estimated to be at 138 Hertz.

Using feeler gages, rattle gaps of 0.005 inch (0.127 mm), 0.010 inch (0.254 mm), and 0.020 inch (0.508 mm) were introduced into the test setups. Numerous experiments were performed with these gaps over flat base acceleration autospectral density levels ranging from 0.000001 g**2/Hz to 0.01 g**2/Hz. The frequency bandwidth of these excitation spectrums was defined from 5 Hertz to 300 Hertz for all experiments.

Several observations may be made upon review of the system's frequency response functions. Fig. 3 illustrates how the system frequency response function is affected by various base excitation autospectral density levels for a constant 0.020 inch rattle gap. The primary effects are the reduction in the system's peak amplification and the smearing of the amplification curve with increasing base

autospectral density levels. In addition, the superposition of additional frequency response appears throughout the analysis bandwidth of the transfer function. The effect on the frequency response function caused by varying the system rattle gap and holding the base autospectrum constant is shown in Fig. 4. A similar loss in amplification is observed. However, this change is approximately the same for all three rattle gaps at this test level.

AUTOSPECTRAL DENSITY EXCITATION COMPARISON
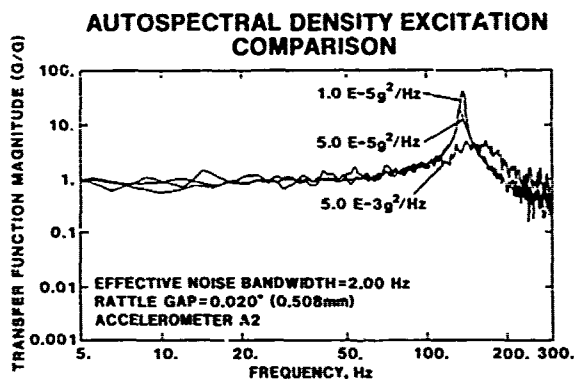
Fig. 3 - Base excitation autospectral density comparison.

RATTLE GAP COMPARISON
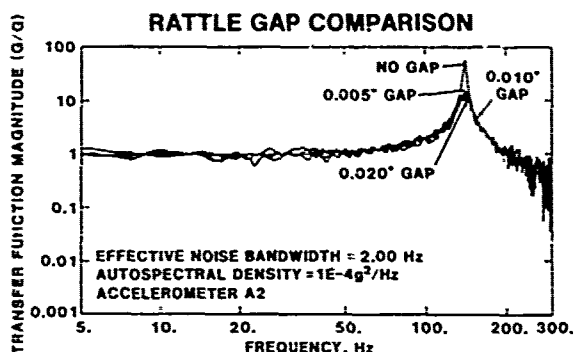
Fig. 4 - Rattle gap comparisons.

NUMERICAL EXAMPLES

Computer generated, system model responses are presented in this section. The numerical examples discussed are based on three parametric variations in the system analysis. The first example investigates the response of mass one when mass two is allowed to rattle in four different system configurations. The configurations are a no gap (m_2 fixed) condition, a 0.005 inch (0.127 mm) gap, a 0.010 inch (0.254 mm) gap, and a 0.020 inch (0.508 mm) gap. These particular intervals were selected to compare numerical analysis results with experimental results. The second example investigates the amplitude dependence of the system frequency response function when the system is excited at different autospectral density levels for a 0.020 inch rattle gap. The final example looks at the effect of modelling the mass collisions as not perfectly elastic ($e \neq 1$).

These numerical examples are generated by defining specific computer program input variables. Example model parameters were assigned values based on the experimental structure tested in the laboratory and the analysis parameters were chosen based on parameter values used in the laboratory analysis. The system model constants measured from the experimental structure and the data analysis constants are,

1. Model masses: $m_1 = 0.249$ kg $m_2 = 0.117$ kg
2. Linear system damping ratio: $\zeta = 0.01$
3. Linear system natural frequency: $f_n = 138$ Hz
4. Frequency step: $\Delta f = 1.00$ Hz
5. Nyquist Frequency: $f_{NYQ} = 1024$ Hz
6. Base excitation bandwidth: BW $= 295$ Hz
7. Coefficient of Restitution: $e = 1.0$
8. Ensemble averages us   o compute
   system frequency   ,unse function: M $= 20$

The linear system (no gap) case defines m_1 equal to m_1 plus m_2 and m_2 equals zero.

The time domain response records are 2048 samples over a one second time interval. These response records were all generated with the same initial conditions on masses one and two as described in the analysis section.

An autospectral density amplitude of 0.0001 g**2/Hz was used to generate a repeatable base acceleration for comparison of rattle gap effects on the system frequency response function. This base acceleration for the first ensemble average is shown in Fig. 5. Figures 6 and 7 illustrate the associated response accelerations of mass one computed at each discrete time step for a linear and nonlinear analysis. It should be noted that Fig. 7 does not show the collision responses which occur within the time step interval. These examples assume a delta function represents the mass acceleration during impact.

89

TIME DOMAIN SYSTEM BASE EXCITATION

RGAP=0.508mm (.020"); N = 2048; DR=0.01
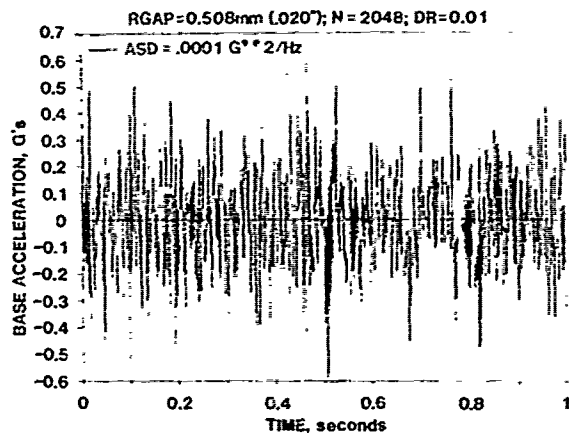
Fig. 5 - Numerically generated base
excitation (autospectral density
equal to 0.0001 G**2/Hz).

TIME DOMAIN NONLINEAR SYSTEM RESPONSE

RGAP = 0.508mm (.020"); N = 2048; DR = 0.01
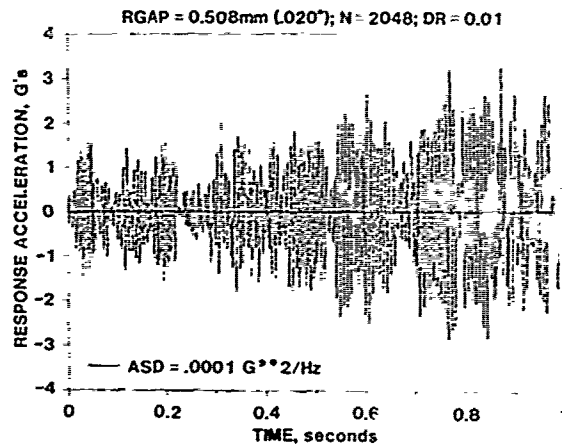
Fig. 7 - Nonlinear model response
acceleration from base excitation
in Fig. 5.

Figures 8 through 10 are graphical
comparisons of the frequency response function
magnitudes for a specific rattle gap interval
and the linear SDF case. The ensemble average
number of impacts between mass one and mass two
during a one second analysis time were 58, 109,
and 175 for Figures 8, 9, and 10, respectively.
As expected, the average number of impacts
increased as the rattle gap interval decreased
from 0.020 inch (Fig. 8) to 0.005 inch (Fig.
10).

Several primary rattle gap effects on the
frequency response function can be observed by
inspection of these graphs. First, a reduction
in the system's peak amplification is observed.
This reduction is greatest for the 0.010 inch
and 0.005 inch rattle gap intervals. Second,
the systems peak amplification response has
shifted frequency and several new peaks are
present. Next, a general spreading in the
amplification curve's sharpness is shown in all
cases. Fourth, the frequency response function
is increased at frequencies away from the
natural frequency of the linear system. The
final effect is found at low frequencies where
the response intercept has shifted upwards from
1.0 to 1.5. As the rattle gap is diminished, a
general smoothing in the response curve is seen
over the 10 to 35 Hertz frequency band.

TIME DOMAIN LINEAR SYSTEM RESPONSE

RGAP = 0.508mm (.020"); N = 2048; DR = 0.01

Fig. 6 - Linear model response acceleration
from base excitation in Fig. 5.

Fig. 11 presents the associated coherence
functions for the linear, 0.005 inch and 0.020
inch rattle gap responses. These curves show
the loss in unity coherence with an increasing
number of collisions between masses.

SYSTEM RATTLE GAP COMPARISON

ASD = 1.0E-4G SH; M = 20; f(Hz) = 138; DR = 0.01

NO GAP

0.020" (0.508mm) GAP
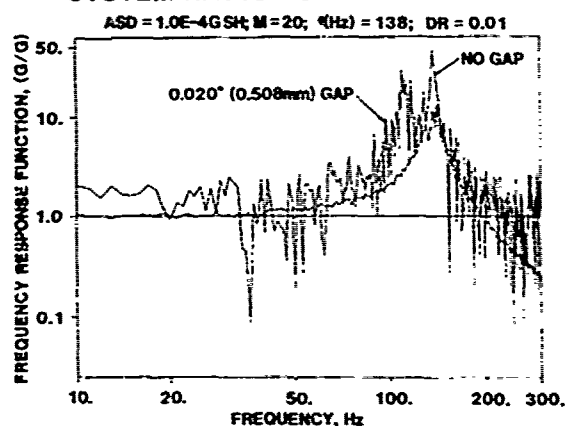
Fig. 8 - The system response with a 0.020
inch (0.508 mm) rattle gap.

SYSTEM RATTLE GAP COMPARISON

ASD = 1.0E-4G SH; M = 20; f(Hz) = 138; DR = 0.01

NO GAP

0.005 (0.127mm) GAP
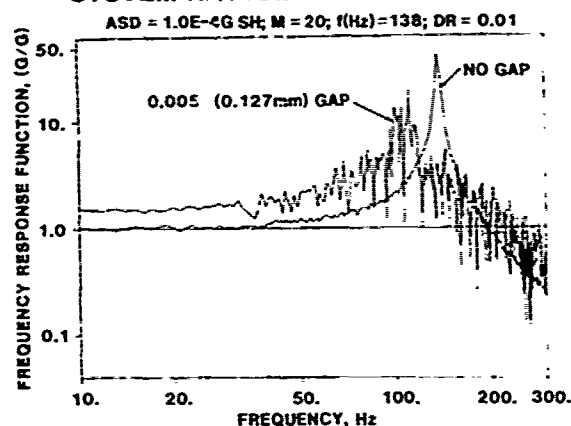
Fig. 10 - The system response with a 0.005
inch (0.127 mm) rattle gap.

SYSTEM RATTLE GAP COMPARISON

ASD = 1.0E-4G SH; M = 20; f(Hz) = 138; DR = 0.01

NO GAP

0.010" (0.254mm) GAP
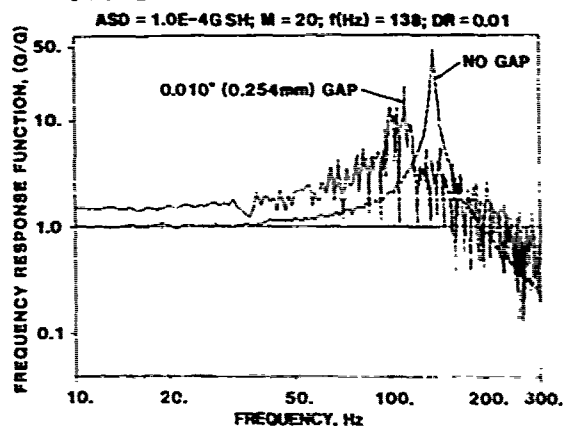
Fig. 9 - The system response with a 0.010
inch (0.254 mm) rattle gap.

SYSTEM RATTLE GAP COMPARISON

ASD = 1.0E-4G SH; M = 20; f(Hz) = 138; DR = 0.01

NO GAP

0.020" GAP

0.005" GAP
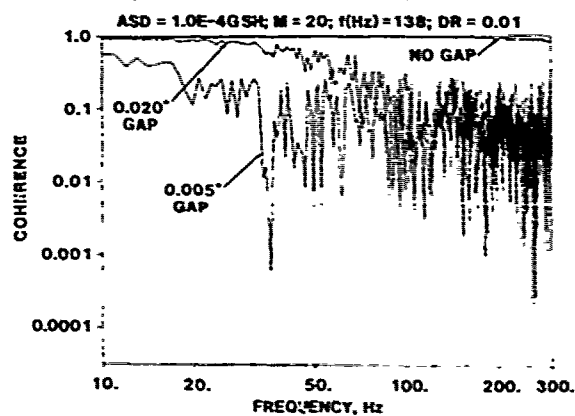
Fig. 11 - Coherence functions for the
rattle gaps compared in Figures
8 through 10.

91

The frequency response effects of exciting the system in a 0.020 inch rattle gap configuration at base excitation levels of 0.000005 g**2/Hz (5.0E-6) and 0.0000055 g**2/Hz (5.5E-6) are shown in Figures 12 and 13. The ensemble average number of impacts per second of excitation is 7 and 9 for Figures 12 and 13, respectively. However, while the average number of impacts for the lower level excitation is indicative of all the individual records, the higher level excitation average number of impacts is not. Specifically, the range of impacts per run at 5.0E-6 was between 0 and 12 unlike the range of impacts per run at 5.5E-6 which was between 0 and 124. With this transition, the shape of the frequency response function begins to change.

Fig. 12 shows a loss in peak amplification and the superposition of additional frequency response throughout the frequency bandwidth. Fig. 13 shows similar results but the amplification curve has spread out over a larger frequency range and multiple response peaks are present. In addition, the peak amplification no longer occurs at 138 Hertz but is now shifted to approximately 105 Hertz. In this example there were two runs (among a total of 20 analyzed) in which approximately 105 impacts occurred during the one second response. The associated coherence functions for these base excitation levels are shown in Fig. 14. Again, a loss in unity coherence appears directly proportional to the number of collisions per sample period.

BASE ASD AMPLITUDE COMPARISON

RGAP = 0.020"; M=20; f(Hz) = 138; DR = 0.01
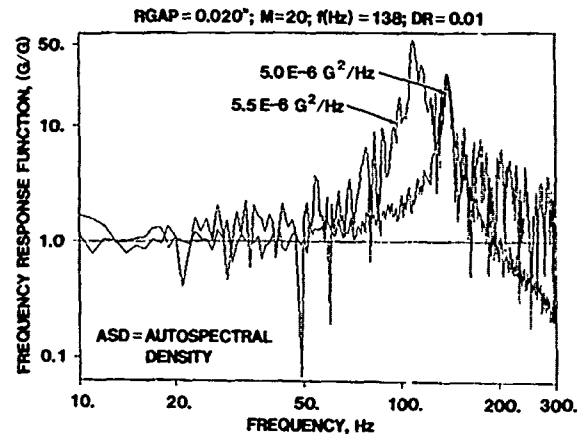
Fig. 13 - System response comparisons
Between two excitation levels
for a 0.020 inch (0.508 mm) gap.

BASE ASD AMPLITUDE COMPARISON

RGAP = 0.020"; M = 20; f(Hz) = 138; DR=0.01
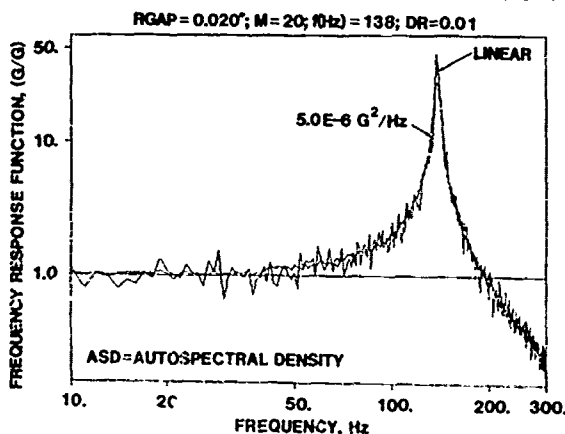
Fig. 12 - System response for a 0.020 inch
(0.508 mm) gap from a 5.0E-6
G**2/Hz autospectral density
excitation.

BASE ASD AMPLITUDE COMPARISON

RGAP = 0.020"; M = 20; f(Hz) = 138; DR=0.01
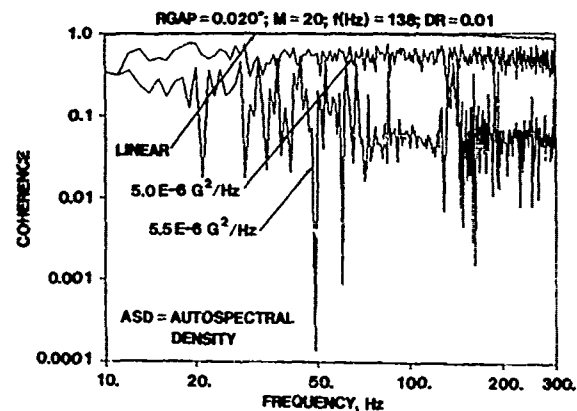
Fig. 14 - Associated coherence functions
for excitation comparisons in
Figures 12 and 13.

The final numerical example investigates the use in analysis of a coefficient of restitution not equal to one. Results obtained using coefficients of restitution equal to 0.75 and 0.90 are presented. A base excitation level of 0.0001 g^{**2}/Hz (1.0E-4) and a 0.020" rattle gap were used in this example.

Fig. 15 and Fig. 16 are the frequency response functions for coefficient of restitution values of 0.75 and 0.90, respectively. Recall Fig. 8 is the same analysis system but used a perfectly elastic collision assumption. Fig. 15 is similar to Fig. 8 but two distinct differences are observed. First, the additional frequency response over the frequency bandwidth has been attenuated in Fig. 15. Second, the peak amplification occurs at the linear system peak amplitude frequency value. This peak amplification has doubled relative to the response amplitude at this frequency (138 Hz) in Fig. 8. The ensemble average number of impacts

in Fig. 15 is 41. The range of impacts per second is 23 to 94.

Fig. 16 also presen several different observations with respect Fig. 8. Amplitude similarities at frequencies between 10 and 35 hertz are observed but the curve in Fig. 16 is much smoother. The additional frequency response in Fig. 8 is significantly attenuated over the remaining analysis frequency bandwidth in Fig. 16. The peak amplification curve is not spread but closely follows the linear system response except for the actual peak. The actual peak amplification is approximately 12 to 1. The response characterized by Fig. 16 had an ensemble average of 35 impacts per second. The number of impacts in each run was fairly uniform with a range of 25 to 48 impacts per second. The low frequency amplitude intercept at 1.5 appears to roll off at approximately 35 Hertz. The coherence functions for these coefficient of restitution comparisons are given in Fig. 17. The coherence for e equal to 0.9 is less than unity but not as poor as for e equal to 0.75.

COEFFICIENT OF RESTITUTION COMPARISON

RGAP = .508mm; ASD = 1.0E-4; f = 138 Hz; DR = .01

COEFFICIENT OF RESTITUTION COMPARISON

RGAP = .508mm; ASD = 1.0E-4; f = 138 Hz; DR = .01

Fig. 15 – System frequency response for a coefficient of restitution equal to 0.75.
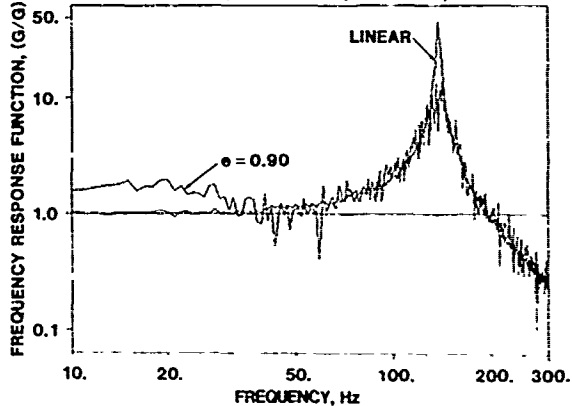
Fig. 16 – System frequency response for a coefficient of restitution equal to 0.90.

93

COEFFICIENT OF RESTITUTION
COMPARISON

RGAP = .508mm; ASD=1.0E-4; f = 138 Hz; DR = 0.1
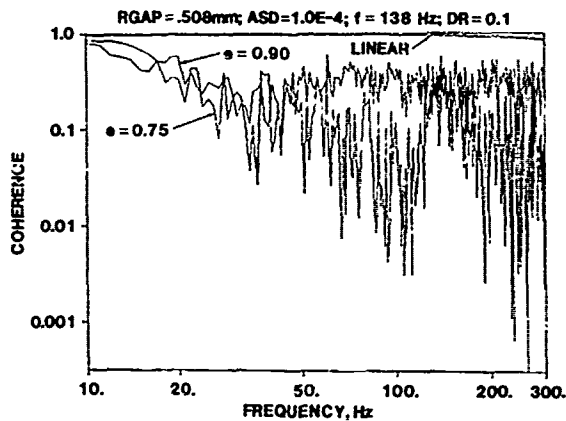
Fig. 17 - Coherence functions for model
responses in Figures 15 and 16.

CONCLUSIONS

This study investigated the frequency response functions of a simple structure containing a rattling component. Parametric variations in system base excitation levels, rattle gap configurations, and coefficient of restitution values were analyzed using a Monte Carlo numerical approach. Experiments were conducted to verify the model's predictions for this type of nonlinear structural system. Five major conclusions come from this investigation.

First, when a structural system is excited so that loose components begin to rattle, there is a reduction in the linear system peak frequency response amplification. This response effect occurs because motion is transferred between the colliding masses and momentum must be conserved. In order for mass two to experience an increase in motion, mass one must experience a decrease in motion. This results in a reduction in the frequency response function amplification for mass one.

Second, the force between masses one and two was modelled, in this analysis, as a delta function at the time of impact. This superimposes delta functions on the acceleration response at the times of impact. (In real structures impacts between structural elements generate short duration forces at impact points. These excite responses at other points on the structure, and these responses may resemble impulse response functions whose characteristics depend on system parameters, points of impact and measurement.) These superimposed delta functions have Fourier transforms which tend to be flat, therefore, the frequency response function tends to increase at all frequencies,

establishing a "whitening" effect related to rattling. This effect is also reflected as a smearing of peaks in the frequency response function.

The third conclusion is that reducing the coefficient of restitution below one has an averaging effect on the rattling phenomenon. Specifically, when the coefficient of restitution is one, there are many situations where parameters can be chosen such that in some numerical experiments much rattling occurs. When the coefficient of restitution is reduced to a realistic level the amount of rattling, while random, tends to be uniform throughout any ensemble of numerical experiments.

The fourth conclusion is that the presence of rattling in the structural response tends to diminish the coherence between excitation and response below unity. The decrease in coherence is proportional to the amount of rattling.

The final conclusion is that modelling the impacts between masses one and two using a coefficient of restitution equal to 0.9 produced a reasonable estimate of the experimental results except at low frequencies.

REFERENCES

[1] William T. Thomson, Theory Of Vibration With Applications, second edition. Prentice-Hall, New Jersey, 1981

[2] "Digital Vibration Control System 5427A", Hewlett-Packard, 1979

[3] Cyril M. Harris and Charles E. Crede, Shock & Vibration Handbook, second edition. McGraw-Hill, New York, 1976

[4] Y. K. Lin, Probabilistic Theory Of Structural Dynamics, McGraw-Hill, New York, 1967

[5] Julius S. Bendat and Allan G. Piersol, Engineering Applications Of Correlation And Spectral Analysis, John Wiley & Sons, New York, 1980

[6] Roy R. Craig, Jr., Structural Dynamics An Introduction To Computer Methods, pp. 139-146. John Wiley and Sons, New York, 1931

94

SYSTEM CHARACTERIZATION IN NONLINEAR RANDOM VIBRATION

Thomas L. Paez
Dan L. Gregory

Sandia National Laboratories
Albuquerque, New Mexico

Linear structural models are frequently used for structural system characterization and analysis. In most situations they can provide satisfactory results, but under some circumstances they are insufficient for system definition. The present investigation proposes a model for nonlinear structure characterization, and demonstrates how the functions describing the model can be identified using a random vibration experiment. Further, it is shown that the model is sufficient to completely characterize the stationary random vibration response of a structure that has a harmonic frequency generating form of nonlinearity. An analytical example is presented to demonstrate the plausibility of the model.

Introduction

Experimental identification of structural systems usually employs a linear model for the structure. The frequency response function of a linear system can be identified using either a deterministic analysis or a probabilistic analysis with random excitation. When the physical system being tested is truly linear then use of the linear model and analysis are appropriate. Further, when the system is slightly nonlinear a reasonable representation of system behavior can, in some senses, be established with the linear model. If the identified model is used for prediction of response or for the computation of the excitation that causes a specific response, then the analysis may, remain satisfactory as long as the nonlinearity effects are negligible.

The procedures commonly used for the identification of the frequency response functions of linear systems involve averaging operations. For example, the stationary random vibration procedure for estimation of the frequency response function (FRF) requires the generation and measurement of a random excitation. This excites structural response which is then measured at points of interest. The measured excitation is used to estimate the auto spectral density of the excitation; the excitation and responses are then used to estimate the cross spectral densities between the excitation and responses. Each cross spectral density is ratioed with the excitation auto spectral density to establish an estimate for the structural FRFs at the points of interest. Details of the procedures described above are given in References 1, 2 and 3.

Modeling and identification of nonlinear systems, however, is not as straightforward as the procedure outlined in the previous paragrph. The literature contains many models for specific types of nonlinear structural systems and describes approaches for computing their responses when the excitation is defined. See, for example, References 4 and 5. In some cases, experimental techniques useful in the identification of system parameters are described. However, the difficulty with using such models in general applicatons is that it is not usually easy to ascertain that a structural system has a nonlinearity that is appropriately modeled with a specific parametric form, and it is usually not clear what error is introduced when one nonlinear model is used to simulate a system with a different form of nonlinearity. This problem has been avoided by the use of the Volterra model for nonlinear systems. This is a nonparametric model that characterizes nonlinear systems using higher order impulse response functions and their Fourier transforms. This type of model and its identification is described, for example, in References 6, 7 and 8. The shortcoming of this model appears to be its inability to model frequency generating forms of nonlinearity.

The harmonic frequency generating form of nonlinearity is one that is commonly seen in practice. This form of nonlinearity is related to harmonic distortion of motion at frequencies where motion is substantial, such as modal frequencies. Response in a nonlinear, harmonic generating system often shows substantial power at a particular fundamental frequency, and some fractional level of that power at odd multiples of the fundamental, whether or not structural excitation power is applied at the higher frequencies. The frequencies where a nonlinear system shows signal content in the response are related to the shapes of the displacement and velocity restoring force functions. The harmonic frequency generating form of nonlinearity appears often in random vibration tests and causes difficulty in system characterization and test control.

The present investigation establishes a model for nonlinear, harmonic generating systems. It is shown first that the model can be identified using a random vibration approach similar to that used in linear system analysis. Second, it is shown that once the system is identified the model can be used to establish the response characteristics for random excitation. An example demonstrates the use of the model.

The Nonlinear Model and Its Identification through Random Vibration Tests

The model established in this investigation is for a nonlinear, harmonic generating system. It is a model that can be used to describe the behavior of a structure which, for a mechanical reason, when excited at a particular frequency, executes response not only at the excitation frequency, but also at harmonics of that frequency. Many real structures display this characteristic. The model is established first and discussed briefly. Then the method for identification of the functions in the model using a random vibration test is established.

Consider a nonlinear, harmonic generating system where the Fourier transform of the response is represented

$$Z(\omega_i) = \sum_{j=1}^{M} \sum_{k=0}^{n} H_j(\omega_k, \omega_i) \, (X(\omega_k))^j$$

$$i=0,\ldots,n \quad (1)$$

$Z(\omega_i)$ is the Fourier transform of the response at frequency ω_i. $X(\omega_k)$ is the Fourier transform of the excitation at frequency ω_k. $H_j(\omega_k, \omega_i)$ is an element in the sequence of coefficients that characterize the structure; the coefficients are deterministic and independent of the excitation, and might be thought of as forming a harmonic

generating transfer function. This model generates a response component, characterized by magnitude and phase, at frequency ω_i as a complex valued, algebraic, power function of excitation components at frequencies ω_k, $k=0,\ldots,n$. The $H_j(\omega_k, \omega_i)$ are coefficients of the power function. A special case of this is the linear excitation - response case. This occurs when $N=1$ and the $H_j(\omega_k, \omega_i)$ are zero except when $\omega_k = \omega_i$. After the $H_j(\omega_k, \omega_i)$ are established using measured excitation and response, the representation (1) can be used to predict the response of the structure to random excitation. Further, the coefficients serve as a descriptor of structural behavior.

A method for establishing the $H_j(\omega_k, \omega_i)$ is now developed. Let the excitation be a zero mean, stationary, normal random process, $(X(t), -\infty < t < \infty)$. Let $X(\omega_k)$ represent the discrete Fourier transform (DFT) of a segment of the excitation whose duration is T seconds. Let the excitation be defined such that all its frequency components are uncorrelated. Multiply both sides of (1) by $(X^*(\omega_\ell))^m$, the mth power of the complex conjugate of $X(\omega_\ell)$, and then take the expected value on both sides of the equation. The result is

$$E(Z(\omega_i)(X^*(\omega_\ell))^m)$$
$$= \sum_{j=1}^{M} \sum_{k=0}^{n} H_j(\omega_k, \omega_i) \, E((X(\omega_k))^j (X^*(\omega_\ell))^m)$$

$$i=0,\ldots,n$$
$$\ell=0,\ldots,n \quad (2)$$

This expression can be simplified. Because the components of the stationary excitation are uncorrelated, the moment $E[(X(\omega_k))^j (X^*(\omega_\ell))^m]$ is zero except when $\omega_k = \omega_\ell$. (The specific reason for this is shown in Appendix 1.) Therefore,

$$E(Z(\omega_i)(X^*(\omega_\ell))^m)$$
$$= \sum_{j=1}^{M} H_j(\omega_\ell, \omega_i) \, E((X(\omega_\ell))^j (X^*(\omega_\ell))^m)$$

$$i=0,\ldots,n$$
$$\ell=0,\ldots,n \quad (3)$$

96

Further, the only situation where the expectation on the right hand side is nonzero occurs when $j=m$. (The reason for this is also shown in Appendix 1.) Because of this

$$E(Z(\omega_i)(X^*(\omega_\ell))^m)$$
$$= H_m(\omega_\ell, \omega_i) \, E(|X(\omega_\ell)|^{2m})$$
$$\begin{aligned} i &= 0, \ldots, n \\ \ell &= 0, \ldots, n \end{aligned} \quad (4)$$

At this point it is possible to conduct a stationary random vibration experiment. First, we would estimate the moments $E[Z(\omega_i)(X^*(\omega_\ell))^m]$ and $E[|X(\omega_\ell)|^{2m}]$ using standard statistical techniques, and then we would ratio the results to obtain an estimate for the coefficient function $H_m(\omega_\ell, \omega_i)$. However, it is useful to establish the relation between the excitation spectral density and the moment $E[|X(\omega_\ell)|^{2m}]$, and to write a special expression for the moment $E[Z(\omega_i)(X^*(\omega_\ell))^m]$ before proceeding to estimate the $H_m(\omega_\ell, \omega_i)$. As mentioned previously, the excitation random process is a zero mean, stationary, normal random process. Let $S_{xx}(\omega)$ denote the spectral density of the excitation, $\{X(t)\}$. Then it can be shown (See Appendix 2.) that

$$E(|X(\omega_\ell)|^{2m}) = m! \, T^m \, S_{xx}^m(\omega_\ell)$$
$$\begin{aligned} m &= 1, \ldots, M \\ \ell &= 0, \ldots, n \end{aligned} \quad (5)$$

when $\omega T \gg 1$, and where T is the time associated with the DFT's (and later, with the statistical analyses). Note that $E[|X(\omega_\ell)|^{2m}]$ is a function of the DFT time interval because $S_{xx}(\omega)$ is time independent.

If the response were a normal random process and the correlation between the frequency components of the excitation and the frequency components of the response were known, then it would be possible to obtain an expression similar to (5) for the moment $E[Z(\omega_i)(X^*(\omega_\ell))^m]$, and this expression would reveal a dependence of that moment on $T^{(m+1)/2}$. However, because of the nonlinearity of the excitation - response relation, the response is not usually normally distributed, and the expression cannot be obtained. Nevertheless, it probably remains a fact that the moment

$E[Z(\omega_i)(X^*(\omega_\ell))^m]$ is a function of $T^{(m+1)/2}$, and this is so assumed. Specifically, it is assumed that

$$E(Z(\omega_i)(X^*(\omega_\ell))^m) = T^{(m+1)/2} \, S_{ZX^{*m}}(\omega_i, \omega_\ell)$$
$$\begin{aligned} i &= 0, \ldots, n \\ \ell &= 0, \ldots, n \end{aligned} \quad (6)$$

where $S_{ZX^{*m}}(\omega_i, \omega_\ell)$ is the spectral function that relates $Z(\omega_i)$ and $(X^*(\omega_\ell))^m$ in the frequency domain, and, as before, T is the time over which the DFTs are taken. $S_{ZX^{*m}}(\omega_i, \omega_\ell)$ is assumed time independent.

Based on (4), (5) and (6), $H_m(\omega_\ell, \omega_i)$ can be used to write a time independent, harmonic generating transfer function. This is

$$F_m(\omega_\ell, \omega_i) = T^{(m-1)/2} \, H_m(\omega_\ell, \omega_i)$$
$$= \frac{S_{ZX^{*m}}(\omega_i, \omega_\ell)}{m! \, S_{xx}^m(\omega_\ell)}$$
$$\begin{aligned} m &= 1, \ldots, M \\ i &= 0, \ldots, n \\ \ell &= 0, \ldots, n \end{aligned} \quad (7)$$

This function describes the harmonic generating character of a structural system.

In order to establish a numerical estimate of (7), statistical estimates of the moments $E[|X(\omega_\ell)|^{2m}]$ and $E[Z(\omega_i)(X^*(\omega_\ell))^m]$ are required. These can be obtained using standard statistical procedures. The approach and formulas required to obtain the statistical estimate for $E[Z(\omega_i)(X^*(\omega_\ell))^m]$ is given in Appendix 3.

The functions established in (7) contain a substantial amount of information that includes, but goes far beyond, the information in a linear FRF. In fact, the harmonic generating transfer functions defined in (7) could be used to describe how response is generated at every frequency given excitation at every frequency. When the response is characterized by Fourier components at n frequencies, the harmonic generating transfer function defined for each value of m contains n^2 points, therefore, when m takes the values 1 through M, Mn^2 items of information can be used to define the discrete functions $F_m(\omega_\ell, \omega_i)$. For realistic values of M and (especially) n it is not realistic to assume that Mn^2 values could be stored. Note, however, that in realistic situations, it is not anticipated that the functions $F_m(\omega_i, \omega_i)$ will

have substantial values at all frequency pairs (ω_ℓ, ω_i). In most situations one would expect substantial values when $\omega_i = \omega_\ell, 3\omega_\ell, 5\omega_\ell$, etc., and possibly when $\omega_i = 2\omega_\ell, 4\omega_\ell$, etc. For example, if knowledge of those elements in $F_m(\omega_\ell, \omega_i)$ which create response at $\omega_i = \omega_\ell$ and $3\omega_\ell$ are desired for $m=1$ and $m=3$, then $4n$ items of information need to be established to characterize $F_m(\omega_\ell, \omega_i)$.

Thus, most practical situations will require a reasonably accomodated amount of data storage.

Random Vibration Analysis Using the Harmonic Generating System Model

Aside from basic system characterization, the fundamental reason for establishing the mathematical model defined in (1) is to provide the capability for random vibration analysis of the harmonic generating system. Given the coefficients $H_j(\omega_k, \omega_i)$, a random vibration analysis can be easily executed. To do this, the complex conjugate of (1) is taken and multiplied times (1). Then the expected value is taken on both sides; the result is

$$E(|Z(\omega_i)|^2) = \sum_j \sum_k \sum_\ell \sum_m H_j(\omega_k, \omega_i) H_\ell^*(\omega_m, \omega_i)$$
$$* E((X(\omega_k))^j (X^*(\omega_m))^\ell)$$

$$i = 0, \ldots, n \quad (8)$$

Recall that the expected value on the right hand side is zero except when $m=k$ and $\ell=j$; therefore, the expression simplifies to

$$E(|Z(\omega_i)|^2) = \sum_j \sum_k |H_j(\omega_k, \omega_i)|^2 E(|X(\omega_k)|^{2j})$$

$$i = 0, \ldots, n \quad (9)$$

Now (6) can be used to simplify the left hand side (using $Z(\omega_i)$ in place of $X(\omega_\ell)$ and $m=1$) and the right hand side, and (7) can be used to establish an expression for $H_j(\omega_k, \omega_i)$ that can be used above. The result is

$$S_{zz}(\omega_i) = \sum_j \sum_k j! \, |F_j(\omega_k, \omega_i)|^2 \, S_{xx}^j(\omega_k)$$

$$i = 0, \ldots, n \quad (10)$$

This formula establishes a means for computing the spectral density of structural response to stationary random vibration excitation. The formula is complete in the sense that it includes all the terms necessary for characterization of the response of a nonlinear, harmonic generating system to stationary, random vibration excitation. The reason for this completeness is the fact that different frequency components of a stationary random process are uncorrelated.

Example

This section presents an example that demonstrates the use of the formulas developed in the previous sections. The system to be considered is a simple Duffing oscillator. Figure 1 is a schematic display of the system. It is governed by the nonlinear, ordinary differential equation

$$\ddot{z} + 2\zeta\omega_n \dot{z} + \omega_n^2 z + \varepsilon z^3 = x \quad (11)$$

where ω_n is the natural frequency of the associated linear system, ζ is the system damping factor, ε is a small positive constant, x denotes the excitation, z denotes the displacement response, and dots denote differentiation with respect to time.
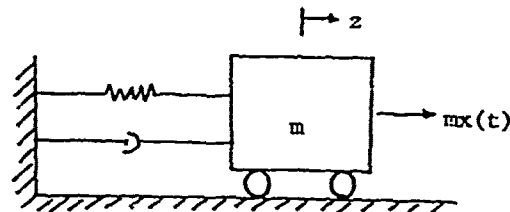
SPRING RESTORING FORCE $= m\omega_n^2 z + m\varepsilon z^3$

DAMPER RESTORING FORCE $= 2m\zeta\omega_n z$

MASS NORMALIZED FORCE $= x(t)$

Figure 1. Duffing oscillator.

An approximate expression for the response can be developed using the perturbation approach. (See Reference 4.) With this approach it is assumed that the response can be expressed as an expansion in the small term ε. That is

$$z(t) = z_0(t) + \varepsilon z_1(t) + \ldots \quad (12)$$

(12) is used in (11), and linear equations governing z_0, z_1, etc., are developed by grouping terms by coefficients of ε^0, ε^1, etc., and noting that the coefficients must equal zero if the components z_0, z_1, etc., are to be independent and arbitrary.

When the excitation is

$$x(t) = \sum_k X_k \exp(i\omega_k t) \qquad (13)$$

it can be shown that the first order approximation to the response is

$$z(t) = \sum_k H(\omega_k) X_k \exp(i\omega_k t)$$
$$+ \sum_j \sum_k \sum_\ell H(\omega_j + \omega_k + \omega_\ell) H(\omega_j) H(\omega_k) H(\omega_\ell)$$
$$* X_j X_k X_\ell \exp(i(\omega_j + \omega_k + \omega_\ell)t)$$
$$\qquad (14)$$

where $H(\omega)$ is the FRF function of a linear single-degree-of-freedom system. This formula includes more terms than (1), therefore (1) can only represent the frequency domain response in an approximate, limited sense, in the general case. However, for stationary, random vibration analysis, the terms in (14) where $j \neq k \neq \ell$, and $j \neq \ell$ are unimportant and

$$z(t) = \sum_k H(\omega_k) X_k \exp(i\omega_k t)$$
$$- \epsilon \sum_k H(3\omega_k) H^3(\omega_k) X_k^3 \exp(i3\omega_k t)$$
$$\qquad (15)$$

represents the response with all the terms necessary for a first order analysis. In view of this, the harmonic generating transfer functions for the first approximation to the Duffing oscillator are

$$H_j(\omega_k, \omega_i) = \begin{cases} H(\omega_i), & j=1, \ k=i \\ -\epsilon H(\omega_i) H^3(\omega_i/3), & j=3, \ k=i/3 \\ 0, & \text{otherwise} \end{cases}$$
$$\qquad (16)$$

The first expression simply establishes the nature of the linear part of the response. The second term transfers excitation at frequency $\omega_i/3$ to response at frequency ω_i. The moduli of these functions (a normalized form, in the second case) are plotted in Figures 2 and 3 for the case where $\omega_n = 1$, $\zeta = 0.05$. The frequency generating nature of $H_3(\omega_i/3, \omega_i)$ is apparent in Figure 3.

Similar analyses are possible for higher approximations to the Duffing oscillator response and for other nonlinear systems.

Figure 2. The first expression in (16). FRF of a linear single-degree-of-freedom system.

Figure3. The second expression in (16). Third harmonic generating transfer function of a Duffing oscillator.

99

Conclusions

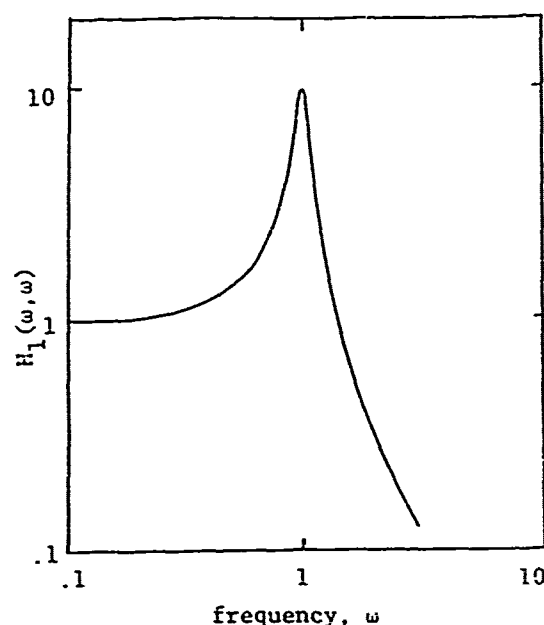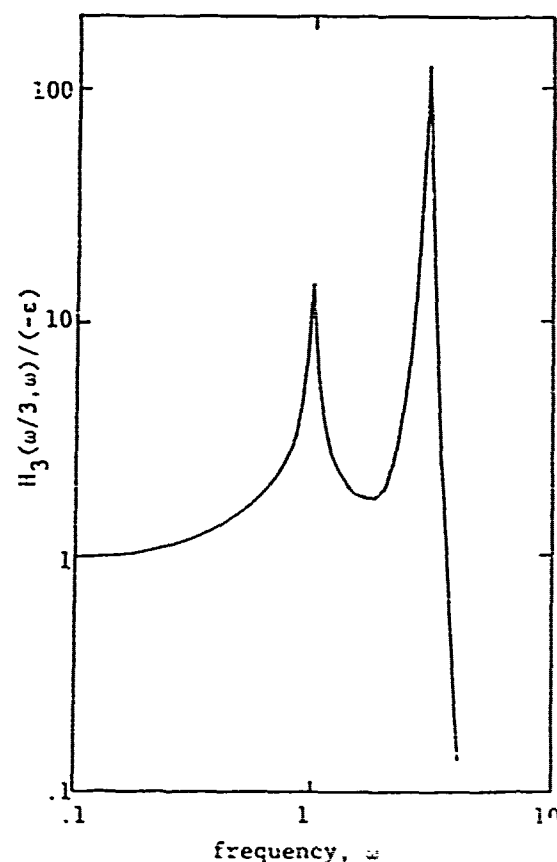The response of a nonlinear, harmonic generating structure to stationary, random vibration excitation can be represented using an expression that is a series of power series in the Fourier transform of the excitation. The coefficients of the power series describe the character of the structure. An analytical example shows that it can be easy to establish the coefficients. Further, it is demonstrated that the coefficient functions required for the nonlinear representation can be obtained experimentally. The magnitudes of the coefficients of the harmonic generating terms can be used to assess the degree of nonlinearity of a structure tested in the laboratory.

Future investigations must demonstrate the usefulness of this model with experimental data, and must consider the use of this model when the excitation is not a stationary random process.

Appendix 1

This appendix considers $\{X(t), 0 < t < T\}$, a segment of mean zero, stationary, normal random process with Fourier representation

$$X(t) = \sum_{k=0}^{n-1} X_k \exp(i2\pi tk/n\Delta t), \qquad 0 < t < T \tag{A1}$$

where

$$X_k = C_k \exp(i\phi_k), \qquad k=0,\dots,n-1 \tag{A2}$$

In this expression $C_0=0$, $C_{n-k}=C_k$, $k=1,\dots,n/2$, are deterministic constants related to the random process spectral density, and $\phi_0=0$, $\phi_{n-k}=\phi_k$, $k=1,\dots,n/2$, are uniformly distributed random variables on $(-\pi,\pi)$, where ϕ_j and ϕ_k are independent for $j\neq k$. Reference 9 establishes (A1) as a valid representation for a stationary random process.

It will be shown that $E[X_k^j(X_\ell^*)^m]$ is zero except when $k=\ell$ and $j=m$. Based on (A2)

$$E(X_k^j(X_\ell^*)^m) = C_k^j C_\ell^m E(\exp(i(j\phi_k - m\phi_\ell))) \tag{A3}$$

Because the ϕ_k, $k=0,\dots,n/2$, are independent

$$
E(\exp(i(j\phi_k - m\phi_\ell)))
= \begin{cases}
E(\exp(i(j-m)\phi_\ell)), & k=\ell \\
E(\exp(ij\phi_k))\,E(\exp(-im\phi_\ell)), & k\neq\ell
\end{cases}
\tag{A4}
$$

Because $E[e^{ir\phi_s}]=0$ for all s and all $r\neq0$, all the moments in (A4) are zero except when $k=\ell$ and $j=m$, and when $j=m=0$. Therefore, (A3) is nonzero only when $k=\ell$ and $j=m$.

Appendix 2

This appendix considers a random process $\{X(t), 0 < t < T\}$, a segment of a mean zero, stationary, normal random process with autocorrelation function $R_{xx}(\tau)$ and spectral density $S_{xx}(\omega)$. The moment $E[|X(\omega_\ell)|^{2m}]$ will be evaluated where

$$X(\omega_\ell) = \int_0^T X(t)\,\exp(-i\omega_\ell t)\,dt \tag{A5}$$

The real and imaginary parts of $X(\omega_\ell)$ are normal random variables given by

$$X_R(\omega_\ell) = \int_0^T X(t)\,\cos(\omega_\ell t)\,dt \tag{A6}$$

$$X_I(\omega_\ell) = \int_0^T X(t)\,\sin(\omega_\ell t)\,dt \tag{A7}$$

The random variables $X_R(\omega_\ell)$ and $X_I(\omega_\ell)$ have zero means. The variance of $X_R(\omega_\ell)$ is

$$E(X_R^2(\omega_\ell)) = \int_0^T dt \int_0^T ds\, R_{xx}(s-t)\,\cos(\omega_\ell t)\,\cos(\omega_\ell s) \tag{A8}$$

Define the change of variables $\tau=s-t$, $Y=s+t$, and allow τ to cover the interval $(-\infty,\infty)$ to establish an approximation. Then

$$E(X_R^2(\omega_\ell)) \cong \frac{T}{2} S_{xx}(\omega_\ell) + \frac{1}{4\omega_\ell} S_{xx}(0)\,\sin(2\omega_\ell T) \tag{A9}$$

When $\omega_\ell T \gg 1$ and $S_{xx}(0)$ is near in value to $S_{xx}(\omega_\ell)$, this is approximately

$$E(X_R^2(\omega_\ell)) \cong \frac{T}{2} S_{xx}(\omega_\ell) \tag{A10}$$

Similarly, it can be shown that

$$E(X_I^2(\omega_\ell)) \cong \frac{T}{2} S_{xx}(\omega_\ell)$$

$$E(X_R(\omega_\ell)X_I(\omega_\ell)) \cong 0 \tag{A11}$$

Note that

$$|X(\omega_\ell)|^2 = X_R^2(\omega_\ell) + X_I^2(\omega_\ell) \qquad (A12)$$

Therefore

$$
\begin{aligned}
&E\{|X(\omega_\ell)|^{2n}\} \\
&= \sum_{r=0}^{n} \binom{n}{r} E((X_R^2(\omega_\ell))^{n-r})\, E((X_I^2(\omega_\ell))^r)
\end{aligned}
$$

$$(A13)$$

Because of (A10) and (A11) and the fact that $X_R(\omega_\ell)$ and $X_I(\omega_\ell)$ are normal random variables

$$
\begin{aligned}
E((X_R(\omega_\ell))^{2n}) &= E((X_I(\omega_\ell))^{2n}) \\
&= \frac{(2n)!}{2^n\, n!}\left[\frac{T}{2}\, S_{xx}(\omega_\ell)\right]^n
\end{aligned}
$$

$$(A14)$$

Use of this expression in (A13) yields

$$E(|X(\omega_\ell)|^{2n}) = n!\,(TS_{xx}(\omega_\ell))^n \qquad (A15)$$

for $\omega_\ell T \gg 1$, which is the desired result.

Appendix 3

This appendix shows how the moment $E[Z(\omega_i)(X^*(\omega_\ell))^n] = S$ can be statistically estimated. Let $\{Z(t)\}$ and $\{X(t)\}$ be stationary and ergodic, mean zero random processes. Assume that measured realizations of the random processes are available; denote these z_j and x_j, $j=1,\ldots,n$. Divide each time series into M blocks of equal length N, such that $MN=n$. Denote the jth elements of the kth blocks z_{jk} and x_{jk}, $j=0,\ldots,N-1$, $k=1,\ldots,M$. Multiply each data block by an amplitude adjusted data window, w_j, $j=1,\ldots,N$, (if desired) to obtain

$$z'_{jk} = z_{jk}\, w_j, \qquad j=0,\ldots,N-1 \quad (A16)$$

$$x'_{jk} = x_{jk}\, w_j, \qquad k=1,\ldots,M \quad (A17)$$

Fourier transform the time series (A16) and (A17) to obtain the DFTs.

$$Z_{\ell k} = \Delta t \sum_{j=0}^{N-1} z'_{jk}\, \exp(-i2\pi j\ell/N) \qquad (A18)$$

$$X_{\ell k} = \Delta t \sum_{j=0}^{N-1} x'_{jk}\, \exp(-i2\pi j\ell/N) \qquad (A19)$$

$$\ell=0,\ldots,N-1$$
$$k=1,\ldots,M$$

The Δt is the sampling period of the measured data. Form products like $Z_{\ell k}(X^*_{\ell k})^n$ and average these over all blocks.

$$\hat{S} = \frac{1}{M} \sum_{k=1}^{M} Z_{\ell k}(X^*_{\ell k})^n \qquad (A20)$$

This is an estimate of the moment that appears in (4) and (6).

References

1. Bendat, J., Piersol, A., Random Data: Analysis and Measurement Procedures, Wiley-Interscience, New York, 1971.
2. Otnes, R., Enochson, L., Applied Time Series Analysis, Volume 1, Basic Techniques, Wiley-Interscience, New York, 1978.
3. Bendat, J., Piersol, A., Engineering Applications of Correlation and Spectral Analysis, Wiley-Interscience, New York, 1980.
4. Stoker, J., Nonlinear Vibrations in Mechanical and Electrical Systems, Interscience Publishers, New York, 1950.
5. Minorsky, N., Introduction to Nonlinear Mechanics, J. W. Edwards, Ann Arbor, Mich., 1947.
6. Schetzen, M., The Volterra and Wiener Theories of Nonlinear Systems, Wylie-Interscience, New York, 1980.
7. Chouchai, T., Vinh, T., "Analysis of Nonlinear Structure by Programmed Impact Testing and Higher Order Transfer Function," Proceedings of the 4th International Modal Analysis Conference, Los Angeles, Ca., 1986.
8. Tomlinson, G., "Detection, Identification, and Quantification of Nonlinearity in Modal Analysis," Proceedings of the 4th International Modal Analysis Conference, Los Angeles, Ca., 1986.
9. Papoulis, A., Probability, Random Variables, and Stochastic Processes, McGraw-Hill, New York, 1965.

AN INTERACTIVE-GRAPHICS METHOD FOR DYNAMIC

SYSTEM MODELLING, APPLYING CONSISTENCY RULES

M. D. C. Dyne,
Institute of Sound and Vibration Research,
University of Southampton, UK.

This paper reviews some reasons why digital simulation
employing bond graph principles has received recent
attention for the study of the dynamics of physical systems
and reports an alternative approach to model synthesis and
validation.

A simplified overview of the bond graph

To render the analysis of a complex system
tractable it may be considered as a network of
subsystems assembled together by links or
bonds representing flow paths. For the
system to be dynamic the equilibrium must be
disturbed by some force (source of effort)
which acts along the bonds. The subsystems
themselves are idealised into lumped parameter
energy dissipative units, capacitive storage
units and inductive storage units - in
mechanical terms dampers, springs and
masses. Power, defined by the product of two
variables effort and flow, is transmitted
along the bonds to these idealised single port
elements.

Subsystems which, whilst conserving power,
alter (transform) the ratio of effort and flow
are defined as two port elements - idealised
as the transformer and the gyrator, examples
of which are the pulley and the flywheel.
Two types of power conserving multiport
elements are defined - one in which there are
multiple effort inputs and a single output and
a second in which a single effort input drives
multiple outputs. These are considered as
junctions of common flow and junctions of
common effort.

The magnitude of power flowing along a bond
connecting subsystems may be modulated
(scaled) by a modulating two port element.
No loss (or gain) of power in the system is
associated with the modulating element though
any change immediately redistributes power
through other bonds in the system.

The cause and effect relationship between
connected elements in the system is called
causality and determines whether effort or
flow is the dependent variable to the port.
Preferred causality is predefined and is
systematically assigned, thus expressing the
input/output relationship. If the preferred
causality cannot be assigned then, in a
restricted number of cases, alternative
elements with opposite causality may be

substituted to yield a consistent model.
A convention is adopted for assigning the
polarity of instantaneous power transfer along
the bond, since power can move in either
direction dependent upon the polarity of the
product of effort and flow.
Finally, because of a bond graph convention
that the output of all elements initially is
positive, the sign of the input may have to be
inverted.

Attractive features of the bond graph method

There are five main reasons for the attention
given to the bond graph method as implemented
in recently available modelling packages.

* ease of model change
* run time interaction
* physical domain swapping
* potential communication with other models
* potential computational efficiency.

Due to the clarity which is established in the
construction of, for example, a bond graph
model of an axle connected to a suspension
system connected to a wheel assembly, it is
easy to remove one suspension system and to
substitute a replacement, eg. mass spring
damper system replaced by a hydroelastic
system. With only limited further effort
and, using the interactive commands provided,
non linear functionality may be introduced
with only minimal disturbance of the model
data structure.

Interactive run time commands enable the
modeller to obtain information from the model
during simulation including the reformatting
of graphical results and the alteration of
simulation step times.

Since the essence of bond graph modelling and
simulation is the study of effort and the
resultant flow (or conversely flow which
results in forces) then, provided the user is
careful to take account of consistent power
units, ready migration from one physical

domain to another physical domain is achieveable. This has been illustrated by considering the garage ramp system in which volts and resultant current drive an electric motor which in turn develops torque and resultant angular velocity to turn a pump. The pump develops hydraulic pressure inducing fluid volumetric flow which then forces the ram, causing it to move (velocity). Communication with other models is achieved by relegating the run time simulation of the model to a Fortran subroutine which can be combined with other subroutine simulations and can be programmed to furnish separate information streams for each time variable of interest. Since interaction with each simulation is made easy, reprocessing of the most recent time step with altered simulation interval, etc., is facilitated.

The particular attraction of this method of simulation arises from the model being broken down into a number of first order differential equations and algebraic equations. With the advent of more powerful optimising compilers and parallel vector processors the potential for efficient solution becomes more attractive.

Weakness of the bond graph method

Formulation of the information representing the bond graph into machine readable codes appears largely to be a rule driven process providing no further insight into the synthesis of the model and an alternative and more familiar method of expressing the model and conveying it to the computer has been the subject of a research investigation. This has extended into model validation and progress of the investigation is reported below.

The method chosen is governed by three pre simulation phases (a) graphical interaction to construct and manipulate the model, (b) model validation and code generation, (c) model dimensioning.

Model synthesis and manipulation

The model builder assembles the model in orthogonal planes visualised as windows with depth of view. Icons representing the bond graph elements may be picked from an icon menu and placed at desired coordinates in the plane and linked together to form a network. Since subsystems may be geometrically distributed, manipulation commands from a displayed menu are used to assign flow lines representing stiff massless physical links and aids to construction and computer calculated dimensions may be invoked. Figure 1 shows the screen layout for a mechanical system. Finally icons representing boundary constraints may be imposed. Model management commands aid the saving, recovery, replication and repositioning of subsystems and the entire model may be filed and reassembled.

The data structure communicated to the validation phase contains a record for each

Figure 1

icon and flow line chosen and comprises several fields: one containing the internal code of the chosen item; a second stating how many link-labels are attached to the element; fields containing unique labels for all link attachments; the precedence for processing of the record (this is default assigned to ensure that source of effort or flow is processed first to assist preferred causality but, for multi inputs the modeller may raise the precedence of a particular input). The last field contains information about the orthogonal plane in which the picture was defined and is passed through to the dimensioning phase.

Figure 2 shows a system and the resultant data structure.

Figure 2

Model validation

The flow lines from the graphical phase do not represent bonds in a bond graph - they merely serve to indicate connectivity in the network. To validate the model, a revised network containing the power flow bonds must be constructed.

Continuing with the example in Figure 2, and starting with the icon (element) with the highest precedence, the linear chain is processed, recording the output of each element in turn as the input of the next in the chain. Where parallelism occurs the subchain is processed in the same way. The transformation of Table 1 to Table 2 in
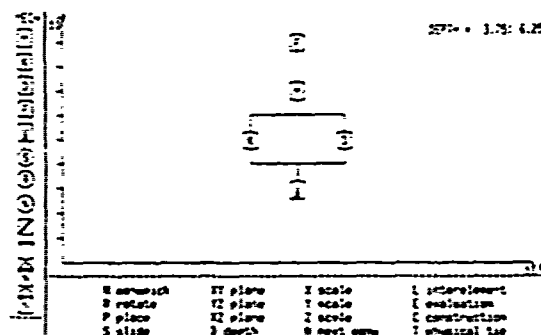
Figure 3 illustrates this operation. Sources of effort or flow have a single output and no input and the remainder have a multiple of two entries in the label columns - more than two entries indicating a splitting of power.

Table 1	Table 2	Table 3	Table 4	Table 5	Table 6	
				9	9	
					39	f5
					▽ e1▷	Δ
M 2 3	F 1	Fe▷0	F ▸ 0	1 F▷0 5		
K 4 5	M 1 3	•	▽	▽	F——0	
V 6	K 3 5	▽	M ◂ 1	2 M◂1 6	−f2	e1
F 1	V 5	M◂f1	▲	▲	Δ −f2▷	▽
L 1 2		Δ	K ◂ 0	3 K◂0 7	M——1	
L 2 3		•	▲	▲	e6◂	
L 5 6	Ke▷0	Ke▷0	V ▸ 1	4 V▷1 8	Δ e3	−f2
		Δ			e3▷	▽
	f	f		10	X——0	
	Vf▷1	Vf▷1			f7◂	
					Δ f4	e3
					f4▷	▽
					V——1	
	S is signal				Δ s10	e/
	e is effort				10	▽
	f is flow					

Figure 3

The rules to process the model are as follows: for each element in turn, look up causality to determine the preferred independent variable:

   If causal stroke is *from* the element, then the independent variable is effort and the bond forms the sole *effort input* to a 0 junction. Attach junctions.

   If causal stroke is *to* the element, then the independent variable is flow and the bond forms the sole *flow output* from a 1 junction. Attach junction.

For each junction in turn:

   If junction is 0 junction then the input is effort and all other efforts are determined on the other bonds and must all be outputs.

   If junction is a 1 junction then the output is flow and all other flows are determined on the other bonds and must all be inputs.

   Table 3 illustrates causality.

For each bond in turn, follow the path directed by causality. If inconsistency detected then back tra... to nearest resistance or integral causality and substitute conductance or derivative function. Recommence from beginning of path. If no substitutions left and still inconsistent then model is incomplete.

Commencing at the highest precedence elements, assign power bond for each element in turn, remembering that both effort and flow are inputs to the system. Table 4 illustrates power flow.

Number each element in turn, then each junction in turn, finally allocate an input for each effort and flow source in turn. Table 5 illustrates numbering. From the causality table, allocate outputs. Remembering that all efforts are common around a 0 junction and all flows are common around a 1 junction, see Figure 4, and substituting where necessary, allocate inputs derived from the one-port elements, as in Table 6.

Common effort junction.   Common flow junction.
e0=e1=e2 ; f0=f1+f2 ;   f0=f1=f2 ; e0=e1+e2 ;

Figure 4

Mod... ...sioning
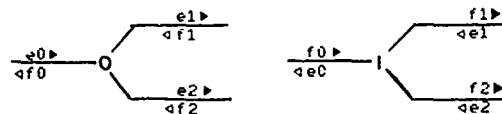
C.... .. data for a consistent bond graph model has been generated then the magnitude of each variable (in self consistent units) must be allocated by the modeller. To assist in this, each element in turn is presented pictorially in the context (plane) in which it was originally drawn and appropriate values elicited.
Once all values have been obtained and the time step specified then the bond graph simulation package solves the model over a presented time interval.

Conclusions

The method described above has been used successfully to built simple models but, eg, automatically invoking transformers to represent pivot ratios of geometrically distributed systems has failed so far. Further developments for a European Economic Community study on vehicle dynamics in connection with road safety are planned.

References:

i   Dixhoorn, J.J. Van, Simulation of Bond Graphs on Minicomputers, J.DYN.SYSTEMS, MEAS, CONTROL, TRANS ASME, Series G, 99, No. 1, 9-14, March 1977.

ii   RARDE Division Note, PA1/3/86, The study of off-road dynamics of wheeled/tracked vehicles, Ministry of Defence, London.

105

Dynamic Response of a Geared Train of Rotors

Subjected to Random Support Excitations

S.V. Neriya, R.B. Bhat and T.S. Sankar

Department of Mechanical Engineering

Concordia University, Montreal, Canada

The response of a geared train of rotors subjected to random support excitations is investigated. Support excitations occur, for instance, on board moving vehicles. These excitations are in general random in nature and the response can be obtained using a statistical analysis. In this paper, the geared train of rotors is modelled using finite elements and the coupling between torsion and flexure is considered. The geared rotor system is excited by a displacement type of support excitation which is the output of a filter, the input to which is a Gaussian, stationary process with a white noise type of PSD. The excitation is assumed to be in the vertical direction only and the excitations through the supports are assumed to be uncorrelated. Results for the response power spectral densities are presented for two kinds of filters.

INTRODUCTION

Rotating shafts are indispensable in mechanical power transmission systems. Dynamic responses of such rotating shafts must be clearly understood for their design. As is very common in power systems, gears are often employed to transmit power between shafts.

In a geared rotor, some of the sources of excitation are mass unbalance, geometric eccentricity and errors of manufacture, all of which originate in the gear pair itself. However, the geared rotor system may be subjected to external forms of excitation such as that from the supports, for instance when on board various types of vehicles. If the support excitations are random in nature with considerable power distributed over a frequency range, the system will respond at those frequencies. Moreover, if one of the system natural frequencies of the geared rotor coincides with the excitation frequencies, the resulting response may be of concern.

There have been several studies on the dynamics of gear systems, but only a few of them have taken into account the coupling between torsional and flexural motions [1-6]. In a geared rotor system, the torsional and flexural motions are coupled due to the presence of mating gears. The coupling occurs in two distinct forms, 1) force coupling and 2) dynamic coupling. The predominant form is the 'force coupling'. This is due to the lateral mesh forces generated by torsional oscillations of the shaft and is of the order of the geometric eccentricity, ϵ. Dynamic coupling is of the order ϵ^2 [2] and is neglected in this analysis. Several investigators have also studied rotors subjected to random support excitations. Lund [7] carried out response spectral density analysis of rotor systems due to stationary random excitations of the base, considering excitations only in the vertical direction. Tessarzik et al [8] analysed the turbo-rotor responses due to external random vibrations. The rotor-bearing system was treated as a linear, three mass model and experimental results were found to compare well with calculations of amplitude power spectral density for the case where the vibrations were applied along the rotor axis. Subbiah et al [9] obtained the amplitude PSD of a simple rotor subjected to random support excitations using modal analysis methods. The excitations were assumed to be stationary and Gaussian with a white noise type of PSD.

In this paper, the geared rotor system is modelled using finite elements and the coupling between torsional and flexural vibrations is considered. The geared rotor system is subjected a displacement type of support excitations which is the output of a linear filter, the input to which is a Gaussian, stationary random process with a white noise type of PSD. This excitation is assumed to be in the vertical direction only and the excitations through the supports are assumed to be uncorrelated. The PSD of the response process is then obtained using a statistical analysis.

NOMENCLATURE

C_{b1} flexural damping of the driving shaft

C_{b2} flexural damping of the driven shaft

$\bar{C}_{tz}$ average flexural damping of the gear tooth in the z-direction

$\bar{C}_{ty}$ average flexural damping of the gear tooth in the y-direction

C_1 lumped torsional damping at the driving gear

C_2 lumped torsional damping at the driven gear

$[C]$ global damping matrix

C_m lumped torsional damping at the motor

C_d lumped torsional damping at the dynamo

F_t tangential component of the transmitted force

F_r radial component of the transmitted force

$\{F\}_R$ Random Support excitation force

$[H(j\omega)]$ frequency response function matrix

I_{1i} moment of inertia of the driving gear in the ith gear pair

I_{2i} moment of inertia of the driven gear in the ith gear pair

J_1 moment of inertia of the motor

J_2 moment of inertia of the dynamo

K_{b1} flexural stiffness of the driving shaft

K_{b2} flexural stiffness of the driven shaft

$\bar{K}_{tz}$ average flexural stiffness of the gear tooth in the z-direction

$\bar{K}_{ty}$ average flexural stiffness of the gear tooth in the y-direction

K_1 torsional stiffness of the driving shaft

K_2 torsional stiffness of the driven shaft

K_{yy} stiffness of the rolling contact bearing in the y-direction

K_{zz} stiffness of the rolling contact bearing in the z-direction

$[K]$ global stiffness matrix

ℓ length of the beam element

m_{1i} mass of the driving gear in the ith gear pair

m_{2i} mass of the driven gear in the ith gear pair

$[M]$ global mass matrix

N number of degrees of freedom of the system

n number of gear pairs

$\{p\}$ modal coordinate vector

$\{q\}$ generalized rotor displacement vector

$\{q_r\}$ relative displacement vector

$\{q_s\}$ support displacement vector

r_{1i} base circle radius of the driving gear in the ith gear pair

r_{2i} base circle radius of the driven gear in the ith gear pair

$[S_F(\omega)]$ matrix of the force PSD

$[S_{qr}(\omega)]$ matrix of the relative displacement PSD

$[S_{qs}(\omega)]$ matrix of the support displacement PSD

$[\gamma]$ diagonal damping matrix

ε_{1i} geometrical eccentricity of the driving gear in the ith gear pair

ε_{2i} geometrical eccentricity of the driven gear in the ith gear pair

ζ_i modal damping in the ith mode

θ_{f1i} angle between the directions of unbalance and eccentricity for the driving gear in the ith gear pair

θ_{f2i} angle between the directions of unbalance and eccentricity for the driven gear in the ith gear pair

$[\kappa]$ diagonal stiffness matrix

λ_i ith eigenvalue

$[\mu]$ diagonal mass matrix

{σ(t)} generalised force vector

{ψ_i} ith eigenvector

ANALYSIS

In the present work, the geared rotor system is modelled using finite elements [10,-11]. In general, the rotor finite element considers gyroscopic effects in addition to rotating inertia and shear deformation effects. However, the gyroscopic terms are skew symmetric in nature and hence a simple normal mode analysis is not possible. A modal analysis employing biorthorganility relations [12] is capable of considering the skew symmetric gyroscopic terms also, however, for simplicity a normal mode analysis was resorted to in the present study by neglecting the gyroscopic effects. The finite element discretisation of the geared train of rotors is carried out as follows. The shafts are divided into beam elements and each node has 5 degrees of freedom. The contact point of the mating gear has two degrees of freedom, one in the z direction and the other in the y-direction. The element mass and stiffness matrices are obtained from the consistent formulation and are then assembled to form the global mass and stiffness matrices. The elemental mass matrix is the sum of translational and rotational mass matrices. These are obtained from [10]. The concentrat d masses and inertias (including transverse moment of inertia) due to the motor, dynamo, gears etc. are introduced into the appropriate locations in the global mass matrix. The stiffnesses of the rolling contact bearings are included in the analysis. The coupling between torsion and flexural obtained from a study of the dynamics of the gear mesh (see Appendix I) are introduced into the appropriate locations in the global stiffness matrix.

The equations of motion for a N degree of freedom geared shaft system subjected to support excitations can be expressed as

$$[M] \{\ddot{q}_r\} + [C] \{\dot{q}_r\} + [K] \{q_r\} = \{F\}_R \quad (1)$$

where   {q} = generalised rotor displacement vector

{q_s} = support displacement vector

{q_r} = {q - q_s}, is the relative displacement vector.

and $\{F\}_R = - [M] \{\ddot{q}_s\}$ (2)

The homogeneous form of Eq. (1) neglecting damping is solved to obtain the eigen values λ_i and eigen vectors {ψ_i} of the system.

Expressing the response {q_r} in terms of the modal coordinates {p} as

$$\{q_r\} = [\psi] \{p\} \quad (3)$$

where   [ψ] is the modal matrix formed using the eigenvector {ψ_i}

Using Eq. (3) in i.. ind premultiplying by [ψ]^T we get,

$$[\mu] \{\ddot{p}\} + [\gamma] \{\dot{p}\} + [\kappa] \{p\} = \{\sigma(t)\} \quad (4)$$

where $[\mu] = [\psi]^T [M] [\psi]$

$$[\kappa] = [\psi]^T [K] [\psi] \quad (5)$$

$$\{\sigma(t)\} = [\psi]^T \{F\}_R$$

Now $\{p(t)\} = [H(\omega)] \{\sigma(t)\}$ (6)

where $H_i(\omega) = \dfrac{1}{(\kappa_i - \mu_i \omega^2) + j(2\zeta_i \omega_i \mu_i \omega)}$ (7)

and ζ_i is the modal damping ratio.

The PSD matrix of the response can be obtained as

$$[S_{qr}(\omega)] = [\psi] [H(j\omega)] [\psi]^T [S_F(\omega)] [\psi]$$
$$\times [H(-j\omega)]^T [\psi]^T \quad (8)$$

The PSD matrix of the random excitation force [S_F(ω)] can be expressed in terms of the PSD matrix of the displacement support excitation [S_{qs}(ω)] as

$$[S_F(\omega)] = \omega^4 [M] [S_{qs}(\omega)] [M]^T \quad (9)$$

The displacement support excitation is assumed as the output of a linear filter, the input to which is an excitation in the vertical direction only. This excitation is an uncorrelated Gaussian stationary process with a white noise type of PSD.

NUMERICAL RESULTS

A geared train of rotors employing two pairs of gears is used to obtain the numerical results. The details of this system are given in Table 1. The pedestals through which the support excitations are transmitted to the geared rotor system are denoted by k_{yy} and k_{zz} respectively. The finite element discretisation of the above system is shown in Fig. 4. The shafts are divided into beam elements 1 to 7 and the ten nodes of the system are denoted by a to j. The details of the beam elements are given in Table 2. The details of the system natural frequencies are given in Table 3. The details of the linear filter are given in Appendix II.

The normalized PSD of relative amplitude

in the y direction at the driven gear location is shown in Fig. 5. The base excitation is assumed to be the output of a first order linear filter, the input to which is an uncorrelated white noise type of PSD only in the vertical direction, and this is plotted on the x axis. The PSD plot shows peak response at modes 2, 3 and 7. There is also a peak response observed midway between the modes 8 and 9, which are very close to each other. The maximum response is seen in mode 8 and corresponds to about 0.1 m^2/Hz.

A similar PSD plot as in Fig. 5 using a second order filter is shown in Fig. 6. T h e behavior of the response is the same as in Fig. 5, but the magnitude is lower for all modes.

The normalized PSD of relative amplitude in the y direction at the driving gear location is shown in Fig. 7. The base excitation is assumed to be the output of a first order linear filter, the input to which is an uncorrelated white noise type of PSD in the vertical direction. The PSD plot shows peak response at modes 2, 3, 7 and 10. The maximum PSD response of about 0.1 m^2/Hz is observed at modes 3 and 7. The response at the driven gear (Fig. 5) is found to be higher than the driving gear at the first mode and comparable at the other modes.

A similar PSD plot as in Fig. 7 using a second order filter is shown in Fig. 8. The behavior of the response is the same as in Fig. 7, but the magnitude is lower for all the modes.

The normalized PSD of relative amplitude in the y direction at the bearing locations (DOF #50 and #45) is shown in Figures 9 and 10. The base excitation is assumed to be the output of a first order linear filter, the input to which is an uncorrelated white noise type of PSD in the vertical direction. The responses are as expected, much smaller than the response at the gear locations. The maximum response is observed at the 10th mode (71.59 Hz) and this corresponds to about 3.1 x 10^{-8} m^2/Hz.

REFERENCES

1. Lund, J.W., "Critical Speeds, Stability and Response of a Geared Train of Rotors", Journal of Mechanical Design, July 1978, Vol. 100, pp. 535-539.

2. Daws, J.W., "An Analytical Investigation of Three-Dimensional Vibration Gear-Coupled Rotor Systems", Ph.D. Dissertation, Virginia Polytechnic and State University, 1979.

3. Iida, H., Tamura, A., Kikuch, K. and Agata, H., "Coupled Torsional-Flexural Vibration of a Shaft in a Geared System of Rotors", Bulletin of the JSME, Vol. 23, No. 186, December 1980, pp. 2111-2117.

4. Neriya, S.V., Bhat, R.B. and Sankar, T.S., "Effect of Coupled Torsional Flexural Vibration of a Geared Shaft System of the Dynamic Tooth Load", Shock and Vibration Bulletin, June 1984.

5. Neriya, S.V., Bhat, R.B. and Sankar, T.S., "Coupled Torsional-Flexural-Vibration of a Geared Shaft System using Finite Element Analysis", Shock and Vibration Bulletin, June 1985.

6. Iwatsubo, T., Arii, S., Kawai, R., "Coupled Lateral-Torsional Vibration of Rotor System Trained by Gears", Bulletin of the JSME, Paper No. 224-28, Feb. 1984.

7. Lund, J.W., "Response Characteristics of a Rotor with Flexible Damped Supports", Symposium of International Union of Theoretical and Applied Mechanics, Lyngby, Aug. 12-16, 1974, pp. 319-349.

8. Tessarzik, J.M., Chiang, T., and Badgley, R.H., "The Response of Rotating Machinery to External Random Vibration", Journal of Engineering for Industry, Trans. ASME, Vol. 96, No. 2, May 1974, pp. 477-489.

9. Subbiah, R., Bhat, R.B. and Sankar, T.S., "Response of Rotors Subjected to Random Support Excitations", Journal of Vibration, Acoustics Stress and Reliability in Design, Oct. 1985, Vol. 107, pp. 453-459.

10. Nelson, H.D., and McVaugh, J.M., "The Dynamics of Rotor-Bearing Systems using Finite Element Approach", Journal of Mechanical Design, Trans. ASME, Jan. 1980, pp. 158-161.

11. Nelson, H.D., "A Finite Rotating Shaft Element using Timoshenko Beam Theory", Journal of Mechanical Design, Trans. ASME, Vol. 102, Oct. 1980, pp. 793-803.

12. Bhat, R.B., Subbiah, R., Sankar, T.S., "Dynamic Behavior of a Simple Rotor with Dissimilar Hydrodynamic bearings by Modal Analysis", Journal of Vibration, Acoustics, Stress and Reliability in Design, Trans. ASME, Vol. 107, April 1985, pp. 267-269.

TABLE 1

Details of the Rotor System under Study

E	1.96×10^{11} N/m^2
G	7.84×10^{10} N/m^2
I_{11}, I_{12}	0.03 kg m^2
I_{21}, I_{22}	0.0628 kg m^2
J_1	0.459 kg m^2
J_2	0.549 kg m^2
$\bar{k}_{ty}$	2.17×10^9 N/m
$\bar{k}_{tz}$	2.60×10^{12} N/m
k_{yy}	8.83×10^8 N/m
k_{zz}	8.83×10^8 N/m
m_{11}, m_{12}	16.69 kg
m_{21}, m_{22}	5.65 kg
$(m_{t1})_i, (m_{t1})_i$ $(i = 1,2)$	0.0049 kg
r_{11}, r_{12}	0.1 m
r_{21}, r_{22}	0.05 m

TABLE 2

Details of the Rotor Elements

Element No.	Length m	Diameter m	Mass per unit length $\bar{m}$ kg/m
1	0.35	0.020	2.51
2	0.3	0.015	1.41
3	0.3	0.020	2.51
4	0.6	0.020	2.51
5	0.6	0.030	5.655
6	0.3	0.030	5.655
7	0.3	0.025	3.93

TABLE 3
System Natural Frequencies 0 - 80 Hz

Mode No.	System natural frequency Hz
1	0.0
2	7.18
3	32.21
4	33.72
5	34.71
6	34.71
7	40.80
8	69.53
9	71.21
10	72.59

APPENDIX I

A schematic representation of a geared train of rotors as shown in Fig. 1. A sectional view x - x at the i th gear pair location is shown in Fig. 2 and it shows the relative positions of the driving and driven gears. O_1 and O_1' represent the geometric centers of the driving and driven gears; O_2 and O_2' represent the centers of the driving and driven shafts when they are rotating and O_3 and O_3' when they are stationary. There exists a coupling between the translational motion of its gear center, y, z, and the rotational motion of the gear θ. At the gear location they correspond to the flexural motion of the shaft carrying the gear and its torsional motion. Fig. 3(a) shows the spring mass representation of the driving gear in the i th gear pair. The mass of the driving tooth is denoted by m_{t1i}. The coordinates y_{t1i} and z_{t1i} describe the gear tooth motion. The time average stiffness and damping of the gear tooth in the y and z directions are denoted by $\bar{k}_{tyi}$, $\bar{k}_{tzi}$, $\bar{c}_{tyi}$ and $\bar{c}_{tzi}$ respectively. k_{b1i} and c_{b1i} denote the stiffness and damping of the shaft carrying the driving gear. The driven gear for i th gear pair is similarly modelled and is shown in Fig. 3(b).

The dynamical equations of motion for the gear pair described above are derived following the approach in [4]. The effects of varying tooth elasticity and backlash are neglected in the analysis. The equations of motion are:

$$m_{1i}\ddot{z}_{1i}+c_{b1i}\dot{z}_{1i}+k_{b1i}z_{1i}$$
$$+\bar{k}_{tzi}(z_{1i}+\epsilon_{1i}\cos\theta_{1i}-z_{t1i})+\bar{c}_{tzi}(\dot{z}_{1i}-\epsilon_{1i}\omega_{1i}$$
$$\sin\theta_{1i}-\dot{z}_{t1i})=U_{1i}\theta_{1i}^2\cos(\theta_{1i}+\theta_{f1i}) \quad (1)$$

$$m_{2i}\ddot{z}_{2i}+c_{b2i}\dot{z}_{2i}+k_{bzi}z_{2i}+\bar{k}_{tzi}(z_{2i}+\epsilon_{2i}\cos\theta_{2i}$$
$$-z_{t2i})+\bar{c}_{tzi}(\dot{z}_{2i}-\epsilon_{2i}\omega_{2i}\sin\theta_{2i}-\dot{z}_{t2i})=U_{2i}\theta_{2i}^2$$
$$\cos(\theta_{2i}+\theta_{f2i}) \quad (2)$$

$$m_{1i}\ddot{y}_{1i}+c_{b1i}\dot{y}_{1i}+k_{b1i}y_{1i}+\bar{c}_{tyi}(\dot{y}_{1i}+\epsilon_{1i}\omega_{1i}$$
$$\cos\theta_{1i}+r_{1i}\theta_{1i}-\dot{y}_{t1i})+\bar{k}_{tyi}(y_{1i}+\epsilon_{1i}\sin\theta_{1i}$$
$$+r_{1i}\theta_{1i}-y_{t1i})=U_{1i}\theta_{1i}^2\sin(\theta_{1i}+\theta_{f1i}) \quad (3)$$

$$m_{2i}\ddot{y}_{2i}+c_{b2i}\dot{y}_{2i}+k_{b2i}y_{2i}+\bar{c}_{cyi}(\dot{y}_{2i}+\epsilon_{2i}\omega_{2i}$$
$$\cos\theta_{2i}+r_{2i}\theta_{2i}-\dot{y}_{t2i})+\bar{k}_{tyi}(y_{2i}+\epsilon_{2i}\sin\theta_{2i}$$
$$+r_{2i}\theta_{2i}-y_{t2i})=U_{2i}\theta_{2i}^2\sin(\theta_{2i}+\theta_{f2i}) \quad (4)$$

$$m_{t1i}\ddot{z}_{t1i}+\bar{c}_{tzi}(\dot{z}_{t1i}-\dot{z}_{1i}+\epsilon_{1i}\omega_{1i}\sin\theta_{1i})$$
$$+\bar{K}_{tzi}(z_{t1i}-z_{1i}\epsilon_{1i}\cos\theta_{1i})=-F_{ri} \quad (5)$$

$$m_{t2i}\ddot{z}_{t2i}+\bar{c}_{tzi}(\dot{z}_{t2i}-\dot{z}_{2i}+\epsilon_{2i}\omega_{2i}\sin\theta_{2i})$$
$$+\bar{K}_{tzi}(z_{t2i}-z_{2i}-\epsilon_{2i}\cos\theta_{2i})=F_{ri} \quad (6)$$

$$m_{t1i}\ddot{y}_{t1i}+\bar{c}_{tyi}(\dot{y}_{t1i}-\dot{y}_{1i}-\epsilon_{1i}\omega_{1i}\cos\theta_{1i}-r_{1i}\theta_1)$$
$$+\bar{K}_{tyi}(y_{t1i}-y_{1i}-\epsilon_{1i}\sin\theta_{1i}-r_{1i}\theta_{1i})=-F_{ti} \quad (7)$$

$$m_{t2i}\ddot{y}_{t2i}+\bar{c}_{tyi}(\dot{y}_{t2i}-\dot{y}_{2i}-\epsilon_{2i}\omega_{2i}\cos\theta_{2i}-r_{2i}\theta_{2i})$$
$$+\bar{K}_{tyi}(y_{t2i}-y_{2i}-\epsilon_{2i}\sin\theta_{2i}-r_{2i}\theta_{2i})=F_{ti} \quad (8)$$

$$I_{1i}\ddot{\theta}_{1i}+k_{1i}(\theta_{1i}-\phi_1)+\bar{c}_{tyi}(\dot{y}_{1i}+\epsilon_{1i}\omega_{1i}\cos\theta_{1i}$$
$$+r_{1i}\theta_{1i}-\dot{y}_{t1i})(r_{1i}+\epsilon_{1i}\cos\theta_{1i})$$
$$+\bar{K}_{tyi}(y_{1i}+\epsilon_{1i}\sin\theta_{1i}+r_{1i}\theta_{1i}-y_{t1i})(r_{1i}$$
$$+\epsilon_{1i}\cos\theta_{1i})+C_{1i}\theta_{1i}=0 \quad (9)$$

$$I_{2i}\ddot{\theta}_{2i}+k_{2i}(\theta_{2i}-\phi_2)+\bar{c}_{tyi}(\dot{y}_{2i}+\epsilon_{2i}\omega_{2i}\cos\theta_{2i}$$
$$+r_{2i}\theta_{2i}-\dot{y}_{t2i})(r_{2i}+\epsilon_{2i}\cos\theta_{2i})$$
$$+\bar{K}_{tyi}(y_{2i}+\epsilon_{2i}\sin\theta_{2i}+r_{2i}\theta_{2i}-y_{t2i})(r_{2i}+\epsilon_{2i}$$
$$\cos\theta_{2i})+C_{2i}\theta_{2i}=0 \quad (10)$$

112

The condition that the mating teeth remain in contact is given by:

$$y_{t1i} = y_{t2i}$$
$$z_{t1i} = z_{t2i} \tag{11}$$

The equations of motion are simplified and put in a matrix form, from which we obtain the stiffness terms coupling the torsional and flexural motions and also the forces occuring at a gear pair.

a. Stiffness Matrix

$$
\begin{Bmatrix} z_{ti} \\ y_{ti} \\ z_{1i} \\ z_{2i} \\ y_{1i} \\ y_{2i} \\ \theta_{1i} \\ \theta_{2i} \end{Bmatrix}
\begin{bmatrix}
2\bar{K}_{tzi} & 0 & -\bar{K}_{tzi} & -\bar{K}_{tzi} & 0 & 0 & 0 & 0 \\
0 & 2\bar{K}_{tyi} & 0 & 0 & -\bar{K}_{tyi} & -\bar{K}_{tyi} & -\bar{K}_{tyi}r_{1i} & -\bar{K}_{tyi}r_{2i} \\
-\bar{K}_{tzi} & 0 & \bar{K}_{tzi} & 0 & 0 & 0 & 0 & 0 \\
-\bar{K}_{tzi} & 0 & 0 & \bar{K}_{tzi} & 0 & 0 & 0 & 0 \\
0 & -\bar{K}_{tyi} & 0 & 0 & \bar{K}_{tyi} & 0 & \bar{K}_{tyi}r_{1i} & 0 \\
0 & -\bar{K}_{tyi} & 0 & 0 & 0 & \bar{K}_{tyi} & 0 & \bar{K}_{tyi}r_{2i} \\
0 & -\bar{K}_{tyi}r_{1i} & 0 & 0 & \bar{K}_{tyi}r_{1i} & 0 & \bar{K}_{tyi}r_{1i}^2 & 0 \\
0 & -\bar{K}_{tyi}r_{2i} & 0 & 0 & 0 & \bar{K}_{tyi}r_{2i} & 0 & \bar{K}_{tyi}r_{2i}^2
\end{bmatrix}
$$

Appendix II

Output Y(t),   Input X(t)

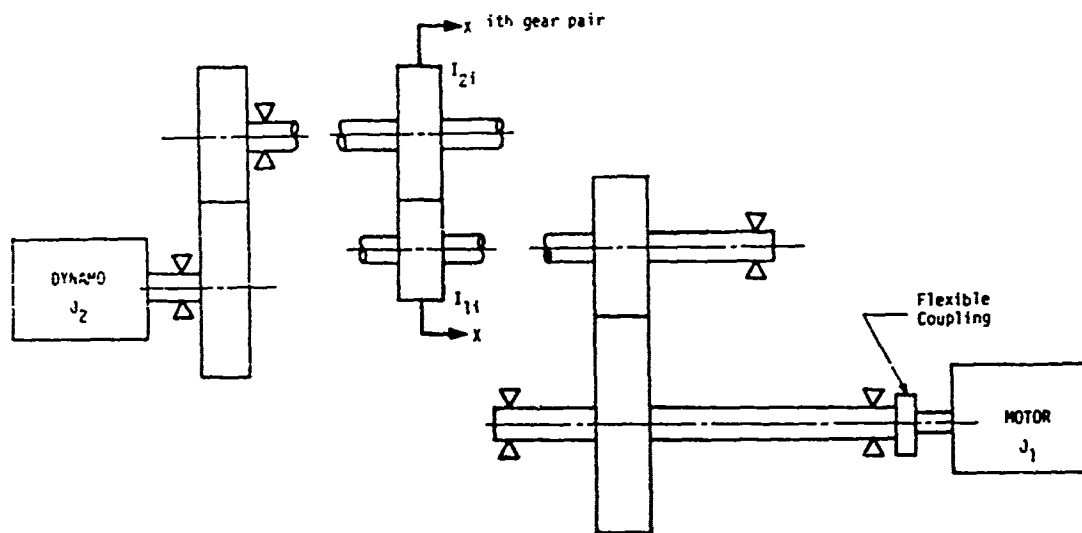| Order	Governing Equation	$\left|H(j\omega)\right|^2$
First	$\alpha \dot{Y} + Y = X$	$\dfrac{1}{1 + \alpha^2\omega^2}$
Second	$\alpha\ddot{Y} + \beta\dot{Y} + Y = X$	$\dfrac{1}{(1 - \alpha\,\omega^2)^2 + (\beta\omega)^2}$

$\alpha = \beta = 1.0$

113

Fig. 1. Geared train of rotors

O_1 geometric center of the driving gear

O_1' geometric center of the driven gear

O_2 center of the driving shaft when it is rotating

O_2' center of the driven shaft when it is rotating

O_3 center of the driving shaft when it is stationary

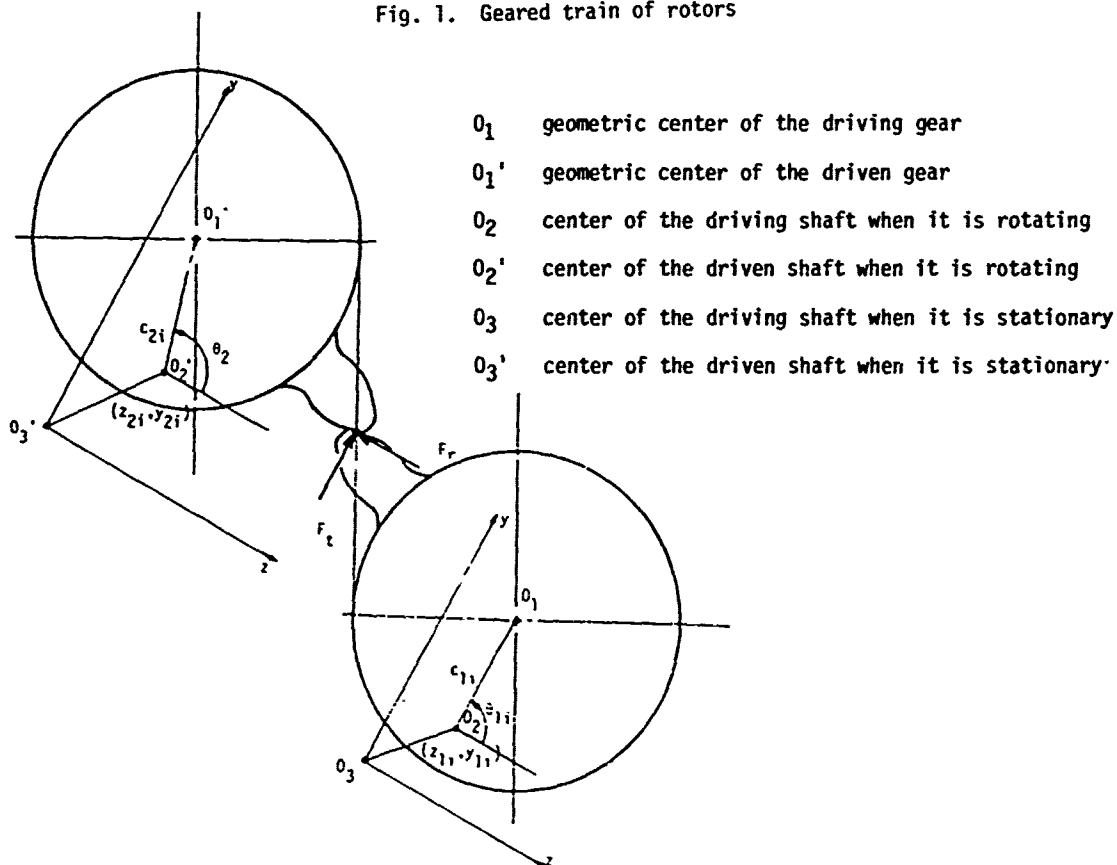O_3' center of the driven shaft when it is stationary·

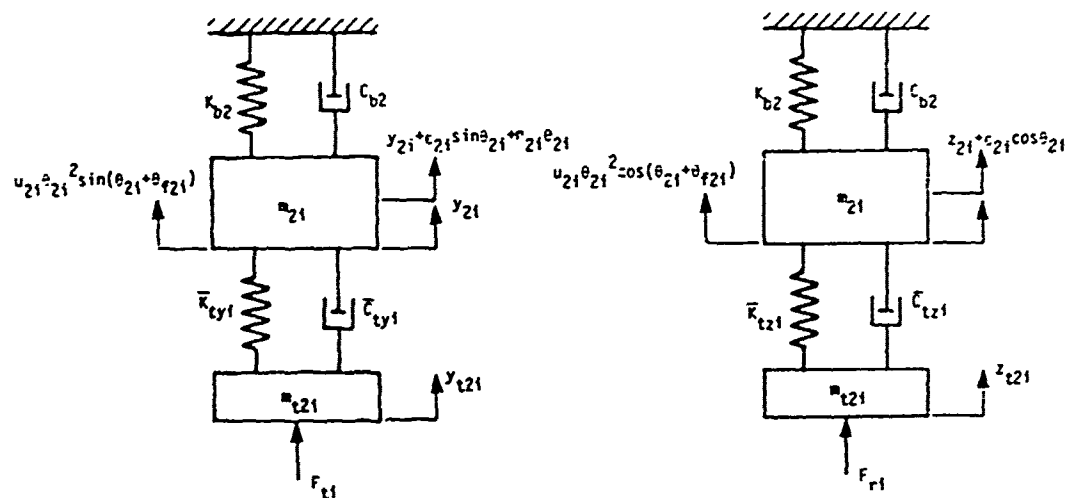Fig. 2. Sectional view at the i th gear pair location

114

Fig. 3a. Driven gear model in the y and z direction
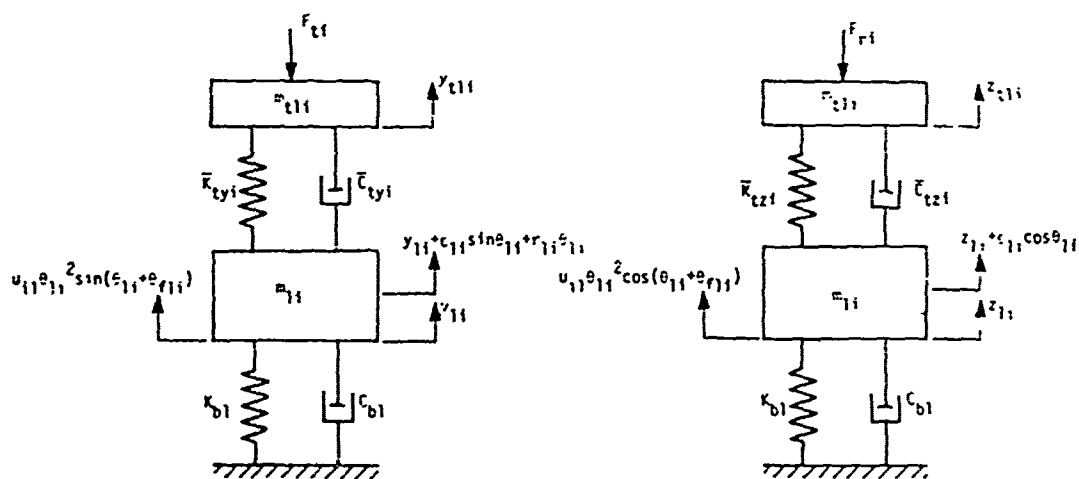for the i th gear pair

Fig. 3b. Driving gear model in the y and z directions
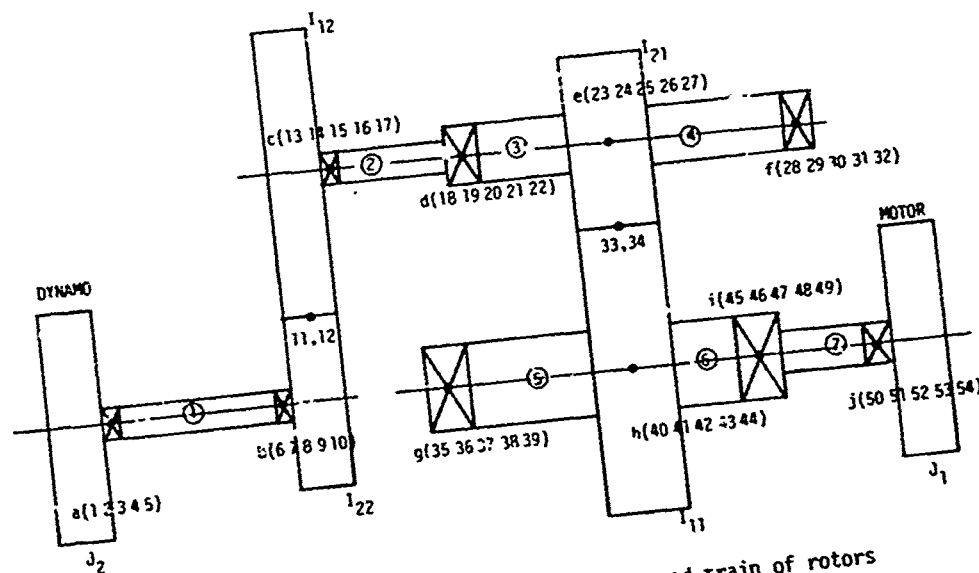for the i th gear pair

115

Fig. 4. Finite element discretisation of the geared train of rotors having two pairs of gears

Fig. 5. Normalized PSD of relative amplitude in the y direction at the driven gear location (DOF #23) against the frequency of excitation. First order filter used.

116

Fig. 6. Normalized PSD of relative amplitude in the y direction at the driven
         gear location (DOF #23) against the frequency of excitation. Second
         order filter used.

Fig. 7. Normalized PSD of relative amplitude in the y direction at the driving
         gear location (DOF #46) against the frequency of excitation. First
         order filter used.

117
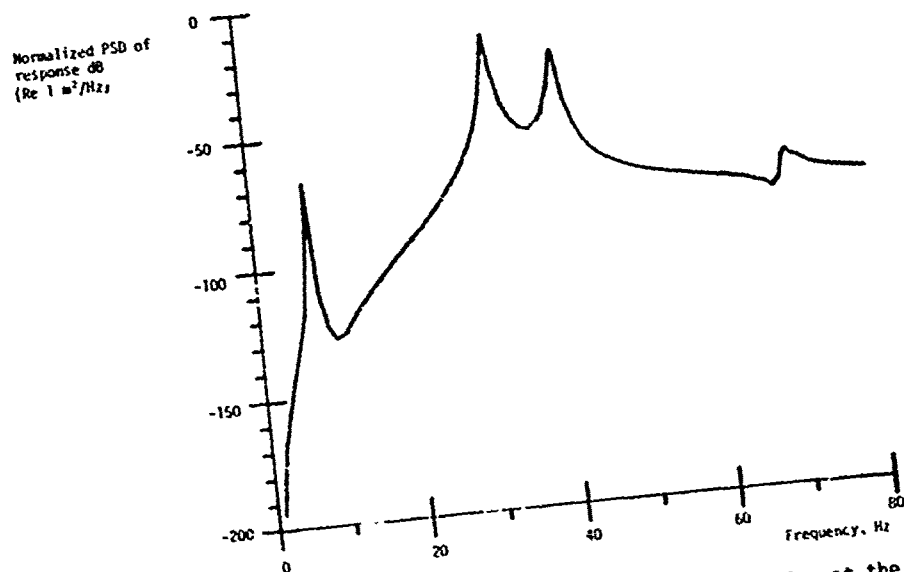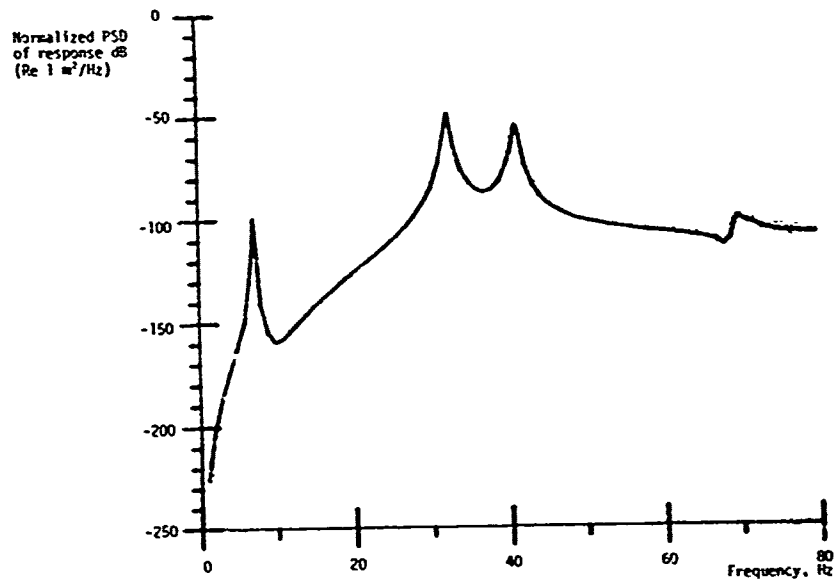
Fig. 8. Normalized PSD of relative amplitude in the y direction of the driven gear location (DOF #40) against the frequency of excitation. Second order filter used.

Figure 9. Normalized PSD of relative amplitude in the y direction at the bearing location (DOF #50) against the frequency of excitation. First order filter used.
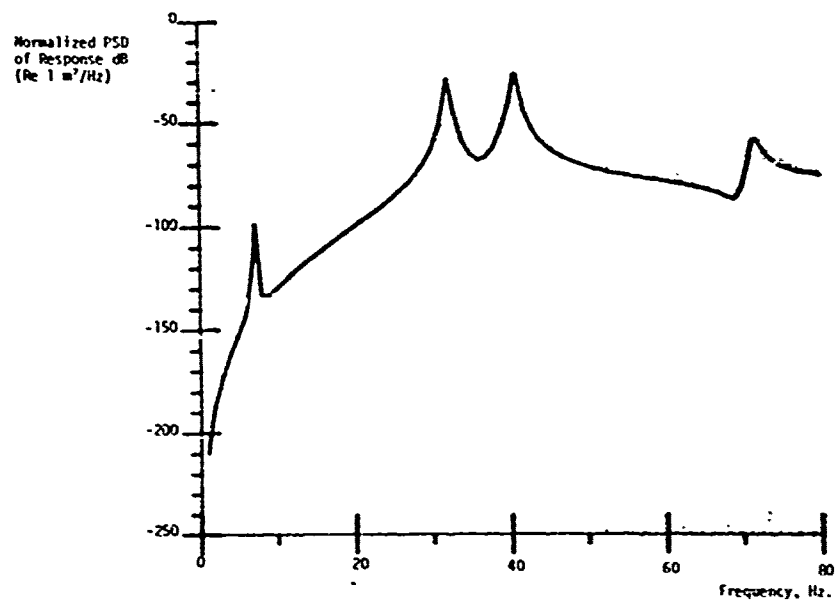
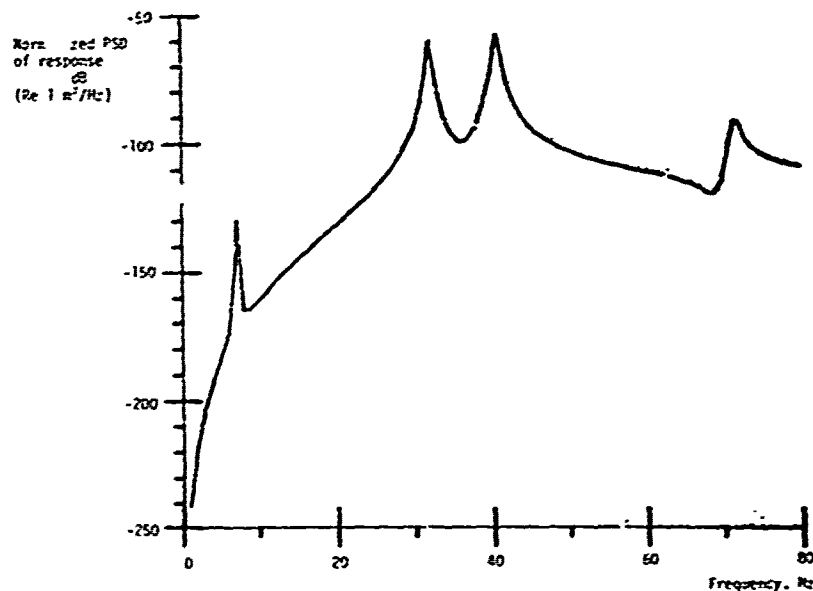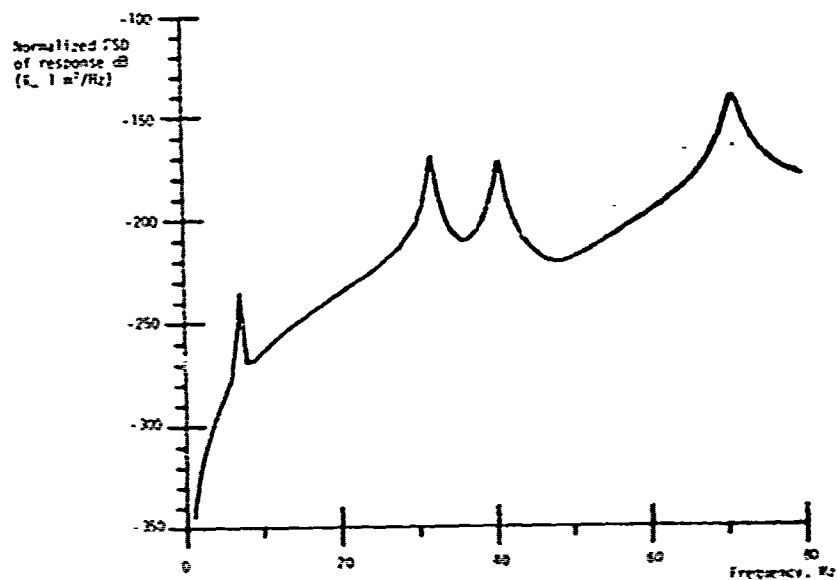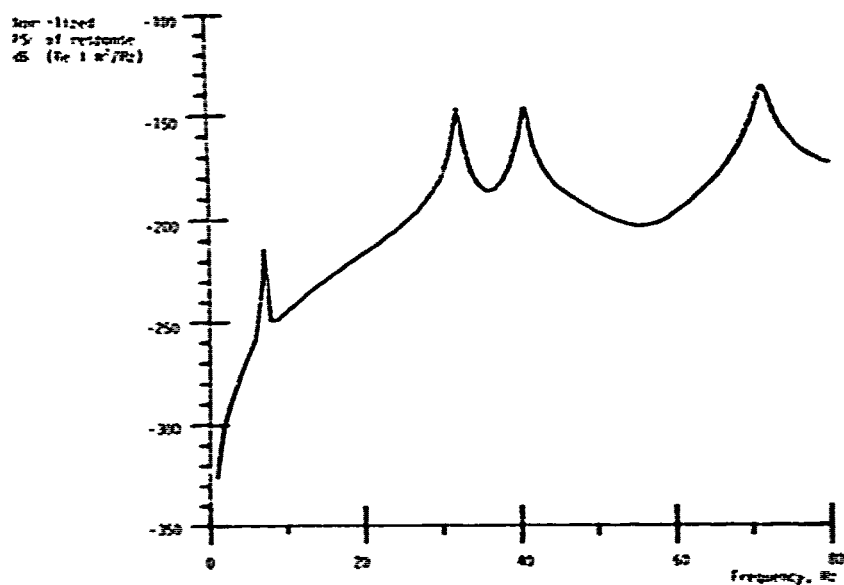Fig. 10. Normalized PSD of relative amplitude in the y direction at the bearing location (DOF #45) against the frequency of excitation. First order filter used.

THE DYNAMICS OF AN OSCILLATING FOUR-BAR LINKAGE

Ping Tcheng, Senior Engineer
Langley Research Center, NASA
Hampton, Virginia 23665-5225

The design, analysis and application of a unique oscillating double four-bar linkage is described. The Lagrange equation for the slightly damped second-order system was derived and verified experimentally. System natural frequencies ranging from 1 to 30 Hertz with a damping coefficient less than 0.001 were observed. Special dynamic characteristics of this linkage and results of a shake test were presented. Various instrumentation application of this simple but rugged mechanism are included.

INTRODUCTION

This paper describes the design, analysis and application of a unique oscillating double four-bar linkage. This linkage is made with two rigid platform links, two coupler links, a fixed link and six flexural pivots. The flexural pivots which serve as torsional springs are the key elements of this lumped-parameter, single-degree-of-freedom system [1]. Nearly sustained oscillation is achieved as the result of restoring moments being generated within the pivots as the system is disturbed.

The equation of motion of this slightly damped second-order system was derived using the energy method and was verified by experimental setups. System natural frequencies ranging from 1 to 30 Hertz were observed experimentally by changing the dimensions and masses of the experimental setup. An extremely low damping coefficient, with $\zeta = 2.6 \times 10^{-4}$, was calculated from oscillation data.

Analysis indicates that this linkage is insensitive to either gravity or inertial effects commonly associated with pendulous systems. In other words, the two platforms can be arbitrarily shaped independent of each other as long as they are counter-balanced with equal masses. This is a useful feature in any closed-loop instrument design application. Motion of this system caused by ground excitations has also been analyzed. It has been proven and verified by a shake test that relative motion between the platforms and ground is zero for rectilinear ground excitations. Relative motion, however, does exist for rotational ground excitations.

The unique features of the linkage can be and have been utilized in various applications. Several transducer designs using this simple linkage as the motion and/or force sensing element are discussed.

SYSTEM DESCRIPTION

The double four-bar linkage is symmetrical and shown in Fig. 1. It consists of two platforms each of mass M, two coupler links each of mass m and length ℓ, six flexural pivots each with torsional stiffness K_t and a fixed link that serves as the ground. There are three pivots installed on coupler link. Connection between the moving platforms and ground is provided through the pivots mounted at the midpoints of the two coupler links.

SYSTEM ANALYSIS

The accompanying appendix provides the derivation of the equation of motion of the system. The equation of motion of the system subjected to a horizontal force f applied on the top platform is

$$2(\tfrac{1}{3} m + M) \, \ddot{x} + 24 \, K_t / \ell^2 \, x = f \qquad (1)$$

where x is the rectilinear displacement of the platform and f is the external force applied on the platform parallel to x (see Eq. (A12)). The natural frequency is

$$\omega_n = \left[\frac{12 K_t}{\left(\tfrac{1}{3} m + M \right) \ell^2} \right]^{1/2} \qquad (2)$$

121

In the following, several unique characteristics of the linkage are presented.

(1) Note that the gravitational constant, g, does not appear in Eq. (2) and the selection of system natural frequency then depends only on the link length ℓ for given flexure stiffness K_t and the two masses M and m. Frequencies from a fraction of a Hertz to 30 Hertz can be easily realized. The absence of the gravitational constant further indicates that the system is insensitive to inertia effects inherent in pendulous systems. The two platforms can be therefore arbitrarily shaped independent of each other as long as they are counterbalanced with equal masses. In other words, if additional masses, e.g., an instrumental package, were placed on one platform, counterbalancing with dead weights on the other platform statically will insure dynamic balance. This is certainly a very useful feature in transducer design.

(2) The linkage is also moment insensitive. That is, the external force f can be applied anywhere on the platform and identical response would result as long as the horizontal component of the external force remains unchanged. This is true because moment arm does not appear in Eq. (1).

(3) The derivation in the appendix further indicates that the relative motion between the platforms and ground is zero for rectilinear ground input motion. The insensitivity of the platform to this type of ground motion is analogous to the response of a semidefinite vibrational system where the system may move as a rigid body without disturbing the forces acting upon it [4].

(4) The system, however, will respond to angular ground vibrations. This should become obvious if one notices that the primary mode of motion of the linkage is rotation about the z-axis. The system's equation of motion to this type of input is included in the appendix.

EXPERIMENTAL RESULTS

The equation of motion derived in the appendix was verified experimentally. Different methods to experimentally determine the two masses M and m, flexure stiffness K_t, and the damping coefficient ζ are described. The results of two shake tests that were conducted to verify some of the linkage characteristics are also presented.

Determination of the Damping Coefficient

The damping of the system was determined experimentally from free oscillatory data. The rectilinear displacement of the platform of the free vibration was measured by an LVDT (linear variable differential transformer). Extremely small values of the damping coefficient ζ amounting to 2.4×10^{-4} and 2.7×10^{-4} were calculated from two different runs.

Static Calibration of the Flexure Stiffness

A string calibration stand described in Ref. [2] was used to determine the system stiffness statically. The calibration stand is schematically shown in Fig. 2. As dead weight is added onto the weighing pan, tension in the horizontal string will displace the moving platform. By using a theodolite and adjusting the vernier screws on the calibration stand, a truly horizontal string force of precise magnitude can be applied to the moving platform. The static force-displacement relationship thus observed can be used to find the flexure stiffness from Eq. (1). By setting $\ddot{x} = 0$, the flexure stiffness becomes

$$K_t = (\ell^2/24)(f/x) \qquad (3)$$

The ratio f/x used above is the slope of the static force-displacement relationship. Experimental data indicated that the force-displacement relationship is very linear, and the computed stiffness agrees well with value quoted in Ref. [3].

Dynamic Calibration of the Flexure Stiffness

Consider the system with adjustable link length shown in Fig. 3. Additional masses were placed on the platforms, and oscillation data were taken for two different link lengths. The results are shown in Table 1. It can be shown the natural frequencies are

$$\omega_n = \left[\frac{12K_t}{\left(\frac{1}{3}m + M + \Delta M\right)\ell^2}\right]^{1/2} = \left[\frac{4K_t}{6.75(M + \Delta M) + 2.25\,m}\right]^{1/2}$$

for $\ell = 9.00$ in (0.2286 m), and

$$\omega'_n = \left[\frac{12K_t}{\frac{1}{3}m\ell^2 + (M + \Delta M)\ell_1^2}\right]^{1/2} = \left[\frac{4K_t}{3(M + \Delta M) + 2.25\,m}\right]^{1/2}$$

for $\ell_1 = 6.00$ in (0.1524 m).

Now, for the same M, the flexure stiffness K_t computed from the two above expressions should be identical. Eliminating K_t and rearranging algebraically yields the following expression

$$\frac{m}{(M + \Delta M)} = \frac{9\omega_n^2 - 4\omega'_n{}^2}{3\left(\omega'_n{}^2 - \omega_n^2\right)}$$

122

Using the experimental values listed in Table 1, the mass ratio $m/(M + \Delta M)$ is found to be

$$m/M = 0.7250,$$

$$m/(M + M') = 0.3267,$$

$$m/(M + 2M') = 0.2125,$$

and

$$m/(M + 3M') = 0.1556,$$

where the incremental mass M' used is

$$M' = 7.764 \times 10^{-3} \text{ slug } (0.113 \text{ kg}).$$

The average platform mass and coupler link mass are next calculated as

$$M = 6.39 \times 10^{-4} \text{ slug } (9.33 \times 10^{-3} \text{ kg})$$

and

$$m = 4.64 \times 10^{-4} \text{ slug } (6.79 \times 10^{-3} \text{ kg}).$$

Finally, using appropriate values of M, m, ℓ, and ω_n for various ΔM, the flexure stiffness can be readily calculated. The results are shown in Fig. 4.

Shake Test

Two different types of shake test were conducted. A linear test was used to verify the system's insensitivity to rectilinear ground input and a rotary test to check for system's characteristics. A new set of flexures were used for this series of test. For this reason the natural frequency of the system for this series of test is different than it was before. The test results are presented as follows.

The symmetrical system shown in Fig. 1 was tested on a long stroke shaker (Model 113, Acoustic Power System, Inc.). Three servo accelerometers (Model Q-Flex 2000, Sunstrand Data Control, Inc.) were mounted on the linkage, one on each of the platform to monitor its response and the third one on the fixed link to monitor the inputs acceleration. Sinusoidal inputs with frequencies ranging from 2 Hertz to 50 Hertz were applied to excite the linkage. The input signal was set at a one g level with a power amplifier (Model 114, Acoustic Power system, Inc.). The accelerometer outputs were measured by a digital multimeter (Model 8520A, John Fluke Mfg. Co., Inc.).

The test results are presented in Fig. 5. The top curve is the frequency plot of the ratio of top platform displacement, x_t, to the input displacement, y, while the lower curve is the frequency plot of the ratio of bottom platform displacement, x_b, to the input displacement y. Several observations are made. It is clearly

seen that the platform are insensitive to this type of ground motion input over the tested frequency range. Resonance at 3.15 Hz, which is the natural frequency of the linkage, was expected since no special effort was made to statically balance the linkage precisely. A second resonance around 40 Hertz was also noted. It is assumed that that came from the higher lateral stiffness of the flexures as reported in Ref. [1].

The same linkage was then modified with extra washers added on the platforms and shake tested again. In several cases, the linkage was made unsymmetrical but statically balanced. Except for different peak values and a slight shift in resonant frequencies, the frequency responses basically remained unchanged qualitatively and hence are not reported here.

The symmetrical linkage without the add-on washers was next tested on a rate table (Model 823, Inland Controls, Inc.). Frequency response data of angular displacement ratio, θ/ϕ, is presented in Fig. 6. The dashed line included in the figure is the asymptote of the dampless second-order term derived in the appendix (see Eq. (A19)). The resonant frequency at around 3.1 Hertz is clearly seen. Deviation between the experimental data and the asymptotic response for frequencies above 10 Hertz is to be assumed caused by the lateral motion of the linkage.

APPLICATIONS

The unique features of the linkage can be and have been utilized in various applications. Two simple applications are given below:

(1) A source for generating rectilinear vibration signals, and

(2) A standard for calibrating damping coefficients of viscous fluids.

Transducers can also be designed using the linkage as a force and/or motion sensing element. Two applications are given below:

(1) A skin friction force balance.- In this application, a linear force motor is mounted on the lower platform which exerts a restoring force to null the skin friction force applied tangentially to the surface of the upper platform over which air flows. The applied skin friction force is measured by sensing the amount of current through the motor coil necessary to achieve null positions. The special vibration isolation characteristics of the linkage also make the balance ideal for flight testing.

(2) An angular accelerometer.- The skin friction force balance can be used as an angular accelerometer for measuring rotational ground excitation. As a special case of this

application, the device can be considered as a tilt meter.

CONCLUSIONS

It has been found that the oscillating linkage described can be conveniently designed and constructed using flexural pivots. The equation of motion of the system was derived and verified experimentally. The system was shown to possess negligible damping and vibration isolation capability. Unique characteristics of the system were discussed for transducer designs.

REFERENCES

[1] Free Flex Flexural Pivot Engineering Data, The Bendix Corporation Electric and Fluid Power Division, 221 Seward Avenue, Utica, New York 13503.

[2] Mason, W. T., "Calibration of a Multi-Component Micro-Force Balance System for Wind Tunnel Model," M.S. Thesis, Mechanical Engineering Department, University of Virginia, Charlottesville, Virginia, June 1966.

[3] Seelig, F. A., "Effectively Using Flexural Pivots," ASME paper 70-DE-51, presented at the Design Engineering Conference and Show, Chicago, Illinois, May 1970.

[4] Tse, F. S., Morse, I. E., and Hinkle, R. T. Mechanical Vibrations, pp. 110-113. Allyn and Bacon, Boston, 1963.

APPENDIX

DERIVATION OF THE EQUATION OF MOTION OF THE SYSTEM

Consider the single-degree-of-freedom system shown in Fig. 1. It consists of two identical platforms each of mass M, two uniform coupler links each of mass m and length ℓ, six flexural pivots each with torsional stiffness K_t and a fixed link.

The total kinetic energy of the system is

$$T = T_c + T_p$$
$$= 2\left[\frac{1}{2} I \dot{\theta}^2\right] + 2\left[\frac{1}{2} M v_p^2\right] \tag{A1}$$

where T_c and T_p are the kinetic energies of the coupler link and platform, respectively, I is the moment of inertia of the coupler link about a parallel axis through its center of mass, θ is the angular displacement of the coupler link about the axis of rotation and

v_p is the absolute velocity of the center of mass of the platform.

Note that

$$v_p = \ell/2 \, \dot{\theta}$$

and

$$I = 1/12 \, m\ell^2 \tag{A2}$$

Substituting Eq. (A2) into Eq. (A1), the total kinetic energy can be expressed as

$$T = \frac{1}{4}\left(\frac{1}{3} m + M\right)(\ell \, \dot{\theta})^2 \tag{A3}$$

Because of system symmetry, the potential energy gained by one platform always cancels out the potential energy lost by the opposing platform when the system is in motion. The potential energy change of the coupler links is also zero since its center of mass is fixed. Therefore, energy stored in the flexures is the only form of potential energy possessed by the system and this can be expressed as

$$V = 6\left(\frac{1}{2} K_t \, \theta^2\right) \tag{A4}$$

The Lagrangian of the system is therefore

$$\mathcal{L} \equiv T - V$$
$$= \frac{1}{4}\left(\frac{1}{3} m + M\right)(\ell \, \dot{\theta})^2 - 3 K_t \, \theta^2 \tag{A5}$$

Noting that

$$\partial\mathcal{L}/\partial\dot{\theta} = \frac{1}{2}\left(\frac{1}{3} m + M\right)\ell^2\dot{\theta} \tag{A6}$$

and

$$\partial\mathcal{L}/\partial\theta = -6 K_t \theta \tag{A7}$$

Largrange's equation finally becomes

$$\frac{1}{2}\left(\frac{1}{3} m + M\right)\ell^2 \, \ddot{\theta} + 6 K_t \, \theta = 0 \tag{A8}$$

This is the differential equation for the system. Since the equation is linear, it is not restricted by the small angle approximation assumption.

The natural frequency of the system is

$$\omega_n = \left[\frac{6K_t}{\frac{1}{2}\left(\frac{1}{3} m + M\right)}\right]^{1/2} \tag{A9}$$

124

The horizontal motion of the platform can be found from the following relation

$$x = \ell/2 \; \theta \qquad (A10)$$

where θ is the solution of Eq. (A8).

Substituting Eq. (A10) into Eq. (A8), the rectilinear motion of the platform is found from the following differential equation:

$$2\left(\frac{1}{3} m + M\right) \ddot{x} + 24 \; K_t/\ell^2 \; x = 0 \qquad (A11)$$

If a horizontal force f is applied on the platform, the system equation is modified as:

$$2\left(\frac{1}{3} m + M\right) \ddot{x} + 24 \; K_t/\ell^2 \; x = f \qquad (A12)$$

This differential equation can be viewed as describing the translational motion of a spring-mass system with an equivalent mass of $2\left(\frac{1}{3} m + M\right)$ and an equivalent spring of stiffness $24 \; K_t/\ell^2$. Note again that the small angle approximation is not used in the above derivation.

In the following, the equation of motion of the system subjected to rectilinear ground motion is derived. Assume that the system is excited by ground motion y and z as shown in Fig. 1, the kinetic energies of the two platforms are respectively expressed as

$$T_{p, \; lower} = \frac{1}{2} M \left[(\dot{z} + \ell/2\dot{\theta} \sin \theta)^2 + (\dot{y} - \ell/2\dot{\theta} \cos \theta)^2 \right]$$

$$T_{p, \; upper} = \frac{1}{2} M \left[(\dot{z} - \ell/2\dot{\theta} \sin \theta)^2 + (\dot{y} + \ell/2\dot{\theta} \sin \theta)^2 \right]$$

The total kinetic energy of the two platforms is therefore equal to:

$$T_p = T_{p, \; lower} + T_{p, \; upper}$$

$$= M[\dot{y} + \dot{z}^2 + (\ell\dot{\theta})^2/4] \qquad (A13)$$

and the potential energy of each platform is

$$V_{p, \; lower} = V_{p, upper} = M \; g \; z \qquad (A14)$$

The kinetic energy and potential energy of each coupler link are respectively

$$T_c = \frac{1}{2} m (\dot{y}^2 + \dot{z}^2) + 1/24 \; m (\ell \; \dot{\theta})^2 \qquad (A15)$$

$$V_c = 2 m g z \qquad (A16)$$

The Lagrangian of the system can be formulated in the usual way using energy expressions shown from Eqs. (A13) through (A16). If the

equation of motion were then derived, it would be noticed that cross-coupling would not exist among the three generalized coordinates θ, y and z. Consequently, Eq. (A8), which was developed for the system not subjected to ground excitation, is also valid for the same system subjected to translational ground excitation. Furthermore, since the system does not respond to any excitation in the direction orthogonal to the yz-plane either, it can be concluded that motion of the system is completely isolated from rectilinear ground vibrations.

As for an angular ground motion input ϕ, the system equation of motion can be derived as

$$\frac{1}{2}\left(\frac{1}{3} m + M\right)\ell^2 \ddot{\theta} + 6 \; k_t = k_t \phi \qquad (A17)$$

This is a typical undamped second-order equation subjected to a motion input in which output θ follows the input ϕ at the low frequency end.

TABLE 1

EFFECT OF ADDED MASS ON NATURAL FREQUENCY

Added Mass, ΔM		Natural Frequency	
slug	(kg)	ω_n rad/sec	ω'_n rad/sec
0.0	(0.0)	9.173	12.34
7.764×10^{-3}	(0.1133)	6.359	9.002
0.01553	(0.2266)	5.152	7.427
0.02329	(0.3399)	4.436	6.458

Note ω_n and ω'_n are the natural frequencies of the system of link length of 9.00 in (0.2286 m) and 6.00 in (0.1524 m), respectively.
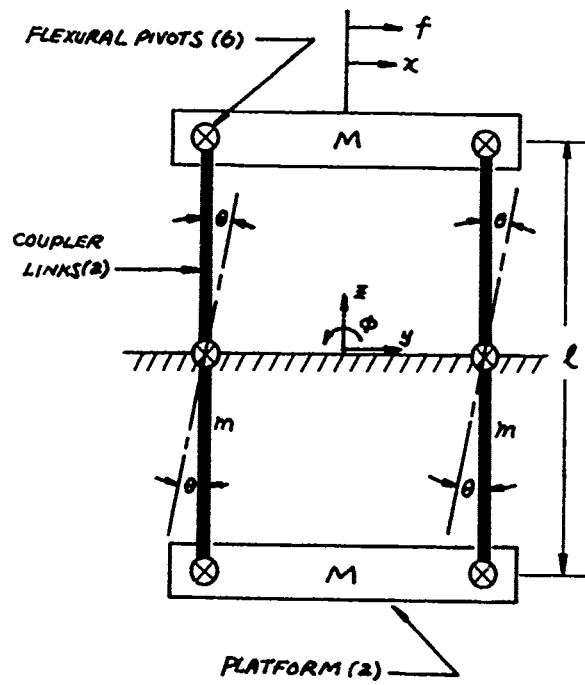
Figure 1. Oscillating four-bar linkage

$$\tan\alpha = \frac{b}{a}$$
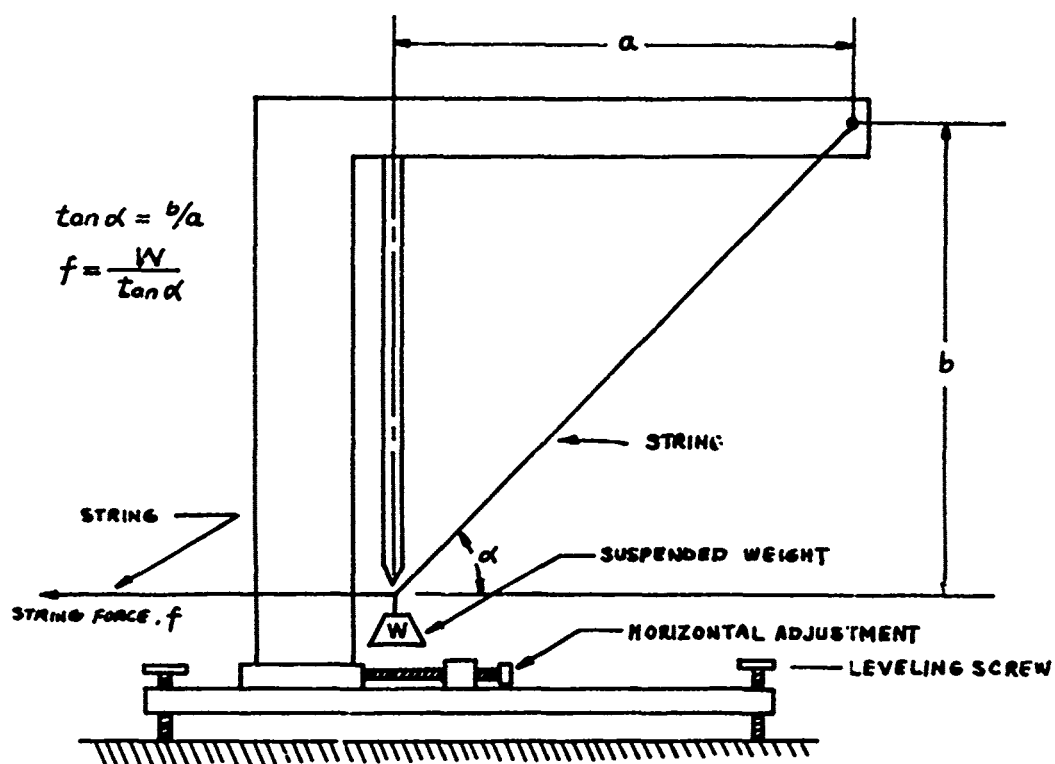
$$f = \frac{W}{\tan\alpha}$$
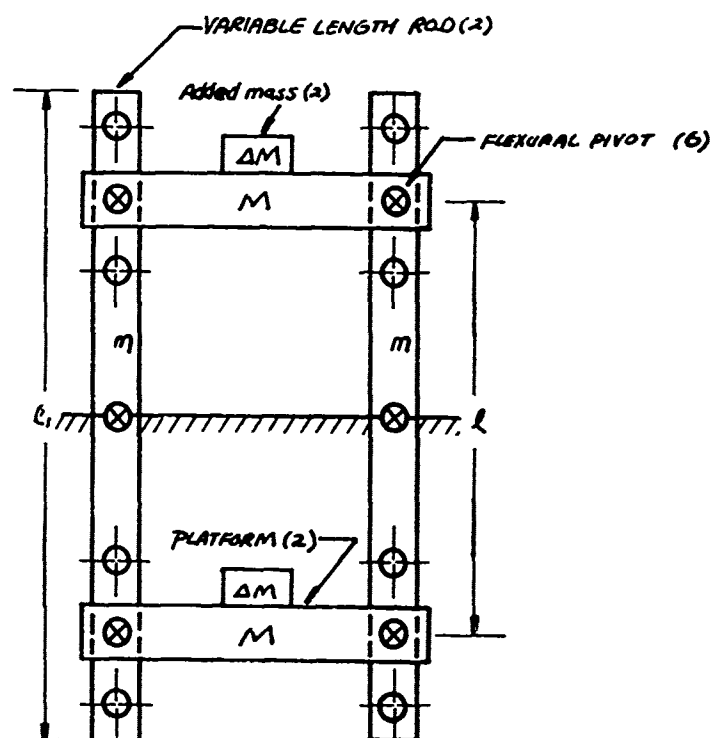
Figure 2. String calibration stand

Figure 3. Oscillating four-bar linkage with adjustable link length
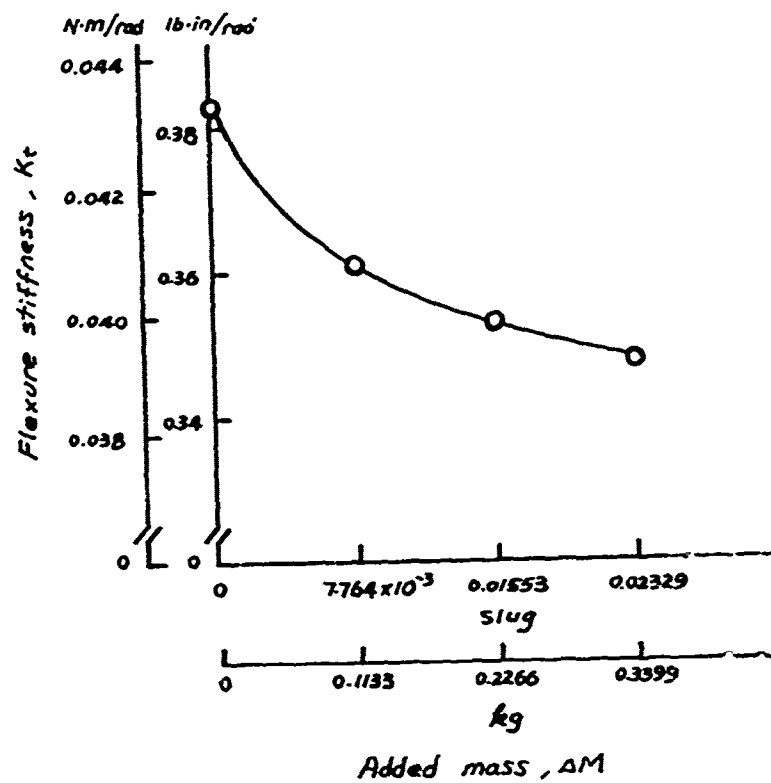
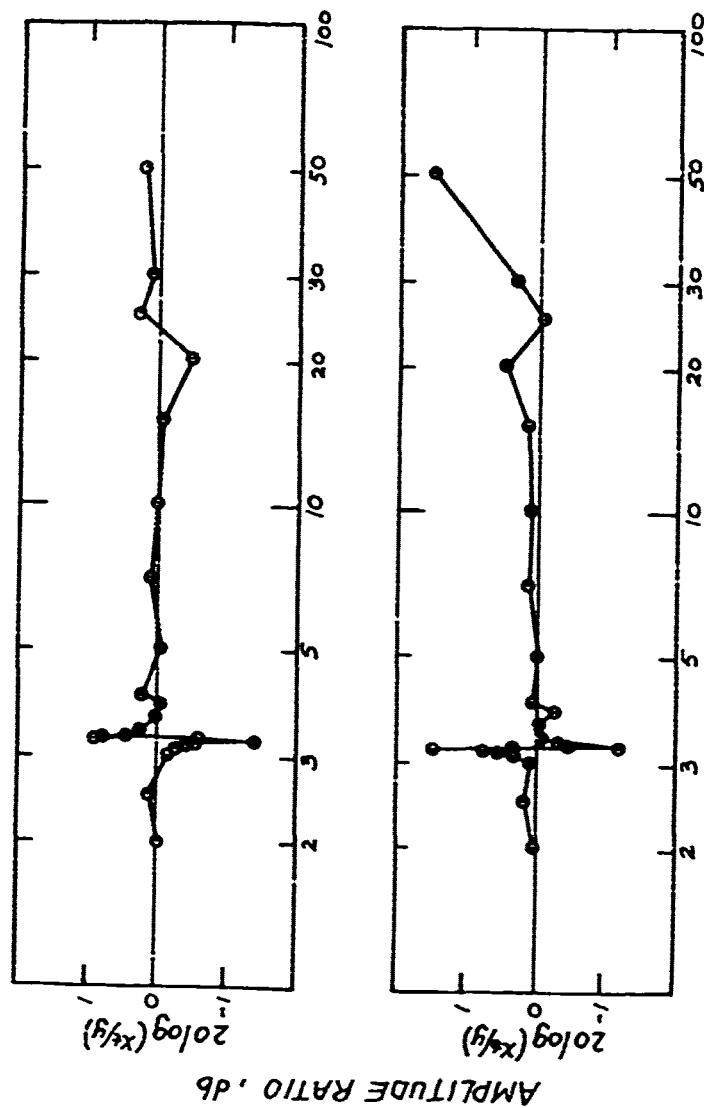Figure 4. Effect of added mass on flexure stiffness
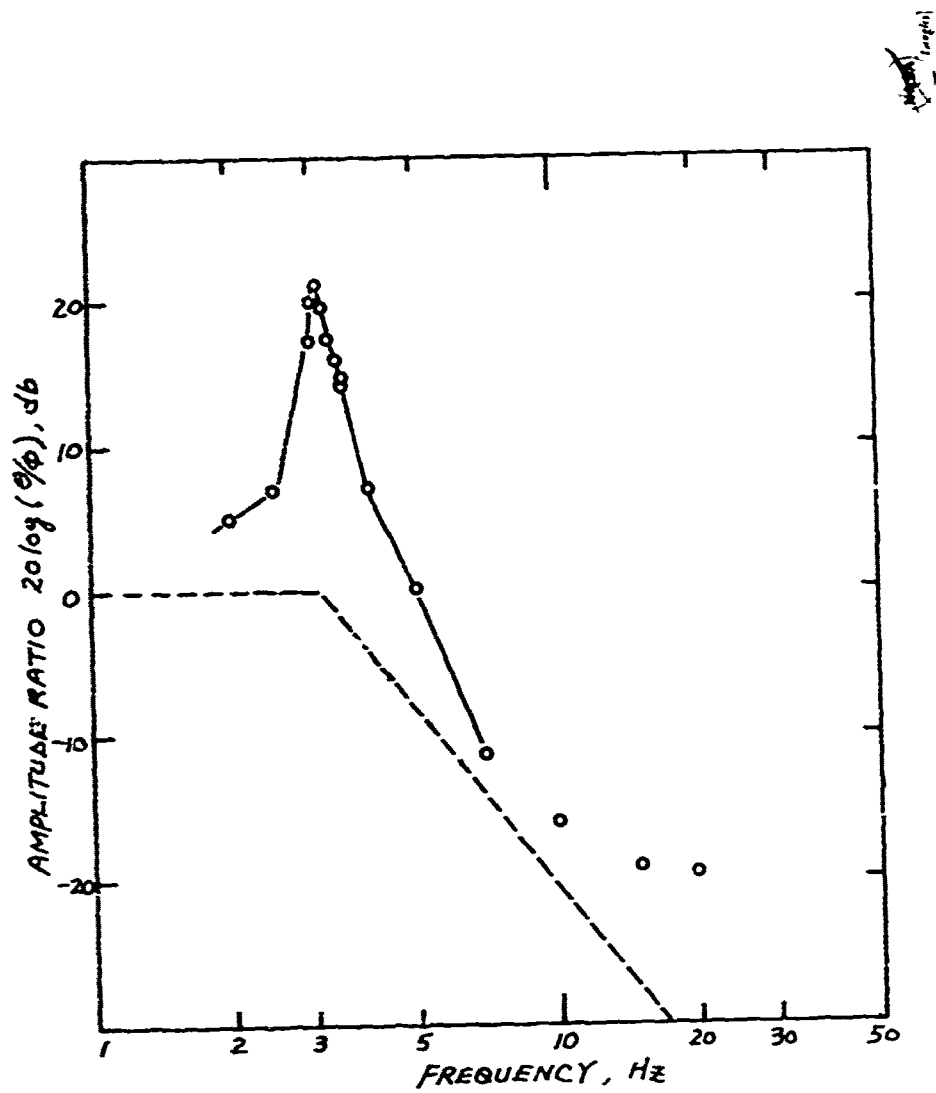
Figure 5. Linkage isolation characteristics

FREQUENCY, Hz

AMPLITUDE RATIO, db

$20 \log (x_t/y)$

$20 \log (x_t/y)$

130

Figure 6. Linkage rotational frequency response

MODAL TEST AND ANALYSIS

CENTAUR G PRIME MODAL TEST

Marc Trubert
Jet Propulsion Laboratory,
California Institute of Technology, MS 157-316
4800 Oak Grove Dr., Pasadena, CA 91109

Art Cutler
General Dynamics Space System Division, MZ C3-8830
P.O. Box 85990, San Diego, CA 92138

Robert Miller
NASA Lewis Research Center, MS 500-120
Cleveland, OH 44135

Don Page
General Dynamics Convair Division, MZ 23-6610
P.O. Box 85357, San Diego, CA 92138

Charles Engelhardt
Structural Dynamics Research Corporation
11055 Roselle St., San Diego, CA 92121

A modal test was conducted on the Centaur G Prime upper stage and its
support structure for which the primary purpose was to verify and/or
update the mathematical model used for preflight validation of the STS
flight. The unique character of the test was its successful completion
in a configuration and environment as representative as possible of
those of the flight condition. In that respect: (1) the actual flight-
type latches with their inherent play, backlash and friction, were used
to support the test article at the eight points of attachment as they
would be in the Shuttle Bay, (2) the Sine Dwell method of testing was
used in order to attain the highest possible level of response in the
structure. The objective sought in measuring normal modes at high level
was to obtain a valid, yet simple, linearization of the otherwise
complex problem of the lateral friction of the trunnions in the latches
and their backlash. A promising method for tuning a mode was implemented
during the test by displaying on the CRT, a scatter diagram in the
complex plane, of selected response accelerometers obtained at various
driving frequencies. A tuned mode was identified as the frequency
producing the minimum scatter or alternately the maximum correlation.

1.0 INTRODUCTION

The Centaur G Prime is a 25,000 kg upper
stage that, prior to the Challenger
accident, was to be used with the STS
Shuttle as a high energy interplanetary
launch vehicle for Galileo, Ulysses and
Magellan. Figure 1 shows the Centaur G
Prime in orbit carrying the Galileo
spacecraft after separation from the STS.

The modal test was conducted on the
Centaur vehicle, as a part of the series
of structural tests that are required for
the validation of the vehicle for STS
flight. The test was performed at the
General Dynamics Corporation Sycamore
Canyon, Site B, Test Facility in June-
July 1985. General Dynamics Corporation
(GDC) conducted the test under contract
to NASA for the NASA Lewis Research
Center. The Jet Propulsion Laboratory
(JPL) was under contract to support the
NASA Lewis Research Center and Structural
Dynamics Research Corporation (SDRC) was
under contract to support GDC.

The primary purpose of the test was to
obtain modal data in the form of resonant
frequencies and mode shapes, in order to
validate and/or update the Centaur finite
element model. This model is used in
conjunction with the STS and Payload
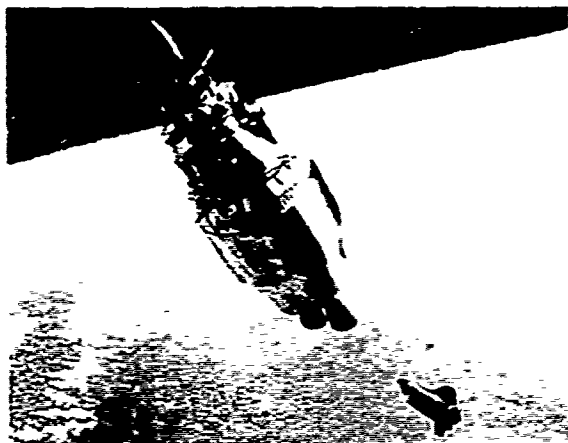models for the pre-flight verification

Figure 1. Centaur G Prime

coupled loads analysis of the entire
STS/Centaur/Payload systems. As a STS
requirement, all models used in the pre-
flight verification analysis must be
validated by test.

The actual test was divided into two
phases. The first phase was the Cargo
Element test for which the test article
comprised the Centaur and its support
structure as it would be in the Shuttle
Bay, in the launch configuration. The
objective of this first phase was to
obtain as mentioned above, data for the
system loads analysis at STS Liftoff and
Landing. The second phase of the test was
the free-free test of the Centaur alone
without its support structure for which
the primary objective was to obtain
structural data for the flight control
analysis of the Centaur vehicle in orbit
after separation from the STS.

The Cargo Element test was in turn
divided into two parts, a modal test with
trunnions free to slide, labelled
"unlocked" and a modal test with
trunnions "locked" to prevent sliding and
eliminate slop in the rails. In addition,
the same setup was also used for a twang
test. Only the Cargo Element with
trunnions free to slide (unlocked) will
be reported here. Details for the entire
series of tests are reported in Refs.
[1,2].

2.0 TEST ARTICLE

The Cargo Element test article consisted
of the Centaur G Prime two tank assembly,
two RL-10 engines from the Atlas /Centaur
mock up, the Galileo rigid simulator
mounted on its actual flight interface
adapter, the Centaur deployment adapter,
the Centaur Support Structure assembly
(CSS), the flight type latches for the

attachment into the STS Cargo Bay and the
simulated various equipment package
masses. Figure 2 shows a schematic
representation of the Cargo Element in
the test tower and Fig. 3 is a photograph
of the actual test setup. The mass
distribution of the major components of
the test article is shown in Table 1.

In all cases the LH2 tank was left empty.
The LOX tank was run either full of water
or empty. Only the case of the LOX tank
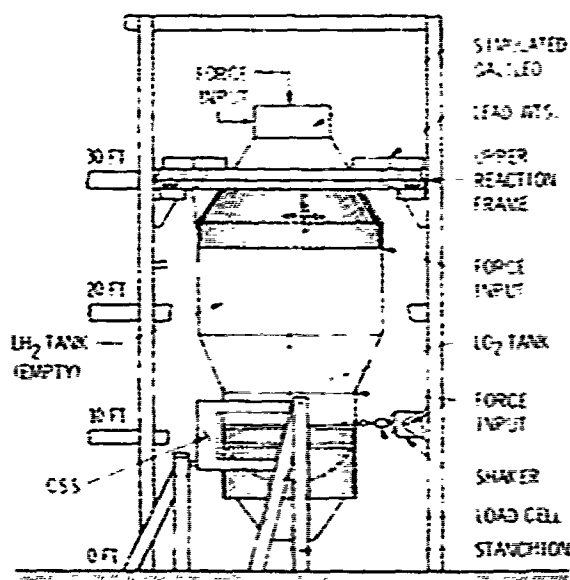full of water is reported here.

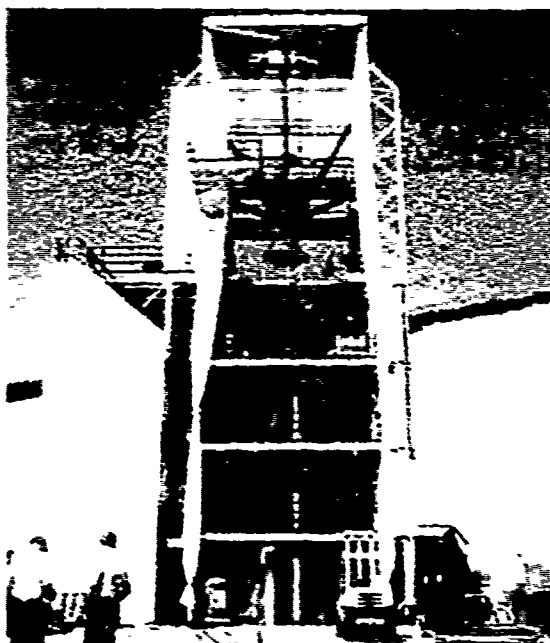Figure 2. Schematic Configuration for
the Cargo Element Test.

Figure 3. Cargo Element in the Test Tower

134

Table 1. Mass of Major Components of the Cargo Element (in kg)

Dry Tank Assembly (LH2 and LOX)	1652
Centaur FWD Adapter	250
Deployment Adapter Assembly	335
Centaur Support Structure (CSS)	1063
Simulated Rigid Galileo	2388
Galileo/Centaur Adapter	45
C1 Engine	145
C2 Engine	145
Other (mocked up equipment)	2226
Fluid in LH2 tank (empty)	0
in LOX tank (water)	14742
Total	22996

Figure 5. Typical Trunnion and Latch

3.0 TEST CONFIGURATION

3.1 Description

The Centaur Cargo Element is attached in the Shuttle Bay at eight (9) points by trunnions and latches for a total of ten (10) restrained degrees of freedom. Figure 4 shows a schematic representation of the overall attachment. Sliding is allowed in the unrestrained degrees of freedom. Figure 5 shows a typical attachment point where the trunnion can slide through the latch in the trunnion axial direction and the latch/trunnion assembly can slide as a whole in a direction perpendicular to the trunnion axis.

3.2 Test Philosophy

Loads for STS payloads are, in general, critical for Liftoff and Landing. Models of the entire STS system used to estimate loads are assembled mathematically by combining models of subsystems that are restrained at the common boundaries between subsystems (Craig-Bampton format). In the case of the Centaur Cargo Element these restrained degrees of freedom are those of the STS/Centaur boundaries of Fig. 4. Since loads are
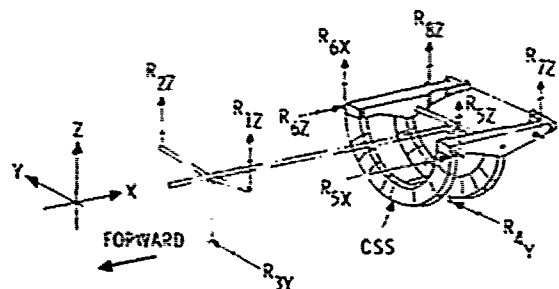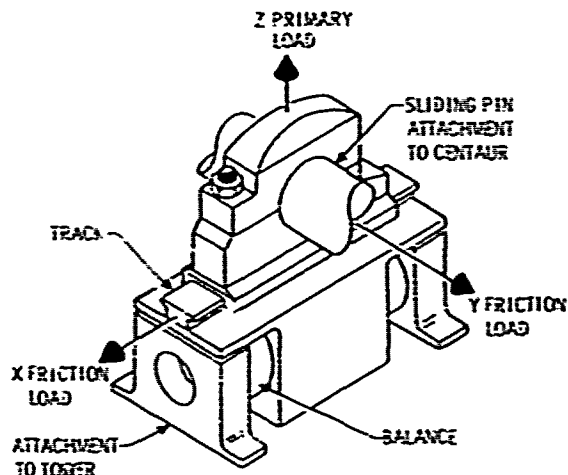
carried from one substructure to another through the boundaries between the substructures, characterization of the boundaries must be one of the primary objectives of the test. The philosophy followed for this test, as for any other payload, was that the modes were to be measured with flight-type trunnions and latches in place, in their near functional conditions i.e. carrying significant loads as representative as possible of the actual flight environment.

This philosophy has raised questions from some segment of the structural community because the trunnion/latch assemblies are inherently non-linear. This difficulty is acknowledged here, however the above philosophy was retained for this test as the one giving the most reliable data within a reasonable cost and schedule. It was postulated that sufficiently high amplitudes attained during the test would exercise the "sliding" of the trunnions, minimize backlash effect and yield a characterization of the non-linear latch/trunnion assemblies by an "equivalent" linearized large amplitude model. The alternate method of separating the latches from the rest of the "otherwise linear" structure, to run separate tests, one on the latches and trunnions to characterize their non-linearities, and one linear test on the rest of the structure, although more satisfying mathematically, was not retained. This alternate method was judged significantly more costly and with no assurance of a better reliability since non-linear characterization and non-linear analysis of structures remain difficult problems with low probability for accurate answers.

Figure 4. Trunnion Load Bearing Degrees of Freedom and Numbering

135

Further, the philosophy presented here is that of <u>not</u> using the test modes for loads analysis but instead, it is that of using the finite element NASTRAN model that has been properly updated after the test in such a way that each measured mode obtained at the <u>highest level of testing</u> is reasonably matched by the corresponding mode of the NASTRAN model. Any non-linearity shown in the test is equivalently linearized, for high amplitudes, by the updated model. In so doing the lack of good orthogonality of the measured modes because of non-linearity is not a primary requirement since these modes are not used for a loads analysis. The loads analysis instead, is done with a set of analytical modes that are orthogonal. Moreover the use of the NASTRAN model also allows the detailed calculation of loads anywhere in the payload while the limited number of measured modes would not.

3.3   Implementation

To implement the philosophy of testing under representative flight conditions the following was done:

a) the Cargo Element was tested upright an a tower creating a 1 g load along the longitudinal axis of the Centaur, the X axis. This is the configuration on the launching pad. During launch the quasi-static load varies from the 1.0 g at rest to 1.6 g's at full thrust of the STS engines. This last load was not simulated but only the 1.0 g was.

b) three (3) rigid stanchions, typically shown in Fig. 6, were erected on and tied to the ground floor on the seismic mass of the test tower, to support the CSS at its forward trunnions (R5X, R5Z, R6X,

R6Z), aft trunnions (R7Z, R8Z) and its keel (R4Y) (see Fig. 4). The weight of the test article (1.0 g loading) was reacted as in flight, only by the two CSS forward trunnions in the vertical direction, reactions R5X and R6X of Fig. 4.

c) another seismic mass of 46,000 kg was floated on air bags about 10 meters above the ground floor near the Centaur forward adapter to react the Centaur forward trunnions (R1Z, R2Z) and forward keel (R3Y). This seismic mass is labelled "upper reaction frame" (see Fig. 7). The mass of the upper reaction frame was determined analytically before the test as the mass necessary for a "near" restraint of each of the above trunnions and keel.

d) actual flight-type latches and rails, lubricated as for flight, were used to tie each trunnion and keel to the stanchions or to the upper reaction frame.

4.0   SHAKERS AND METHOD OF TESTING

Three (3) electromechanical shakers of approximately 4500 Newtons capability each were available for the test (Fig. 8). Only one (1) of these shakers was used at any one time to isolate the modes.

Because of the high level of response desired to overcome the backlash effect and induce slipping in the trunnions, the Sine Dwell method was retained as the primary method of testing to measure the modes. Multiple point Random excitation method was also used for exploratory identification of the modes at the low level of response. Also a limited amount of testing was done using the Sine Sweep method, broad band as well as narrow band. Only the Sine Dwell results are reported here.
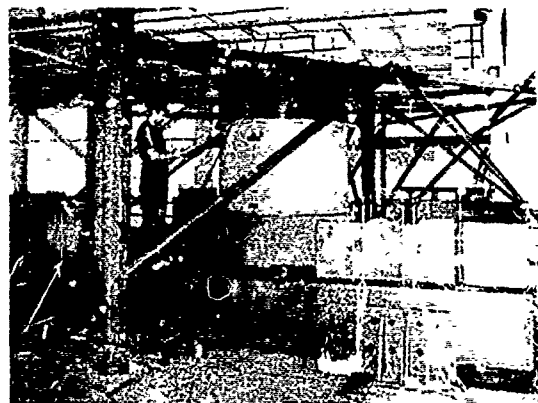

Figure 6.   Typical Support Stanchion

Figure 7.   Upper Reaction Frame
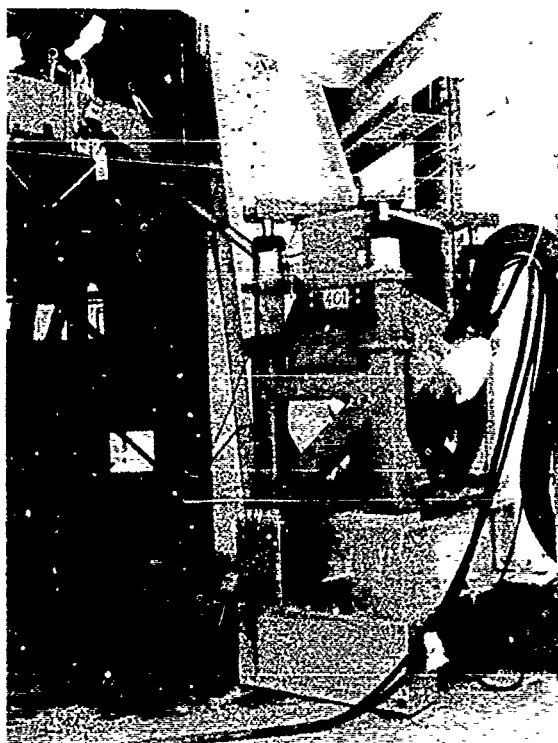
Figure 8. Electomechanical Shaker

5.0 EQUIPMENT

Figure 9 shows a simplified diagram of the electromechanical and electronics setup that was implemented for the test. In this setup, the heart of the system was made of:

a. the GENRAD 2515 analyzer for limited data acquisition and on site data processing,

b. the SRDC "MODAL PLUS" software for supporting the GENRAD 2515,

c. the CYBER Data Acquisition System for large volume data acquisition,

d. the VAX computer, not located at the test site, for large volume post processing of the data.

Other major components were:

Unholtz-Dickie Power Amplifiers and Shakers (2) (4450 Newtons)

Ling Power Amplifier and MB Shaker (1) (5340 Newtons)

Accelerometers (131)

Loads Cells (3).

Figure 9. Instrumentation Block Diagram

137

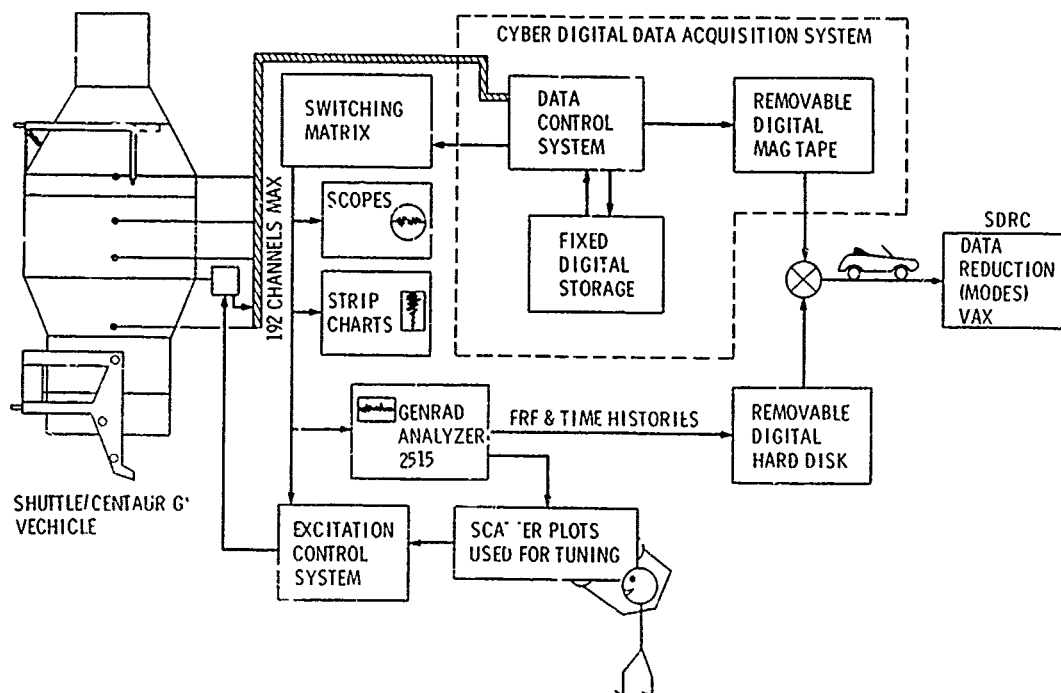In addition a variety of more standard equipment such as Oscillator, Co-Quad analyzer, Phase meter, Counters, Oscilloscopes, Tape Recorders, Oscillographs, etc... were also used in support of the main components.

6.0 TUNING OF A MODE FOR SINE DWELL

6.1 Tuning by Scatter Diagram

Real and imaginary components of the complex response of a structure excited by a sinusoidal force have been used in one way or another for many years in modal testing. The advent of Computer Aided Testing has allowed a systematic use of the complex response in the complex plane as a tuning aid to isolate a mode. This was reported in Refs. [3,4] for the Galileo spacecraft modal test and also in Ref. [5].

A practical use of the technique was done for the Centaur modal test. For a given shaker location, the power amplifier was driven by a sinewave at a chosen frequency f near the resonant frequency of the mode to be measured. The time response of 15 selected accelerometers were recorded and analyzed in the GENRAD 2515, to extract the real and imaginary parts (FRF) of the complex response at the fundamental driving frequency f. Displaying on the CRT (Fig. 10), the points which components are the real and imaginary parts of the complex responses, produces a diagram that in general, tends to be "scattered" over the whole plane when the exciting frequency falls outside a resonance. Since at resonance all the responses from the

accelerometers are expected "ideally" to be all in phase, the scatter will tend to disappear showing the displayed points gathering in a preferential direction, a regression line (least square best fit), indicating the correlation of phase between the responses of all the accelerometers. We note that all the displayed points would align on a single straight line only for a perfectly linear system excited perfectly to bring out only one mode eliminating all the others.

The observation that the complex responses in the complex plane tend to gather in a preferential direction, suggests a rather convenient way to look for a resonance. One systematically dwells at discrete frequencies and makes a diagram of the complex response points for each dwell, creating a family of diagrams. The diagram showing the minimum scatter or alternately the largest correlation, will indicate a resonance. As an additional aid, this scatter can be quantified by computing some statistical quantity indicative of the deviation from the best fit.

Figure 10 shows a typical scatter diagram for 15 selected accelerometers which was retained for a tuned mode obtained during the test. The MIF is the modal indicator function defined below which is a way to measure the maximum correlation between the points. We have,

$$MIF = 1.0 - SDM/SMM \qquad (1)$$

where

$$SDM = \Sigma(D(I)*M(I))$$

$$SMM = \Sigma(M(I)*M(I))$$

$D(I)$ = PL (Fig. 11) is the distance from the ith point to the best fit line,

$M(I)$ = OP (Fig. 11) is the vector magnitude of the ith point in the complex plane.

A MIF of 1.0 would indicate a perfectly tuned mode. The plotting of the scatter diagram and the MIF calculation were programmed by SDRC in the MODAL PLUS software and added to the GENRAD 2515 for the test. MIF values varying from .83 to .96 were achieved during the test. This method using the scatter diagram and looking for maximum correlation to tune a mode was found to be very effective and practical.

Figure 11 shows a good estimate of the physical mode shape MS(I) by projecting all the measured points in the complex plane on the best fit line making an angle A with the imaginary axis, Ref.[4].
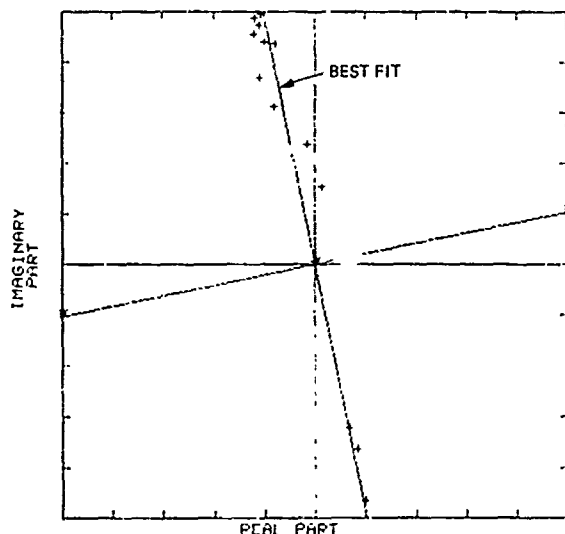

Figure 10. Typical Scatter Diagram

$$MS(I) = Y(I)*COS(A) - X(I)*SIN(A) \qquad (2)$$

6.2 Generalized Force as a Tuning Aid

For the Centaur modal test, the calculation of the generalized force, as a generalization of the method in Ref.[4], was also added to the diagram in an attempt to use the property that, at resonance, the generalized force vector must be perpendicular to the best fit line. However, this capability did not prove to be very useful since it became obvious during the course of the test that, at least, the local elastic deformations in the vicinity of the shaker attachment prevented a good phase measurement of the response at that point. The result of this poor phase definition for the point of application of the force did not allow a precise calculation of the generalized force (force times acceleration), making the generalized force data not directly usable except for the cases of attachment of the shaker on, locally, a very rigid part of the Centaur structure.

6.3 Damping

The damping of each measured mode was determined by the log decrement from the decay of selected accelerometers obtained on a strip chart by shutting off the force input. The modal damping shown in Table 2 is an average calculated from several accelerometer measurements.

7.0 PRE-TEST ANALYSIS

7.1 Test Analysis Model (TAM)

A NASTRAN analytical model of the test article was prepared before the test. This model comprised:

a) the Centaur G Prime Liftoff loads model (5.0) without fluid in any of the
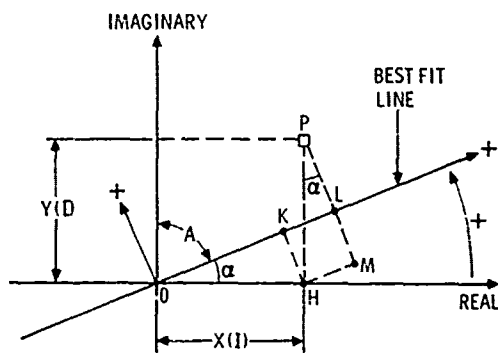

Figure 11. Mode Shape From Tuned Scatter Diagram

LH2 and LOX tanks and modified to reflect the differences between the flight structure and the test structure (Ref. [1])

b) the simulated rigid Galileo and its adapter

c) the support stanchions

d) the upper reaction frame

e) the fuel model for the LOX tank for the test condition labelled "full".

Modes were calculated for an "empty" and "full" LOX tank and with 3 kinds of boundary conditions that differ from one another by the support trunnion degrees of freedom allowed to react load to the rest of the support, namely:

case 1. CSS forward trunnions R5 and R6 do not slip (in Y)

case 2. all trunnions slip as in Fig. 4

case 3. all trunnions locked.

Case 1, with the LOX tank full, was judged the closest to the test results.

7.2 Target Modes

The target modes are the modes of significance that control the loads analysis for the Centaur and the Orbiter in the vicinity (bridge fittings) of the Orbiter/Centaur interfaces. These target modes were selected from the pre-test analysis done on the TAM, prior to the start of the test. The criteria for this selection [Ref. 4] was the effective mass of each mode (Appendix A) calculated from the pre-test analysis. The effective mass of the payload in the STS Orbiter (Centaur/Galileo test article here) for a given mode of the payload, is the mass that the STS Orbiter will "feel" through the trunnions and keels at the Centaur/Orbiter interface. Payload modes with large effective mass will intuitively influence the Orbiter much more than those with a small effective mass. Six target modes varying in frequency from 4.76 to 16.87 Hz were identified prior to the test, they are shown with corresponding resonant frequencies and effective masses as part of Table 3 under the TAM column.

8.0 TEST RESULTS

8.1 Non-linearity

All modes were measured for at least three (3) levels of excitation. The target modes were all measured.

The test showed the existence of a rather strong non-linearity of the resonant frequency and damping for most modes with respect to the level of the shaker force. The observed non-linearity is summarized in Table 2, the acceleration is that of the Galileo simulated payload. The data is also plotted in Fig. 12. It can be seen that the resonant frequencies tend to become constant for large forces. Only the modes obtained with the largest force of excitation were retained for subsequent analyses as being the most representative of the structure in flight.

Table 2. Variation of Major Resonant Frequencies and Dampings with Shaker Force (full, unlocked)

MODE	FORCE (N)	FREQ (Hz)	ACC (G)	DAMPING
FWD YAW	547	5.50	–	–
	885	5.27	–	–
	1290	5.08	–	–
	1721	4.73	–	–
	2224	4.60	.08	–
	3559	4.41	.14	.090
FWD PITCH	1134	7.64	.34	.034
	2282	7.97	.58	.035
	2318	7.87	.79	.035
AFT YAW	1112	8.38	–	.031
	2224	8.00	.24	.056
	3599	7.66	.42	.061
AXIAL	2224	8.42	.16	.028
	3336	8.27	.27	.026
	4448	8.22	.32	.027
AFT PITCH	2269	9.25	.50	.013
	3514	9.19	.66	.016

Figure 12. Variation of Resonant Frequencies with Shaker Force

8.2 Measured Modes and Effective Masses

Table 3 shows the correspondence of the effective mass (Appendix A1) of each measured mode to that of the pre-test analysis (TAM) for the case of the full LOX tank, retaining only the modes obtained with the largest force of excitation. This table shows that a discrepancy existed between the pre-test model and test results as far as frequency and effective mass are concerned. Table 3 also shows that all the modes with large effective masses were measured as evidenced by the sum of the effective mass of all measured modes
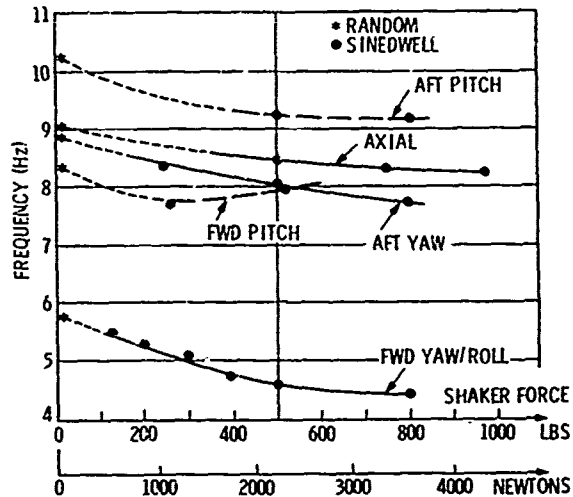
with comes very close to the total physical mass of the Cargo Element. The first two rows of Table 3 correspond to the slosh modes which were not attempted to be measured or analyzed in the pre-test model. However, their effective mass was estimated. In the pre-test TAM the fluid was assumed to be frozen.

The discrepancy of the pre-test model was subsequently corrected and the corrected model (post test TAM) used to create the loads model for the pre-flight verification analysis. The corrections will not be discussed here, they have been reported in Refs. [1,6]. The loads model was derived from the post test TAM, it reflects all the differences from the test article to the flight hardware, including the proper amount of fluid in both tanks, LOX and LH2.

8.3 Mass Matrix [m] for Measured Degrees of Freedom

In Table 3 the mass matrix [m] used for the calculation of the effective mass (Appendix A) was assembled from inspection of the test article on site and using the masses reported in Table 1. This mass matrix [m] describes the detail distribution of the mass assigned to each measured degree of freedom (110 measurements) on the Centaur and on the CSS (Cargo Element), excluding all the measurements made on latches and upper reaction frame. This mass matrix was judged to be more representative of the test article than the mass matrix obtained from a Guyan reduction of the pre-test NASTRAN model [Ref. 4]. This is because discrepancies in the original pre-test NASTRAN model are folded from

140

Table 3. Comparison of Target Modes for Test and pretest Analysis

MEASURED				PRE-TEST TAM			
FRZQ (Hz)	AXIAL (kg)	YAW (kg)	PITCH (kg)	FREQ (Hz)	AXIAL (kg)	YAW (kg)	PITCH (kg)
–	0	2270	0	–	–	–	–
–	0	0	2270	–	–	–	–
4.41	3	16960	2C	4.76	0	18667	0
7.66	0	588	19	7.81	0	964	0
7.87	0	6	15530	7.15	5310	0	13355
8.?2	21928	1	244	5.85	16882	0	4118
9.19	580	0	6370	10.97	22	0	2948
20.25	2	480	0	16.87	0	1094	0
TOTAL EFF.	22513	20305	24453		22214	20725	20421
TOTAL PHYS.	22996	22996	22996		22996	22996	22996
RATIO	.98	.88	1.06		.97	.90	.89

the very large (approximately 20,000) original degrees of freedom to the reduced mass matrix needed for the measured degrees of freedom (110). In other words the pre-test NASTRAN reduced mass matrix contains errors that would be eliminated only when the original NASTRAN model would have been appropriately corrected for stiffness to match the test results.

8.4 Orthogonality

Although orthogonality is not a very good criteria for goodness of the test when a structure shows non-linearities [Ref. 4] it was nevertheless calculated using the same matrix [m] in the equation of Appendix A as used for the effective mass. It is shown in Table 4.

8.5 Goodness of Test Data

The scatter diagram for the 110 accelerometer measurements of a tuned mode can be used to judge the goodness of the measurements by calculating the correlation derived from the least square fit of the data corresponding to the 110 points of the scatter diagram.

The least square calculation for the best fit minimizes the mean square value SDD of the perpendicular distance D(I) = LP (Fig. 11) between all the points and the best fit line. The square root of SDD is a statistical measure of the deviation

from the best fit in a direction perpendicular to it. It should be normalized to the root mean square value of the mode shape MS(I) = OL (Fig. 11) i.e. along the best fit line calculated over all the points (all the degrees of freedom of the mode). We will call "scatter" twice the normalized deviation:

$$SCTR = 2*\sqrt{SDD/SMM} \qquad (3)$$

where

$$SDD = \Sigma(D(I)*D(I))$$

$$SMM = \Sigma(MS(I)*MS(I))$$

The "correlation "is defined by:

$$CORR = \sqrt{1.0 - SCTR*SCTR} \qquad (4)$$

The scatter can also be assessed by an angle:

$$ANG = ASIN(SCTR) \qquad (5)$$

By taking twice the deviation for the scatter we can say that approximately 95% of the measurements will have a phase angle deviating from that of the best fit line by less than ANG.

The correlation as just defined above is derived from statistical concepts and is similar to the modal indicator function MIF of section 6.1. It could be used as an alternate for the tuning of a mode.

Table 4. Orthogonality of measured modes

MODE	FREQ (HZ)	1	2	3	4	5	6	7
1	4.41	1.00	.13	.05	-.02	-.03	-.04	.01
2	7.66	.13	1.00	-.01	-.02	.06	.12	-.01
3	7.87	.05	-.01	1.00	-.05	-.16	.00	-.04
4	8.22	-.02	-.02	-.05	1.00	.00	.01	.05
5	9.19	-.03	.06	-.16	.00	1.00	-.01	-.02
6	20.25	-.04	.12	.00	.01	-.01	1.00	.00
7	27.88	.01	-.01	-.04	.05	-.02	.00	1.00

It should be noted that MIF was calculated on site but only for a set of 15 selected points while CORR was calculated as a postprocessing step but for all the 110 measured degrees of freedom. It is used here for an overall assessment of the goodness of the test from a statistical view point. Table 5 shows the correlation for all measured modes for the case of the full LOX tank, again the modes are those obtained with the largest force of excitation. It is significant that this correlation is totally independent of any analysis on the structure with respect to stiffness and mass distribution. Therefore, it is truly an assessment of the quality of the measurements alone.

AS for the MIF, a correlation of 1.0 would mean that all the points fall on a straight line i.e. are in phase indicating a perfectly tuned mode. The value of the actual correlation for the test results varies from .853 to .997 indicating a very acceptable goodness of the test.

Table 5 also shows the values of MIF that are similar to those of the correlation.

8.6 Mode Shapes

Appendix B contains plots of selected significant measured modes.

Table 5. Goodness of Test Data (full case)

MODE	FREQ (HZ)	ANG (DEG)	CORR	MIF
1	4.41	10.3	.984	.963
2	7.66	31.4	.853	.895
3	7.87	10.8	.982	.950
4	8.22	4.2	.997	.899
5	9.19	11.7	.979	.894
6	20.25	26.3	.897	.828
7	27.88	13.5	.972	.929

9.0 CONCLUSION

The Centaur G Prime modal test resulted in sets of modes (frequencies, mode shapes and damping) with an accuracy similar to or better than that normally obtained from the modal testing of linear structures with no backlash and small damping. In other words, performing the test at high level greatly minimized the backlash effect and provided a valid, simple linearization of the trunnion friction problem for the Centaur in the Shuttle Cargo Bay. All the most important modes (target modes) were measured and provided the data base for updating the finite element model for the pre-flight verification loads analysis.

REFERENCES

1. Cutler,A., "Centaur G Prime Modal Survey, Final Report", General Dynamics Space System Division, San Diego, CA., Rep. No.GDSS-SSC-86-009, to be published, 1986.

2. Page,D., "Design Evaluation Test No.65A7758 Test Report for Shuttle/Centaur G Prime Modal Test P/N 65-07701-1",General Dynamics Convair Div., Vols.1-5, May 7, 1986.

3. Stroud,R., "The modal Survey of the Galileo Spacecraft", Sound and Vibration, Vol 18/Number 4, Ap. 1984.

4. Trubert,M., "Galileo System Modal Test", Vol. 1, Jet Propulsion Laboratory, California Institute of Technology, Report JPL D-950, January 31, 1984, (Internal Document).

5. Hunt,D., Matthews,J., Williams,R., "An Automated Tuning and Data Collection System for Sine Dwell Modal Testing", Paper 84-1058, Proceedings of the 24th AIAA/ASME/ASCE/AHS Structures, Structural Dynamics and Materials Conference, Part 2, Palm Spring, CA, May 1984.

6. Chen,J., Rose,T., Trubert,M., Wada,B., Shaker,F., "Modal Test/Analysis Correlation for Centaur G Prime Launch Vehicle", Proceedings of the 26th AIAA/ASME/ASCE/AHS

Structures, Structural Dynamics and
Materials Conference, Part 2,
pp 621-633, San Antonio, TX,
May 19-21, 1986.

APPENDIX A - MATHEMATICAL DEFINITIONS

A1. EFFECTIVE MASS

Call:
    d   the number of measured
         degrees of freedom
         (d = 110)
    [m] the mass matrix (diagonal)
         (110 x 110)
    {PHIEn} the nth elastic mode shape
         (1 x 110)
    [PHIR] the 6 rigid body modes
         (6 x 110).

The rigid elastic coupling column
(size 6) for the nth mode is

$$\{MREn\} = [PHIR][m]\{PHIEn\}$$

Then the effective mass (6 x 6) for the
nth mode is

$$[MEFFn] = \{MREn\}<MERn>$$

where $<MERn>$ is the transpose of $\{MREn\}$.

Only the three translation degrees of
freedom of the effective mass have been
retained here.

A2. ORTHOGONALITY

Call [PHIE] the matrix for all the
measured modes {PHIEn}, n = 1,...7,

$$[PHIE] = [PHIE1, PHIE2, \ldots, PHIE7]$$

the orthogonality matrix is

$$[ORTH] = [PHIE][m][PHIE]^T$$

where the superscript T means transpose.

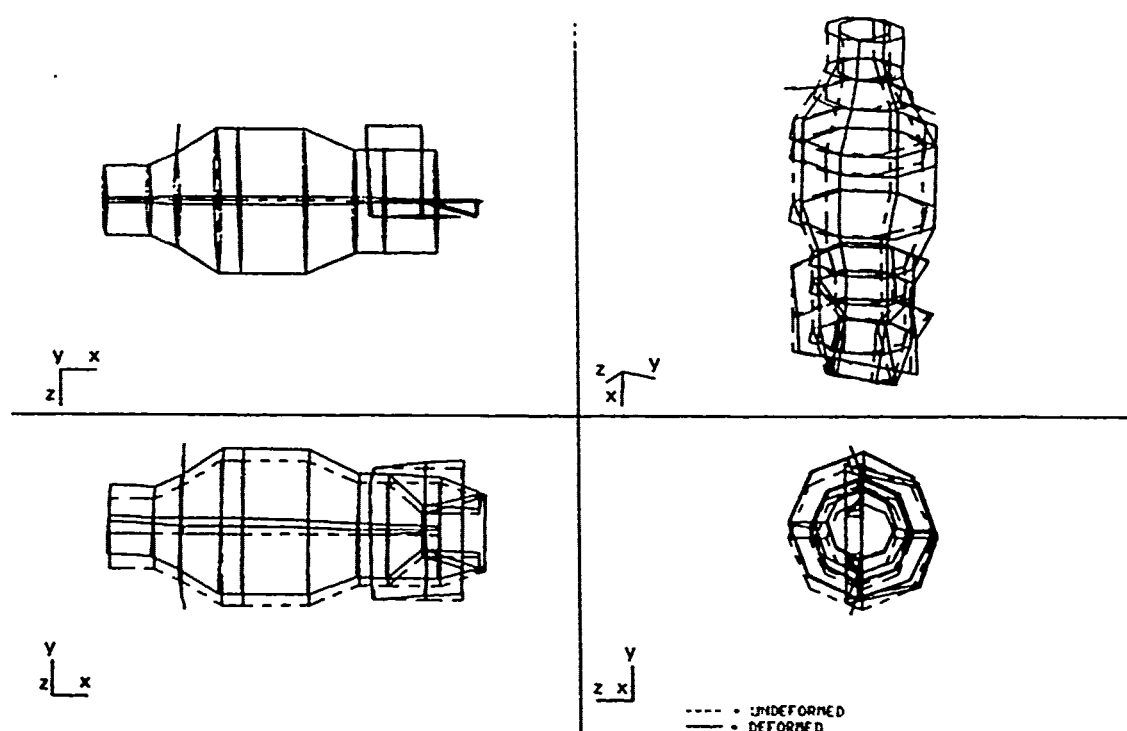## APPENDIX B - SELECTED MEASURED MODE SHAPES

---- • UNDEFORMED
——— • DEFORMED

Figure B1. FWD YAW/ROLL Mode at 4.41 Hz

143